

**DEVELOPING PATHWAYS FOR THE ELECTRIFIED PRODUCTION
OF FUELS AND CHEMICALS**

by
Wesley Luc

A dissertation submitted to the Faculty of the University of Delaware in partial fulfillment of the requirements for the degree of Doctor of Philosophy in Chemical Engineering

Spring 2019

© 2019 Wesley Luc
All Rights Reserved

**DEVELOPING PATHWAYS FOR THE ELECTRIFIED PRODUCTION
OF FUELS AND CHEMICALS**

by

Wesley Luc

Approved: _____

Eric M. Furst, Ph.D.

Chair of the Department of Chemical and Biomolecular Engineering

Approved: _____

Levi T. Thompson, Ph.D.

Dean of the College of Engineering

Approved: _____

Douglas J. Doren, Ph.D.

Interim Vice Provost for Graduate and Professional Education

I certify that I have read this dissertation and that in my opinion it meets the academic and professional standard required by the University as a dissertation for the degree of Doctor of Philosophy.

Signed: _____
Feng Jiao, Ph.D.
Professor in charge of dissertation

I certify that I have read this dissertation and that in my opinion it meets the academic and professional standard required by the University as a dissertation for the degree of Doctor of Philosophy.

Signed: _____
Bingjun Xu, Ph.D.
Member of dissertation committee

I certify that I have read this dissertation and that in my opinion it meets the academic and professional standard required by the University as a dissertation for the degree of Doctor of Philosophy.

Signed: _____
Raul F. Lobo, Ph.D.
Member of dissertation committee

I certify that I have read this dissertation and that in my opinion it meets the academic and professional standard required by the University as a dissertation for the degree of Doctor of Philosophy.

Signed: _____
Jingguang G. Chen, Ph.D.
Member of dissertation committee

ACKNOWLEDGEMENTS

First and foremost, I would like to sincerely thank my advisor, Prof. Feng Jiao, for the years of advice and support during my Ph.D. studies. His enthusiasm for tackling challenging problems and his constant pursuit to push the boundaries of science always amaze me, and will certainly have a lasting impact long after my time at University of Delaware. He has always pushed me to be the best researcher that I can be, constantly reminding me that we should always strive to be the best. I am grateful for the freedom and opportunities he has given me to explore and learn, as I was able to work on various types of projects. I would also like to thank my committee members: Prof. Bingjun Xu, Prof. Raul F. Lobo, and Prof. Jinguang G. Chen for serving on my committee and giving me advice throughout the years. I would like to specifically thank Prof. Bingjun Xu for allowing me to “borrow” chemicals/tools/equipment from his laboratory and Prof. Jinguang G. Chen for the many collaborative efforts. I would also like to thank Prof. Yushan Yan for giving me access to his laboratory and equipment.

I would like to thank my co-workers for all the support and intellectual conversations as many of my accomplishments would not have been possible without their help. I would like to thank the previous Jiao lab members: Prof. Qi Lu, Dr. Greg Hutchings, Dr. Bryan T. Yonemoto, and Dr. Jonathon Rosen for teaching me the ways of the Jiao lab. When I first joined the group, I was truly inspired by how much the group has accomplished in such a short period of time. I would like to thank the current members: Matthew Jouny, Emily Jeng, Byung Hee Ko, Sean Overa, Haeun Shin, Jing-Jing Lv, and Dr. Hongjie Tang. Work would certainly not be as fun without them, and each of them brought their unique personality and skills to the group from which I learned from. I especially want to thank Matthew Jouny for his creativity in instrumentation

and reactor designs, and Byung Hee Koo for his constant willingness to help with my research. I would also like to give a special shout-out to Charles Collins, who was an amazing undergraduate researcher that I worked closely with during the beginning of my studies. In addition, I would like to thank the Center for Catalytic Science & Technology and all its members for providing me resources and help throughout my time at University of Delaware.

Outside of work, I would like to thank all my friends that I have made at Delaware. Coming from San Diego, it is amazing to have a family away from home. Although there are too many people to name, I would like to specifically thank Matt Gilkey, Camil Diaz, Jared Nash, Nick Gould, Kat Wiley, Chen-Yu Chou, and Tamas Prileszky for all their support academically and for all the fun experiences, from going to concerts, food adventures, morning basketball sessions, learning to enjoy whiskey, and everything in between. At home, I would like to thank my lifelong friends, Jeff Lin, Lawrence Ho, Jian Yeung, Jon Choi, Michael Qian, Shida Salehi, and Emily Echeverria for all their support and efforts to visit me.

I would like to thank my Mom, Mytieg Lam, and Dad, Hueng Wing Luc, for the unconditionally love and support. Without them I would not be who I am today. They have always taught me to work hard and have always been there for me when I needed them the most. Words cannot describe how grateful I am. I would like to thank my older brother, Shaun Luc, and my younger sister, Joycelin Luc, for their constant support and belief in my studies. Lastly, I would like to thank my girlfriend, Jenni Shin, for her constant love and kindness. She has been a pillar in my graduate studies, always supporting my endeavors and teaching me how to become a better person.

TABLE OF CONTENTS

LIST OF TABLES	xi
LIST OF FIGURES	xii
ABSTRACT	xviii
Chapter	
1 INTRODUCTION	1
1.1 Development of Renewable Energy and Motivation for Electrochemical Processes	1
1.2 The Basics	2
1.2.1 Electrocatalysts	2
1.2.2 Electrochemical Reactors	6
1.3 The Hydrogen Evolution Reaction	7
1.4 The Electrochemical Conversion of CO ₂ to High-Value Chemicals	10
1.5 Thesis Scope and Structure	15
REFERENCES	17
2 EXPERIMENTAL SECTION	20
2.1 Techniques for the Fundamental Study of Electrocatalytic Systems	20
2.1.1 Three-Electrode Setup	20
2.1.2 Two-Electrode Setup	23
2.2 Electrochemical Reactor Design	23
2.2.1 Architecture	24
2.2.2 Polymer Electrolyte Membrane	25
2.2.3 Gas Diffusion Layer	27

2.2.4	Flow-Field Plate and Current Collector	28
2.2.5	Gasketing	29
REFERENCES	30
3	THE ROLE OF SURFACE OXOPHILICITY IN COPPER-CATALYZED WATER DISSOCIATION	32
3.1	Introduction	32
3.2	Experimental Methods	33
3.2.1	Preparation of Cu-based Bimetallic Systems	33
3.2.2	Structural Characterization	35
3.2.3	Electrochemical Evaluation	35
3.2.4	Computational Methods	36
3.3	Results	37
3.3.1	Hydrogen Binding Energy Calculations	37
3.3.2	Experimental Validation using Model Catalysts	39
3.3.3	Role of Oxophilic Dopants	41
3.4	Conclusions	45
3.5	Acknowledgment	45
REFERENCES	46
4	CARBON DIOXIDE SPLITTING USING AN ELECTRO-THERMOCHEMICAL HYBRID LOOPING STRATEGY	48
4.1	Introduction	48
4.2	Experimental Methods	51
4.2.1	Fabrication of Nanoporous Ag Electrode	51
4.2.2	Construction of the Ir-catalyst coated Nafion Membrane	51
4.2.3	Design and Operation of the CO ₂ Electrolysis Cell	51
4.2.4	Design and Operation of the CO Catalytic Bed Reactor	52
4.3	Results	53
4.3.1	Electrochemical Reduction of CO ₂	53

4.3.2	CO Thermochemical Conversion	57
4.4	Conclusions	60
4.5	Acknowledgment	61
REFERENCES		62
5	TWO-DIMENSIONAL COPPER NANOSHEETS FOR ELECTROCHEMICAL REDUCTION OF CARBON MONOXIDE TO ACETATE	64
5.1	Introduction	65
5.2	Experimental Methods	66
5.2.1	Synthesis of Cu Nanosheets	66
5.2.2	Synthesis of Cu Nanocubes	66
5.2.3	Preparation of Electrodes	67
5.2.4	Material Characterization	67
5.2.5	CO electrolysis	68
5.2.6	Labelled C ¹⁸ O experiment	69
5.2.7	Computational Methods	70
5.3	Results	70
5.3.1	Synthesis of Cu nanosheets	70
5.3.2	CO reduction performance	74
5.3.3	DFT Calculations	79
5.4	Conclusions	81
5.5	Acknowledgment	81
REFERENCES		83
6	SULFUR DIOXIDE-INDUCED SELECTIVITY CHANGE IN CARBON DIOXIDE ELECTROLYSIS	86
6.1	Introduction	86
6.2	Methods	89
6.2.1	Electrode preparation	89
6.2.2	CO ₂ electrolysis in flow-cell electrolyzer	89
6.2.3	Material characterization	90

6.2.4	Computational methods	91
6.3	Results	91
6.3.1	Initial Characterization and Experimental Procedures	91
6.3.2	Influence of SO ₂ on Ag and Sn–catalyzed CO ₂ reduction	92
6.3.3	Influence of SO ₂ on Cu–catalyzed CO ₂ reduction	94
6.3.4	Density Functional Theory Calculations	99
6.4	Conclusions	102
6.5	Acknowledgments	103
REFERENCES		104
7 CONCLUSIONS AND RECOMMENDATIONS		106
7.1	Conclusions	106
7.2	Recommendations	108
7.2.1	Nanostructured Catalysts for the HER	108
7.2.2	System Integration of the Two-Step Process for CO ₂ conversion to C ₂₊ products	109
7.2.3	Electrolyzer Development for Acetic Acid Production	110
7.2.4	Development of SO ₂ -Resistant Catalysts and Study of Other Gaseous Impurities	111
REFERENCES		113
Appendix		
A	ASSEMBLY OF THE FLOW-CELL ELECTROLYZER	114
B	SUPPLEMENTARY INFORMATION FOR CHAPTER 3: THE ROLE OF SURFACE OXOPHILICITY IN COPPER-CATALYZED WATER DISSOCIATION	126
C	SUPPLEMENTARY INFORMATION FOR CHAPTER 4: CARBON DIOXIDE SPLITTING USING AN ELECTRO-THERMOCHEMICAL HYBRID LOOPING STRATEGY	134
D	SUPPLEMENTARY INFORMATION FOR CHAPTER 5: TWO-DIMENSIONAL COPPER NANOSHEETS FOR ELECTROCHEMICAL REDUCTION OF CARBON MONOXIDE TO ACETATE	142
E	SUPPLEMENTARY INFORMATION FOR CHAPTER 6: THE	

	INFLUENCE OF SULFUR DIOXIDE IMPURITY ON CARBON DIOXIDE ELECTROLYSIS	160
F	ORIGINAL CONTRIBUTIONS	173
G	COPYRIGHT PERMISSIONS	175

LIST OF TABLES

3.1	Calculated HBEs and OBEs for Cu–M(111) and Cu(111) surface	39
3.2	Bulk and surface compositions of Cu–M bimetals and Cu	41
B.1	Calculated HBEs and OBEs for Cu–M(111) and Cu(111) surface	126
B.2	Calculated HBEs and OBEs for Pt(111) surface	127
B.3	Calculated HBEs and OBEs for sub-layer substitution surface model	127
B.4	Calculated HBEs and OBEs for metal oxide cluster on Cu(111) surface model	127
C.1	Long-duration test results of CO catalytic bed reactor	135
E.1	Surface atomic concentrations of metal sulfides in Ag, Sn, and Cu samples obtained from XPS	160
E.2	Surface atomic concentrations of Cu ₂ S in Cu samples	172
E.3	DFT calculated binding energies (in eV) of HER and CO ₂ RR intermediates	172

LIST OF FIGURES

1.1	Schematic of electrified pathways for fuel and chemical production	3
1.2	Summary of CO ₂ reduction performances toward various products	12
1.3	Schematic of CO ₂ electrolysis for C ₂₊ products formation	14
2.1	Schematic of the three-electrode setup and electrochemical techniques	22
2.2	Schematic representation of the two common electrochemical reactors for CO ₂ /CO electrolysis	25
2.3	Schematic representation of polymer electrolyte membranes	26
2.4	Schematic representation of a gas diffusion layer	29
3.1	Photograph images of Cu–M electrodes	34
3.2	DFT models of Cu–M surfaces	38
3.3	XRD characterization of Cu–M bimetallics and Cu	40
3.4	Electrochemical characterization of Cu-M bimetallic alloys	42
3.5	Electrochemical characterization of Cu/MO/OH.	43
4.1	Schematic representation of the electro-thermochemical hybrid looping process	50
4.2	Electrochemical reduction of CO ₂	55
4.3	Single pass conversion study for CO ₂ electrolyzer	57
4.4	CO catalytic bed reactor.	59
4.5	Thermochemical conversion of CO.	61

5.1	Characterization of Cu nanosheets and Cu nanocubes	72
5.2	CO reduction performance of Cu nanosheets	75
5.3	Comparison of Cu nanosheets with commercial Cu particles	78
5.4	DFT calculations	80
6.1	Schematic of CO ₂ electrolyzer and potential feed sources	88
6.2	Performance of CO ₂ + SO ₂ electrolysis over Ag and Sn catalysts	94
6.3	Performance of CO ₂ + SO ₂ electrolysis over Cu catalyst	98
6.4	DFT calculations for S–doped Cu surfaces	101
7.1	Schematic of a two-step process for CO ₂ conversion with separation	109
A.1	Photograph of flow-cell electrolyzer components	114
A.2	Photograph of the electrodes and supports	115
A.3	Flow-cell electrolyzer assembly: Step 1	116
A.4	Flow-cell electrolyzer assembly: Step 2	116
A.5	Flow-cell electrolyzer assembly: Step 3	117
A.6	Flow-cell electrolyzer assembly: Step 4	117
A.7	Flow-cell electrolyzer assembly: Step 5	118
A.8	Flow-cell electrolyzer assembly: Step 6	118
A.9	Flow-cell electrolyzer assembly: Step 7	119
A.10	Flow-cell electrolyzer assembly: Step 8	119
A.11	Flow-cell electrolyzer assembly: Step 9	120
A.12	Flow-cell electrolyzer assembly: Step 10	120
A.13	Flow-cell electrolyzer assembly: Step 11	121

A.14	Flow-cell electrolyzer assembly: Step 12	121
A.15	Flow-cell electrolyzer assembly: Step 13	122
A.16	Flow-cell electrolyzer assembly: Step 14	122
A.17	Side view of the assembled flow-cell electrolyzer	123
A.18	Photograph of the three-electrode setup for flow-cell electrolyzer testing	124
A.19	Photograph of the overall setup for electrochemical evaluation	125
B.1	Sub-layer substitution surface model	126
B.2	Metal oxide cluster on Cu(111) surface model	128
B.3	XPS characterization of as-prepared Cu–M bimetallics	129
B.4	XPS characterization of as-prepared Cu/MO/OH catalysts	130
B.5	SEM images of Cu/MO/OH catalysts	131
B.6	SEM image and HER performance of Cu/TiO ₂ at higher loading	132
B.7	HER activity of Pt	133
C.1	Photograph of the CO ₂ electrolyzer	134
C.2	CO ₂ electrolyzer electrodes	136
C.3	In-line CO ₂ contactor design	137
C.4	Photograph of CO catalytic bed reactor	138
C.5	XPS analysis of np–Ag	139
C.6	Calculation of required O ₂	140
D.1	XRD pattern of randomly deposited Cu nanosheets	142
D.2	Control experiments for Cu nanosheets synthesis	143

D.3	Stability of as-synthesized Cu nanosheets	144
D.4	XRD patterns to confirm the stability of Cu nanosheets	145
D.5	UV-vis absorption spectrum of Cu nanosheets	146
D.6	DRIFT spectra of the Cu nanosheets	147
D.7	Oxidation-tolerance of Cu nanosheets {111} facets	148
D.8	CO reduction performance for Cu nanosheets in 0.5 M KOH	149
D.9	CO reduction performance for Cu nanosheets in 1.0 M KOH	149
D.10	Photograph of <i>operando</i> XAS flow-cell electrolyzer	150
D.11	<i>Operando</i> XAS measurements	150
D.12	Partial current densities plotted versus the absolute potential and Tafel analysis	151
D.13	GC-MS analysis of labelling study	152
D.14	Catalyst structural characterization of commercial Cu catalysts	153
D.15	<i>In-situ</i> OH _{ads}	153
D.16	CO reduction performance for 1 μm Cu particles	154
D.17	CO reduction performance for 25 nm Cu particles	154
D.18	ECSA characterization	155
D.19	CO reduction performance for ascorbic acid treated 25 nm Cu particles	156
D.20	CO reduction performance of Cu nanocubes Cu	157
D.21	Energy and structure evolution for water incorporation into ketene and *CH–CO	158
D.22	CO reduction reaction free energy profiles	158

D.23	CO reduction reaction free energy profiles for acetate formation from ketene intermediate and ethanol formation	159
E.1	SEM images of as-prepared electrodes	160
E.2	PXRD pattern of commercial particles	161
E.3	XPS spectrum of as-prepared electrodes	161
E.4	XPS spectrum of Ag-catalyzed CO ₂ + 1% SO ₂ electrolysis	162
E.5	XPS spectrum of Sn-catalyzed CO ₂ + 1% SO ₂ electrolysis	162
E.6	SEM images of Ag catalysts at various time points of CO ₂ + 1% SO ₂ experiment	163
E.7	SEM images of Sn catalysts at various time points of CO ₂ + 1% SO ₂ experiment	163
E.8	CO ₂ reduction over Cu catalyst	164
E.9	XPS spectrum of Cu standards	164
E.10	SEM images of Cu catalysts at various time points of CO ₂ + 1% SO ₂ experiment	165
E.11	HRTEM of surface Cu ₂ S	165
E.12	Additional HAADF-STEM images and EELS mapping of Cu catalyst	166
E.13	HAADF-STEM images and EELS mapping of as-prepared Cu catalyst	167
E.14	CO ₂ reduction over Cu catalyst with FAA ionomer	168
E.15	HAADF-STEM images and EELS mapping of Cu catalyst after 5 hour of electrolysis	169
E.16	CO ₂ reduction over commercial Cu ₂ S particles	170
E.17	CO ₂ reduction over Cu catalyst with 0.1% SO ₂ feed	170
E.18	CO ₂ reduction over Cu catalyst with 0.01% SO ₂ feed	171

E.19	Attempted recovery of Cu catalyst	171
------	---	-----

ABSTRACT

The electrochemical conversion of Earth abundant resources such as water and CO₂ to value-added fuels and chemicals powered by renewable energy is a promising avenue toward a sustainable future. In this thesis, I report a series of studies ranging from more fundamental investigation of bulk metallic surfaces, to reactor engineering/process design, to the synthesis of nanostructured catalysts, and finally to the study of catalytic degradation in efforts to develop highly active, selective, and efficient processes for the H₂ evolution and CO₂/CO reduction reactions. I will show how various efforts can be utilized in conjunction with one another to solve key challenges faced in the development of these electrochemical systems.

I will first begin by examining bulk Cu-based bimetallic catalysts for the H₂ evolution reaction in alkaline conditions to identify key descriptors to guide the design of non-precious catalysts. Through a systematic study using a series of first-row transition metal dopants, I will show that we can enhance the H₂ evolution activity by doping Cu with highly oxophilic metals. The enhancement is due to the synergistic effects between the oxophilic dopant and Cu which help absorption and activation of the water molecule to form the first H_{ads} intermediate, thus enhancing activity.

In the second work, I will present a reactor engineering/process design study where we scale up a nanoporous-silver catalyst and design an electrochemical reactor that can continuously convert CO₂ to CO with high selectivity and activity. Through engineering design, I will demonstrate how we can take advantage of the solubility of CO₂ in aqueous electrolyte to achieve a high single-pass conversion of ~86% with a CO Faradaic efficiency as high as ~96%.

Taking the lessons learned from the previous studies, I will demonstrate CO reduction at high reaction rates ($\geq 100 \text{ mA cm}^{-2}$), which has not been previously achieved,

by utilizing a novel flow-cell electrochemical reactor. In addition, we will study carbon to carbon bond formation in Cu-catalyzed CO₂/CO reduction at commercially-relevant rates of reaction by designing and integrating nanostructured catalysts that selectively exposed specific surfaces. In particular, Cu nanosheets that selectively expose the (111) facets demonstrate high selectivity toward acetate formation with an acetate Faradaic efficiency as high as ~48% and an acetate partial current density up to 131 mA cm⁻² in alkaline conditions. Further analysis suggest that the improved acetate formation is due to the suppression of ethylene and ethanol formation.

Next, I will demonstrate that Cu catalysts are highly susceptible to SO₂ impurity in CO₂ reduction. Using a combination of electrochemical activity studies, computation predictions, and advanced microscopic efforts, I will show that the formation of surface Cu sulfides is responsible for the irreversible suppression of multi-carbon products.

I conclude by describing emerging directions stemming from these studies in efforts to further push these electrochemical systems toward commercial applications.

Chapter 1

INTRODUCTION

1.1 Development of Renewable Energy and Motivation for Electrochemical Processes

Developing sustainable pathways for fuel and chemical production is critical as the human population is expected to increase from 7.4 to 9.4 billion by year 2040. This exponential growth will be accompanied by an increased in energy demand as well as carbon dioxide (CO_2) emission (32 Gt yr^{-1} in 2013 to 36 Gt yr^{-1} by 2040) since fossil resources (e.g. coal, oil, gas) are expected to remain the dominant feedstock for the transportation, energy, and industrial sectors.[1, 2] The critical challenge is to support prosperity and enhanced living standards while reducing environment impacts. For this reason, developing new technologies that lessen society's reliance on fossil resources is essential.

In regards to these concerns, the development of renewable energy such as wind and solar has attracted much attention in recent years as these energy sources are expected to show significant growth due to technological advances, reduction in production costs, and legislative policies.[3, 4] For example, the global photovoltaic (PV) industry has experienced an order of magnitude growth from ~ 3 to ~ 30 GW between 2007 and 2012 and is expected to reach or exceed a growth rate of $\sim 100 \text{ GW yr}^{-1}$ by 2020.[5] Advances in solar cell efficiency up to $\sim 24\%$, improvement in modular durability with lifetime exceeding 30 years, more efficient manufacturing practices, and implementation of feed-in-tariff policies to encourage deployment of renewable energy have enabled fast growth and reduction in PV module prices, with a projected electricity price from PVs to be low as $\$0.03 \text{ kWh}^{-1}$ by 2030.[5] However, while the

U.S. Energy Information Administration (EIA) estimated that renewable sources will account for over 31% of the total electricity generation by year 2050, renewable energy in the transportation and industrial sectors are expected to be <1% and ~10.5%, respectively, even though these sectors account for a total of ~50% of the US CO₂ emissions.[6] Therefore, a greater penetration of renewable energy into the transportation and industrial sectors are urgently required.

One possible solution is using renewable energy to power the electrochemical transformation of Earth abundant feedstocks such as water (H₂O) and CO₂ to produce value-added fuels and chemicals as shown in Figure 1.1.[7, 8] For example, electricity from PVs can drive the water-splitting reaction to produce green hydrogen (H₂) that can be used in fuel cells to power vehicles. CO₂ captured from the atmosphere or from point sources can be used as carbon feedstocks as alternatives to fossil resources to produce fuels and commodity chemicals, potentially providing a net-zero emission solution. The advantage of electrochemical technologies is that they are scalable due to modular reactor designs and therefore, can be easily integrated with distributed renewable energy sources. A recent techno-economic analysis has emphasized that the ability to obtain cheap electricity ($\leq \$0.03 \text{ kWh}^{-1}$) is critical as this reduced price will make electrochemical processes more economically competitive toward existing technologies.[9] Thus, the foreseen inexpensive electricity price from PVs further motivates the development of electrochemical technologies for fuel and chemical production. Centered to the deployment of electrochemical processes is the development of improved electrocatalysts and electrochemical reactors (electrolyzers) that can efficiently and selectively facilitate chemical transformation.

1.2 The Basics

1.2.1 Electrocatalysts

Electrocatalysts help facilitate the electrochemical transformation of chemical species by lowering activation barriers.[7] As such, they help enable electrochemical reactions to proceed at faster rates than otherwise possible. There are various forms of

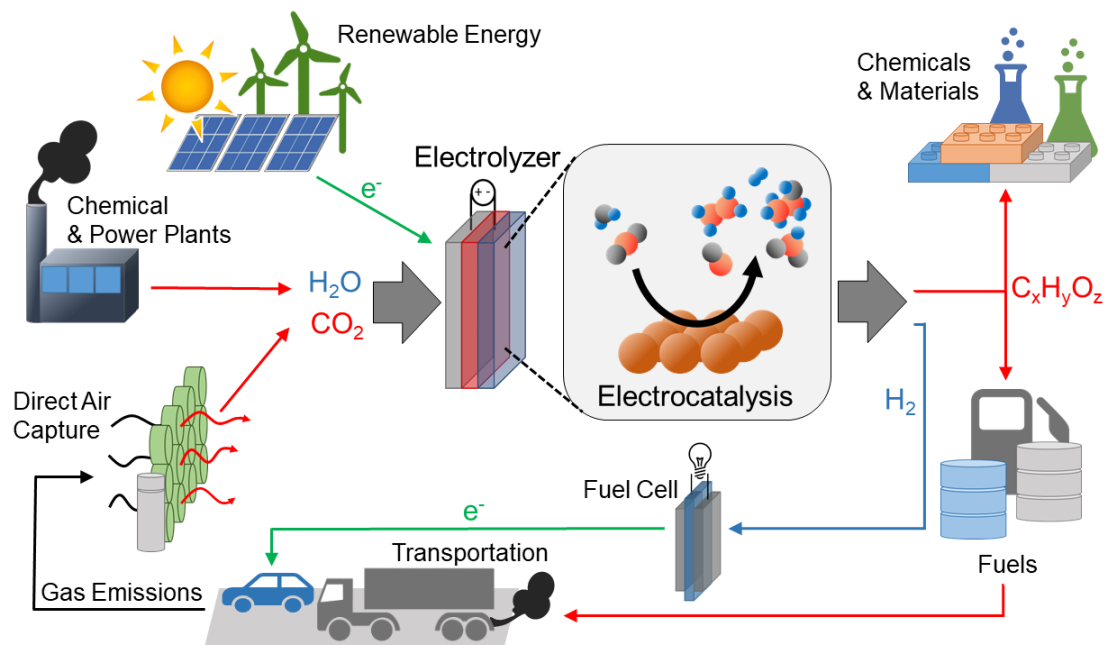
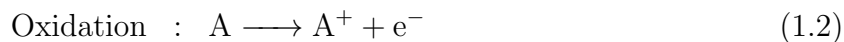
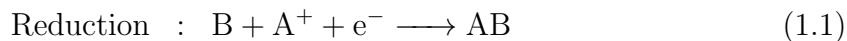


Figure 1.1: Schematic of electrified pathways for fuel and chemical production.

electrocatalysts such as molecular and surface-mediated catalysts each with their own advantages and disadvantages. The latter is also known as heterogeneous catalysts and will be the main focus of this thesis. In heterogeneous electrocatalysis, reactant species are typically first adsorbed onto the active sites of the catalyst surface. Upon adsorption, exchange of electrons and/or bond formation or cleavage occurs at a lower activation energy, thus enhancing the rate of reaction. After the reactions have proceeded, the products then desorb, leaving the catalytic sites unchanged and allowing for the sites to facilitate further chemical transformations, if ideally the catalyst surface is not deactivated.

In electrochemistry, there are two types of reaction: reduction where chemical species gain electrons and oxidation where they lose electrons. The general forms are

written as follow:



where reduction occurs at the cathode and oxidation occurs at the anode. Equations 1.1 and 1.2 are the reductive and oxidative half-reactions, respectively, that make up the overall reaction (Equation 1.3). As these reactions occur on the surface in heterogeneous electrocatalysis, the general forms of these reactions can further be written into series of elementary steps involving the formation of adsorbed states on the catalytic surface. This will become clear when describing the mechanism of the hydrogen evolution reaction on a catalytic surface in the following section.

To promote the overall reaction, a voltage is applied between the anode and cathode, thus changing the free energy of reaction. The change in free energy can be described as the following:

$$\Delta G = -nFE \quad (1.4)$$

where ΔG is the change in free energy of the reaction, n is the number of moles of e^- transferred, F is the Faraday constant ($96\,485.3365(21) \text{ C mol}^{-1}$), and E is the applied cell potential. The minimum potential needed to drive the reaction is dependent on the two half-reactions which is dictated by thermodynamics. Typically, additional potential on top of the theoretical potential is applied to drive the reaction, which is also referred as the overpotential. The overpotential is defined as:

$$\eta = E - E^o \quad (1.5)$$

where η is the overpotential, E is the applied voltage, and E^o is the thermodynamic potential. The overpotential is the additional energy input into the overall system which can significant increase the operating cost of the reaction.

The reaction rate in electrocatalysis can be described by the following Tafel equation:

$$i = nFke^{-\alpha F\eta/RT} \quad (1.6)$$

where i is the current density, n is the number of moles of e^- transferred, k is the reaction rate constant, α is the charge transfer coefficient, F is the Faraday constant, η is the overpotential, R is the universal gas constant and T is the reaction temperature. The current density is defined as the current flow divided by the active electrode area at a given potential and is a measurement of the electrochemical reaction rate. As shown, the current density has a direct response to the overpotential and can be precisely controlled by changing the applied voltage. Thus, electrochemical processes benefit from being able to operate at ambient conditions (e.g. room temperature and atmospheric pressure) with quick startups and shutdowns. A high current density is ideal since it minimizes the electrode size and potentially reduces capital investment. Electrocatalysts are critical as they help lower the overpotential needed to drive the reaction in order to obtain a desired rate of reaction, thus minimizing the energy input into the electrochemical system.

There are two general approaches toward improving the activity of an electrocatalytic system: increasing the number of active sites (e.g. increasing the catalyst loading on a given electrode size) or increasing the intrinsic activity of each catalytic site. In the former case, there are physical limits to how much catalyst can be loaded without affecting physical stability, charge transfer, and mass transport of reactants. On the contrary, improving the intrinsic activity directly improves the performance of the catalyst, potentially allowing for a decrease in catalyst loading and reduction in cost. One possible strategy toward improving intrinsic activity is manipulating the material composition such as alloying two metals together, where the binding energy of the active sites can be altered by changing the electronic properties. Another strategy is changing the local structure by exposing favorable surfaces, as different coordination environments have different binding strengths that can potentially stabilize key

reaction intermediates. Generally, a combination of various strategies is used to design highly active and selective electrocatalysts. More details about tuning the activity of electrocatalysts can be found in References [7, 10].

1.2.2 Electrochemical Reactors

A electrochemical reactor (electrolyzer) is essentially a device that takes in energy to facilitate a chemical reaction. Thus, a typically electrolyzer not only consists of catalysts to facilitate both half-reactions, but also a polymer electrolyte membrane that separates the cathode and anode chambers, flow-field plates, and current collectors. As commercial-relevant electrolyzers are more dynamic and complex in nature, only focusing on improving the activity of the catalysts will have its limitations. In many cases, the overall performance of an electrolyzer is not only dictated by the catalysts, but also by the how efficient the reactants/products are delivered to and away from the catalytic sites, how well electrons and ions are transported, and how stable the device operates under working conditions. Therefore, reactor engineering to develop novel electrolyzers is also as critical as discovering new catalysts toward achieving high performing and stable electrochemical systems. The architecture and design of electrolyzers are further discussed in Chapter 2.2.

Although the characterization of every individual feature of an electrolyzer is quite complex, there are several key figures of merit that are commonly used to characterize the performance of an electrolyzer. The Faradaic efficiency, also known as the current efficiency, for a given product is defined as follows:

$$\varepsilon_{Faradaic} = \frac{z * n * F}{Q} \quad (1.7)$$

where z is the number of required electrons to produce a given product, n is the number of moles of the given product, F is the Faraday constant, and Q is the total charged passed. In other words, the Faradaic efficiency is the selectivity of reducing the reactant toward a specific product and is commonly used in CO₂ reduction as CO₂

can be reduced to various products. A high Faradaic efficiency toward one product is desired to minimize post-reaction separation costs.

The energetic efficiency is defined as follows:

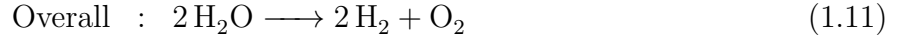
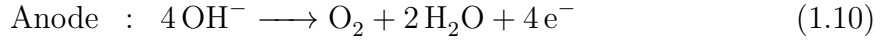
$$\varepsilon_{energetic} = \sum_i \frac{E_i^o \varepsilon_{i, Faradaic}}{E_i^o + \eta} \quad (1.8)$$

where E_i^o is the equilibrium cell potential for product i , $\varepsilon_{i, Faradaic}$ is the Faradaic efficiency of product i , and η is the total cell overpotentials including the anodic and cathodic kinetic activation, mass transport limitations, and ohmic resistances (e.g. ionic and electronic conductivity). A high energetic efficiency is desired as it signifies that a small energy penalty is needed to produce a desired product. Ideally, a commercial-ready electrolyzer should have able to operate at high current densities, high Faradaic efficiency toward one desired product, high energetic efficiency, high conversion, and good long term stability that utilizes inexpensive materials.

1.3 The Hydrogen Evolution Reaction

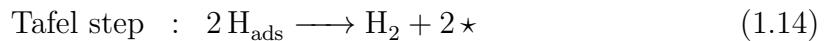
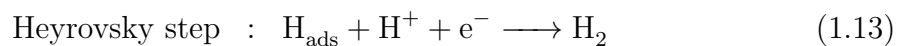
The advancement of fuel cells and their deployment in the automobile industry have motivate the development of new processes to obtain H_2 fuel. Although H_2 can be obtained from steam reforming of natural gas, which is currently the dominant method of producing H_2 , this process relies heavily on fossil resources, mainly methane (CH_4), that releases large amounts of CO_2 . Another alternative is electrochemical water-splitting that uses renewable energy to power the chemical conversion of H_2O to produce H_2 and oxygen (O_2) at ambient conditions, thus providing a potential pathway for producing green H_2 .^[11–13] Although there are significant efforts in developing water-splitting electrolyzers that operate in acidic conditions, it is well known that very few materials outside of the platinum (Pt)–group metals are stable as well as active. Therefore, Pt and iridium oxide (IrO_2) are typically used as the cathode and anode catalysts, respectively, thus driving up the cost of these devices.^[14] On the contrary, if an alkaline-based counterpart can be developed, cheaper materials such as

transition metals like nickel (Ni) and copper (Cu) can be used. The overall water-splitting reaction in alkaline conditions can be described as follow:



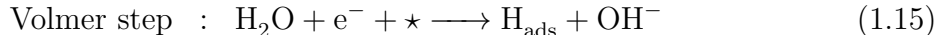
where Equation 1.9 is known as the hydrogen evolution reaction (HER) and Equation 1.10 is known as the oxygen evolution reaction (OER). These two reactions make up the overall water-splitting reaction as described in Equation 1.11. In a typically water-splitting electrolyzer, these two half-reactions are performed in individual compartments separated by a polymer electrolyte membrane. This helps with product separation as H_2 and O_2 are generated separately. More details about these membranes are discussed in Chapter 2.2.2. As mentioned, electrocatalysts are essential to minimize the overpotentials needed to drive both the H_2 evolution and O_2 evolution half-reactions. Currently, iron (Fe) and Ni oxide-based materials are the state-of-the-art OER catalysts in alkaline conditions.[15] When normalized to the surface area, many of these non-precious metal oxides exhibit similar OER activities as their precious metal oxide counterparts. On the contrary, Pt is still the most active HER catalyst, as non-precious HER catalysts in basic conditions are still underdeveloped, and further work is necessary.[14]

The HER is a two-electron transfer reaction with one catalytic intermediate, adsorbed hydrogen (H_{ads}), and may occur through either the Volmer-Heyrovsky or the Volmer-Tafel mechanism. The exact mechanism for the HER is still under great debate despite its simplicity. In acidic conditions, the steps are described as follow:



where \star denotes a site on the catalyst surface. As H_{ads} is the key reaction intermediate, it is widely accepted that the overall reaction rate is dictated by the hydrogen adsorption free energy (ΔG_H), also known as the hydrogen binding energy (HBE).[16–19] If the catalytic surface binds too weakly to the hydrogen intermediate, then the adsorption (Volmer) step will be rate limiting; whereas, if the surface binds too strongly, then the desorption (Heyrovsky/Tafel) step will be limiting. Pt has a near optimum HBE with an intermediate binding energy that doesn't bind too strongly or too weakly, and thus, Pt is generally regarded as the state-of-the-art HER catalyst. The ability to control the binding energies of key reaction intermediates is critical toward designing materials with improved performance.

In alkaline electrolytes, H_2O is the proton source as the abundance of protons is low, and therefore, Equations 1.12 and 1.13 can be rewritten as follow:

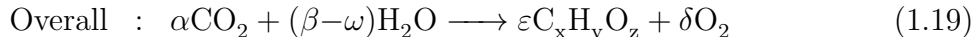


where again, \star denotes a site on the catalyst surface.[20] The Tafel step is identical to the Tafel step in acid (Equation 1.14), and likewise, the exact mechanism of the HER in alkaline conditions is still unclear. Although it is widely accepted that the precise control of the HBE is critical toward developing improved HER catalysts in acidic conditions, it still remains a question whether solely controlling the HBE in alkaline conditions is universal as H_2O instead of H^+ is the proton source. For example, it has been shown that depositing transition metal hydroxide clusters (e.g. $Ni(OH)_2$) on Pt surface enhances HER activity in alkaline conditions compared to pure Pt.[21–23] It was concluded that the metal hydroxide clusters promote water dissociation (Volmer step) and H_{ads} formation on Pt, consequentially improving the overall rate of H_2 generation. However, the scarcity and high cost of Pt still remains a barrier toward the widespread utilization of water-splitting electrolyzers, and has motivated significant efforts in finding cheaper alternatives. In efforts toward finding a cheaper alternative

and to further elucidate governing parameters for catalytic design, the fundamental study of non-precious Cu-based bimetallics as HER catalysts in alkaline conditions is presented in Chapter 3.

1.4 The Electrochemical Conversion of CO₂ to High-Value Chemicals

The electrochemical conversion of CO₂ (CO₂ electrolysis) powered by renewable energy provides a net-zero or potentially negative CO₂ emission pathway for producing value-added fuels and chemicals.[7] For example, ethanol and ethylene can be electrochemically produced from CO₂, and these chemicals have large uses in the transportation and industrial sectors, thus allowing for the penetration of renewable energy into these sectors.[9] The overall CO₂ reaction can be described as follow:



where CO₂ is reduced at the cathode to form carbon-based products and water is oxidized at the anode to produce O₂. As similar to water-splitting electrolyzers, these two half-reactions are typically performed in separated compartments divided by a polymer electrolyte membrane. This is crucial as it prevents reduction products that are generated at the cathode from being transported to and subsequently oxidized at the anode. As CO₂ is a thermodynamically stable molecule, energy is required to transform CO₂ into more desirable products. Thus, electrocatalysts are needed to lower the activation barriers to minimize this energy input. Furthermore, as represented (C_xH_yO_z), there are a vast number of CO₂ reduction products that can be produced such as carbon monoxide (CO), formate, CH₄, and multi-carbon (C₂₊) products such as ethanol, ethylene, and n-propanol, each involving multiple proton/electron transfers with a number of possible reaction intermediates. Therefore, designing a catalyst that can steer product selectivity as well as lower the activation barriers is a critical

challenge. Furthermore, as CO_2 reduction is typically done in aqueous electrolyte as a proton source is needed in the reaction, the HER is also a competitive side reaction since thermodynamically, the half-reaction potentials for reducing CO_2 to most CO_2 reduction products are comparable to H_2 evolution. This further adds another level of complexity beyond just avoiding unwanted carbon-based by-products.[24–27]

The study of electrocatalysts for CO_2 reduction can be dated back to the mid-1980s when Hori and co-workers investigated a wide range of heterogenous elemental surfaces to determine their selectivity as well as activity toward different CO_2 reduction products.[26, 27] It was shown that metals such as gold (Au), silver (Ag), and zinc (Zn) are CO selective, while lead (Pb) and tin (Sn) are formate selective. Metals such as Fe, Ni, and Pt mainly produced H_2 due to favorable proton adsorption. Interestingly, Cu is the only monometallic that can reduce CO_2 to C_{2+} products with appreciable selectivities. Since these initial studies, there have been significant efforts toward developing new CO_2 reduction catalysts such as nanostructured materials (e.g. nanoporous Ag),[28, 29] bimetallics (e.g. Cu-Ag, Cu-Zn),[30–32] and even exploring materials beyond just simple metals, such as nitrogen-doped carbon-based materials[33] and chalcogenides.[34] Furthermore, there also have been significant developments toward designing high-performing electrolyzers with novel architectures that can efficiently and selectively convert CO_2 . [32, 35–40] As shown in Figure 1.2, the development of processes that can convert CO_2 to CO and formate has reached commercially relevant rates of reaction ($\geq 100 \text{ mA cm}^{-2}$) with high selectivities ($\geq 85\%$). However, the production of C_{2+} products are far from ready, reflecting the difficulties in producing C_{2+} products as these products require carbon-carbon (C–C) bond formation and multiple proton/electron transfers.

Despite the inherent challenges, there are continual interests in developing electrochemical processes aimed at producing these C_{2+} products at commercially relevant rates of reaction ($\geq 100 \text{ mA cm}^{-2}$) as the global market size of ethanol and ethylene is \$65 and \$160 billion, respectively.[9] This represents a significant market as ethanol is heavily used in the transportation sector as fuel additives and ethylene is a major

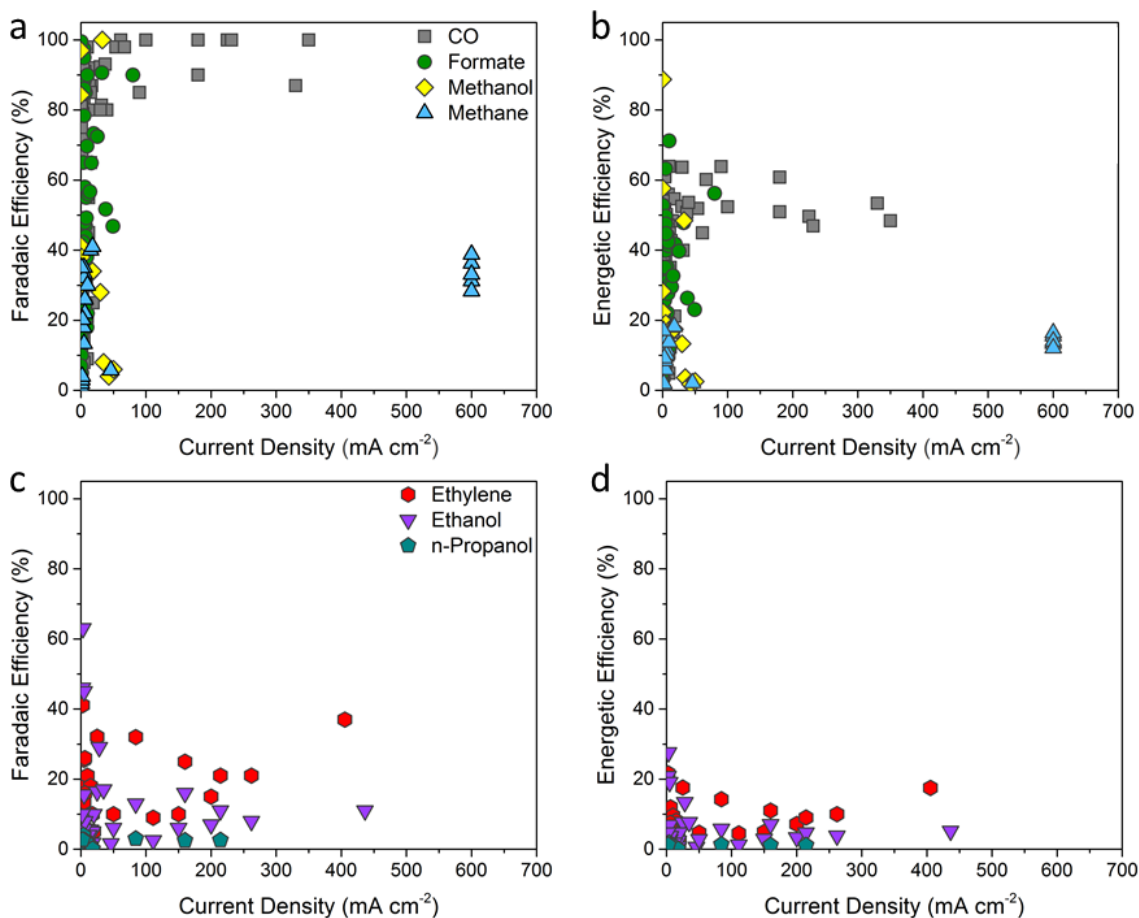


Figure 1.2: Summary of CO₂ reduction performances. Faradaic efficiency versus total current density for a) C₁ and c) C₂-C₃ products and energetic efficiency versus total current density for b) C₁ and d) C₂-C₃ products.[9]

industrial chemical precursor toward plastics. As Cu is the only monometallic that can reduce CO₂ to C₂₊ products at appreciable selectivities, significant efforts including single-crystal studies [41–43], spectroscopic investigations [44, 45], and computational works [46, 47] have been devoted toward gaining a deeper understanding of why Cu is unique. Similar to the HBE for HER, studies have indicated that controlling the binding strength of adsorb CO (CO_{ads}) is critical, as Cu has an intermediate CO binding strength that allows for further reduction and eventual C–C bond formation.[25] Other studies have also indicated that the surface atomic arrangement of Cu is ideal

for C–C coupling. For example, previous works have shown that the Cu (100) surface is favorable for ethylene formation, while the Cu (110) surface is more favorable for ethanol.[41–43] However, vast majority of these fundamental studies are conducted in batch electrochemical cells operating at low current densities (a few tens of mA cm^{-2}) due to the low solubility of CO_2 in aqueous electrolytes ($\sim 33 \text{ mM}$ in H_2O at ambient conditions). This presents a gap between fundamental research and device-level studies, and little is known at a molecular-level about how Cu catalyst behaves at more commercially relevant rates of reaction ($\geq 100 \text{ mA cm}^{-2}$). As catalytic phenomenon observed at low rates can be very different at high rates, it is critical to bridge this gap in order to further develop high-performing electrochemical systems for industrial applications.

Another hurdle toward the development of CO_2 electrolysis is developing a sustainable process for CO_2 conversion to C_{2+} products. Recent studies using flow-cell electrolyzers have shown that conducting CO_2 reduction in alkaline electrolytes significantly enhances the formation of C_{2+} products due to the suppression of the competitive HER and enhancement in C–C coupling.[35, 38] However, operating direct CO_2 reduction in alkaline electrolyte (Figure 1.3a) is not sustainable at a practical level as CO_2 strongly reacts with hydroxide ions (OH^-) to form bicarbonate (HCO_3^-) and carbonate (CO_3^{2-}) mixtures, thus degrading the electrolyte and reducing the efficiency of CO_2 utilization (Figure 1.3b).[37, 48] To address this issue, a two-step process (Figure 1.3c) has been proposed as an alternative to direct CO_2 reduction. In the first electrolyzer, CO_2 is first converted to CO in neutral conditions using a Ag catalyst. The produced CO is then further converted using a Cu catalyst in a second electrolyzer that operates in alkaline conditions to produce C_{2+} products. As it is believed that CO reduction shares reaction pathways similar to those of CO_2 reduction after CO_2 is converted to CO_{ads} , a direct CO feed as reactant may promote C–C coupling by increasing the local CO concentration near the catalyst surface. Furthermore, by doing CO reduction, it allows for a deeper understanding of C_{2+} product formation on Cu due to a less complex reaction interface as CO does not react with OH^- and avoids

potential catalyst-poisoning effects from the formation of formate. However, the critical challenge for CO reduction is that CO has orders of lower solubility (~ 0.1 mM in H_2O at ambient conditions) than CO_2 , and thus the rate of reaction is greatly limited by the mass transport of CO to the catalytic surface. Furthermore, developing a high-performing CO_2 electrolyzer with high-single pass conversion is critical to minimize unreacted CO_2 from entering the CO electrolyzer that otherwise would increase separation costs. With these challenges in mind, the design of an electrolyzer for the electrochemical conversion of CO_2 to CO with high single-pass conversion is the main focus of Chapter 4, while the study of CO reduction over well-defined nanostructured Cu catalysts at high rates of reaction is presented in Chapter 5.

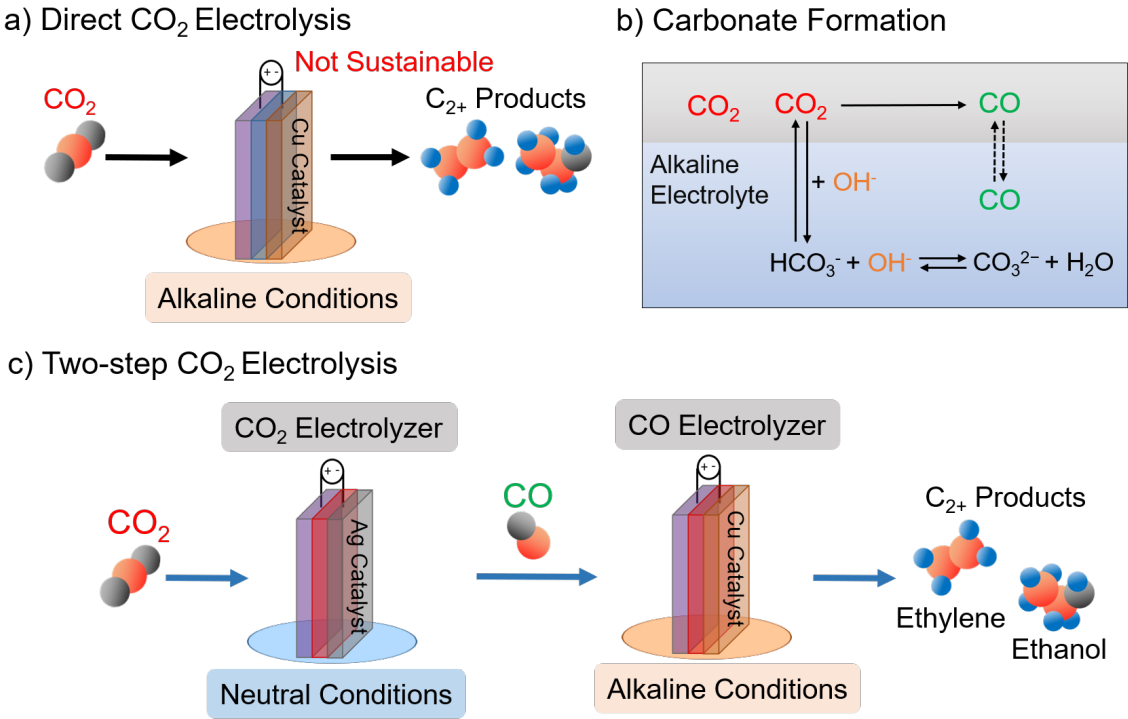


Figure 1.3: Schematic of CO_2 electrolysis for C_{2+} products formation. a) Direct CO_2 reduction, b) Mechanism of carbonate formation, and c) two-step process for CO_2 reduction

Finally, critical toward the commercialization of CO_2 electrochemical processes

is identifying mechanisms for performance degradation in order to develop strategies to mitigate these effects. While significant studies have concluded that trace metal impurities in the electrolyte (e.g. Fe^{2+} , Zn^{2+}) can dramatically degrade CO_2 reduction performance where the catalytic surface can be irreversibly altered through the deposition of these metal ions,[49, 50] few works have studied the influence of gaseous impurities in CO_2 electrolysis. The CO_2 feedstock will likely be obtained from point sources such as power plants or chemical facilities in the near future,[51, 52] as direct air capture is currently expensive and still being developed.[53, 54] As these exhaust streams contain impurities such as SO_x , NO_x , or volatile organic compounds, it is important to understand how these impurities can affect CO_2 reduction for practical applications. The study of gaseous impurities (mainly SO_2) in CO_2 electrolysis is presented in Chapter 6.

1.5 Thesis Scope and Structure

The goals of this thesis are to establish guiding principles for the rational design of electrocatalysts, engineer high performing electrolyzers that can operate at commercially-relevant rates of reaction, and to identify degradation mechanisms in efforts to address several key issues toward the development and commercialization of electrochemical processes for water-splitting and CO_2/CO conversion. Following the introductory chapter, there are six chapters describing these efforts.

In Chapter 2, an overview of experimental methods and reactor designs that are utilized throughout this thesis is presented. Experimental techniques such as the two-electrode and three-electrode setup will be reviewed. Details of electrolyzers including the membrane electrode assembly-based electrolyzer and the flow-cell electrolyzer will be discussed.

In Chapter 3, the study of Cu-based bimetallics for the electrochemical H_2 evolution is presented. In this study, a combined computational and experimental effort was used to identify key descriptors for the rational design catalysts. We concluded

that the oxophilicity of transition metals is also an important parameter to consider when designing non-precious electrocatalysts for the HER in alkaline conditions

In Chapter 4, a high-performing CO₂ electrolyzer was developed to selectively convert CO₂ to CO through reactor engineering, achieving a high single-pass conversion of ~86% with a CO Faradaic efficiency up to ~96%. In particular, the CO₂ electrolyzer was utilized as part of a proof-of-concept for an electro-thermochemical hybrid looping strategy for O₂ recovery applications for deep space manned missions.

In Chapter 5, well-defined nanostructured Cu catalysts that selectively exposed specific surfaces such as the Cu(111) and Cu(100) were examined for CO reduction at high rates of reaction using a novel flow-cell electrolyzer. In alkaline environment, the Cu nanosheets that selectively expose the (111) surface exhibit an acetate Faradaic efficiency of ~48% and an acetate partial current density up to 131 mA cm⁻², which is among the highest reported to date toward acetate formation. Further analysis suggest that the improved acetate selectivity is due to the suppression of ethylene and ethanol formation.

In Chapter 6, the influence of gaseous SO₂ impurity on CO₂ electrolysis over Ag, Sn, and Cu catalysts were studied. Experimental results show that Cu is highly susceptible to SO₂ impurity, as SO₂ impurity alters the catalytic surface through the formation of surface metal sulfides and shifts the selective toward formate, while suppressing C₂₊ products. Computational results suggest that sulfur-doped Cu surfaces are favorable for formate formation, as consistent with experimental results.

In Chapter 7, the overall conclusions are presented along with possible direction for future work. These suggestions are related to the future designs and implementations of water-splitting and CO₂ electrolyzers.

REFERENCES

- (1) Exxon Mobil Corporation Outlook for Energy:A view to 2040.; 2018.
- (2) International Energy Agency World Energy Outlook 2018.; 2018.
- (3) Chu, S.; A., M. *Nature* **2012**, *488*, 294–303.
- (4) Lewis, N.; Nocera, D. *Proceedings of the National Academy of Sciences of the United States of America* **2006**, *103*, 15729–15735.
- (5) Haegel, N. M. et al. *Science* **2017**, *356*, 141–143.
- (6) U.S. Energy Information Administration Annual Energy Outlook 2019 with projections to 2050.; 2019.
- (7) Seh, Z. W.; Kibsgaard, J.; Dickens, C. F.; Chorkendorff, I. B.; Norskov, J. K.; Jaramillo, T. F. *Science* **2017**, *355*.
- (8) Newman, J.; Hoertz, P. G.; Bonino, C. A.; Trainham, J. A. *Journal of Electrochemical Society* **2012**, *159*, A1722.
- (9) Jouny, M.; Luc, W.; Jiao, F. *Industrial & Engineering Chemistry Research* **2018**, *57*, 2165–2177.
- (10) Mistry, H.; Varela, A.; Kuhl, S.; Strasser, P.; Cuenya, B. *Nature Reviews Materials* **2016**, *1*, 16009.
- (11) Turner, J. A. *Science* **2004**, *305*, 972–974.
- (12) Shaner, M. R.; Atwater, H. A.; Lewis, N. S.; McFarland, E. W. *Energy Environmental Science* **2016**, *9*, 2354.
- (13) Ball, M.; Weeda, M. *International Journal of Hydrogen Energy* **2015**, *40*, 7903.
- (14) McCrory, C. C. L.; Jung, S.; Ferrer, I. M.; Chatman, S. M.; Peters, J. C.; Jaramillo, T. F. *Journal of the American Chemical Society* **2015**, *137*, 4347–4357.
- (15) McCrory, C. C. L.; Jung, S.; Peters, J. C.; Jaramillo, T. F. *Journal of the American Chemical Society* **2013**, *135*, 16977–16987.
- (16) Nørskov, J. K.; Bligaard, T.; Logadottir, A.; Kitchin, J. R.; Chen, J. G.; Pandelov, S.; Stimming, U. *Journal of The Electrochemical Society* **2005**, *152*, J23–J26.
- (17) Trasatti, S. *Journal of Electroanalytical Chemistry and Interfacial Electrochemistry* **1972**, *39*, 163–184.

- (18) Parsons, R. *Transactions of the Faraday Society* **1958**, *54*, 1053–1063.
- (19) Sheng, W.; Gasteiger, H. A.; Shao-Horn, Y. *Journal of The Electrochemical Society* **2010**, *157*, B1529–B1536.
- (20) Strmcnik, D.; Uchimura, M.; Wang, C.; Subbaraman, R.; Danilovic, N.; van der Vliet, D.; Paulikas, A. P.; Stamenkovic, V. R.; Markovic, N. M. *Nature Chemistry* **2013**, *5*, 300–306.
- (21) Subbaraman, R.; Tripkovic, D.; Strmcnik, D.; Chang, K.-C.; Uchimura, M.; Paulikas, A. P.; Stamenkovic, V.; Markovic, N. M. *Science* **2011**, *334*, 1256–1260.
- (22) Subbaraman, R.; Tripkovic, D.; Chang, K.-C.; Strmcnik, D.; Paulikas, A. P.; Hirunsit, P.; Chan, M.; Greeley, J.; Stamenkovic, V.; Markovic, N. M. *Nature Materials* **2012**, *11*, 550–557.
- (23) Danilovic, N.; Subbaraman, R.; Strmcnik, D.; Chang, K.-C.; Paulikas, A. P.; Stamenkovic, V. R.; Markovic, N. M. *Angewandte Chemie International Edition* **2012**, *51*, 12495–12498.
- (24) Kuhl, K. P.; Cave, E. R.; Abram, D. N.; Jaramillo, T. F. *Energy & Environmental Science* **2012**, *5*, 7050–7059.
- (25) Kuhl, K. P.; Hatsukade, T.; Cave, E. R.; Abram, D. N.; Kibsgaard, J.; Jaramillo, T. F. *Journal of the American Chemical Society* **2014**, *136*, 14107–14113.
- (26) Hori, Y.; Wakebe, H.; Tsukamoto, T.; Koga, O. *Electrochimica Acta* **1994**, *39*, 1833–1839.
- (27) Hori, Y.; Murata, A.; Takahashi, R. *Journal of the Chemical Society-Faraday Transactions I* **1989**, *85*, 2309–2326.
- (28) Lu, Q.; Rosen, J.; Zhou, Y.; Hutchings, G. S.; Kimmel, Y. C.; Chen, J. G.; Jiao, F. *Nature Communications* **2014**, *5*, 3242.
- (29) Rosen, J.; Hutchings, G. S.; Lu, Q.; Forest, R. V.; Moore, A.; Jiao, F. *ACS Catalysis* **2015**, *5*, 4586–4591.
- (30) Clark, E. L.; Hahn, C.; Jaramillo, T. F.; Bell, A. T. *Journal of the American Chemical Society* **2017**, *139*, 15848–15857.
- (31) Ren, D.; Ang, B.; Yeo, B. *ACS Catalysis* **2016**, *6*, 8239–8247.
- (32) Ma, S.; Sadakiyo, M.; Heima, M.; Luo, R.; Haasch, R. T.; Gold, J. I.; Yamauchi, M.; Kenis, P. J. A. *Journal of the American Chemical Society* **2017**, *139*, 47–50.
- (33) Wu, J. et al. *Nature Communications* **2016**, *7*, 13869.
- (34) Asadi, M. et al. *Science* **2016**, *353*, 467–470.
- (35) Ma, S.; Sadakiyo, M.; Luo, R.; Heima, M.; Yamauchi, M.; Kenis, P. J. A. *Journal of Power Sources* **2016**, *301*, 219–228.

- (36) Verma, S.; Lu, X.; Ma, S. C.; Masel, R. I.; Kenis, P. J. A. *Physical Chemistry Chemical Physics* **2016**, *18*, 7075–7084.
- (37) Verma, S.; Hamasaki, Y.; Kim, C.; Huang, W.; Lu, S.; Jhong, H.-R. M.; Gewirth, A. A.; Fujigaya, T.; Nakashima, N.; Kenis, P. J. A. *ACS Energy Letters* **2018**, *3*, 193–198.
- (38) Lv, J.-J.; Jouny, M.; Luc, W.; Zhu, W.; Zhu, J.-J.; Jiao, F. *Advanced Materials* **2018**, *0*, 1803111.
- (39) Masel, R. I.; Liu, Z.; Sajjad, S. *ECS Transactions* **2016**, *75*, 1143–1146.
- (40) Delacourt, C.; Ridgway, P. L.; Kerr, J. B.; Newman, J. *Journal of the Electrochemical Society* **2008**, *155*, B42–B49.
- (41) Schouten, K. J. P.; Qin, Z.; Pérez Gallent, E.; Koper, M. T. M. *Journal of the American Chemical Society* **2012**, *134*, 9864–9867.
- (42) Schouten, K. J. P.; Gallent, E. P.; Koper, M. T. M. *ACS Catalysis* **2013**, *3*, 1292–1295.
- (43) Hahn, C.; Hatsukade, T.; Kim, Y. G.; Vailionis, A.; Baricuatro, J. H.; Higgins, D. C.; Nitopi, S. A.; Soriaga, M. P.; Jaramillo, T. F. *Proceedings of the National Academy of Sciences of the United States of America* **2017**, *114*, 5918–5923.
- (44) Malkani, A.; Dunwell, M.; Xu, B. *ACS Catalysis* **2018**, *9*, 474–478.
- (45) Zhu, S.; Jiang, B.; Cai, W.; Shao, M. *Journal of the American Chemical Society* **2017**, *139*, 15664–15667.
- (46) Calle-Vallejo, F.; Koper, M. T. M. *Angewandte Chemie-International Edition* **2013**, *52*, 7282–7285.
- (47) Liu, X. Y.; Schlexer, P.; Xiao, J. P.; Ji, Y. F.; Wang, L.; Sandberg, R. B.; Tang, M.; Brown, K. S.; Peng, H. J.; Ringe, S.; Hahn, C.; Jaramillo, T. F.; Norskov, J. K.; Chan, K. R. *Nature Communications* **2019**, *10*, 32.
- (48) Dinh, C. T.; Garcia de Arquer, F. P.; Sinton, D.; Sargent, E. H. *ACS Energy Letters* **2018**, *3*, 2835–2840.
- (49) Hori, Y.; Konishi, H.; Futamura, T.; Murata, A.; Koga, O.; Sakurai, H.; Oguma, K. *Electrochimica Acta* **2005**, *50*, 5354–5369.
- (50) Wuttig, A.; Surendranath, Y. *ACS Catalysis* **2015**, *5*, 4479–4484.
- (51) Koytsoumpa, E. I.; Bergins, C.; Kakaras, E. *Journal of Supercritical Fluids* **2018**, *132*, 3–16.
- (52) Wu, X. M.; Yu, Y. S.; Qin, Z.; Zhang, Z. X. *Energy Procedia* **2014**, *63*, 1339–1346.
- (53) Sanz-Perez, E. S.; Murdock, C. R.; Didas, S. A.; Jones, C. W. *Chemical Reviews* **2016**, *116*, 11840–11876.
- (54) Keith, D. W.; Holmes, G.; Angelo, D. S.; Heidel, K. *Joule* **2018**, *2*, 1573–1594.

Chapter 2

EXPERIMENTAL SECTION

2.1 Techniques for the Fundamental Study of Electrocatalytic Systems

The studies in Chapters 3, 5, and 6 use the three-electrode setup to evaluate the catalytic performance of materials, while Chapter 4 uses the two-electrode setup to evaluate the overall performance of a CO₂ electrolyzer. Details of these techniques are further described in this section.

2.1.1 Three-Electrode Setup

The three-electrode setup is ideal for isolating the activity of a single electrode, thus allowing for the fundamental study of a material's electrocatalytic properties. A schematic of the three-electrode setup is shown in Figure 2.1a, which consists of a working, counter, and reference electrode. The material under investigation is the working electrode, which may be the anode or cathode, depending on the applied potential and current. A counter electrode is employed to complete the circuit and allows for the flow of electrons. Pt or graphite is typically used depending on the reaction of interest. For the fundamental study of CO₂/CO electrolysis or Pt-free materials, it is critical to avoid using Pt as the counter electrode as Pt can dissolve and redeposit on the working electrode under electrolysis conditions, potentially impacting the quality of electrochemical measurements.^[1] The reference electrode is especially important in the three-electrode setup, as it allows for the activity of the working electrode to be deconvoluted from the counter electrode. The reference electrode is designed to be inert at a fixed potential during electrochemical measurements, and the applied potential of the working electrode is determined by measuring the potential against the reference electrode. As different reference electrodes can be used, electrochemical measurements

are normalized to the same reference scale. Typically, measurements are normalized to the standard hydrogen electrode (SHE) scale, which is defined as the potential of a Pt wire in a theoretical pH 0 solution under 1 atm H_2 . For example, a self-containing Ag/AgCl electrode in 3 M NaCl saturated with AgCl has a fixed potential of 0.21 V vs. SHE. When measurements involve H_2 evolution, it is often further adjusted to the reversible hydrogen electrode (RHE) by accounting for the proton concentration of the solution using the Nernst equation. It must be noted that there are various configurations of the three-electrode setup. For example, in the study of the HER and hydrogen oxidation reaction (HOR), the working electrode is usually rotated in the electrolyte, also known as the rotating disk electrode (RDE) setup, to enhance the mass transport of reactants to the catalytic surface. For CO_2/CO electrolysis, a two-compartment electrochemical cell is typically used, where the two compartments are separated by a polymer electrolyte membrane with the reference and working electrodes in one compartment and the counter electrode in the other. This helps prevent CO_2/CO reduction products that are generated at the working electrode from being oxidized at the counter electrode. Furthermore, it is critical to purge the electrolyte and the headspace of the electrochemical cell with the correct gas to prevent unwanted side-reactions. For example, inert gases such as Ar are used for surface adsorption studies, H_2 gas is used for HER/HOR studies, and CO_2 or CO is used for CO_2/CO electrolysis studies.

There are various types of electrochemical techniques that can be employed with the three-electrode setup, depending on the application. One of the most common is linear sweep voltammetry (LSV, Figure 2.1b), in which the potential is varied at a linear rate in a specific scanning direction of interest and results in a polarization curve that shows oxidative or reductive currents. LSV is commonly used for HER studies, as the only product is H_2 gas, and theoretically, H_2 evolution can occur at any potential below 0 V vs. RHE. A wide range of potentials can be easily scanned using this technique. On the contrary, in the case of CO_2/CO electrolysis, LSVs do not fully capture the catalytic property of a material, as multiple products can

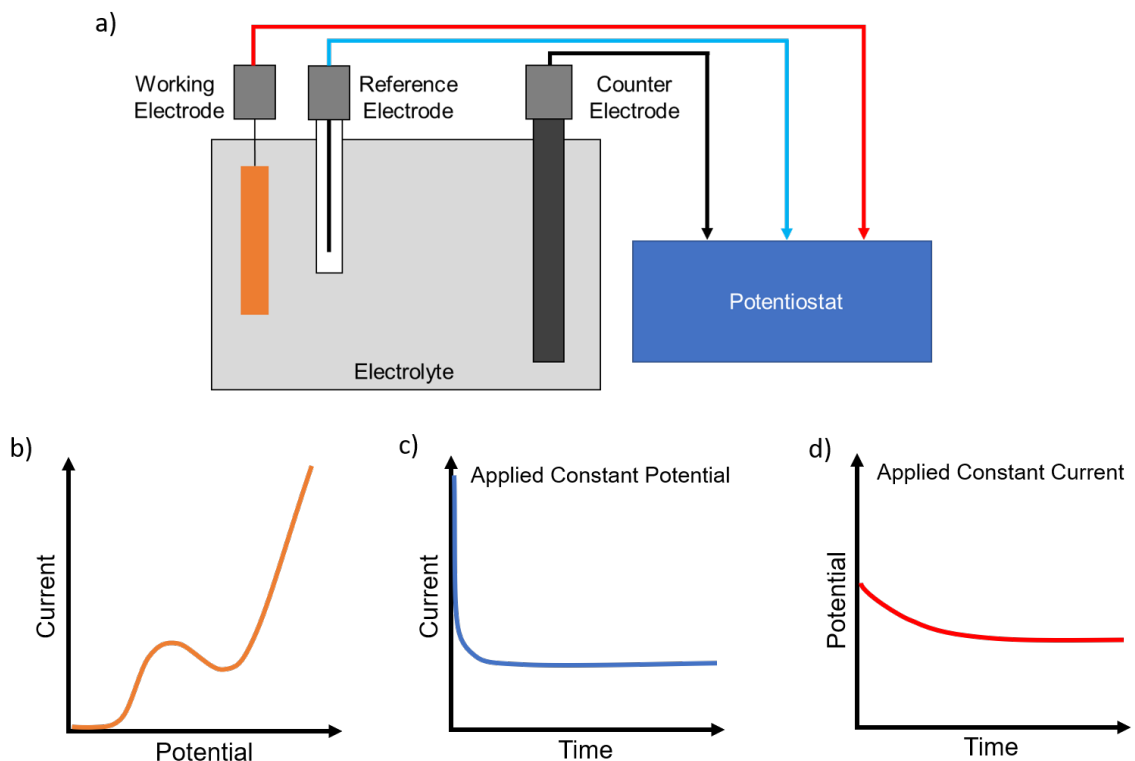


Figure 2.1: a) Schematic of the three-electrode setup and illustrations of three common electrochemical techniques: b) linear sweep voltammetry, c) chronoamperometry, and d) chronopotentiometry.

be produce simultaneously. Typically, chronoamperometry (Figure 2.1c), applying a constant potential while measuring the current as a function of time, or vise-versa, chronopotentiometry (Figure 2.1d), applying a constant current while measuring the potential as a function of time, is used. A constant potential or current is applied for a duration of electrolysis to allow for steady-state operation and sufficient time to quantify products via gas chromatography (GC) or nuclear magnetic resonance (NMR) spectroscopy. By doing so, the product selectivity of a catalyst can be determined. A series of experiments is commonly performed to characterize a material over a wide range of potentials for CO_2/CO electrolysis, and this can provide additional insight in the catalyst's stability. In addition, some of the observed electrochemical measurements

are attributed to the solution resistance, and thus iR correction is frequently employed at high currents where the solution resistance is prevalent in order to deconvolute the actual property of the material under investigation from the electrolyte. The studies in Chapter 3 used LSVs for determining HER activities of Cu-based bimetals, while the studies in Chapters 5 and 6 were completed with chronopotentiometry to characterize materials for CO₂/CO electrolysis. Although studies completed in Chapter 4 used a two-electrode setup, the work was completed with chronoamperometry to characterize the performance of a CO₂ electrolyzer.

2.1.2 Two-Electrode Setup

The two-electrode setup is commonly used for the development of practical devices and consists of only the working and counter electrode. The lack of a reference electrode prevents the ability to dissect each component of the cell. This technique is used to evaluate the overall performance of the cell, which includes all the ohmic losses of each component such as the electrolyte, anode and cathode catalysts, membrane, and current collectors. This technique is useful in testing performance of electrochemical reactors and is extensively used in Chapter 4. Electrochemical reactors are further describe in more details in the following section.

2.2 Electrochemical Reactor Design

While vast majority of fundamental studies utilize batch electrochemical cells to establish structure-activity correlation for catalyst development, majority of these studies are limited to low rates (few tens of mA cm⁻²) due to mass transport limitation of reactants to the catalytic surface. Not only is it critical to develop electrochemical reactors that can achieve high rates of reaction (≥ 100 mA cm⁻²) for commercial applications, it is also important for fundamental studies such that catalysts can be evaluated at working conditions close to industrial levels. The studies in Chapters 4, 5, and 6 utilize variations of electrochemical reactors that are presented in this section.

2.2.1 Architecture

One of the most widely studied class of CO₂/CO electrolyzers is membrane electrode assembly (MEA)-based electrolyzers as shown in Figure 2.2a.[2–6] The overall architecture is based on well-established low-temperature water-splitting electrolyzers and fuel cells in which an ion conducting polymer electrolyte membrane is positioned between the anode and cathode compartments. The membrane facilitates the flow of ions between the two compartments and minimizes product crossover. On the cathode compartment, CO₂ reactant is either delivered to the catalytic sites in dissolved electrolyte or directly in the gas phase. If the CO₂ reactant is fed in dissolved electrolyte, the rate of reaction will be limited by the inherently low diffusion and solubility limits of CO₂ (~33 mM) in aqueous solution. Alternatively, if gaseous CO₂ is fed directly to the cathode, this can provide a means to overcome mass transport limitation by increasing the local concentration of reactants near the catalytic sites, and thus, higher rates of reaction can be achieved.[7, 8] In the case of CO, CO is typically fed directly in the gas phase due to its extremely low solubility (~0.1 mM) in aqueous solution.[9, 10] On the anode, O₂ is typically generated via the water oxidation reaction.[11, 12] Catalysts are often deposited onto highly-porous gas diffusion layers (GDLs) to form gas diffusion electrodes (GDEs) which are then pressed between the current collectors and the membrane to ensure good electrical and ionic conductivity. The GDEs also help promote prolonged contact between the reactant molecules and catalysts.[13] It must be noted that there are various configurations reported in literature. For example, catalysts can be sprayed and hot-pressed directly onto the membrane or the catalyst itself can be monolithic and self-supporting.[12]

An alternative configuration based on microfluidic devices that has recently attracted much attention in CO₂/CO electrolysis is the flow-cell electrolyzer as shown in Figure 2.2b.[14–16] The most striking feature of this device is the positioning of the GDL that separates the CO₂/CO gaseous reactant from the liquid catholyte. The cathode catalyst is deposited on the GDL and gaseous CO₂/CO reactant is directly fed on one side while catholyte is fed on the other side. This configuration relies on

the precise control of the electrode-electrolyte interface to effectively overcome mass transport limitation and to enable high rates of electrolysis ($\geq 100 \text{ mA cm}^{-2}$). If the interface is not well controlled, electrolyte can flood the GDL, obstructing pathways for gaseous CO_2/CO to diffuse toward the catalytic sites and limit the rate of reaction. Controlling the back pressure of the gas and electrolyte chambers is critical for maintaining this interface. In addition, this configuration allows for the study of CO_2/CO reduction activity with various electrolyte pH's and compositions at high rates that cannot be typically done in batch cells. The assembly of a flow-cell electrolyzer used in this thesis is detailed in Appendix A.

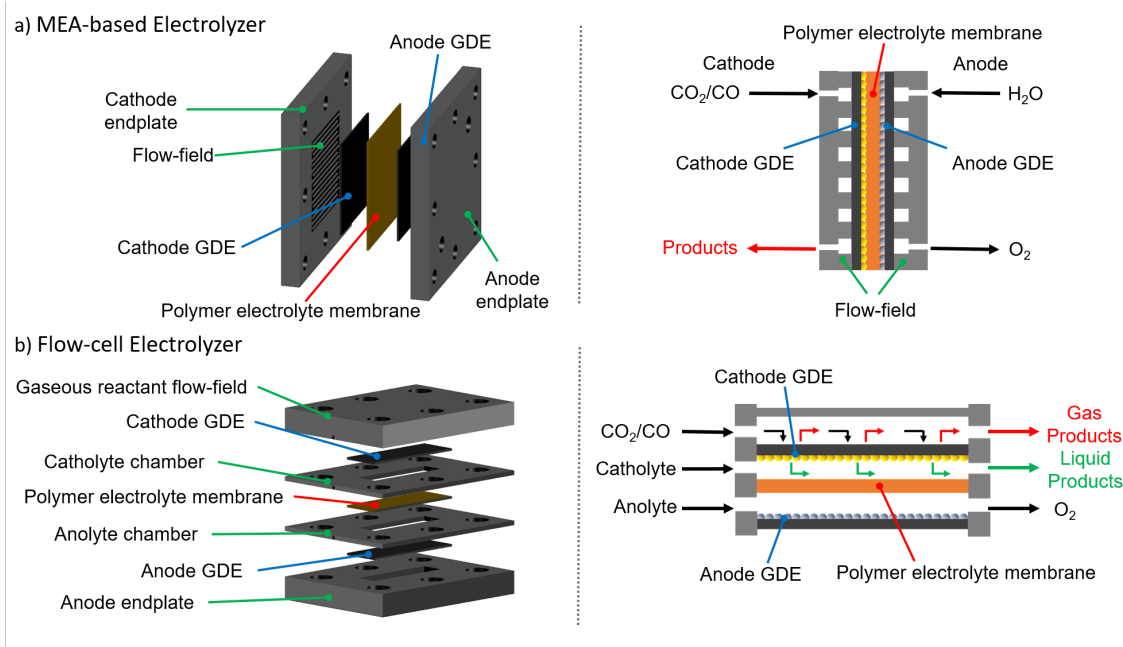


Figure 2.2: Exploded (left) and cross-sectional (right) diagrams of two common electrochemical reactors for CO_2/CO electrolysis: a) membrane electrode assembly-based and b) flow-cell electrolyzers.

2.2.2 Polymer Electrolyte Membrane

The polymer electrolyte membrane (PEM) is a semi-permeable membrane composed of an array of polymer backbone chains with ionized functional groups that

mediate the transport of charged ionic species.[17] The PEM separates the cathode and anode compartments and facilitates the flow of ions from one compartment to another while minimizing product crossover. There are three classes of membranes: cation exchange membranes (CEMs)[2], anion exchange membranes (AEMs),[18] and bipolar membranes (BPMs)[19, 20] as shown in Figure 2.3. Since CEMs and AEMs are the most widely used in CO₂ electrolyzers, the focus will be these two. It must be noted that most commercially available PEMs are designed for water-splitting electrolyzers and fuel cells, and very few are specifically designed for CO₂/CO electrolysis.

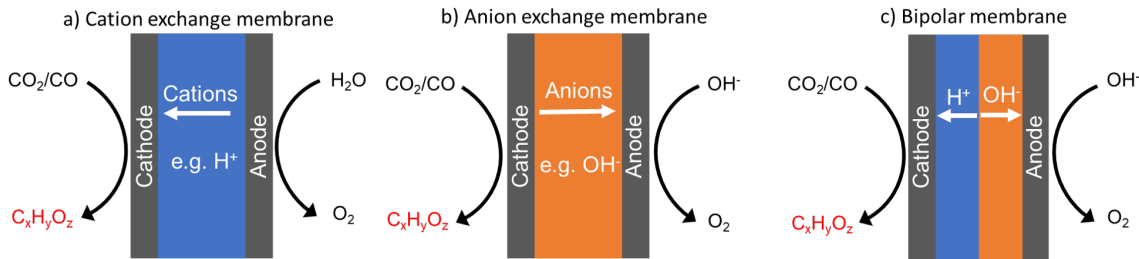


Figure 2.3: Overview of different ionic transport in three common polymer electrolyte membranes: a) cation exchange, b) anion exchange, and c) bipolar membranes.

CEMs facilitate the flow of positively charged ions (e.g. H⁺) from the anode to the cathode as shown in Figure 2.3a. The most widely used CEM is Nafion which has fluorinated polymer backbone chains and sulfonic acid groups. These membranes have excellent proton conductivity and durability and are widely used in water electrolyzers and fuel cells. However, the contamination and build-up of larger cations (e.g. K⁺ and Na⁺) within the membrane can lower the ionic mobility.[21–23] Owing to its low glass transition temperature ($\sim 125^\circ\text{C}$) and excellent durability, catalysts can be sprayed and hot pressed directly onto the membrane with Nafion ionomer binder to create a dense immobilized catalyst layer with excellent ionic conductivity. This typically cannot be done with less durability AEMs.

AEMs conduct negatively charged ions (e.g. OH⁻) from the cathode to the

anode as shown in Figure 2.3b. AEMs often consist of hydrocarbon polymer backbone with quaternary ammonium groups and have attracted much attention toward the development of Pt-free fuel cells that operate in alkaline conditions.[24] Currently, there is an array of AEMs that are commercially available. However, under CO₂ electrolysis conditions, CO₂ can rapidly react with OH⁻ to form HCO₃⁻ and CO₃²⁻, thus reducing the efficiency of converting CO₂ to desired products.[25] In addition, the build-up of these larger anions can ultimately reduce ionic mobility throughout the membrane. Recently, Masel and co-workers have developed an imidazolium functionalized styrene and vinylbenzylchloride copolymer as AEM material to improved the transport of HCO₃⁻ with direct application for CO₂ electrolysis.[26]

2.2.3 Gas Diffusion Layer

The gas diffusion layer (GDL) is a porous structure often comprised of an array of carbon fibers as the backbone support with a more densely packed micro porous layer (MPL), typically constructed from pressed carbon powder and often treated with polytetrafluoroethylene (PTFE) to provide hydrophobicity (Figure 2.4).[27] The MPL provides a smooth layer with high surface area where catalysts are immobilized with polymeric binders to form and to ensure good electrical contact with the catalyst layer.[13] Most importantly, the MPL is key to maintaining the separation between the liquid electrolyte and the gaseous reactant, which is achieved through high surface tension of the liquid-gas-solid interface within the pores, also known as the triple-phase boundary. The extent of this surface tension can be manipulated by changing the hydrophobicity of the MPL.[28] In a MEA-based electrolyzer, the cathode and anode GDEs are situated on both sides of the PEM and sandwiched between the flow-field plates. While in the flow-cell electrolyzer, the cathode GDE helps maintain the electrode-electrolyte interface. By precisely controlling the triple-phase boundary, mass transport limitation can be circumvented, thus achieving high rates of electrolysis. In more details, if the GDE pores are completely flooded, this eliminates gas channels which results in high mass transport resistance of gaseous reactant. If the pores are

dry, the GDE will be inactive due to the lost of ionic pathways and lack of aqueous electrolyte needed for the reaction. Ideally, the pores should be partially wet, with an electrolyte film thin enough to minimize gaseous transport resistance to the catalytic sites but thick enough to maintain ionic conductivity.[29] Controlling this electrode-electrolyte interface is especially critical in CO electrolysis as the solubility of CO in aqueous electrolyte is extremely low. Recently, Sargent and co-workers have developed a new polymer-based GDL configuration in which carbon nanoparticles were deposited onto a PTFE membrane. The carbon nanoparticles serve as both the catalyst support and current collector while the PTFE membrane prevents electrolyte crossover by maintaining an abrupt interface.[30] The pure PTFE membrane serves as a more stable hydrophobic layer than the conventional PTFE-treated GDL. As for the anode, since most GDLs are carbon-based materials, the use of GDLs as support should be avoided due to potential carbon oxidation that can lead to instability. Titanium support can be used as a suitable alternative.

2.2.4 Flow-Field Plate and Current Collector

The flow-field plates, also often serving as the current collectors, provide the structural support for the GDEs and mechanical stability of the electrolyzer as it makes up majority of the electrolyzer's body.[31, 32] In addition, the flow-field plates supply reactant to the GDEs, help remove products and moisture accumulation, and allow for electrons to travel to and from an external circuit to drive electrolysis.[33, 34] Therefore, the flow-field plates need to be mechanically strong, chemically inert, and possess high electronic conductivity. It is especially important to use a suitable material for the anode flow-field since the anode will be under an oxidative potential. Typical materials include stainless steel, Cu, titanium (Ti), and aluminum (Al) which are further coated with gold to increase electronic conductivity and chemical stability. Exfoliated graphite have also been explored as flow-field materials; however, this material is prone to cracking under stress and is unstable under a corrosive environment.

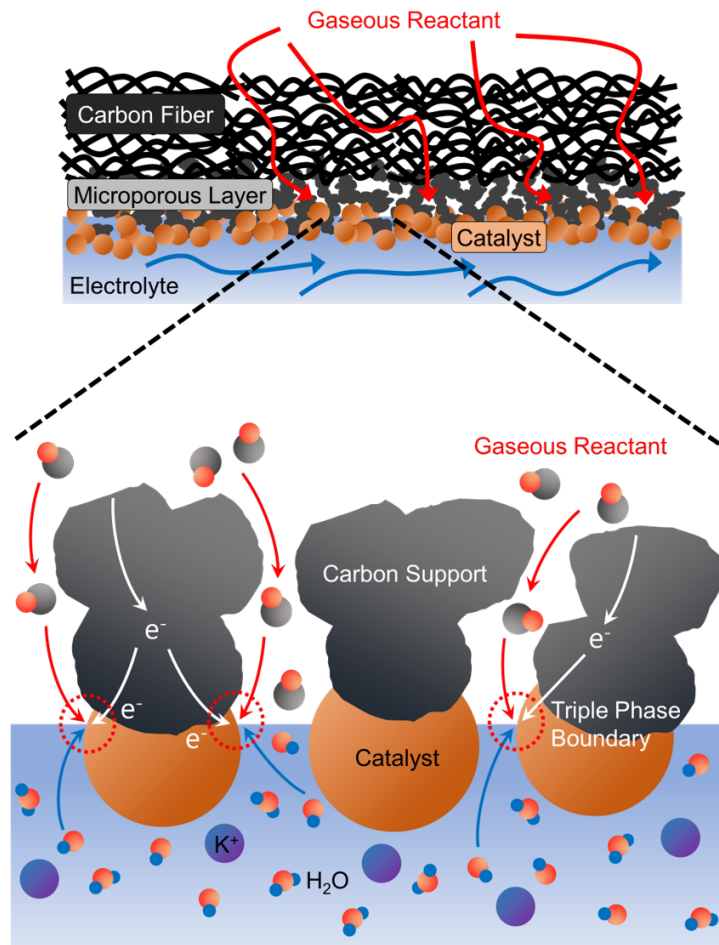


Figure 2.4: Schematic of a gas diffusion layer and the triple-phase boundary.[9]

2.2.5 Gasketing

Gaskets, often overlooked and not shown in Figure 2.2, are critical to provide correct compression to minimizing contact resistance while preventing leaks in the electrolyzer. Gaskets are typically made from insulating materials such as silicone and teflon. The gaskets need to be slightly thinner than the GDE to ensure that the catalyst layer is firmly pressed against the membrane. Since the flow-field plates may not be exactly parallel with each other when pressed, the gaskets also needs to be thick enough to accommodate for the misalignment and to provide sufficient sealant.

REFERENCES

- (1) Dunwell, M.; Lu, Q.; Heyes, J. M.; Rosen, J.; Chen, J. G.; Yan, Y.; Jiao, F.; Xu, B. *Journal of the American Chemical Society* **2017**, *139*, 3774–3783.
- (2) Delacourt, C.; Ridgway, P. L.; Kerr, J. B.; Newman, J. *Journal of the Electrochemical Society* **2008**, *155*, B42–B49.
- (3) Cook, R. L.; MacDuff, R. C.; Sammells, A. F. *Journal of The Electrochemical Society* **1988**, *135*, 1470.
- (4) Li, H.; Oloman, C. *Journal of Applied Electrochemistry* **2005**, *35*, 955.
- (5) Ripatti, D. S.; Veltman, T. R.; Kanan, M. W. *Joule* **2018**, *3*, 240–256.
- (6) Wu, J.; Risalvato, F. G.; Sharma, P. P.; Pellechia, P. J.; Ke, F.-S.; Zhou, X.-D. *Journal of The Electrochemical Society* **2013**, *160*, F953–F957.
- (7) Weekes, D. M.; Salvatore, D. A.; Reyes, A.; Huang, A. X.; Berlinguette, C. P. *Accounts of Chemical Research* **2018**, *51*, 910–918.
- (8) Dinh, C. T.; Li, Y. G. C.; Sargent, E. H. *Joule* **2019**, *3*, 13–15.
- (9) Jouny, M.; Luc, W.; Jiao, F. *Nature Catalysis* **2018**, *1*, 748–755.
- (10) Li, C. W.; Ciston, J.; Kanan, M. W. *Nature* **2014**, *508*, 504.
- (11) McCrory, C. C. L.; Jung, S.; Peters, J. C.; Jaramillo, T. F. *Journal of the American Chemical Society* **2013**, *135*, 16977–16987.
- (12) Luc, W.; Rosen, J.; Jiao, F. *Catalysis Today* **2017**, *288*, 79–84.
- (13) Jhong, H. R.; Brushett, F. R.; Kenis, P. J. A. *Advanced Energy Materials* **2013**, *3*, 589.
- (14) Whipple, D. T.; Finke, E. C.; Kenis, P. J. A. *Electrochemical and Solid-State Letters* **2010**, *13*, B109–B111.
- (15) Ma, S.; Sadakiyo, M.; Luo, R.; Heima, M.; Yamauchi, M.; Kenis, P. J. A. *Journal of Power Sources* **2016**, *301*, 219–228.
- (16) Ma, S.; Sadakiyo, M.; Heima, M.; Luo, R.; Haasch, R. T.; Gold, J. I.; Yamauchi, M.; Kenis, P. J. A. *Journal of the American Chemical Society* **2017**, *139*, 47–50.
- (17) Smitha, B.; Sridhar, S.; Khan, A. A. *Journal of Membrane Science* **2005**, *259*, 10.
- (18) Kutz, R. B.; Chen, Q.; Yang, H.; Sajjad, S. D.; Liu, Z.; Masel, I. R. *Energy Technology* **2017**, *5*, 929–936.

- (19) Li, Y. C.; Zhou, D.; Yan, Z.; Gonçalves, R. H.; Salvatore, D. A.; Berlinguette, C. P.; Mallouk, T. E. *ACS Energy Letter* **2016**, *1*, 1149.
- (20) Reiter, R. S.; White, W.; Ardo, S. *Journal of Electrochemical Society* **2016**, *163*, H3132.
- (21) Kienitz, B.; Pivovar, B.; Zawodzinski, T.; Garzon, F. *Journal of The Electrochemical Society* **2011**, *158*, B1175–B1183.
- (22) Hongsirikarn, K.; Goodwin Jr, J.; Greenway, S.; Creager, S. *Journal of Power Sources* **2010**, *195*, 7213–7220.
- (23) Chaudhary, S.; Agarwal, C.; Goswami, W. *The Journal of Physical Chemistry B* **2015**, *119*, 10566–10572.
- (24) Gottesfeld, S.; Dekel, D.; Page, M.; Bae, C.; Yan, Y.; Zelenay, P.; Kim, Y. *Journal of Power Sources* **2018**, *375*, 170–184.
- (25) Dinh, C. T.; Garcia de Arquer, F. P.; Sinton, D.; Sargent, E. H. *ACS Energy Letters* **2018**, *3*, 2835–2840.
- (26) Masel, R. I.; Liu, Z.; Sajjad, S. *ECS Transactions* **2016**, *75*, 1143–1146.
- (27) Park, S.; Lee, J.; Popov, B. *International Journal of Hydrogen Energy* **2011**, *37*, 5850–5865.
- (28) Kim, B.; Hillman, F.; Ariyoshi, M.; Fujikawa, S.; Kenis, P. J. A. *Journal of Power Sources* **2016**, *312*, 192–198.
- (29) Weng, L.; Bell, A.; Weber, A. *Physical Chemistry Chemical Physics* **2018**, *20*, 16973–16984.
- (30) Dinh, C.-T.; Burdyny, T.; Kibria, M. G.; Seifitokaldani, A.; Gabardo, C. M.; García de Arquer, F. P.; Kiani, A.; Edwards, J. P.; De Luna, P.; Bushuyev, O. S.; Zou, C.; Quintero-Bermudez, R.; Pang, Y.; Sinton, D.; Sargent, E. H. *Science* **2018**, *360*, 783.
- (31) Lobato, J.; Cañizares, P.; Rodrigo, M. A.; Pinar, F. J.; Mena, E.; Úbeda, D. *International Journal of Hydrogen Energy* **2010**, *35*, 5510.
- (32) Millet, P.; Ngameni, R.; Grigoriev, S. A.; Mbemba, N.; Brisset, F.; Ranjbari, A.; Etiévant, C. *International Journal of Hydrogen Energy* **2010**, *35*, 5043.
- (33) Kumar, A.; Reddy, R. *Journal of Power Sources* **2003**, *113*, 11–18.
- (34) Li, W.; Sabir, I. *International Journal of Hydrogen Energy* **2005**, *30*, 359–371.

Chapter 3

THE ROLE OF SURFACE OXOPHILICITY IN COPPER-CATALYZED WATER DISSOCIATION

In the previous chapters, the motivation for developing non-precious HER electrocatalysts in alkaline conditions was presented. This work titled, “Role of Surface Oxophilicity in Copper-catalyzed Water Dissociation,” is published in *ACS Catalysis* 8, 9327-9333 (2018). As an author, I performed all the material synthesis, characterization, and electrochemical experiments, while Zhao Jiang performed the DFT calculations. This work focuses on the fundamental understanding of catalytic parameters for the design of non-precious Cu-based catalysts for the HER in alkaline conditions. In addition, this study also provides insights on strategies to avoid for designing of CO₂/CO reduction catalysts as H₂ evolution is a competing side reaction in CO₂/CO electrolysis.

3.1 Introduction

Cu-based materials are widely studied as potential catalysts for water-splitting and CO₂ reduction.[1–6] In the case of water-splitting, a catalyst surface that highly favors HER activity is desirable; however, in the case of CO₂ reduction, the suppression of HER activity is necessary to maximize CO₂ reduction Faradaic efficiency. As such, the ability to predict and control HER activity of Cu-based catalysts can enable one to design more efficient catalysts for both reactions. Recently, we reported a non-precious Cu–Ti bimetallic electrocatalyst that is able to reduce water to H₂ under a mild overpotential at a rate orders of magnitude greater than that of pure Cu catalyst in alkaline conditions.[7] DFT calculations show that the combination of Cu and Ti creates unique Cu–Cu–Ti hollow sites, exhibiting very similar HBE values to that of

Pt. Although the findings clearly show that HBE is a good descriptor for HER activity under alkaline conditions, the question whether HBE is the sole descriptor remains unclear and further investigation is required to answer this fundamental question.

Herein, we synthesize a series of bulk Cu-based bimetals (Cu-M) using an arc melting process, where the HBEs of active sites are tuned using a range of metal dopants, such as Ti, Co, and Ni. The experimental results show that the Cu-M bimetals exhibit much better HER activities than pure Cu with a trend of Cu-Ti > Cu-Co > Cu-Ni > Cu. However, when the HBE is used as the sole descriptor, the observed experimental trend does not follow that as predicted by DFT calculations. Further studies combining both computational efforts and experimental investigation of metal oxide/hydroxide (MO/OH) clusters deposited on Cu surfaces suggest that the oxophilicity of the secondary metal can assist water dissociation through weak interactions with the oxygen atom of the water molecule. Therefore, although the HBE is still the dominant descriptor for HER in alkaline conditions, the oxygen binding energy (OBE) of the dopant metal should also be considered as a descriptor to characterize HER activity for Cu-M bimetals. Additionally, the results on Cu-M bimetals suggest that incorporating an highly oxophilic metal with Cu may not be a valid strategy to improve CO₂ reduction performance on Cu-based catalysts due to the promotion of the undesired HER.

3.2 Experimental Methods

3.2.1 Preparation of Cu-based Bimetallic Systems

The Cu-M alloys (Figure 3.1a) were prepared by arc melting highly pure metal precursors with desired atomic ratios under argon atmosphere. All precursor metals were obtained from Alfa Aesar with purity of 99.99% or greater. The resulting bimetallic ingots were milled and machined down to standard RDE disk inserts with an outer diameter of 5.0 mm and length of 4.0 mm (Figure 3.1b). Subsequently, the as-machined disks were then sealed in a quartz tube (Quartz Scientific, Inc) under Ar atmosphere (Keen, Grade 5) (Figure 3.1c), heated to 950 °C in a furnace (MTI) for 24 h, and then

rapidly quenched in an ice bath. The surface rust was removed using fine grade sand papers (400, 600, 1000, and 2000 Grit) and was finally polished with 0.5 μm alumina particles to a mirror finish. The disks were then sonicated and thoroughly washed to remove residual alumina particles. Finally, the disks were inserted into E4 Series RDE tips (Figure 3.1d). As for pure Cu, a highly pure copper rod with a diameter of 7.0 mm was obtained from Alfa Aesar and then machined down to standard RDE disk inserts. Similarly, the Cu RDE disks were sanded and polished to a mirror finish.

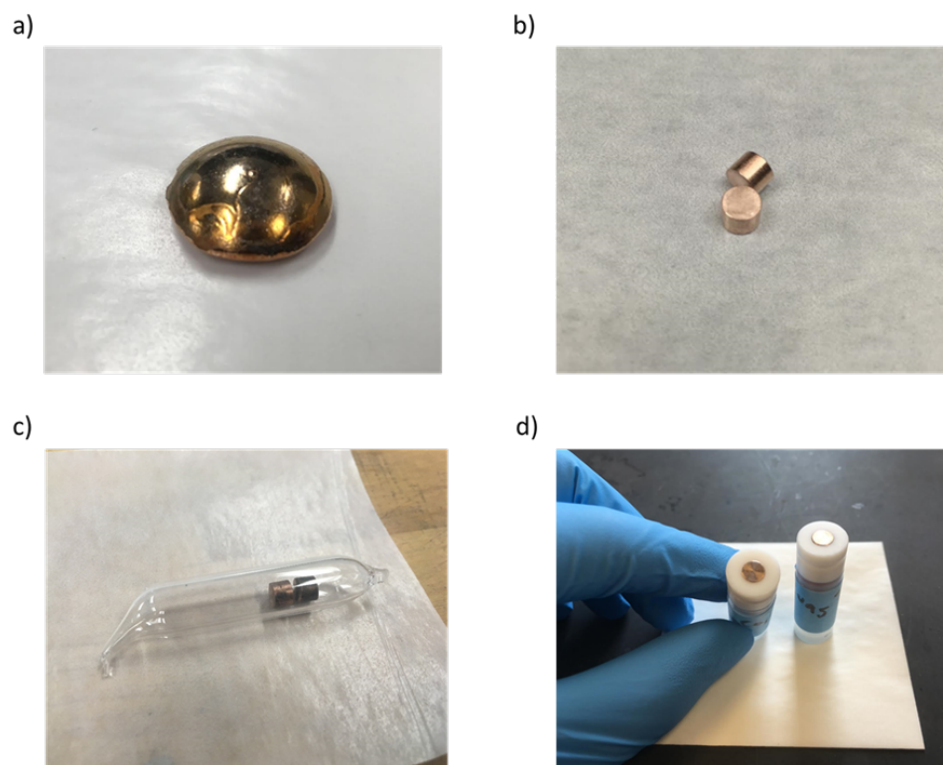


Figure 3.1: Photograph image of as-synthesized Cu–M ingot using arc melting, b) as-machined Cu–M RDE disks, c) Cu–M RDE disks sealed in quartz tube under Ar atmosphere, and d) Cu–M disks inserted into E4 Series RDE tips.

The Cu/MO/OH catalysts were prepared by chemical deposition through the hydrolysis of metal ions. This procedure was found to be facile approach for depositing desired MO/OH clusters. In general, a polished Cu RDE disk was immersed and

equilibrated into a solution of 0.1 M metal chloride aqueous salt solution for about 0.5 or 12h. Nickel(II) chloride and cobalt(II) chloride salts were obtained from Sigma Aldrich. As for the deposition of TiO_2 clusters, a 0.01 M solution of titanium(IV) isopropoxide mixed with ethanol as the solution was used instead. For high loadings of TiO_2 , a 0.1 M solution was used. After deposition, the electrodes were washed thoroughly.

3.2.2 Structural Characterization

The crystal structure of the as-made Cu–M disks were examined using X-ray diffraction (XRD) on a Bruker D8 Discovery diffractometer using a Cu $K\alpha$ radiation source. Bulk compositions were determined using energy-dispersive X-ray spectroscopy (EDS) technique using a Zeiss Auriga-60 scanning electron microscopy (SEM) setup. EDS analysis was conducted at five different positions on each bimetallic electrode to determine uniformity of the bulk composition. The standard deviation of the measured composition was <1 at.%, confirming that the bulk composition was uniform throughout the electrode. To analyze the atomic stoichiometric and oxidation states near the electrode surface of both Cu–M and Cu/MO/OH catalysts, a Thermo Scientific K-Alpha X-ray Photoelectron Spectrometer (XPS) System was used. XPS fitting was conducted with CasaXPS software with the adventitious carbon peak being calibrated to 284.8 eV. All peaks were fitted using a Gaussian/Lorentzian product line shape and a Shirley background. The surface roughness factors were determined using an atomic force microscopy (AFM, Dimension 3100, Veeco instruments Inc.). Four random areas ($25 \times 25 \mu\text{m}^2$) for each sample were scanned in tapping mode with a scan rate of 1 Hz. The roughness factor was determined by averaging the four measured values.

3.2.3 Electrochemical Evaluation

To characterize the electrocatalytic activity of the various Cu–M and Cu/MO/OH catalysts, a typical three-electrode RDE setup was used. The RDE tip was mounted onto a rotator (Pine Instruments) as the working electrode. The reference electrode was

a saturated calomel electrode (SCE, Princeton Applied Research), while the counter electrode was a graphite rod (Sigma-Aldrich, 99.999%). A graphite rod was used instead Pt to avoid any potential Pt contamination. The electrolyte was 0.1 M potassium hydroxide (KOH, Sigma-Aldrich, 99.99%) made with MilliQ water (18.2 M Ω) and was continuously purged with H₂ (Keen, Grade 5) during electrochemical measurements. Pre-electrolysis of the electrolyte was conducted with a sacrificial electrode for at least 24 h prior to electrochemical measurements. The reference electrode was calibrated to the reversible hydrogen electrode using a polished Pt disk as the working electrode and a Pt wire as the counter electrode in the same electrolyte. A sweep rate of 10 mV s⁻¹ was used in voltammetry studies and all polarization curves were corrected for iR lost. The 5th scan of each experiment was reported. Impedance measurements were conducted with potentiostatic electrochemical impedance spectroscopy (PEIS) at a constant potential with a 10 mV applied perturbation. All measurements were completed with a VMP2 Multichannel Potentiostat (Princeton Applied Research) with EC-Lab (V11.10) software.

3.2.4 Computational Methods

Density Functional Theory calculations were carried out using the Vienna *ab initio* Simulation Package (VASP). The plane-wave calculations were conducted with an energy cutoff of 400 eV using projector augmented-wave (PAW) potentials. The Perdew-Wang-91 (PW91) functional with the generalized gradient approximation was used to deal with the electronic exchange and correlation energies. The Brillouin-zone integration was performed on a grid of $3 \times 3 \times 1$ Monkhorst-pack special k-points. The Cu(111), Pt(111) and Cu-M(111) where (M = Ti, Co, Ni) were modeled with a four-layer 3×3 super-cell with the coverage of selected adsorbates of 1/9 monolayer. The bottom two layers were fixed, and the top layers were allowed to relax until the forces were below 0.02 eV \AA^{-1} . A vacuum layer of 15 \AA was added perpendicular to the slab to avoid artificial interactions between the slab and its periodic images. An inverse model was used to describe the oxide support on the activity of Cu toward HER. The oxide

clusters were deposited on the four-layer 5×5 super-cell Cu(111) surface. In all models (Cu–M(111) and oxide cluster), the electronic structure of Ti, Co, and Ni was treated in the DFT+U formalism with a U value of 4.5 eV. Spin-polarization was included for all surfaces and van der Waals interactions were considered. To describe the van der Waals effect, the PW91 functional with the zero damping DFT–D3 correction using Grimme method was implemented.

The binding energies (BE) for H and O atoms are calculated as follows:

$$BE = E_{adsorbate/slab} - 0.5 \times E_{adsorbate} - E_{slab} \quad (3.1)$$

where $E_{adsorbate/slab}$ is the energy of the surface with 1/9 ML hydrogen or oxygen adsorbed, $E_{adsorbate}$ is the energy of hydrogen or oxygen in the gas phase, and E_{slab} is the energy of the slab in a vacuum.

3.3 Results

3.3.1 Hydrogen Binding Energy Calculations

In our previous work, it was shown that doping Cu with low concentrations of Ti creates highly active sites for HER in alkaline conditions, possessing similar HBEs as Pt.[7] To reveal the HER activity trend of Cu–M bimetals, computational modeling was conducted to screen other first-row transition metals as dopants. A 3×3 Cu(111) surface with either one or two surface Cu atoms replaced with Ti, Co, or Ni atoms, corresponding to a surface concentration of 11.1% or 22.2%, respectively, was used as the model system as shown in Figure 3.2. The HBE was calculated for five types of adsorption sites (Tables 3.1 and B.1): three Cu–Cu–M and two Cu–M–M hollow sites where M = Ti, Co, or Ni. For comparison, HBE values for pure Cu(111) and Pt(111) (Table B.2) were also determined. In addition, a sub-layer substitution surface and a metal oxide cluster on Cu(111) surface were also investigated (Figures B.1 and B.2). Lastly, OBE values were also calculated with the same model surface (Tables 3.1, B.1-B.4).

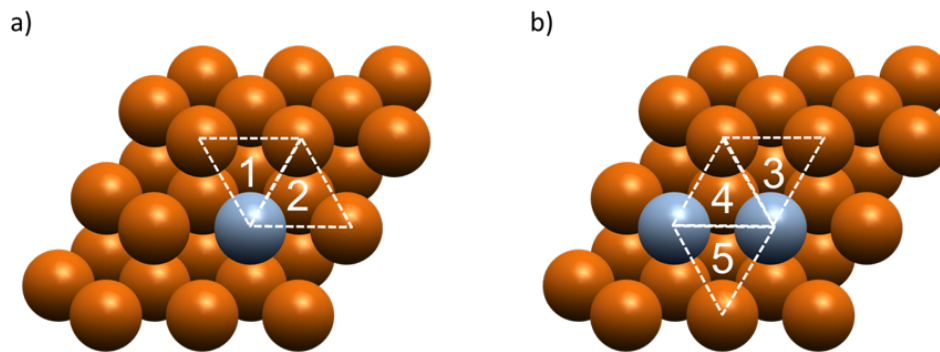


Figure 3.2: DFT models of a) Cu(111) surface with one Cu atom replaced with a M atom and b) Cu(111) surface with two Cu atoms replaced with two M atoms. Cu atoms are represented in orange. M = Ti, Co, or Ni atoms are represented in blue.

Although pure Cu is a poor HER catalyst as reflected by its relatively weak HBE values, computational predictions show that doping a small amount of Ni, Co, or Ti can dramatically shift the HBE toward that of Pt. To facilitate the discussion, three HBE values and three OBE values (two for hollow Cu–Cu–M sites and one for hollow Cu–M–M sites) of each Cu–M system are shown in Table 3.1. The remaining calculated binding energies are tabulated in Table B.1. Based on the calculations, Cu–Cu–M hollow sites exhibit HBE values very close to Pt’s, in which Cu–Ti(111) sites exhibit the closest HBE values while Cu–Co(111) sites exhibit slight stronger HBEs. On the contrary, Cu–M–M hollow sites bind hydrogen too strongly as reflected by its large negative HBE values. In the cases of the sub-layer substitution and metal oxide cluster on Cu(111) surfaces, the adsorption sites exhibit weak HBEs with similar values to those of pure Cu(111) surface, suggesting that these types of surfaces are not favorable for HER (Tables B.3 and B.4). Ideally, a 3×3 surface Cu unit cell with the middle Cu atom replaced with a dopant atom would be an ideal catalytic surface such that the surface would maximize the number of Cu–Cu–M sites without introducing undesired Cu–M–M sites. Based on the calculated HBEs, the predicted HER activity of Cu–M bimetals and pure Cu should follow the trend of Cu–Ti >

Table 3.1: Calculated HBEs and OBEs for Cu–M(111) and Cu(111) surfaces

Model	Cu-Cu-M[1] HBE (eV)	Cu-Cu-M[1] OBE (eV)	Cu-Cu-M[2] HBE (eV)	Cu-Cu-M[2] OBE (eV)	Cu-M-M[4] HBE (eV)	Cu-M-M[4] OBE (eV)
Cu-Ti (111)	-0.47	-3.71	-0.46	-3.65	-0.88	-4.95
Cu-Co (111)	-0.57	-2.56	-0.59	-2.48	-0.71	-3.06
Cu-Ni (111)	-0.49	-2.12	-0.50	-2.12	-0.63	-2.40
Cu (111)	-0.29	-1.73	-0.28	-1.64		

[#]: Corresponding adsorption site on Figure 3.2. See Table B.1 for binding energies over the remaining surfaces.

Cu–Ni > Cu–Co > Cu.

3.3.2 Experimental Validation using Model Catalysts

To verify the computational predictions, experimental investigation began with the synthesis of bulk Cu–M bimetallic alloy ingots by melting desired amounts of dopant metals (Ti, Co, or Ni) with Cu to achieve the desired bulk atomic ratios of 5-10% via arc melting in vacuum. The as-synthesized ingots were then machined down to RDE disks, as shown in Figure 3.1. Figure 3.3 shows the XRD patterns of the final state of each sample after arc melting, machining, and subsequent heating and quenching. In all cases, solid solution mixtures were achieved, as indicated by the clear FCC peaks and expected peak shifts due to alloy formation (Figure 3.3b). The surface composition of each bimetallic was determined using XPS (Figure B.3). In the case of Cu–Ti, a dopant atomic ratio of 5% was chosen such that that the surface compositions of all alloys were close to consistent at $\sim 11\%$. The discrepancy between the surface and bulk compositions is likely due to the larger Ti atoms tending to aggregate toward the surface to minimize the overall lattice strain as consistent with our previous work.[7] Furthermore, XPS analysis indicated that majority of the surface Cu atoms in all Cu–M materials were metallic Cu^0 , whereas majority of surface Ti, Co, and Ni atoms were in their oxidized Ti^{4+} , Co^{2+} , and Ni^{2+} states, respectively.[8, 9]

We note that the exact surface nature of the bimetallic catalysts under HER conditions remains unclear due to lack of developed *in-situ* techniques that can resolve the valence state of surface atoms in presence of electrolyte under reaction conditions. The bulk compositions, measured with EDS, were consistent with the expect nominal values as reported in Table 3.2. The roughness factors (R_f) for all Cu–M surfaces were nearly identical as determined by AFM.

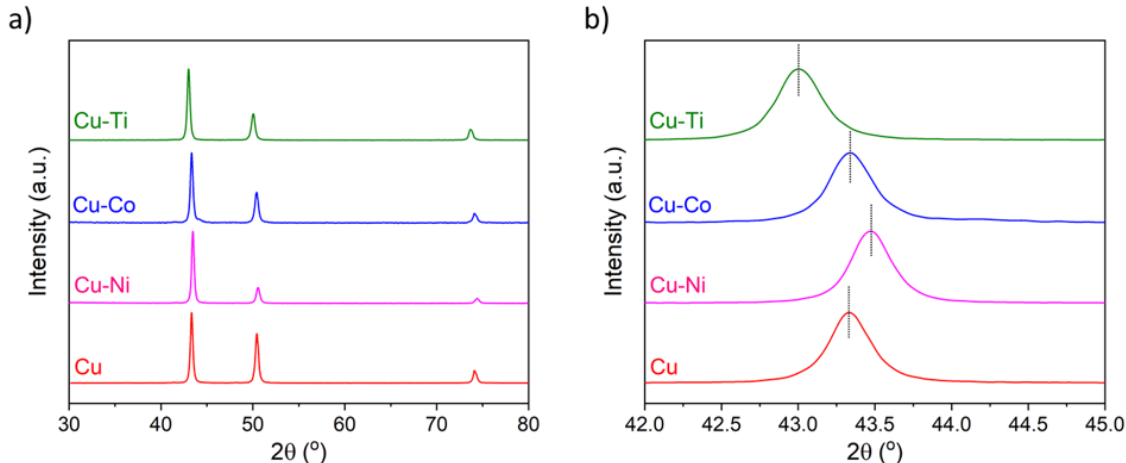


Figure 3.3: XRD characterization. a) The XRD patterns of Cu–M bimetallics and Cu and b) the enlarged region of Cu(111) diffraction peaks.

The as-synthesized Cu–M bimetallics were evaluated for HER activity in H_2 saturated 0.1 M KOH using a three-electrode RDE setup with the working electrode rotating at 1800 rpm. A high purity graphite rod was used as the counter electrode in all the experiments to avoid any potential contamination issues.[10] Figure 3.4a shows the HER polarization curves of the current normalized to the geometric surface area vs. the applied potential after iR -correction. In addition, Tafel slopes (b in $\eta = b \log |i| + a$) were obtained from the polarization curves between -1 mA cm^{-2} and -8 mA cm^{-2} as shown in Figure 3.4b, while the exchange current densities at the reversible potential were determined by extrapolating the Tafel plots to 0 V vs. RHE. The polarization curves show that alloying Cu with Ti, Co, or Ni dramatically improves

Table 3.2: Bulk and surface compositions of Cu–M bimetallics and Cu

Samples	EDS bulk compositions (dopant at. %)	XPS surface compositions (dopant at. %)	R_f
Cu-Ti	Ti:5.4	Ti:11.8	1.01
Cu-Co	Co:10.0	Co:12.0	1.01
Cu-Ni	Ni: 10.2	Ni:11.2	1.00
Cu	N/A	N/A	1.02

the HER performance in comparison to pure Cu. It is clear that the Cu–Ti material exhibits the best performance in terms of current density vs. applied potential as well as exchange current density. Based on experimental investigation, the HER activity trend for the Cu–M bimetallics and pure Cu decrease in the following order Cu–Ti > Cu–Co > Cu–Ni > Cu, which deviates from the theoretical predictions when HBE is used as the sole descriptor.

3.3.3 Role of Oxophilic Dopants

The discrepancy in the HER-predicted activity trend strongly suggests that HBE is unlikely the sole descriptor for determining HER activity in alkaline conditions. Looking closely at the calculated OBEs for the Cu–M bimetallics and pure Cu, it is striking that the trend in catalytic improvement follows the trend in OBEs. Among the catalysts investigated, Cu–Ti and Cu has the highest and lowest HER activity with Cu–Ti and Cu sites bonding to oxygen the strongest and weakest, respectively. This suggests that oxophilicity could be an important factor for determining HER activity. However, as indicated by DFT calculations (Table 3.2), alloying Cu with Ti, Co, or Ni can change both the HBEs and OBEs, thus making it difficult to differentiate the effects of HBE and OBE on HER activity. In order to deconvolute the effects, a second system of Cu–based catalysts was also investigated. Metal oxide/hydroxide

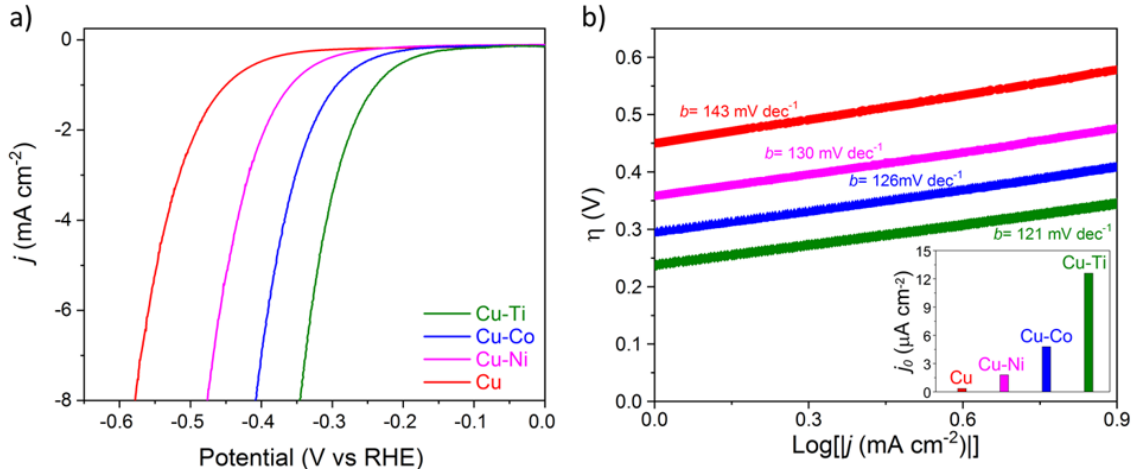


Figure 3.4: Electrochemical characterization of Cu-M bimetallic alloys. a) Typical HER activities for Cu-M bimetallics and Cu evaluated in H_2 saturated 0.1 M KOH solution with a rotation speed of 1800 rpm at room temperature with a scan rate of 10 mV s^{-1} . b) Corresponding Tafel plots and (inset graph) exchange current densities.

(MO/OH) clusters of the same dopant metals (TiO_2 , $\text{Co}(\text{OH})_2$, or $\text{Ni}(\text{OH})_2$) were chemically deposited on Cu such that the HBE can be pseudo-fixed while the HER activity can be studied as a sole function of oxophilicity. XPS analysis confirmed the presence of the deposited TiO_2 , $\text{Co}(\text{OH})_2$, or $\text{Ni}(\text{OH})_2$ clusters on the Cu surface and the surface concentrations were kept between $\sim 15\text{-}20$ at.% (Figure B.4). SEM images show the presence of these deposited clusters (Figure B.5) with cluster sizes of $\sim 20\text{-}100$ nm. The HER activity trend for the Cu/MO/OH catalysts decreases in the order $\text{Cu}/\text{TiO}_2 > \text{Cu}/\text{Co}(\text{OH})_2 > \text{Cu}/\text{Ni}(\text{OH})_2 > \text{Cu}$ as shown in Figure 3.5. Since Cu/TiO_2 has the highest activity, the loading of TiO_2 was further increased ($>40\%$). However, a reduction in performance was observed (Figure B.6), indicating that a delicate balance between Cu and TiO_2 clusters is needed for enhancing HER activity. Most likely the increased amount of surface TiO_2 blocks necessary Cu sites that are needed to form the key H_{ads} intermediate, consequentially leading to a decrease in HER activity.

Experimental results clearly show that the oxophilicity of the dopant metal

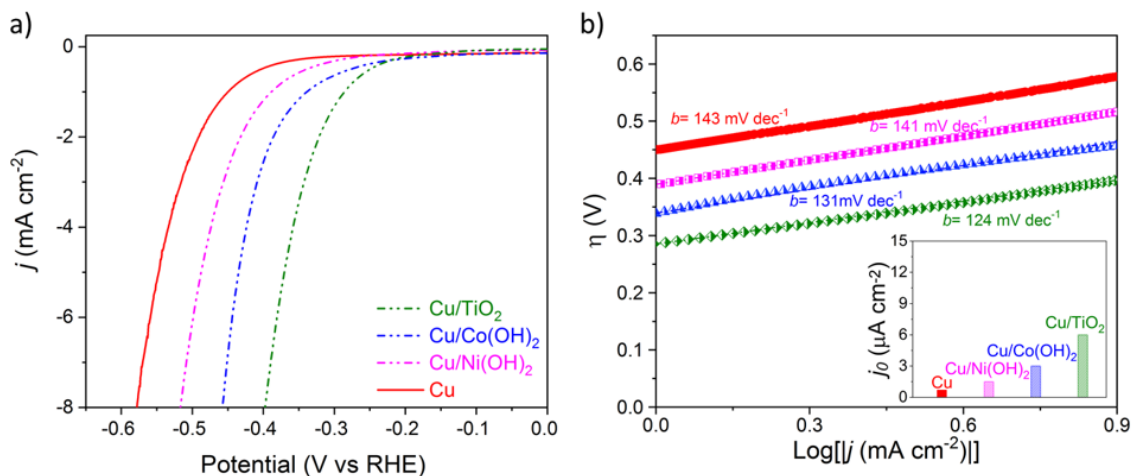


Figure 3.5: Electrochemical characterization of Cu/MO/OH. a) Typical HER activities for Cu/MO/OH and Cu evaluated in H_2 saturated 0.1 M KOH solution with a rotation speed of 1800 rpm at room temperature with a scan rate of 10 mV s^{-1} . b) Corresponding Tafel plots and (inset graph) exchange current densities.

and metal oxide/hydroxide plays a critical role in facilitating water dissociation on Cu-based catalytic surfaces. Previous studies have indicated that the Volmer step, the water activation step to form the first H_{ads} , is likely the critical step for HER in alkaline conditions.[11–15] Because Cu has weak hydrogen binding sites, the adsorption of water molecule through the interaction of the proton group and eventual formation of H_{ads} is rather difficult. However, with the addition of an oxophilic site such as Ti, the oxophilic site can help adsorb water to the surface through weak interactions with the oxygen atom of the hydroxyl group while a nearby Cu site can facilitate the formation of H_{ads} , and thus the Volmer step. In a recent work, Markovic and co-workers clearly demonstrated that $\text{Ni}(\text{OH})_2$ deposited on Pt had the greatest improvement in HER activity, while more oxophilic metals (e.g. $\text{Mn}(\text{OH})_2$) led to the poisoning of the active sites.[14] However, in the Cu system, $\text{Ni}(\text{OH})_2$ had the least while TiO_2 had greatest enhancement. We speculate the difference is likely due to the weak hydrogen binding strength of Cu in comparison to Pt; and therefore, a more oxophilic dopant

(Ti) is needed to help facilitate the activation of water. In the case of pure Pt, Pt sites have near optimal HBEs; therefore, the formation of H_{ads} is efficient without the need of an oxophilic dopant. Thus, Pt has the highest HER activity compared to both Cu–M bimetallics and Cu/MO/OH catalysts even though it has the lowest OBE values (Figure B.7).[16] Stemming from these observations, we concluded that the HBE is still the dominant descriptor for HER in base, while the presence of an oxophilic metal or metal oxide/hydroxide could increase HER activity where the OBE can be used as a secondary descriptor to predict the level of enhancement. A recent work by Koper and co-workers using a laser-induced temperature-jump method have also suggested that the addition of $\text{Ni}(\text{OH})_2$ on Pt helps lower the energy barrier for interfacial water reorganization, leading to an enhancement in H_2 evolution.[17] Future work employing a similar technique in conjunction with computational efforts that incorporate solvation effects can further elucidate the HER activity enhancement over Cu–based bimetallic catalysts.

Understanding the role of oxophilic dopant in Cu–M bimetallics for water dissociation is also critical for the rational design of CO_2 reduction catalysts. Cu–M bimetallics have been proposed as potential candidates for enhancing CO_2 reduction activity, where the addition of a second metal can potentially alter the binding energies of key reaction intermediates.[18] For example, it has been proposed that a Cu–M bimetallic surface that contains two different metal sites with one site having high oxygen affinity can stabilize the CHO^* key reaction intermediate by simultaneously interacting with both the carbon and oxygen atoms. However, the results presented in this work show that alloying Cu with oxophilic metals can also significantly enhance HER activity, the key side reaction that competes with CO_2 reduction. This signifies that alloying Cu with a highly oxophilic metal may not be a suitable approach and other strategies maybe needed to promote CO_2 reduction while simultaneously suppressing HER activity. For example, Sargent and co-workers have shown that engineering surface defects such as vacancies on Cu catalysts can help steer product selectivity toward alcohol formation.[19]

3.4 Conclusions

In summary, we studied a series of Cu–M bimetallics and Cu/MO/OH catalysts to identify descriptors to guide the rational design of non-precious metal catalysts for water dissociation in alkaline conditions. We showed that alloying Cu with low concentrations of oxophilic metals (Ti, Co, or Ni) or depositing oxophilic metal oxide/hydroxide clusters (TiO_2 , $\text{Co}(\text{OH})_2$, or $\text{Ni}(\text{OH})_2$) can dramatically improve the catalytic performance compared to pure Cu. The enhancement in the HER activity is likely due to the synergistic interactions between Cu and the oxophilic dopant. Combining both DFT and experimental investigations, we concluded that HBE is the dominant descriptor for HER in base, while the OBE can be used as a secondary descriptor to describe the level of enhancement. Although this work primarily focused on bulk Cu–M bimetallic systems, this discovery can aid in the rational design of other non-precious bimetallic catalysts.

3.5 Acknowledgment

This work was supported by the NASA EPSCoR/RID program and the National Science Foundation CAREER Program (Award No. CBET-1350911). I would like to thank Dr. Zhao Jiang and Prof. Jinguang G. Chen of Columbia University for the DFT calculations and computation insights. I would also like to thank Prof. George C. Hadjipanayis for access to the vacuum arc remelting instrument and I would like to thank Jared Nash for help with electrochemical measurements and helpful discussions.

REFERENCES

- (1) Kuhl, K. P.; Cave, E. R.; Abram, D. N.; Jaramillo, T. F. *Energy & Environmental Science* **2012**, *5*, 7050–7059.
- (2) Kuhl, K. P.; Hatsukade, T.; Cave, E. R.; Abram, D. N.; Kibsgaard, J.; Jaramillo, T. F. *Journal of the American Chemical Society* **2014**, *136*, 14107–14113.
- (3) Kim, D.; Kley, C. S.; Li, Y.; Yang, P. *Proceedings of the National Academy of Sciences* **2017**, *114*, 10560–10565.
- (4) Clark, E. L.; Hahn, C.; Jaramillo, T. F.; Bell, A. T. *Journal of the American Chemical Society* **2017**, *139*, 15848–15857.
- (5) De Luna, P.; Quintero-Bermudez, R.; Dinh, C.-T.; Ross, M. B.; Bushuyev, O. S.; Todorović, P.; Regier, T.; Kelley, S. O.; Yang, P.; Sargent, E. H. *Nature Catalysis* **2018**, *1*, 103–110.
- (6) Jiang, K.; Sandberg, R. B.; Akey, A. J.; Liu, X.; Bell, D. C.; Nørskov, J. K.; Chan, K.; Wang, H. *Nature Catalysis* **2018**, *1*, 111–119.
- (7) Lu, Q.; Hutchings, G. S.; Yu, W.; Zhou, Y.; Forest, R. V.; Tao, R.; Rosen, J.; Yonemoto, B. T.; Cao, Z.; Zheng, H.; Xiao, J. Q.; Jiao, F.; Chen, J. G. *Nature Communications* **2015**, *6*, 6567.
- (8) Biesinger, M. C.; Lau, L. W. M.; Gerson, A. R.; Smart, R. S. C. *Applied Surface Science* **2010**, *257*, 887–898.
- (9) Biesinger, M. C.; Payne, B. P.; Grosvenor, A. P.; Lau, L. W. M.; Gerson, A. R.; Smart, R. S. C. *Applied Surface Science* **2011**, *257*, 2717–2730.
- (10) Dunwell, M.; Lu, Q.; Heyes, J. M.; Rosen, J.; Chen, J. G.; Yan, Y.; Jiao, F.; Xu, B. *Journal of the American Chemical Society* **2017**, *139*, 3774–3783.
- (11) Parsons, R. *Transactions of the Faraday Society* **1958**, *54*, 1053–1063.
- (12) Subbaraman, R.; Tripkovic, D.; Strmcnik, D.; Chang, K.-C.; Uchimura, M.; Paulikas, A. P.; Stamenkovic, V.; Markovic, N. M. *Science* **2011**, *334*, 1256–1260.
- (13) Danilovic, N.; Subbaraman, R.; Strmcnik, D.; Chang, K.-C.; Paulikas, A. P.; Stamenkovic, V. R.; Markovic, N. M. *Angewandte Chemie International Edition* **2012**, *51*, 12495–12498.
- (14) Subbaraman, R.; Tripkovic, D.; Chang, K.-C.; Strmcnik, D.; Paulikas, A. P.; Hirunsit, P.; Chan, M.; Greeley, J.; Stamenkovic, V.; Markovic, N. M. *Nature Materials* **2012**, *11*, 550–557.

- (15) Gong, M.; Zhou, W.; Tsai, M.-C.; Zhou, J.; Guan, M.; Lin, M.-C.; Zhang, B.; Hu, Y.; Wang, D.-Y.; Yang, J.; Pennycook, S. J.; Hwang, B.-J.; Dai, H. *Nature Communications* **2014**, *5*, 4695.
- (16) Sheng, W.; Gasteiger, H. A.; Shao-Horn, Y. *Journal of The Electrochemical Society* **2010**, *157*, B1529–B1536.
- (17) Ledezma-Yanex, I.; Wallace, W. D. Z.; Sebastian-Pascual, P.; Climent, V.; Feliu, J. M.; Koper, M. T. M. *Nature Energy* **2017**, *2*.
- (18) Peterson, A. A.; Nørskov, J. K. *The Journal of Physical Chemistry Letters* **2012**, *3*, 163–184.
- (19) Zhuang, T.-T. et al. *Nature Catalysis* **2018**, *1*, 421–428.

Chapter 4

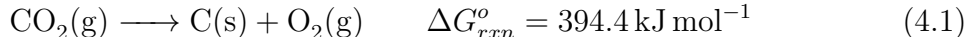
CARBON DIOXIDE SPLITTING USING AN ELECTRO-THERMOCHEMICAL HYBRID LOOPING STRATEGY

In Chapter 1, I introduced the concept of a two-step process for CO₂ electrolysis and presented the motivation for developing a high-performing CO₂ electrolyzer that can efficiently convert CO₂ to CO with high selectivities and high single-pass conversion. In Chapter 3, I presented a more fundamental work involving the study of bulk Cu-based bimetallic surfaces in a batch electrochemical cell for catalyst development. The focus of this chapter is reactor engineering and process design to develop a high-performing electrochemical system for continuous CO₂ to CO conversion. In particular, this work demonstrates a proof-of-concept for an electro-thermochemical hybrid looping strategy for O₂ recovery applications for deep space manned missions, and was a collaboration between University of Delaware and NASA Glenn Research Center. At University of Delaware, the CO₂ electrolyzer system was developed, and this project was summarized in a paper titled, “Carbon Dioxide Splitting Using an Electro-thermochemical Hybrid Looping Strategy,” published in *Energy & Environmental Science* 11, 2928-2934 (2018). As an author, I was involved with the scale-up of a nanoporous silver (np-Ag) catalyst, design of the CO₂ electrolyzer, and performance evaluation. Matthew Jouny also helped with performance evaluation, and Jonathon Rosen helped with the initial reactor design and setup.

4.1 Introduction

O₂ recovery from metabolically produced CO₂ has been investigated as a critical life support technology to sustain long-duration manned deep space missions. The current state-of-the-art technology is based on a high-temperature Sabatier reactor

that operates at over 1000 K and can only recover 50% of the O_2 from CO_2 . The low O_2 recovery is mainly due to the continual overboard venting of CH_4 , a waste by-product, which causes the loss of H_2 (in the form of CH_4) needed to further reduce CO_2 . [1, 2] To enable long-duration manned missions beyond Earth’s orbit, a technology that is able to split CO_2 into elemental carbon (C) and O_2 stoichiometrically is ideal for O_2 recovery because it allows for 100% O_2 recovery from CO_2 . However, CO_2 is a thermodynamically stable molecule and the direct splitting of CO_2 into C and O_2 is highly unfavorable as shown in Equation 4.1.[3] Therefore, the direct splitting of CO_2 requires extremely high reaction temperatures ($\gg 2000$ K) which is not suitable on spacecrafts (Figure 4.1a).



Recent development in electrochemical reduction of CO_2 in aqueous electrolytes with a focus on transforming CO_2 to value-added fuels and chemicals has opened new pathways for activating CO_2 at ambient conditions.[4–11] In a typical CO_2 electrolyzer, CO_2 is converted at the cathode to reduced carbon-containing species, such as CO and formate, while O_2 is generated at the anode via the water oxidation reaction.[12] Often in these electrolysis studies, the generated O_2 is viewed as a non-valued product. However, in the case of O_2 recovery, this technology can be used as an alternative method to generate valuable O_2 . Similar to thermal conversion of CO_2 , there are no electrochemical reduction catalysts that can directly transform CO_2 to elemental C with appreciable selectivities.

Herein, we propose a novel electro-thermochemical hybrid looping (ETHL) process as an alternative method for O_2 recovery, which combines an electrochemical CO_2 reduction step that operates at ambient conditions and a thermochemical CO decomposition step that operates at ambient pressure and relatively mild temperatures. This ETHL process as shown in Figure 4.1b provides a new approach to convert CO_2 into

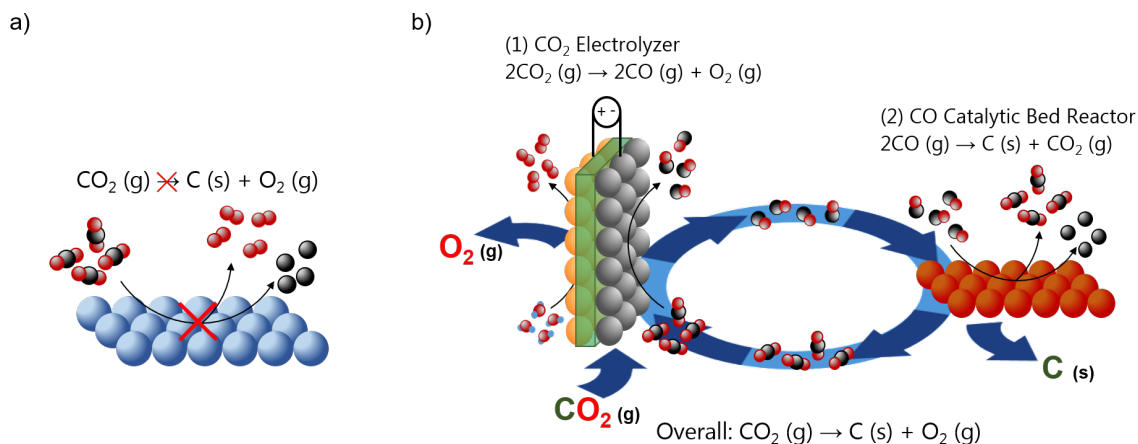


Figure 4.1: a) Direct CO_2 splitting is nearly impossible. b) Schematic representation of the ETHL process for O_2 recovery.

elemental C and O_2 that cannot be accomplished through any single-step electrochemical or thermochemical processes. In the first step, the electrochemical reduction of CO_2 occurs at ambient conditions (298 K and 1 bar) in a CO_2 electrolyzer, where CO and O_2 are produced at the cathode and anode, respectively. The cathode and anode chambers are separated by a PEM, which ensures the physical separation of CO and O_2 . Due to the low solubility of CO in water, the CO product can be easily separated from the aqueous electrolyte using a porous membrane gas/liquid separator. In the second step, the produced CO from the electrolyzer is fed into a catalytic bed reactor, where CO is thermally decomposed into elemental C and CO_2 at an operating temperature of ~ 723 K. Through a solid/gas separator, the solid C product is accumulated and removed from the catalytic bed reactor, whereas the CO_2 gas product along with captured CO_2 is then fed back to the CO_2 electrolyzer. The net result is the stoichiometric splitting of CO_2 to elemental C and O_2 at separate stages with minimal by-products. The experimental results in this work show that a theoretical 96% recovery of O_2 from CO_2 can be achieved, representing a significant improvement from the current state-of-the-art system ($\sim 50\%$) on the International Space Station.

4.2 Experimental Methods

4.2.1 Fabrication of Nanoporous Ag Electrode

np–Ag cathodes were fabricated using a modified dealloying technique. In brief, a $40 \times 5 \times 5 \text{ cm}^3$ Ag–Al ingot that was synthesized using a vacuum induction process was purchased from Sophisticated Alloys, Ltd (USA). The ingot was then cut in to 25 cm^2 Ag–Al precursor sheets with thickness of $500 \text{ }\mu\text{m}$ using electrical discharge machining. The precursor sheets were then annealed at $546 \text{ }^\circ\text{C}$ for 24 h and then quenched in an ice water bath to achieve the desired phase. Subsequently, the precursor sheets were leached in dilute hydrochloric acid, rinsed several times in deionized (DI) water, and then immediately placed into the CO_2 electrolyzer.

4.2.2 Construction of the Ir-catalyst coated Nafion Membrane

Iridium–catalyst coated membrane (Ir–CCM) anode was constructed via a hand-airbrush technique. A catalyst ink was prepared by sonicating a slurry containing commercial Ir black nanoparticles (surface area $55\text{--}65 \text{ m}^2 \text{ g}^{-1}$, Premetek Co.), Nafion solution (5 wt%, DuPont), DI water, and isopropanol. The weight ratio of catalyst to dry Nafion ionomer was 4:1. The Ir containing slurry was then sprayed on to Nafion XL that has been sandwiched between two self-adhesive Mylar laminate (DuPont) with a 25 cm^2 window. The resulting Ir–CCM anode was dried at $40 \text{ }^\circ\text{C}$ for one hour. The procedure was repeated until a catalyst loading of 1 mg cm^{-2} was achieved. After the desired weight was obtained, the as-sprayed Ir–CCM was then hot pressed at $135 \text{ }^\circ\text{C}$ and 2 MPa for 1 min.

4.2.3 Design and Operation of the CO_2 Electrolysis Cell

The CO_2 electrolyzer was a two-compartment MEA-based electrolyzer which was constructed out of stainless steel and then plated with a $2 \text{ }\mu\text{m}$ gold layer to prevent corrosion as shown in Figure C.1. The np–Ag catalyst was used as the cathode, while the Ir–CCM was used to separate the two compartments as well as the catalyst for the anode. A CO_2 –saturated 0.5 M sodium bicarbonate (NaHCO_3) (99.9999%,

Sigma Aldrich) aqueous electrolyte solution was fed and recirculated at a flowrate of 150 mL min^{-1} through the cathode compartment. Prior to experiments, the NaHCO_3 solution was purified of trace metal by stirring the as-made solution with Chelex® 100 Resin (50-100 mesh, Sigma Aldrich) overnight. A gear pump (EW-74013-40, Cole-Parmer) was used to drive the electrolyte from a reservoir, through a flow meter (1XLX3, Brooks), then through an in-line CO_2 contactor, and then finally to the cathode compartment. For activity testing, CO_2 gas (Grade 5, Keen) was fed at 20 mL min^{-1} through a porous ceramic (Refractron) in a custom built in-line CO_2 contactor (Figure C.3). To optimize single pass CO_2 conversion at 3.0 V, CO_2 gas was fed at 7.25 mL min^{-1} . The outlet stream from the electrolyzer was then fed to a gas/liquid separator. The separator was a homemade stainless steel knockout drum with a bore through union tee on the inlet and back pressure regulator on the outlet. Low solubility gases such as CO and H_2 were separated for quantification while the electrolyte was recycled back to the reservoir for continuous operation. No electrolyte was used for the anode compartment and this prevented water from crossing over from the anode to cathode that could dilute the catholyte and degrade performance. Gas products from the gas/liquid separator were fed into a 1 mL sample loop of a GC (Shimadzu, GC-2010) equipped with PLOT Mol Sieve 5A and Q-bond PLOT columns to confirm and separate the CO and H_2 products. Argon (99.999%) was used as the carrier gas and a thermal conductivity detector was used for product quantification. An Autolab PGSTAT128N potentiostat with a 10 A booster was used for chronoamperometry experiments.

4.2.4 Design and Operation of the CO Catalytic Bed Reactor

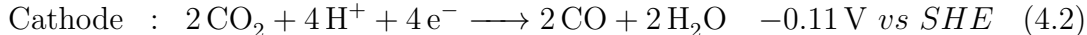
The reactor assembly (Figure C.4) consisted of 5 parts: the reactor chamber which was fabricated from Aluminum Bronze 614, tee sections on either side of the reactor, ball valves at each end, servicing assembly, and a carbon/catalyst receiving assembly. A “clamp shell” type furnace was used to heat up the reactor chamber to $500 \text{ }^\circ\text{C}$. During operation, CO was fed to the reactor chamber through a tee valve at one

end. CO decomposed into elemental C and CO₂ within the reactor chamber. Carbon was retained, while CO₂ exited the other tee valve on the other end. The ball valves at either end of the tee valves sealed the whole reactor assembly during operation. After reaction, the servicing assembly consisted of a ram was attached. The ball valves were opened, and the ram was used to push the carbon/catalyst material out of the reactor into the receiving assembly. New catalyst materials were loaded in a similar manner. As for the catalyst, GMT grade 0 steel wool was dipped in 10 vol% acetic acid solution for 3 min followed by rinsing with DI water and air drying prior to being loaded into the reactor chamber for testing. In addition, a recuperative heat exchanger was connected to the reactor chamber to heat the inlet gaseous stream with the hot outlet gaseous stream. The power of the furnace and the temperature were controlled by a furnace controller (Mellen). A custom-built data acquisition system recorded the temperatures and pressures within the reactor assembly. The CO₂ concentration of the outlet stream was continuously monitored with an infrared carbon dioxide analyzer (GD-888, CEA Instruments, Inc.) with a reading resolution of 0.1% and accuracy of ±5%.

4.3 Results

4.3.1 Electrochemical Reduction of CO₂

Recent advances in electrochemical reduction of CO₂ has demonstrated the feasibility of converting CO₂ selectively into CO and O₂ using a MEA-based electrolyzer at ambient conditions.[13–15] The half-reactions along with their theoretical potentials are listed as follow:



For the CO₂ electrolyzer, the utilization of catalysts is critical to avoid the production of undesirable by-products and to reduce the overpotentials associated with

activation losses. We recently developed a np–Ag catalyst that was able to reduce CO₂ to CO with a 92% selectivity at a reaction rate approximately 100 times higher than its polycrystalline counterpart under mild overpotentials.[16, 17] In a typical two-compartment batch cell, a maximum CO partial current density of 35 mA cm⁻² was achieved at an overpotential of 0.7 V. The superior performance was attributed to the highly active internal surfaces of the nanoporous structure, large surface area, and the monolithic self-supporting structure that allows for fast electron transport. In addition, the scalability of the np–Ag has been recently demonstrated as well.[18] As for the water oxidation catalyst, Ir was chosen due to its high water oxidation activity as well as stability in a wide range of pH values.[19] Therefore, both np–Ag and Ir–based catalysts were chosen for this ETHL proof-of-concept study.

The demonstration of the electrochemical reduction of CO₂ to CO and O₂ was conducted in a 25 cm² gold-plated stainless steel continuous MEA-based electrolyzer (Figure C.1) where the np–Ag catalyst was used to facilitate the conversion of CO₂ to CO while Ir nanoparticles that were sprayed and hot pressed onto a Nafion XL membrane were used to facilitate water oxidation to produce O₂ (Figure C.2). The overall schematic of the electrolyzer system for the CO₂ electrolysis cell is shown in Figure 4.2a. In short, chelex-pretreated CO₂–saturated NaHCO₃ solution[20] was circulated continuously through the cathode compartment of the electrolyzer, while the anode compartment was left open to air without the presence of liquid electrolyte. The hydrophilicity of the Nafion membrane allows sufficient water transport from the cathode compartment to the Ir nanoparticles at the anode for the water oxidation reaction. CO₂ gas was fed into the system through a custom designed CO₂ contactor (Figure C.3) to ensure re-saturation of the circulating electrolyte while CO was separated in a gas/liquid separator. Quantification of gaseous products were analyzed with a GC. Chronoamperometry experiments were conducted by varying the applied cell potential and measuring the current and the Faradaic efficiencies of each product in the span of one hour. In addition, long-term stability testing was conducted to determine the durability of the CO₂ electrolyzer.

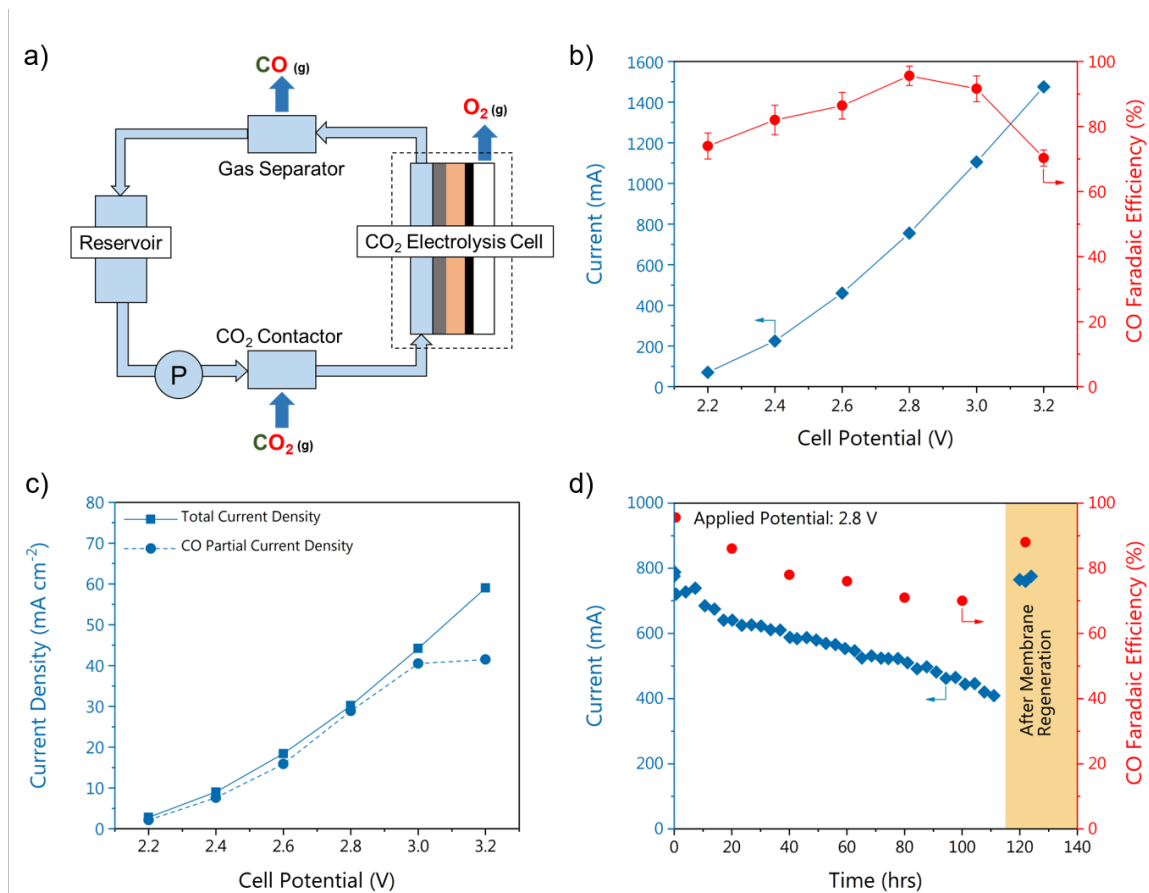


Figure 4.2: Electrochemical reduction of CO₂. a) A simplified schematic of the CO₂ electrolyzer flow system, b) overall performance of CO₂ electrolysis cell, c) total current density and CO partial current density, and d) long term stability testing.

The performance of the CO₂ electrolyzer is summarized in Figure 4.2b-d. The only CO₂ reduction product observed was CO and the remaining electron balance is attributed to the competing HER with a trace amount of formate (< 1%). As the cell potential increases from 2.2 to 3.2 V, the total current density increases from 70 mA (2.8 mA cm⁻²) to 1475 mA (59 mA cm⁻²), while the CO Faradaic efficiency reaches a maximum of 96% at 2.8 V. It must be noted that the reported cell potential includes the cathodic and anodic losses as well as transport and ohmic losses in the entire electrolysis cell. The slight decrease in Faradaic efficiency at 3.2 V is likely due to CO₂

transport limitation from the bulk solution to the catalytic surface and the low solubility of CO_2 in aqueous solution ($\sim 33\text{ mM}$ at ambient conditions) as indicated by the plateauing of the CO partial current density vs. the applied potential as shown in Figure 4.2c. Long-term stability testing was conducted at 2.8 V over the span of 110 h. As shown in Figure 4.2d, the current decays by $\sim 50\%$ and is accompanied by a drop in CO Faradaic efficiency. Since the electrolyzer operated in sodium bicarbonate electrolyte with a proton-exchange membrane (Nafion XL), the observed decay in the performance is likely due to Na^+/H^+ cation exchange in the Nafion membrane that caused a decrease in ionic conductivity with an increased internal resistance within the electrolyzer. The increased potential losses affected the applied overpotential on the cathode; and thus, a decrease in CO Faradaic efficiency was observed. Residual Cu contamination on the np-Ag catalyst was also observed with post-reaction XPS as shown in Figure C.5, most likely from the reduction of metal impurities from the electrolyte. To recover the performance, the used membrane was regenerated in dilute sulfuric acid and the performance of the CO_2 electrolyzer was recovered (Figure 4.2d), confirming that the Na^+ cations from the electrolyte are the major source of degradation. A potential solution to circumvent this issue is to utilize an AEM; and until recently, these membranes have demonstrated long-term stability for CO_2 electrolyzers.[21, 22] In general, the CO_2 electrolyzer achieved greater than 1 A of CO partial current and high selectivities, demonstrating the feasibility of electrochemically transforming CO_2 to CO.

Despite the limiting CO partial current density, this system configuration benefits from high single-pass conversion. To optimize conversion, CO_2 gas was fed (7.25 mL min^{-1}) to the recirculating CO_2 -saturated bicarbonate electrolyte to closely match the calculated CO_2 consumption at 3.0 V (Figure 4.2b). An average single pass CO_2 conversion of $\sim 86\%$ was observed in the span of one hour as shown in Figure 4.3. In theory, complete conversion can be obtained; however, further optimization of CO_2 feed rate and the pore size of the contactor is needed to enhance the surface/volume ratio of the gas bubbles such that CO_2 can rapidly dissolve into the electrolyte.[23]

Ideally, the rate of fed CO₂ gas dissolving into the electrolyte should be equal to the rate of CO₂ consumption such that the electrolyte is always CO₂ saturated at steady-state without introducing excess CO₂. More importantly, since CO₂ is dissolved in the electrolyte, the gaseous CO product, which has orders of magnitude lower solubility than CO₂, can be easily separated to produce a highly pure CO stream. This is critical as unreacted CO₂ could impede the performance of the CO catalytic bed reactor in the second stage.

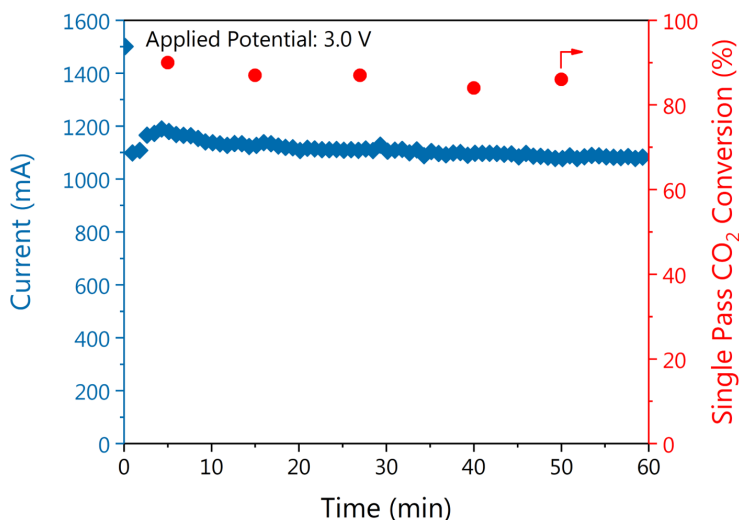
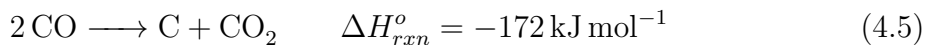


Figure 4.3: Single pass conversion study for CO₂ electrolyzer. The CO₂ gas feed rate was set to 7.25 mL min⁻¹. The CO Faradaic efficiency ranged from 81 to 86%

4.3.2 CO Thermochemical Conversion

The thermochemical conversion of CO via the Boudouard reaction occurs in a catalytic bed reactor in which CO is converted to elemental C and CO₂. The reaction is as follows:



where the deposited C is primarily in the forms of amorphous carbon, graphite, and carbon nanofibers.[24, 25] The Boudouard process thermodynamically favors the deposition of carbon at much lower temperatures (~ 723 K) than that of the Bosch reaction (~ 923 K) as well as operating temperatures of CO_2 solid oxide electrolysis (~ 1023 K).[26] As such, the overall ETHL process benefits from much lower operating temperatures than other alternatives that are currently being investigated for O_2 recovery.

To demonstrate the thermochemical conversion of CO to elemental C and CO_2 , a tubular reactor assembly was designed and constructed with an inner diameter of ~ 2.5 cm and a length of ~ 60 cm to study the decomposition of CO as shown in Figures 4.4a and C.4. CO was fed into the tubular reactor where CO was catalytically decomposed to elemental C and CO_2 . Elemental C was retained within the reactor, while CO_2 existed the assembly. The composition of the inlet and the outlet gaseous mixtures were continuously monitored with a gas mixture analyzer. Because of the carbon accumulation inside the Boudouard reactor, the process was operated in a semi-continuous fashion and the removal/replenish of the catalyst pellets was conducted routinely to remove the deposits (Figure 4.4b). Although the catalyst can be regenerated through thermal oxidation, this process would require precious O_2 and therefore was avoided. Instead, the reactor was designed to operate via a cartridge system where fresh catalyst can be rapidly loaded to minimize additional inputs into the overall ETHL process besides CO_2 and new catalysts. Thus, the reactor was engineered such that the catalyst change-out did not require the reactor to be cooled and reheated, a long process that could take up to 17 h. Since Fe is known to adsorb CO strongly, a range of Fe-based materials were initially screened as the potential catalysts for CO decomposition.[27–29] Among all the materials, 40-mesh Fe and $5\ \mu\text{m}$ Fe_2O_3 exhibited minimal activity in carbon formation, while GTM grade 0 steel wool was found to be highly active for CO decomposition; and therefore, it was further used for catalytic studies.

The performance of the CO catalytic bed reactor was evaluated using the steel wool catalyst under various CO flow rates. The outlet CO_2 concentration was measured and the single-pass conversion was also calculated. Prior to testing, the steel wool

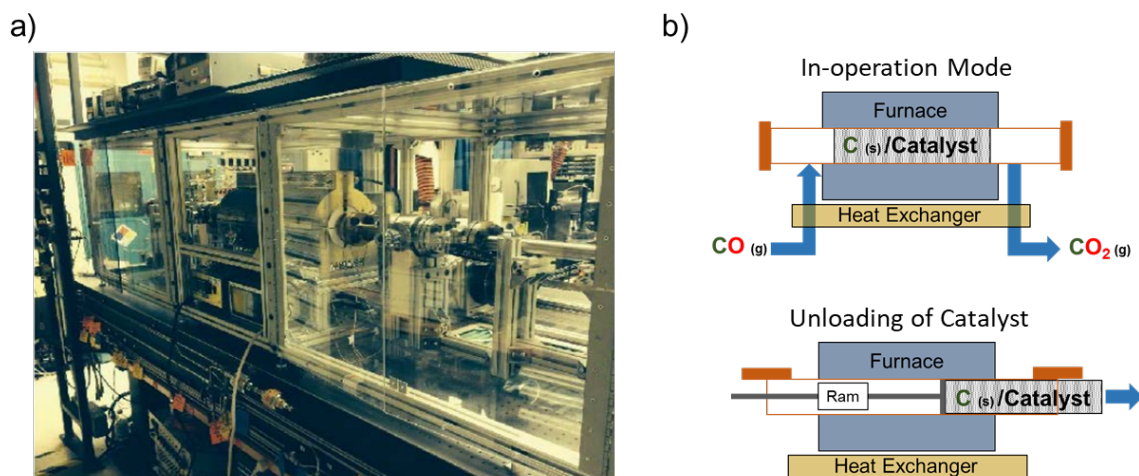


Figure 4.4: CO catalytic bed reactor. a) Photograph of the front view of the reactor assembly, and b) Schematic of the catalytic bed reactor under operating conditions and routine catalyst change out. New catalysts were also positioned in the catalytic bed reactor with the ram.

catalyst (~ 5 g) was pretreated in dilute acetic acid and washed with de-ionized water to remove residual anti-oxidation agents on the surface. The pretreatment of the catalyst with acetic acid is highly critical for successful carbon deposition as shown in Figure 4.5a. Regardless of orientation, carbon deposition did not occur on areas that were not pretreated. For each experiment, a gas mixture containing 95% CO and 5% H_2 was fed into the reactor at a reaction temperature of 773 K. The gas feed composition was chosen to simulate the outlet stream from the CO_2 electrolysis cell assuming a CO Faradaic efficiency of 95% during electrolysis. At flow rates of 0.355 and 0.710 slpm CO, a sharp rise in outlet CO_2 concentration was observed (~ 60 to 70%) over the first 30 min, followed by a gradual rise to $\sim 80\%$ (Figure 4.5b). This translated to a rapid rise of CO conversion to $\sim 85\%$, followed by a gradual increase to $>90\%$. The high single-pass conversion means that there is no need to recycle the unreacted gases within the reactor, thus simplifying the overall CO reactor design. At the highest flow rate of 1.065 slpm CO, the performance was more sluggish as indicated by a gradual rise in CO_2 outlet concentration and CO single-pass conversion in the first 30 min of

operation. No other gases besides H_2 , CO , and CO_2 were detected. Overall the rate of C deposition was significant (Figure 4.5c) and the final weight ratios of deposited C to catalyst were ~ 2 -4, which were determined by weighing the initial catalyst and the unloaded mass after reaction (Table C.1). This weight ratio was deemed acceptable based on calculations as shown in the Appendix C. However, future investigation using higher surface area catalysts can further increase the deposited C to catalyst ratio and this will reduce the required catalyst. Since unreacted CO_2 from the CO_2 electrolyzer could be present in the inlet feed to the CO catalytic bed reactor, the effects of CO_2 on the CO decomposition reaction were also studied with a gas mixture of 60% CO, 20% H_2 , and 20% CO_2 . With the presence of 20% CO_2 in the CO feed, the CO_2 outlet concentration gradually increase to 60% in 2h, corresponding to a CO single-pass conversion of 40% as shown in Figure 4.5d. Both the outlet CO_2 concentration and the CO single-pass conversion were lower than the results obtained from the 95% CO feed (Figure 4.5b), suggesting that a high purity CO inlet stream is necessary. This further motivates the development of a CO_2 electrolyzer that can achieve high single-pass conversion. Overall, the CO catalytic bed reactor was able to efficiently decompose CO to elemental C and CO_2 .

4.4 Conclusions

In this work, a new electro-thermochemical hybrid looping strategy that combines an electrochemical CO_2 reduction step with a thermochemical CO decomposition step for O_2 recovery from CO_2 was proposed. We successfully demonstrated the feasibility of each step in the proposed looping scheme individually. Through reactor engineering, we developed an electrolyzer system that can convert CO_2 to CO at high rates of reaction (greater than 1 A of CO partial current) with high single-pass conversion ($\sim 86\%$). We also showed the scalability of nanoporous materials, as majority of these materials prior to this study have only been produced at small scales ($< 0.5 \text{ cm}^2$). Combining these two steps, the newly developed hybrid looping process is able to reach a theoretical 96% of O_2 recovery, exceeding that of the current state-of-the-art

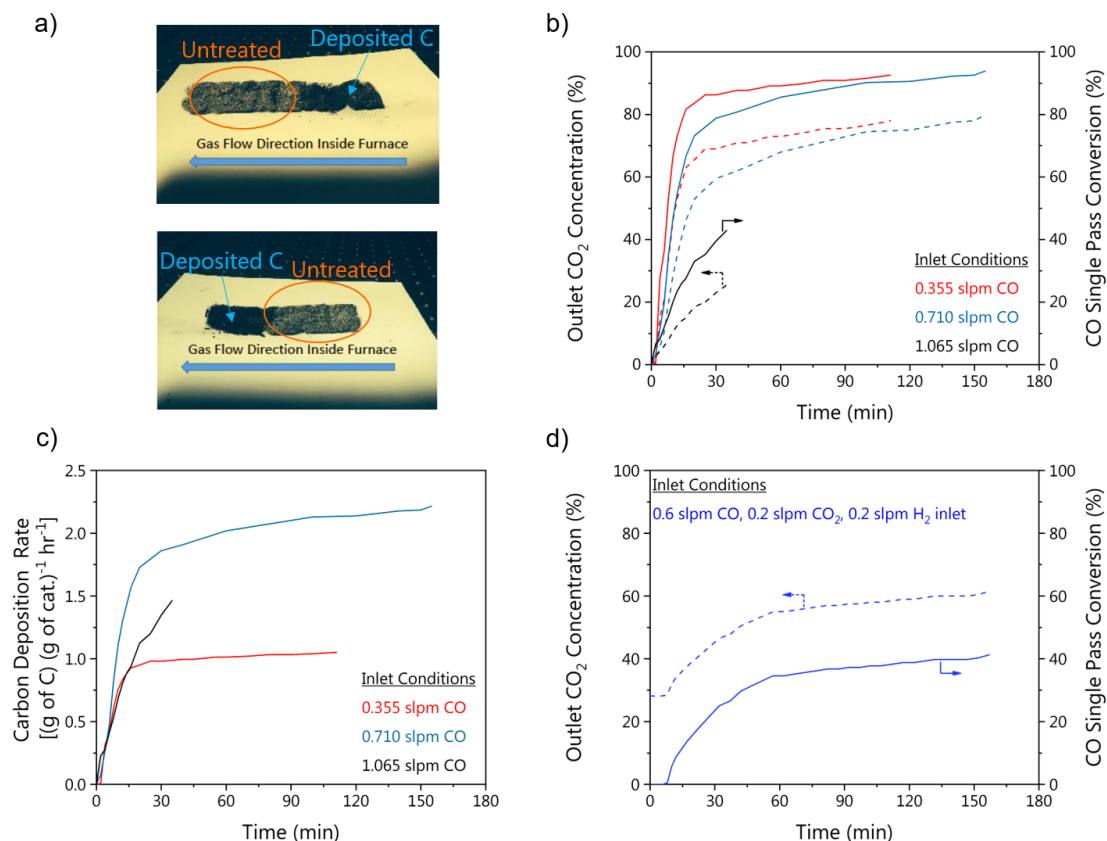


Figure 4.5: Thermochemical conversion of CO. a) The effect of pretreatment on the catalyst performance, b) outlet CO₂ concentration profiles under various CO feed rates, c) carbon deposition rate under various CO feed rates, and d) the effect of CO₂ on the CO reactor performance.

O₂ recovery system. Furthermore, this CO₂ electrolyzer can also be integrated into a two-step process for CO₂ conversion to C₂₊ products as introduced in Chapter 1.

4.5 Acknowledgment

This work was supported by the National Aeronautics and Space Administration (NASA) EPSCoR/RID program and the NASA Game Changing Development Program (Contract No. NNC15CA04C). I would like to thank Mr. Kenneth A. Burke at NASA Glenn Research Center for technical support and data of the CO catalytic bed reactor.

REFERENCES

- (1) NASA NASA Technology Roadmaps TA 6: Human Health, Life Support, and Habitation Systems., 2015.
- (2) NASA International Space Station Environmental Control and Life Support System., 2008.
- (3) Oehlschlaeger, M.; Davidson, D.; Jeffries, J.; Hanson, R. *International Journal of Research in Physical Chemistry and Chemical Physics* **2005**, *219*, 555.
- (4) Hori, Y.; Wakebe, H.; Tsukamoto, T.; Koga, O. *Electrochimica Acta* **1994**, *39*, 1833–1839.
- (5) Kuhl, K. P.; Hatsukade, T.; Cave, E. R.; Abram, D. N.; Kibsgaard, J.; Jaramillo, T. F. *Journal of the American Chemical Society* **2014**, *136*, 14107–14113.
- (6) Kortlever, R.; Shen, J.; Schouten, K. J. P.; Calle-Vallejo, F.; Koper, M. T. M. *The Journal of Physical Chemistry Letters* **2015**, *6*, 4073–4082.
- (7) Li, C. W.; Ciston, J.; Kanan, M. W. *Nature* **2014**, *508*, 504.
- (8) Kortlever, R.; Peters, I.; Koper, S.; Koper, M. T. M. *ACS Catalysis* **2015**, *5*, 3916–3923.
- (9) Singh, M. R.; Goodpaster, J. D.; Weber, A. Z.; Head-Gordon, M.; Bell, A. T. *Proceedings of the National Academy of Sciences* **2017**, *114*, E8812–E8821.
- (10) Clark, E. L.; Hahn, C.; Jaramillo, T. F.; Bell, A. T. *Journal of the American Chemical Society* **2017**, *139*, 15848–15857.
- (11) Kim, D.; Kley, C. S.; Li, Y.; Yang, P. *Proceedings of the National Academy of Sciences* **2017**, *114*, 10560–10565.
- (12) Lu, Q.; Jiao, F. *Nano Energy* **2016**, *29*, 439–456.
- (13) Delacourt, C.; Ridgway, P. L.; Kerr, J. B.; Newman, J. *Journal of the Electrochemical Society* **2008**, *155*, B42–B49.
- (14) Whipple, D. T.; Finke, E. C.; Kenis, P. J. A. *Electrochemical and Solid-State Letters* **2010**, *13*, B109–B111.
- (15) Verma, S.; Lu, X.; Ma, S. C.; Masel, R. I.; Kenis, P. J. A. *Physical Chemistry Chemical Physics* **2016**, *18*, 7075–7084.
- (16) Lu, Q.; Rosen, J.; Zhou, Y.; Hutchings, G. S.; Kimmel, Y. C.; Chen, J. G.; Jiao, F. *Nature Communications* **2014**, *5*, 3242.

- (17) Rosen, J.; Hutchings, G. S.; Lu, Q.; Rivera, S.; Zhou, Y.; Vlachos, D. G.; Jiao, F. *ACS Catalysis* **2015**, *5*, 4293–4299.
- (18) Luc, W.; Rosen, J.; Jiao, F. *Catalysis Today* **2017**, *288*, 79–84.
- (19) McCrory, C. C. L.; Jung, S.; Peters, J. C.; Jaramillo, T. F. *Journal of the American Chemical Society* **2013**, *135*, 16977–16987.
- (20) Wuttig, A.; Surendranath, Y. *ACS Catalysis* **2015**, *5*, 4479–4484.
- (21) Masel, R. I.; Liu, Z.; Sajjad, S. *ECS Transactions* **2016**, *75*, 1143–1146.
- (22) Hunt, J.; Ferrari, A.; Lita, A.; Crosswhite, M.; Ashley, B.; Stiegman, A. E. *The Journal of Physical Chemistry C* **2013**, *117*, 26871–26880.
- (23) Lobaccaro, P.; Singh, M.; Clark, E.; Kwon, Y.; Bell, A.; Ager, J. *Physical Chemistry Chemical Physics* **2016**, *18*, 26777–26785.
- (24) Holmes, R. F. *Automation of Bosch Reaction for CO₂ reduction*; Report; 1972.
- (25) Homes, R. F.; Keller, E. E.; D., K. C. *A carbon dioxide reduction unit using Bosch reaction and expendable catalyst cartridges*; Report; 1970.
- (26) Ebbesen, S. D.; Mogensen, M. *Journal of Power Sources* **2009**, *193*, 349–358.
- (27) Sunderlin, L. S.; Wang, D.; Squires, R. R. *Journal of the American Chemical Society* **1992**, *114*, 2788–2796.
- (28) Sunderlin, L. S.; Wang, D.; Squires, R. R. *Journal of the American Chemical Society* **1993**, *115*, 12060–12070.
- (29) González-Blanco, O.; Branchadell, V. *The Journal of Chemical Physics* **1999**, *110*, 778–783.

Chapter 5

TWO-DIMENSIONAL COPPER NANOSHEETS FOR ELECTROCHEMICAL REDUCTION OF CARBON MONOXIDE TO ACETATE

In Chapter 1, I introduced the typical challenges faced in performing CO electrolysis in batch electrochemical cells. As the solubility of CO is extremely low in aqueous electrolyte, the rate of reaction is greatly limited by the mass transport of CO to the catalytic surface. In order to overcome this limitation, a flow-cell electrolyzer can be utilized where gaseous reactant can be directly fed to the electrolyte-electrode interface, and more details can be found in Chapter 2. In Chapter 3, I suggested that doping Cu with oxophilic metals may not be a valid strategy for designing CO₂/CO reduction catalysts as these bimetallics would enhance the unwanted HER. With that in mind, I sought to understand CO₂/CO reduction by tuning the local structure of the Cu catalyst by exposing specific surfaces. In this work, I demonstrate CO electrolysis at high rates of reaction on well-defined nanostructured Cu catalysts that selectively expose the (111) and (100) surfaces in efforts to understand C₂₊ product formation on Cu and to bridge gaps between fundamental (e.g. single-crystal studies, operating at low current densities) and device-level studies. This work, titled “Two-Dimensional Copper Nanosheets for Electrochemical Reduction of Carbon Monoxide to Acetate,” is published in *Nature Catalysis* 2019, *in press*. This work was a collaboration between University of Delaware, University of Electronic Science and Technology of China, The University of Texas at Austin, and Northwestern University. As a co-first author, I led the electrocatalytic evaluations while Xianbiao Fu led the synthesis of the nanostructured Cu catalysts. JianJian Shi performed the DFT calculations. Jing-Jing Lv, Matthew Jouny, and Byung Hee Ko helped with electrocatalytic evaluations and XAS

studies. Yaobin Xu, Qing Tu, Xiaobing Hu, Xiaobing Hu, and Jingsong Wu assisted in material characterization.

5.1 Introduction

As mentioned in Chapter 1, Cu is unique and one of the most widely studied material because it is able to convert CO_2 or CO_2 -derived CO to C_{2+} products at relatively high selectivities in comparison to other monometallics in CO_2/CO electrolysis.[1–13] Many efforts have been devoted toward engineering Cu-based catalysts, such as nanostructuring, thermal annealing, and alloying, in the hopes of steering product selectivity and boosting catalytic activity. Although some progresses have been made, a good understanding of the structure-activity relationship is still lacking in Cu-catalyzed CO_2/CO reduction, which is mainly due to the difficulties in synthesizing well-defined Cu materials with surfaces terminated with desired facets as well as examining such materials at practical rates of reaction. For example, the well-defined Cu(111) model surface at nanoscale is still missing, while the Cu(100) has been offered by solution-phase-synthesized Cu nanocubes.[14–17]

Recently we have shown that micron-sized and oxide-derived Cu (OD-Cu) catalysts are able to reduce CO to C_{2+} products at high rates in an alkaline electrolyte. Among all the C_{2+} products, acetate with a Faradaic efficiency of $\sim 20\%$ was observed, which is higher than what is typically observed in CO_2 electrolysis ($< 5\%$).[3, 12] Transport modeling suggests a highly alkaline environment (a high pH value) near the electrode-electrolyte interface may promote the formation of acetate.[3] However, it is still unclear whether the surface nature of the catalyst also plays a role in enhancing acetate production. Because of the polycrystalline nature of both catalysts, correlating the observed acetate selectivity with the catalytic surface structure is difficult. Therefore, new synthetic methods for engineering Cu nanomaterials with well-controlled surfaces are urgently required.

Herein, we report the synthesis of freestanding high-quality Cu nanosheets with two-dimensional (2D) triangular shaped morphology using a solution-phase synthesis

procedure. The as-synthesized Cu nanosheets are ~ 5 nm thick, which selectively expose Cu {111} facets. As a model catalyst for CO electrolysis, the Cu nanosheets exhibit an acetate Faradaic efficiency as high as 48%, representing among the highest acetate selectivity that has been achieved in electrochemical CO₂/CO electrolysis at practical rates of reaction (>100 mA cm⁻²). The enhanced acetate formation is attributed to the suppression of other C₂₊ products, due of the reduction of exposed (100) and (110) surfaces that are known to be favorable toward ethylene and ethanol formation. Furthermore, computation studies suggest that the pathway toward acetate formation goes through a ketene intermediate, with the incorporation of one oxygen atom from the electrolyte and the other originating from the CO reactant.

5.2 Experimental Methods

5.2.1 Synthesis of Cu Nanosheets

In a typical synthesis of Cu nanosheets, copper(II) nitrate trihydrate (50 mg), L-ascorbic acid (100 mg) and 15.0 mL DI water were added into a vial (volume: 20 mL). After forming a homogeneous solution, hexadecyltrimethylammonium bromide (CTAB, 100 mg) and hexamethylenetetramine (HMTA, 100 mg) were added. After 30 min stirring, the vial of solution was capped and heated from room temperature to 80 °C (~ 2 °C min⁻¹) and kept at 80 °C for 3 h in an oil bath. The resulting products were collected by centrifugation and washed three times with an ethanol/DI water mixture.

5.2.2 Synthesis of Cu Nanocubes

In a typical synthesis of Cu nanocubes, 35 mL oleylamine and 3.0 g trioctylphosphine oxide were mixed at room temperature and were heated to 60 °C (~ 5 °C min⁻¹) under vacuum. After kept at 60 °C for 20 min, the vacuum was replaced by Ar atmosphere, and 215.0 mg CuBr was rapidly added into the mixture. The solution was then heated 265 °C (~ 7 °C min⁻¹) and kept for 20 min before naturally cooling to room temperature. The resulting products were collected by centrifugation and washed three times with hexane/ethanol.

5.2.3 Preparation of Electrodes

To construct the cathode electrode, a catalyst slurry containing 25 mg of as-synthesized Cu nanosheets, 3 mL isopropanol, and 20 μL of Nafion ionomer solution (5 wt% in water) was first mixed and sonicated. Next, the catalyst slurry was slowly dropcast onto a Sigracet 29 BC GDL (Fuel Cell Store) to achieve a catalyst loading of $\sim 0.5 \text{ mg cm}^{-2}$. A similar procedure was used for commercial 1 μm Cu particles (0.5-1.5 μm), 99%; Alfa Aesar) and 25 nm Cu particles (25 nm nanopowder; Sigma-Aldrich). As for the anode electrode, IrO_2 nanoparticles (99%; Alfa Aesar) was used instead.

5.2.4 Material Characterization

Transmission electron microscopy (TEM) images were taken with a Hitachi 8100 at an acceleration voltage of 200 kV. High-resolution TEM images were taken with a JEOL ARM300F at an acceleration voltage of 200 kV. AFM measurements were performed on a Dimension Icon (Bruker) to obtain 3D profiles of the patterns. XRD spectra were collected on a Rigaku SmartLab Thin-film Diffraction Workstation with a Cu $K\alpha$ source. A high intensity 9 kW Cu rotating anode X-ray source is coupled to a multilayer optic. An Auriga 60 Cross Beam SEM instrument was used to obtain SEM images of the Cu nanosheets. To analyze the composition near the surface, a K-Alpha X-ray Photoelectron Spectrometer System (Thermo Fisher Scientific) was used. CasaXPS software was used to analyze the XPS data and conduct peak analysis. The adventitious carbon peak was calibrated to 284.5 eV and all peaks were fitted using a Gaussian/Lorentzian product line shape with a Shirley background.

The electrochemical surface area (ECSA) was determined by measuring the double-layer capacitance (C_{DL}) of the as-prepared electrodes in Ar-purged 0.1 M HClO_4 in a H-cell. The scan rate was varied from 10 to 100 mV s^{-1} in the non-Faradaic potential region and the observed current was plotted as a function of scan rate to obtain the C_{DL} . The ECSA was determined by normalizing the C_{DL} to that of a Cu foil.

Electrosorption of hydroxide (OH_{ads}) studies were conducted by performing cyclic voltammetry in an Ar-purged 1 M KOH in a H-cell. The voltammogram was collected at 100 mV s^{-1} . *In-situ* OH_{ads} studies was conducted by flowing Ar in the flow-cell electrolyzer. The electrolyte flow rate was stopped to minimize the fluctuation in the voltammogram. Next, CO electrolysis was conducted at constant current density of 100 mA cm^{-2} for 1 h by switching the gas feed to CO and flowing the electrolyte. Immediately after electrolysis, the gas feed was switch back to Ar, the electrolyte flow rate was stopped, and then cyclic voltammetry was performed.

Operando X-ray absorption spectroscopy (XAS) was performed at the 8-ID Beamline of the National Synchrotron Light Source II at Brookhaven National Laboratory. A modified two-compartment flow-cell electrolyzer made from acrylic was used for *operando* XAS studies (Figure D.10). The gas chamber had a small window cut out sealed with Kapton film to allow fluorescence signals to pass from the electrode to the detector. XAS data were processed using the IFEFFIT package, including ATHENE and ARTEMIS.

5.2.5 CO electrolysis

CO reduction was conducted in a three-chamber flow-cell electrolyzer as previously described in Chapter 2. The dimension of the flow channels was $2 \text{ cm} \times 0.5 \text{ cm} \times 0.15 \text{ cm}$. The CO gas flow rate was controlled using a mass flow controller (MKS GE50) and set to 15 sccm. Aqueous KOH solution (99.99%; Sigma-Aldrich) was used as both the catholyte and the anolyte. Peristaltic pumps were used to control the flow rate of the electrolytes at 0.5 to 2 mL min^{-1} . An AEM (FAA-3; Fumatech) was used to separate the cathode and anode chambers. The gas outlet backpressure of the flow cell was modulated to atmospheric pressure with a backpressure controller (Cole-Parmer).

Electrolysis experiments were conducted using chronopotentiometry with a potentiostat (Autolab PGSTAT204). The cathode potentials were measured against an external Ag/AgCl reference electrode (Pine Research), and the solution resistance between the reference electrode and the cathode was measured using a current-interrupt

technique before each electrolysis experiment. The measured potential was converted to the RHE scale using E (vs. RHE) = E (vs. Ag/AgCl) + 0.210 V + 0.0591 × pH and was iR-corrected. For each current density, products were quantified over a period of 200 s and at least three replicates were conducted to get an average and standard deviation.

During electrolysis, gas products were quantified using an in-line Multiple Gas Analyzer gas chromatography system (SRI Instruments) equipped with a HayeSep D and Molsieve 5 A columns connected to a thermal conductivity detector and a flame ionization detector. Argon (99.999%) was used as the carrier gas. Liquid products were analyzed using a Bruker AVIII 600 MHz nuclear magnetic resonance (NMR) spectrometer. In short, 500 μ L of sampled catholyte was mixed with 100 μ L D₂O containing 20 ppm (v/v) dimethyl sulphoxide ($\geq 99.9\%$; Alfa Aesar) as the internal standard. The one-dimensional ¹H spectrum as measured with water suppression using a pre-saturation method.

5.2.6 Labelled C¹⁸O experiment

Labelling studies were conducted with a C¹⁸O lecture bottle (95 at% ¹⁸O; Sigma Aldrich). In short, C¹⁸O gas was extracted using a 30 mL syringe and a syringe pump was used to control the feed rate into the flow-cell electrolyzer. The feed rate was set to 5 mL min⁻¹. Constant current electrolysis was conducted at 300 mA cm⁻² for 5 min and the liquid product was collected for analysis. The liquid products were slightly acidified to a pH value of ~ 2 using hydrochloric acid to allow detection of acetate as acetic acid. Mass spectrum analysis was conducted with an integrated GC-MS (Agilent 59771A) system equipped with a DB-FFAP column and a mass spectrometry system (Agilent 59771A). Mass fragmentation patterns, focused on the parent ion of the molecules, were compared with those of the National Institute of Standards and Technology library.

5.2.7 Computational Methods

DFT calculations were performed using the Vienna Ab-initio Simulation Package (VASP)[18, 19] with PAW pseudopotential[20] and the Perdew-Burke-Ernzerhof (PBE) exchange-correlation functional.[21] The Cu(111) surface was modeled by a 4×4 slab with 4 layers, and (100) surface was modeled by a 4×4 slab with 3 layers. The slabs are separated by $\sim 15 \text{ \AA}$ from its periodic images. We used $3 \times 3 \times 1$ Monkhorst Pack[22] k-points, and a kinetic energy cut-off of 400 eV. All atomic positions were fully relaxed until the final force on each atom being less than 0.01 eV \AA^{-1} . The free energy of the solid system was calculated by adding the adsorbate vibration contribution to the electronic energy, and the free energy of a molecule is calculated by adding the vibration, translation, and rotation (if applicable) contributions (calculated using Gaussian software)[23] to the electronic energy. The pH and potential effects are included using the computational hydrogen electrode model.[24] The transition state barriers were calculated using CI-NEB method.[25]

5.3 Results

5.3.1 Synthesis of Cu nanosheets

The 2D Cu nanosheets were synthesized through a chemical reduction of copper(II) nitrate by L-ascorbic acid in the presence of CTAB and HMTA. TEM image (Figures 5.1a) reveals that the as-synthesized Cu nanosheets are triangular with an average edge length of $\sim 1.7 \pm 0.5 \mu\text{m}$. The high resolution TEM (HRTEM) image shows the projection of the basal plane exhibiting angles of $\sim 60^\circ$ between fringes (Figure 5.1b). The hexagonal pattern seen in HRTEM as well as in the selective area electron diffraction (SAED) can be attributed to either $1/3\{422\}$ of the face centered cubic (*fcc*) structure along the $[111]$ direction (Figure 1c, inset) or (100) of the hexagonal close packed (*hcp*) structure along the $[001]$ direction.[26] However, further analysis with XRD (Figure 5.1c and Figure D.1) confirmed that the structure of the Cu nanosheets is *fcc* and not *hcp*. Note that, the $1/3\{422\}$ reflections of a *fcc* structure should be forbidden; however, exceptions may exist for non- $3n$ layers with thicknesses within a

few nanometers.[26] The substantially enhanced (111) peak shown in the XRD pattern (Figure 5.1c), which was obtained from assembling the nanosheets on a Si wafer, indicates that the preferentially oriented $\{111\}$ planes were parallel to the Si substrate. The fringe distances of 0.15 nm and 0.13 nm as shown in Figure 5.1b closely match the $\text{Cu}\{112\}$ and $\text{Cu}\{220\}$ lattice distances, respectively. This suggests that the projection seen in the HRTEM image (Figure 5.1b) is indeed $\{111\}$ in the $\langle 111 \rangle$ direction. In the region where two nanosheets overlapped, a Moire pattern can be seen directly in the HRTEM image (Figure 5.1d) as well as in the corresponding fast Fourier transform (FFT) pattern (Figure 5.1e). The observed secondary pattern in the FFT pattern further confirms the presence of $\{111\}$ basal planes. The AFM line scan (Figure 5.1f) reveals that the thickness of the Cu nanosheets is ~ 5 nm. With these observations, it was concluded that the as-synthesized Cu nanosheets are ultra-thin and enclosed by two $\{111\}$ basal planes. In addition, Cu nanocubes that selectively expose $\{100\}$ facets as the $\text{Cu}(100)$ model surface were also synthesized by a modified method as previously reported.[17] TEM image (Figure 5.1g) shows an edge length of 41.4 ± 3.6 nm, and the HRTEM image (Figure 5.1h) confirms the presence of $\{100\}$ planes by the cubic arrangement of Cu atoms. The fringe distance of 0.18 nm matches the lattice spacing of $\text{Cu}\{200\}$. The XRD pattern (Figure 5.1i) of the preferentially oriented Cu nanocubes shows an enhanced (200) peak, further indicating the dominant $\{100\}$ planes.

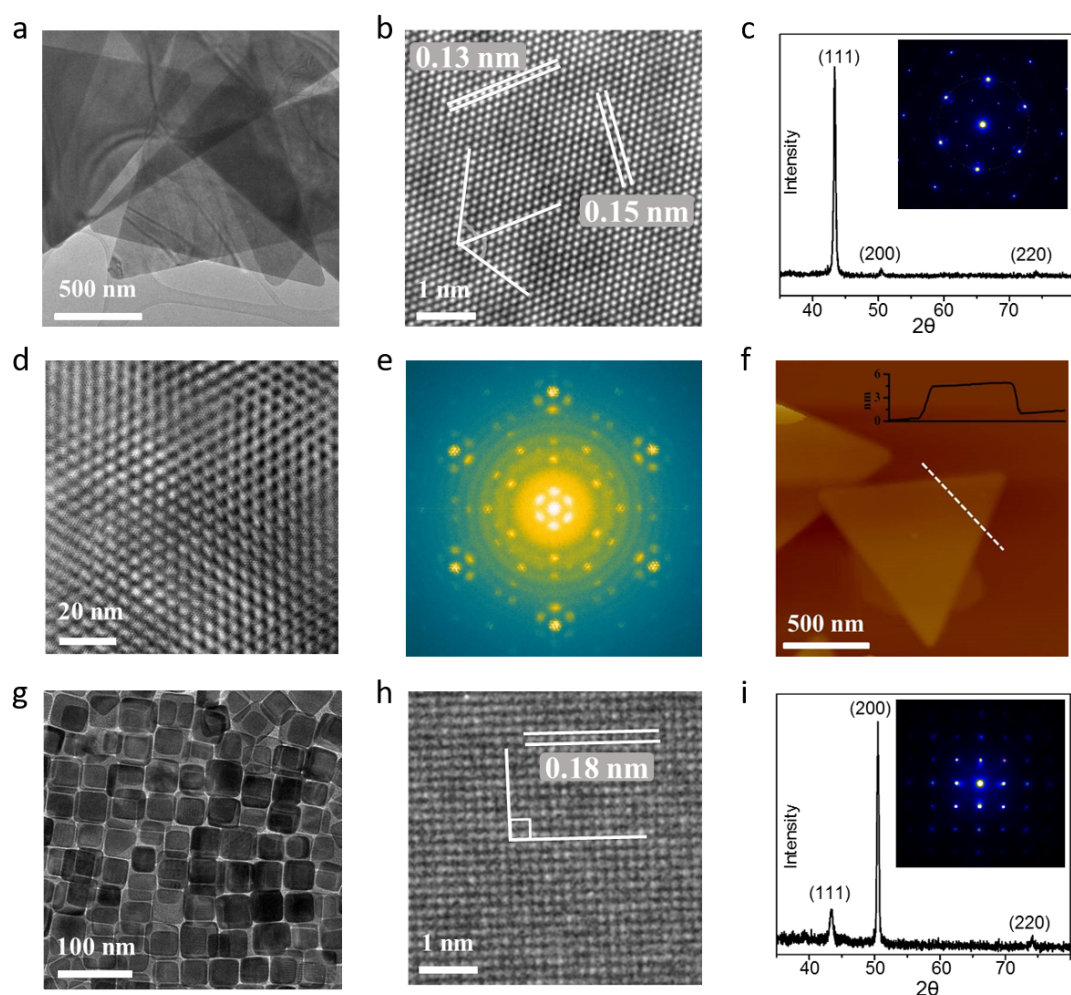


Figure 5.1: Characterization of Cu nanosheets and Cu nanocubes. a) TEM image of triangular Cu nanosheets; b) HRTEM image showing the basal plane projection of a Cu nanosheet; c) XRD pattern of Cu nanosheets assembled on a Si wafer, preferentially showing the (111) peak, inset of c) SAED pattern of Cu nanosheets; d) HRTEM image and e) corresponding FFT pattern showing a Moiré pattern from two overlapped Cu nanosheets; f) AFM image showing the thickness of a single Cu nanosheet; g) TEM image and h) HRTEM image of Cu nanocubes; and i) XRD pattern of Cu nanocubes assembled on a Si wafer, preferentially showing (200) peak, inset of i) SAED pattern of Cu nanocubes. Scale bars: a, f) 500 nm, b, h) 1 nm, d) 20 nm, and g) 100 nm.

The combination of appropriate reducing agent, ligand, and surfactant was the key for the successful synthesis of $\{111\}$ -enclosed Cu nanosheets (Figure D.2). As a long-life reducing agent, L-ascorbic acid not only reduces Cu (II) to Cu (0) via Cu (I), but also protects the final product from oxidation. The as-synthesized Cu nanosheets exhibited a red color (Figures D.3a, D.4, and D.5) which suggests the presence of Cu (0), and the observed liquid-crystal-like texture was the result of stacking of nanosheets. Such appearance remained unchanged for at least four months under ambient conditions (Figure D.4). However, Cu nanoparticles were completely oxidized within one hour (Figures D.3c and D.3d), as indicated by a red-to-blue color change. Diffuse reflectance infrared Fourier transform spectroscopic (DRIFT) measurement (Figure D.6) shows the presence of ascorbic acid in the Cu nanosheets sample. It is likely that surface absorbed ascorbic acid is responsible for the improved chemical stability. Although ascorbic acid was used as the surfactant, an acidic environment is not preferred during synthesis as the Cu nanocrystal growth cannot be controlled. The cuprous ions easily disproportionate in an acidic solution, resulting in an uncontrolled rate of reduction. To provide an alkaline environment, CTAB and HMTA were both used to stabilize the cuprous ion in the aqueous solution. By doing so, the coordination number of the cuprous ion was three and the coordination geometry was trigonal planar, which directed the anisotropic growth of the Cu nanosheets.

With an edge length of $\sim 1.7\mu\text{m}$ and a thickness of $\sim 5\text{nm}$, theoretically, at least 99% of the exposed surface (i.e. basal planes) should be (111). As shown in SEM and TEM images (Figures D.7a and D.7b), the majority of the nanosheet (shaded area) has a single-crystal morphology with $\{111\}$ basal plane while the edges are polycrystalline and oxidized. This was confirmed with XPS, as the as-synthesized Cu nanosheets show partial oxidization to Cu(II) (Figure D.7d). The single-crystal region remained intact even after CO reduction; however, the oxidized region corroded away (Figure D.7c). This was also confirmed by post-reaction XPS as majority of the Cu is in its reduced state. Slight oxidation was observed likely due to sample handling after CO reduction experiments. These observations indicate that the most striking feature

of the Cu nanosheets have extraordinarily stable (111) surface, and such a stable zero-valence Cu(111) surface is crucial for catalysis studies. As surface reconstruction is well known[27, 28] (e.g. the oxidation/reduction cycles may change the atomic arrangement of metal surfaces), it is difficult to obtain Cu(111) directly from reducing CuO(111) or Cu₂O(111).

5.3.2 CO reduction performance

The CO reduction properties of Cu nanosheets were evaluated using a three-compartment flow-cell electrolyzer. As described in previous works,[3, 8, 29–31] the use of a flow-cell electrolyzer enables high-rate of CO conversion ($>100\text{ mA cm}^{-2}$) which cannot be typically achieved with conventional batch reactors due to the low solubility limitation of CO in aqueous electrolytes. The CO reduction performances in 0.5-2 M KOH electrolyte are summarized in Figure 5.2a and Figures D.8 and D.9. The current densities increased near-exponentially with increasing applied potentials, indicating that the mass transport limitation of CO was minimal. In 2 M KOH, a maximum C₂₊ products Faradaic efficiency of $\sim 70\%$ was achieved with the major C₂₊ products being ethylene (C₂H₄) and acetate with minor amounts of ethanol (EtOH) and n-propanol n-PrOH). At more negative potentials, small amount of CH₄ was produced. Interestingly, a maximum acetate Faradaic efficiency of $\sim 48\%$ (Figure 5.2a) and an acetate partial current density up to 131 mA cm^{-2} were achieved in 2 M KOH (Figure 5.2c), among the highest reported to date toward acetate formation. The stability of Cu nanosheets was also examined under a constant current of 100 mA cm^{-2} for 3 h in 2 M KOH (Figure 5.2b). The results show a stable acetate Faradaic efficiency over the span of the stability test, except for the first 30 min, which could be caused by initial activation of catalyst layer. The oscillation of the potential is due to bubble accumulation and sudden flush out in the cathode chamber during electrolysis. *Operando* XAS was also used to investigate the structural change of the Cu nanosheets under CO reduction conditions in a flow-cell electrolyzer (Figure D.10). Both the X-ray absorption

near-edge spectroscopy (XANES) and extended X-ray absorption fine structure (EXAFS) spectrums (Figure D.11) show that the catalyst was in its metallic Cu^0 state and appear similar throughout the reaction, further confirming the structural stability of the catalyst.

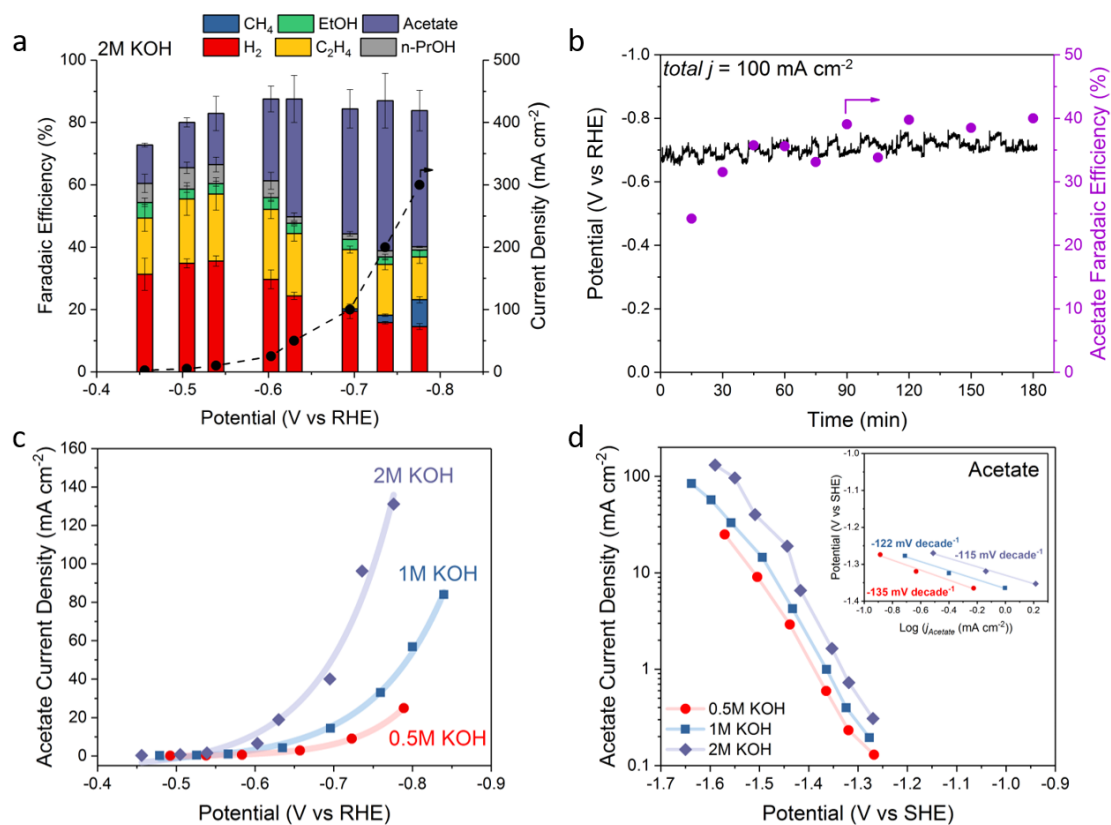


Figure 5.2: CO reduction performance of Cu nanosheets. a) Total current density and Faradaic efficiencies versus applied potential for CO reduction on Cu nanosheets in 2M KOH. b) Stability test over a span of 3 h electrolysis in 2M KOH. c) The acetate production performance on Cu nanosheets in various KOH concentrations. d) Acetate partial current density and inset) Tafel analysis on the SHE scale. Error bars represent the standard deviation from at least three independent measurements and Tafel lines were determined with linear fit.

To examine the influence of pH on acetate formation in CO reduction, the acetate partial current densities in different electrolytes (0.5-2 M) were plotted against the absolute potential scale (SHE), and Tafel slopes were derived from the three lowest partial current densities (Figure 5.2d). The other reduction products are shown in Figure D.12. Low current densities were chosen to obtain Tafel slopes as accurately as possible, since at higher current densities, significant amount of gas products was produced which can cause voltage fluctuation. It must be noted that Tafel analyses have limitations and are typically done at low overpotentials and low currents to avoid mass transport limitation caused by not only the transport of reactant to the catalytic surface, but also by the adsorption of cations.[32] From Figure 5.2d, it is clear that acetate production has a strong pH dependence. As the hydroxide ion concentration increased, a positive shift in onset potential for acetate and a change to lower Tafel slopes (Figure 5.2d, inset) were observed, indicating that acetate formation is favored in highly alkaline environments. C¹⁸O labeling studies (Figure D.13) on Cu nanosheets show that the produced acetate in the form of acetic acid is partially-labeled where one oxygen of the acetate is originated from the CO feed and the other oxygen is originated from the electrolyte as consistent with previous studies,[3, 33] further supporting that acetate formation is strongly dependent on the alkalinity of the electrolyte. Ethanol, n-propanol, and acetaldehyde were also detected (Figures D.13, b-d), and the labeling results were similar to our previous work.[3] Kanan and co-workers have also observed an enhancement in acetate formation, accompanied with a decrease in ethanol, at high pH on OD-Cu and have attributed to the attack of a OH⁻ ion to a surface-bound ketene or other carbonyl-containing intermediate.[7] The formation of H₂ and ethylene are insensitive to the changes in pH (Figure D.12), as consistent with other reports;[13, 34-36] while ethanol has a small pH dependence at low overpotentials.

To further understand the high acetate selectivity of Cu nanosheets, CO reduction was performed on commercial 1 μm and 25 nm Cu particles (Figure D.14) with a similar catalyst loading of 0.5 mg cm^{-2} , and the catalytic performances were compared. OH_{ads} studies were first performed to probe the surface structure of the commercial Cu particles and Cu nanosheets (Figure 5.3a).^[37, 38] Qualitatively, the Cu nanosheets have a pronounced (111) OH_{ads} feature, suggesting a high surface density of (111) (Figure 5.3a). As for the commercial particles, the (100), (110), and (111) OH_{ads} peaks are similar in relative intensities, reflecting the polycrystalline surface nature of the commercial particles. *In-situ* OH_{ads} studies on the Cu nanosheets were also conducted in the flow-cell electrolyzer prior to and immediate after CO electrolysis by switching the gas feed to avoid potential oxidation during sample handling. The pre- and post-reaction voltammograms (Figure D.15) show similar features, indicating that the high surface density of (111) was preserved and that the catalytic performance of the Cu nanosheets is not attributed to surface reconstruction. In comparison to the commercial Cu particles, the Cu nanosheets have a higher acetate molar production fraction (excluding H_2) in the similar potential region, indicating that the Cu nanosheets are more selective toward converting CO to acetate (Figure 5.3b). To further compare the reaction rates, the performances (Figures D.16 and D.17) were normalized to the ECSA (see Figure D.18 for measurements). Surprisingly, the trend in specific acetate current density of the Cu nanosheets is similar to commercial Cu particles (Figure 5.3c), suggesting that all Cu catalysts have similar intrinsic activity toward acetate formation. However, the intrinsic activities toward ethylene and ethanol formation are much lower on the Cu nanosheets than commercial Cu particles (Figure 5.3d and 5.3e). To rule out the effects of ascorbic acid, which was critical for the successful synthesis of the Cu nanosheets, commercial 25 nm Cu particles were treated with ascorbic acid and tested for CO reduction. The performance of the treated Cu particles (Figure D.19) is similar to the untreated Cu particles, demonstrating that ascorbic acid has a minimal effect on catalytic performance. With these observations, we therefore attribute the overall enhancement of acetate formation on Cu nanosheet to the suppression of ethylene and

ethanol formation. Previous single-crystal studies on CO reduction have shown that the (111) surface is unfavorable for the formation of ethylene and ethanol; while, (100) and (110) surfaces are more favorable.[39, 40] The Cu nanosheets selectively expose {111} surfaces, theoretically 99% of the as-synthesized surface is (111), which reduce the overall surface density of (100) and (110). This consequentially suppresses ethylene and ethanol formation while enhancing the overall selectivity toward acetate. However, to the best of our knowledge, the mechanistic understanding of acetate on Cu surfaces has yet been fully elucidated and further work is needed. In addition, Cu nanocubes with exposed {100} surfaces exhibits similar CO reduction performance (Figure D.20) as the 25 nm commercial Cu particles.

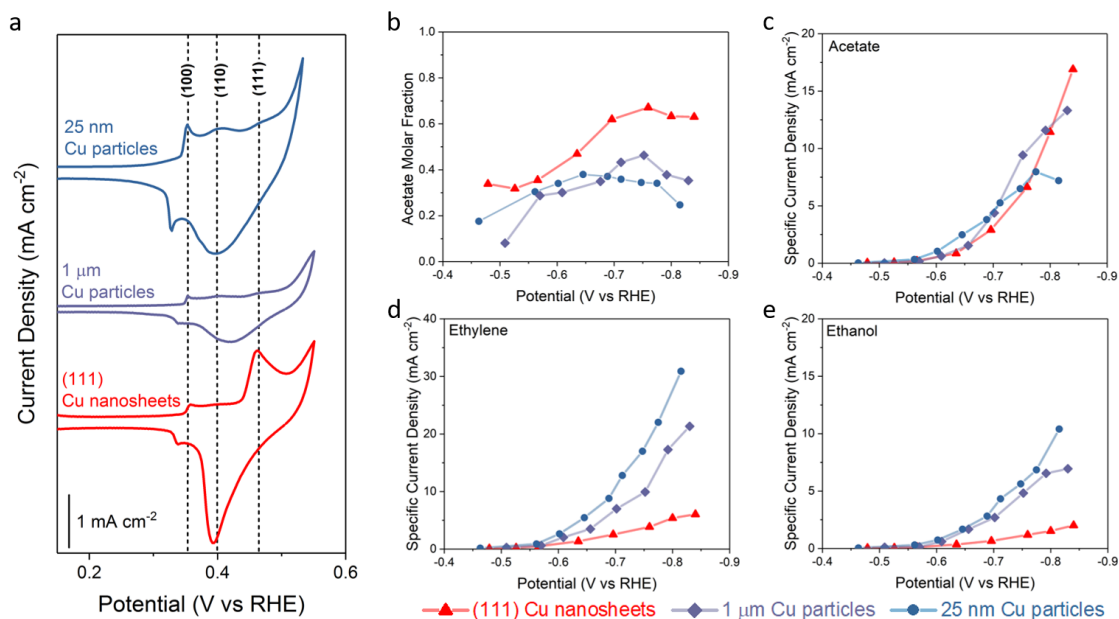


Figure 5.3: Comparison of Cu nanosheets with commercial Cu particles in 1 M KOH. a) Voltammograms of OH_{ads} peaks collected in Ar-purged 1 M KOH batch cell. b) Acetate molar production fraction excluding hydrogen. c-e) ECSA corrected acetate, ethylene, and ethanol partial current densities of various Cu catalysts, respectively.

5.3.3 DFT Calculations

To understand the acetate formation pathway on Cu surfaces, DFT calculations were performed and the calculation details can be found in Methods. Based on the isotopic labelling studies, water incorporation must be involved during acetate formation to introduce ^{16}O . As $^*\text{CO}-\text{COH}$ (* denotes a binding site) is known to be a common intermediate proposed in literature for the formation of C_{2+} products,[41–44] we focused our calculations from this initial intermediate. It must be noted that the pathway toward acetic acid, the protonated form of acetate, was determined such that the intermediate species are charge neutral. Starting from $^*\text{CO}-\text{COH}$, acetic acid may form through: $^*\text{CO}-\text{COH} + \text{H}_2\text{O} + \text{e}^- \longrightarrow ^*\text{C}-\text{CO} + \text{H}_2\text{O} + \text{OH}^-$, $^*\text{C}-\text{CO} + \text{H}_2\text{O} + \text{e}^- \longrightarrow ^*\text{CH}-\text{CO} + \text{OH}^-$, $^*\text{CH}-\text{CO} + \text{H}_2\text{O} + \text{e}^- \longrightarrow ^*\text{CH}_2-\text{CO} + \text{OH}^-$, $^*\text{CH}_2-\text{CO} + \text{H}_2\text{O} \longrightarrow \text{CH}_3-\text{COOH}$ (Figure 5.4a). Note that in alkaline conditions, no protons are available for reaction, and thus, water is likely the proton donor.[36] This pathway involves the water incorporation into ethenone (CH_2-CO), a ketene specie, to form acetic acid (CH_3-COOH), and the DFT calculations of the free energy evolutions show that this pathway is thermodynamically feasible (Figure 5.4b). In addition, the barrier for water incorporation into the ketene is only 0.61 eV (Figure D.21), suggesting it is also kinetically feasible. We also found that ethenone is weakly adsorbed on Cu surfaces with a binding energy of 0.06 eV for (111) and 0.21 eV for (100); therefore, the water incorporation into the ketene specie to form acetic acid is less affected by the difference in Cu surfaces, explaining its weak surface dependence. Lastly, acetic acid may also form without involving a ketene as the intermediate, through: $^*\text{CH}-\text{CO} + \text{H}_2\text{O} \longrightarrow ^*\text{CH}_2-\text{COOH}$, $^*\text{CH}_2-\text{COOH} + \text{H}_2\text{O} + \text{e}^- \longrightarrow \text{CH}_3-\text{COOH} + \text{OH}^-$ (Figure D.22). However, calculations show that this pathway has a higher energy barrier for water incorporation (0.76 eV, Figure D.21). Therefore, the formation pathway involving ethenone, the ketene specie, is more likely. As OH^- ions are more nucleophilic than H_2O , it is likely that OH^- ions also interact with the ketene intermediate to form acetate; however, the computation assessment of charged species is currently difficult. The alcohol pathway (Figure 5.4a) shares a common $^*\text{CH}-\text{CO}$ intermediate with the

acetic acid pathway and this could explain the competitive formation of ethanol and acetate that have been previously observed.[7] The $^*CH-CO$ intermediate was proposed by Calle-Vallejo and Koper as a possible intermediate toward C_{2+} products,[44] and our calculations show that the pathway toward ethanol through $^*CH-CO$ is thermodynamically feasible (Figure D.23). To further elucidate the influence of pH, future work should also focus on calculating the kinetic barriers of each step as a function of pH, as the pH could affect the overall pathways toward various C_{2+} products.

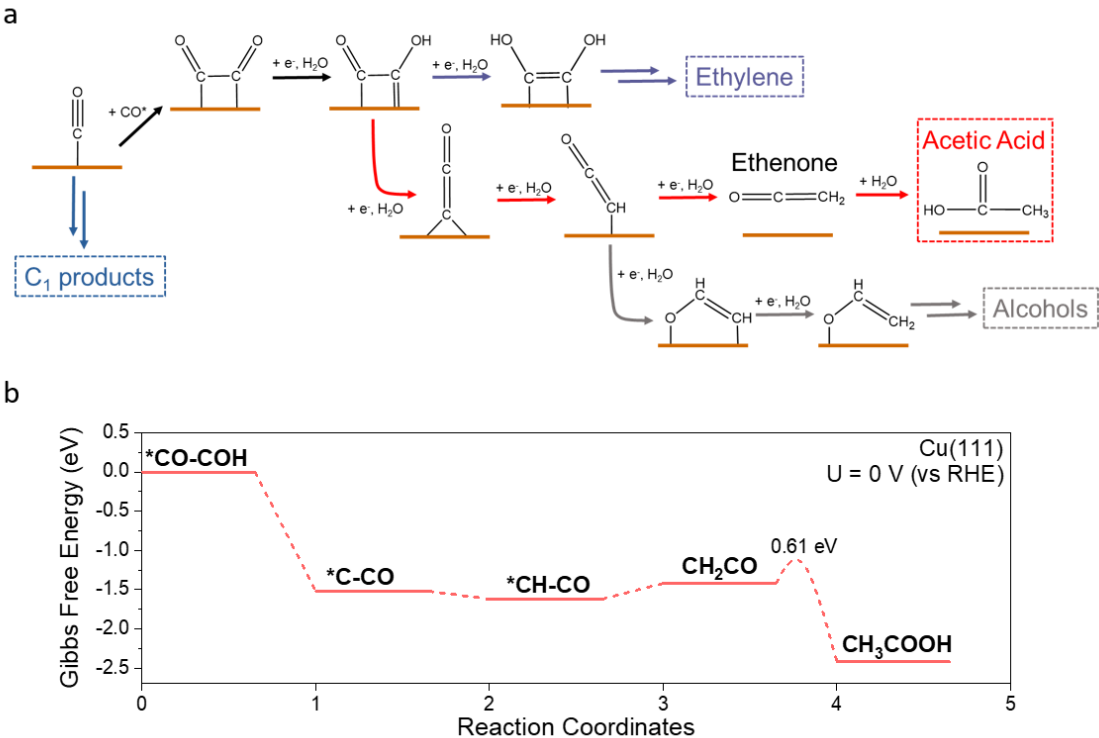


Figure 5.4: DFT calculations. a) Proposed mechanism for the reduction of CO to C_{2+} products. b) Energy evolution for acetic acid formation on Cu(111) at 0 V (vs. RHE).

5.4 Conclusions

In summary, facile synthesis procedures of freestanding Cu nanosheets and Cu nanocubes, that selectively expose the (111) and (100) surfaces, respectively, were introduced. By using a flow-cell electrolyzer, high rates of CO electrolysis were demonstrated which cannot be achieved in batch electrochemical cells. In a 2 M KOH electrolyte, the Cu nanosheets exhibited an acetate Faradaic efficiency as high as 48% with an acetate partial current density up to 131 mA cm^{-2} in electrochemical CO reduction. Further analysis suggested that the high acetate selectivity is attributed to the suppression of ethylene and ethanol formation, likely due to the reduction of exposed (100) and (110) surfaces. Although previous single-crystal studies have reported the formation of ethylene and ethanol on well-defined bulk Cu surfaces, the formation of acetate has yet been reported. It is likely because majority of previous studies were conducted in batch electrochemical cells, where CO mass transport limitations prevented the study of bulk surfaces at high overpotentials and current densities. By developing well-defined nanostructured Cu catalysts, we can integrate these materials in a flow-cell electrolyzer, thus allowing for the deeper understanding of C_{2+} product formation over Cu surfaces at commercially-relevant rates of electrolysis and ultimately bridging the gap between fundamental and device-level studies.

5.5 Acknowledgment

The work was supported by the DOE (USA) under Award Number DE-FE0029868 and National Natural Science Foundation of China, under Award 51601030, 21773023. We also thank the National Science Foundation Faculty Early Career Development program (Award No. CBET-1350911). We acknowledge the support from International Institute for Nanotechnology (IIN) and Institute for Sustainability and Energy at Northwestern University. The theoretical calculation was the supported by Welch Foundation (Grant No. F-1959-20180324) and the startup grant from UT Austin, and used computational resources sponsored by the DOE's Office of Energy Efficiency and Renewable Energy and located at the National Renewable Energy Laboratory, and the

Texas Advanced Computing Center at UT Austin. This work made use of the Electron Probe Instrumentation Center (EPIC) facility of Northwestern University's Atomic and Nanoscale Characterization Experimental Center, which has received support from the Soft and Hybrid Nanotechnology Experimental (SHyNE) Resource (NSF ECCS-1542205); the Materials Research Science and Engineering Centers (MRSEC) program (NSF DMR-1121262) at the Materials Research Center; the IIN. This work made use of the J.B. Cohen X-Ray Diffraction Facility supported by MRSEC and SHyNE. We acknowledge Dr. Dong Su (Brookhaven National Laboratory), Prof. Xingchen Ye (Indiana University), and Prof. Amanda Petford-Long (Northwestern University) for help in discussion. This research used resources at the 8-ID Beamline of the National Synchrotron Light Source II, a DOE (USA) Office of Science User Facility operated for the DOE Office of Science by Brookhaven National Laboratory under Contract No. DE-SC0012704. The authors acknowledge Dr. Eli Stavitski (8-ID Beamline, NSLS-II, Brookhaven National Laboratory) for assistance in XAS measurements. I would like to personally thank Matthew Jouny, who developed the flow-cell electrolyzer. Without his initiate efforts, this study would not be possible.

REFERENCES

- (1) Zhuang, T.-T. et al. *Nature Catalysis* **2018**, *1*, 421–428.
- (2) Ripatti, D. S.; Veltman, T. R.; Kanan, M. W. *Joule* **2018**, *3*, 240–256.
- (3) Jouny, M.; Luc, W.; Jiao, F. *Nature Catalysis* **2018**, *1*, 748–755.
- (4) Jiang, K.; Sandberg, R. B.; Akey, A. J.; Liu, X.; Bell, D. C.; Nørskov, J. K.; Chan, K.; Wang, H. *Nature Catalysis* **2018**, *1*, 111–119.
- (5) Dinh, C.-T.; Burdyny, T.; Kibria, M. G.; Seifitokaldani, A.; Gabardo, C. M.; García de Arquer, F. P.; Kiani, A.; Edwards, J. P.; De Luna, P.; Bushuyev, O. S.; Zou, C.; Quintero-Bermudez, R.; Pang, Y.; Sinton, D.; Sargent, E. H. *Science* **2018**, *360*, 783.
- (6) De Luna, P.; Quintero-Bermudez, R.; Dinh, C.-T.; Ross, M. B.; Bushuyev, O. S.; Todorović, P.; Regier, T.; Kelley, S. O.; Yang, P.; Sargent, E. H. *Nature Catalysis* **2018**, *1*, 103–110.
- (7) Li, C. W.; Ciston, J.; Kanan, M. W. *Nature* **2014**, *508*, 504.
- (8) Lv, J.-J.; Jouny, M.; Luc, W.; Zhu, W.; Zhu, J.-J.; Jiao, F. *Advanced Materials* **2018**, *0*, 1803111.
- (9) Raciti, D.; Livi, K. J.; Wang, C. *Nano Letters* **2015**, *15*, 6829–6835.
- (10) Hori, Y.; Wakebe, H.; Tsukamoto, T.; Koga, O. *Electrochimica Acta* **1994**, *39*, 1833–1839.
- (11) Kuhl, K. P.; Cave, E. R.; Abram, D. N.; Jaramillo, T. F. *Energy & Environmental Science* **2012**, *5*, 7050–7059.
- (12) Kuhl, K. P.; Hatsukade, T.; Cave, E. R.; Abram, D. N.; Kibsgaard, J.; Jaramillo, T. F. *Journal of the American Chemical Society* **2014**, *136*, 14107–14113.
- (13) Hori, Y.; Takahashi, R.; Yoshinami, Y.; Murata, A. *Journal of Physical Chemistry B* **1997**, *101*, 7075–7081.
- (14) Yang, H.-J.; He, S.-Y.; Chen, H.-L.; Tuan, H.-Y. *Chemistry of Materials* **2014**, *26*, 1785–1793.
- (15) Jin, M.; He, G.; Zhang, H.; Zeng, J.; Xie, Z.; Xia, Y. *Angewandte Chemie International Edition* **2011**, *50*, 10560–10564.
- (16) Huang, J. F.; Hormann, N.; Oveisi, E.; Loiudice, A.; De Gregorio, G. L.; Andreussi, O.; Marzari, N.; Buonsanti, R. *Nature Communications* **2018**, *9*, 3117.

- (17) Guo, H. Z.; Chen, Y. Z.; Cortie, M. B.; Liu, X.; Xie, Q. S.; Wang, X.; Peng, D. L. *Journal of Physical Chemistry C* **2014**, *118*, 9801–9808.
- (18) Kresse, G.; Furthmüller, J. *Physical Review B* **1996**, *54*, 11169–11186.
- (19) Kresse, G.; Hafner, J. *Physical Review B* **1993**, *47*, 558–561.
- (20) Kresse, G.; Joubert, D. *Physical Review B* **1999**, *59*, 1758–1775.
- (21) Perdew, J. P.; Burke, K.; Ernzerhof, M. *Physical Review Letters* **1996**, *77*, 3865–3868.
- (22) Monkhorst, H. J.; Pack, J. D. *Physical Review B* **1976**, *13*, 5188–5192.
- (23) Scott, A. P.; Radom, L. *J. Phys. Chem.* **1996**, *100*, 16502–16513.
- (24) Peterson, A. A.; Abild-Pedersen, F.; Studt, F.; Rossmeisl, J.; Nørskov, J. K. *Energy & Environmental Science* **2010**, *3*, 1311–1315.
- (25) Henkelman, G.; Uberuaga, B. P.; Jonsson, H. *Journal of Chemical Physics* **2000**, *113*, 9901–9904.
- (26) Salzemann, C.; Urban, J.; Lisiecki, I.; Pileni, M. P. *Advanced Functional Materials* **2005**, *15*, 1277–1284.
- (27) Tao, F.; Grass, M. E.; Zhang, Y.; Butcher, D. R.; Renzas, J. R.; Liu, Z.; Chung, J. Y.; Mun, B. S.; Salmeron, M.; Somorjai, G. A. *Science* **2008**, *322*, 932–934.
- (28) Tao, F.; Dag, S.; Wang, L.-W.; Liu, Z.; Butcher, D. R.; Bluhm, H.; Salmeron, M.; Somorjai, G. A. *Science* **2010**, *327*, 850.
- (29) Verma, S.; Hamasaki, Y.; Kim, C.; Huang, W.; Lu, S.; Jhong, H.-R. M.; Gewirth, A. A.; Fujigaya, T.; Nakashima, N.; Kenis, P. J. A. *ACS Energy Letters* **2018**, *3*, 193–198.
- (30) Zhuang, T.-T. et al. *Nature Catalysis* **2018**, *1*, 946–951.
- (31) Weekes, D. M.; Salvatore, D. A.; Reyes, A.; Huang, A. X.; Berlinguette, C. P. *Accounts of Chemical Research* **2018**, *51*, 910–918.
- (32) Dunwell, M.; Luc, W.; Yan, Y. S.; Jiao, F.; Xu, B. J. *ACS Catalysis* **2018**, *8*, 8121–8129.
- (33) Lum, Y. W.; Cheng, T.; Goddard, W. A.; Ager, J. W. *Journal of the American Chemical Society* **2018**, *140*, 9337–9340.
- (34) Liu, X. Y.; Schlexer, P.; Xiao, J. P.; Ji, Y. F.; Wang, L.; Sandberg, R. B.; Tang, M.; Brown, K. S.; Peng, H. J.; Ringe, S.; Hahn, C.; Jaramillo, T. F.; Nørskov, J. K.; Chan, K. R. *Nature Communications* **2019**, *10*, 32.
- (35) Wang, L.; Nitopi, S. A.; Bertheussen, E.; Orazov, M.; Morales-Guio, C. G.; Liu, X. Y.; Higgins, D. C.; Chan, K. R.; Nørskov, J. K.; Hahn, C.; Jaramillo, T. F. *ACS Catalysis* **2018**, *8*, 7445–7454.

- (36) Strmcnik, D.; Uchimura, M.; Wang, C.; Subbaraman, R.; Danilovic, N.; van der Vliet, D.; Paulikas, A. P.; Stamenkovic, V. R.; Markovic, N. M. *Nature Chemistry* **2013**, *5*, 300–306.
- (37) Droog, J. M. M.; Schlenter, B. *Journal of Electroanalytical Chemistry* **1980**, *112*, 387–390.
- (38) Raciti, D.; Cao, L.; Liv, K. J. T.; Rottmann, P. F.; Tang, X.; Li, C. Y.; Hicks, Z.; Bowen, K. H.; Hemker, K. J.; Mueller, T.; Wang, C. *ACS Catalysis* **2017**, *7*, 4467–4472.
- (39) Schouten, K. J. P.; Gallent, E. P.; Koper, M. T. M. *ACS Catalysis* **2013**, *3*, 1292–1295.
- (40) Hahn, C.; Hatsukade, T.; Kim, Y. G.; Vailionis, A.; Baricuatro, J. H.; Higgins, D. C.; Nitopi, S. A.; Soriaga, M. P.; Jaramillo, T. F. *Proceedings of the National Academy of Sciences of the United States of America* **2017**, *114*, 5918–5923.
- (41) Cheng, T.; Xiao, H.; Goddard, W. A. *Proceedings of the National Academy of Sciences of the United States of America* **2017**, *114*, 1795–1800.
- (42) Cheng, T.; Xiao, H.; Goddard, W. A. *Journal of the American Chemical Society* **2017**, *139*, 11642–11645.
- (43) Xiao, H.; Cheng, T.; Goddard, W. A.; Sundararaman, R. *Journal of the American Chemical Society* **2016**, *138*, 483–486.
- (44) Calle-Vallejo, F.; Koper, M. T. M. *Angewandte Chemie-International Edition* **2013**, *52*, 7282–7285.

Chapter 6

SULFUR DIOXIDE-INDUCED SELECTIVITY CHANGE IN CARBON DIOXIDE ELECTROLYSIS

Up until now, majority of the studies presented in this thesis utilized either highly pure electrolytes or gaseous reactants for evaluating catalytic or device performances. For example, pre-electrolysis was performed in the study of Cu-based bimetals for the HER in Chapter 3, while metal-chelating resin was used to purify the electrolyte for the CO₂ electrolyzer development in Chapter 4. Research grade gases (99.999%) were also used for these studies. While highly pure reactants are appropriate for fundamental studies, most feedstocks in commercial applications may not be as pure. As mentioned in the introduction, understanding the effects of potential impurities on catalytic and device performances is important toward identifying potential degradation mechanism in efforts to develop mitigation strategies. In this work titled, “Sulfur Dioxide-Induced Selectivity Change in Carbon Dioxide Electrolysis,” that is currently submitted for publication under the ACS publishing group, we sought to understand how gaseous impurities (mainly SO₂) can effect CO₂ electrolysis. This work is a collaboration between University of Delaware, Columbia University, and Brookhaven National Laboratory. As co-first authors, Byung Hee Ko and I led the catalytic evaluation and initial characterization. Shyam Kattel performed the DFT calculations and Shuang Li performed advanced characterization including HRTEM, STEM, and EELS mapping.

6.1 Introduction

It has been well studied that trace impurities in the electrolyte such as metal ions (e.g. Fe²⁺ and Zn²⁺)[1] can dramatically degrade CO₂ reduction performance

where the catalytic surface can be irreversibly altered through the deposition of these metal ions under reducing potentials, shifting selectivities toward undesirable products. Strategies such as pre-electrolysis using sacrificial electrodes,[2] pretreatment of the electrolyte with metal-chelating resin,[3] and designing catalysts where the catalytic surface can reconstruct under operating conditions[4] have been proposed to overcome these challenges. Overall, the electrolyte most likely needs to be relatively pure and free of residual metal ions for commercial electrochemical conversion of CO₂. On the contrary, the effect of gaseous impurities in the CO₂ feed have barely been studied,[5] and further work is necessary to elucidate the impact of such impurities on CO₂ electrolysis.

The CO₂ feedstock for commercial CO₂ electrolysis can be obtained from direct air capture[6, 7] or point sources such as power plants or chemical facilities.[8, 9] The former is currently an area of intensive research due to the advantage of not being geographically limited; however, such technology is currently expensive and still under development. The latter accounts for a large fraction of anthropogenic CO₂ emissions with the current state-of-the-art CO₂ capture technology being amine-based absorption technologies. However, the exhaust streams from point sources such as power plants contain impurities such as SO_x, NO_x, or volatile organic compounds.[10] Although current carbon capture processes can purify these exhaust streams using energy intensive processes involving series of scrubbing and separating units, it is critical to understand how these impurities affect CO₂ electrolysis to establish engineering criteria. To the best of our knowledge, majority of CO₂ research to date use highly pure CO₂ gas as reactant and little is known on the effect of gaseous impurities.

Herein, we study the influence of sulfur dioxide (SO₂) in the electrochemical conversion of CO₂ in a flow-cell electrolyzer. Three different catalysts, Ag, Sn, and Cu as selective catalysts for producing CO, formate, and C₂₊ products, respectively, are investigated as these materials are the most commonly studied in CO₂ electrolysis (Figure 6.1).[1] The catalysts are examined for CO₂ reduction free of SO₂ impurity, during the presence of SO₂, and finally after SO₂ exposure to determine if the gaseous

impurity has an irreversible effect on the catalytic performance. The CO_2 reduction products are tracked over the course of electrolysis and *ex-situ* surface characterization is conducted at various time points during operation to elucidate the underpinning of catalytic change. The results show that the presence of SO_2 impurity in the incoming CO_2 feed reduces the efficiency of converting CO_2 due to the preferential reduction of SO_2 , as it is thermodynamically more favorable to reduce SO_2 than CO_2 . In the case of Ag and Sn catalysts, SO_2 impurity does not change the CO_2 production selectivities and full recovery of the catalytic activities can be observed after the catalysts were subjected to SO_2 . However, in the case of the Cu catalyst, SO_2 impurity has an irreversible, detrimental effect as the overall selectivity is shifted toward formate while suppressing the formation of C_{2+} products. Characterization and computational efforts indicate that the formation of copper(I) sulfide (Cu_2S) is likely responsible for the change in selectivity for Cu-catalyzed CO_2 electrolysis.

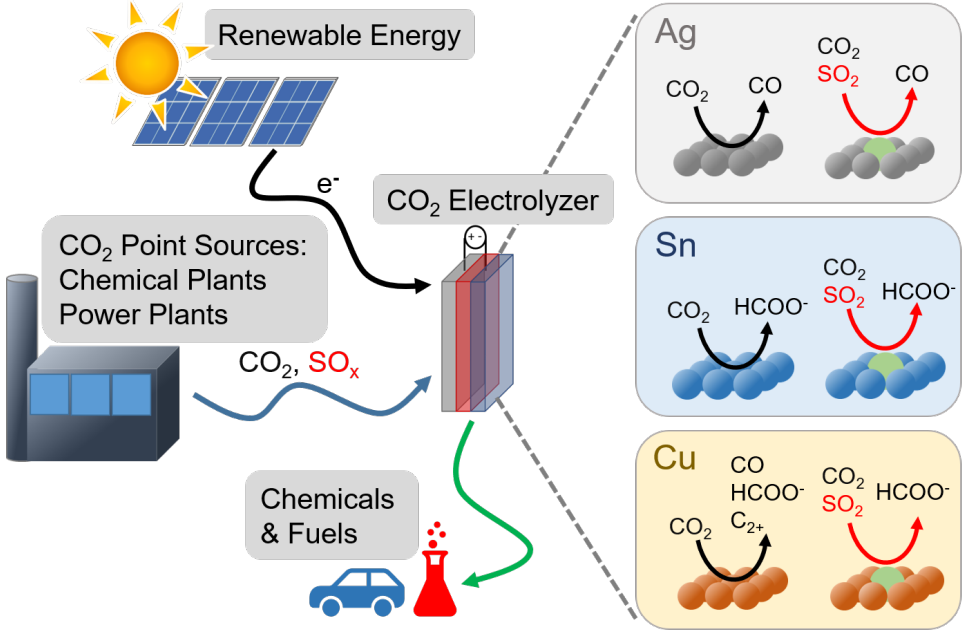


Figure 6.1: Schematic of CO₂ electrolyzer and potential feed sources.

6.2 Methods

6.2.1 Electrode preparation

Commercial Ag (<100 nm, 99.5%) and Cu (25 nm) powders were purchased from Sigma Aldrich. Commercial Sn (0.1 μm), IrO₂ (99.99%), Cu₂S (99.5%), and copper(II) sulfide (CuS) (99.8%) powders were purchased from Alfa Aesar. The catalyst inks were prepared by mixing 25 mg of metal particles, 20 μL of Nafion solution (5 wt.% in 50/50 water and isopropanol) and 3 mL of isopropanol. The catalyst inks were sonicated for at least 30 min and were dropcast onto a Sigracet 29 BC GDL (Fuel Cell Store) to achieve a catalyst loading of 0.3 mg cm⁻². Ag, Sn, and Cu electrodes were used as cathodes while IrO₂ electrodes were used as anodes.

6.2.2 CO₂ electrolysis in flow-cell electrolyzer

The electrochemical measurements were conducted in a three chamber flow-cell electrolyzer as previous described in Chapter 5. 1 M KHCO₃ (99.95%, Sigma Aldrich) was fed to the catholyte and anolyte chamber at $\sim 1 \text{ mL min}^{-1}$ with peristaltic pumps. CO₂ was fed to the flow-cell electrolyzer at 17 sccm via a Brooks GF40 mass flow controller while SO₂ was fed from a syringe via a syringe pump (Cole-Parmer) at 0.17, 0.017, and 0.0017 sccm. The cathode and anode chambers were separated by a FAA-3 membrane (Fumatech). The backpressure of the gas in the gas chamber was controlled via a backpressure controller (Cole-Parmer). To obtain SO₂ gas, a H-cell was continuously purged with SO₂ (Matheson Gas) for 30 min and then a 10 mL gas-tight syringe (#1010, Hamilton Company) was used to extract the gas.

Chronopotentiometry experiments were conducted via an Autolab PG128N. The half-cell potentials were measured using an external Ag/AgCl reference electrode (Pine Research). The resistance between the cathode and reference electrode was determined using the current-interrupt technique prior to electrolysis, and the measured applied potential was *iR*-corrected after electrolysis. The gas products were sampled directly to a Multiple Gas Analyzer gas chromatography system (SRI Instruments) equipped with a Molsieve 5A and a HayeSep D columns connected to a thermal conductivity

detector (TCD) and a flame ionization detector (FID). The electrolytes containing liquid products were collected at the exit of the electrolyzer for 200 s and were analyzed using ^1H NMR following a similar procedure as describe in Chapter 5. To prevent SO_2 from entering the GC during SO_2 injection, a base trap was positioned between the outlet of the flow-cell electrolyzer gas chamber and the inlet of the GC. Ar was fed at 15 sccm through a tee-connector to push the gas products along with unreacted CO_2 through the base trap before entering the GC for quantification. As for the catalyst recovery, a National Instrument power source (RMX-4121) was used to achieve a current density of 1 A cm^{-2} . After 30 min of electrolysis under Ar, the flow-cell electrolyzer was disassembled, the cathode was quickly dried due to severe flooding, and a new anode was replaced prior to CO_2 electrolysis.

6.2.3 Material characterization

XRD was conducted using Cu $K\alpha$ radiation source (Bruker D8 Discover diffractometer). SEM images were obtained from Auriga 60 CrossBeam. XPS was performed with a K-Alpha X-ray Photoelectron Spectrometer System (Thermo Fisher Scientific). All peaks were fitted with Thermo Advantage software with the C 1s signal calibrated to 284.8 eV.

For TEM characterization, the samples were thoroughly washed with DI water immediately after reaction to remove the residual electrolyte and then gently abraded from the GDL support to acquire particles for the TEM experiment. In order to distinguish the sulfur atoms that correspond to Cu_2S , FAA ionomer binder was used instead of Nafion binder. Bright field (BF), HRTEM images and SAED were performed with a TEM (JEM-2100F, JEOL) at an acceleration voltage of 200 kV. High angle annular dark field scanning transmission electron microscopy (HAADF-STEM) images and electron energy loss spectrum (EELS) were obtained on a Hitachi HD2700C STEM with a probe aberration corrector.

6.2.4 Computational methods

Computational methods Spin polarized periodic DFT calculations[11, 12] were performed at the GGA level within the PAW-PW91 formalism[13, 14] using the Vienna Ab-Initio Simulation Package (VASP) code.[15, 16] The total energy calculations were performed using a $3 \times 3 \times 1$ Monkhorst-Pack grid[17] and a plane wave cut-off energy of 400 eV.

Cu(111), Ag(111) and Sn(111) surfaces were modeled using a four layer 3×3 surface slabs. One surface Cu, Ag, and Sn atom was replaced with a S atom to model S-doped Cu(111), Ag(111) and Sn(111) surfaces, respectively. A vacuum layer of $\sim 15 \text{ \AA}$ thick was added in the slab cell along the direction perpendicular to the surface to minimize the artificial interactions between the surface and its periodic images. During geometry optimization, atoms in the bottom two layers were fixed and all other atoms including adsorbates were allowed to relax until the force on each ion was smaller than 0.02 eV \AA^{-1} . The binding energy (BE) of an adsorbate was calculated as:

$$BE_{adsorbate} = E_{slab+adsorbate} - E_{slab} - E_{adsorbate} \quad (6.1)$$

where $E_{slab+adsorbate}$, E_{slab} and $E_{adsorbate}$ are the total energy of slab with adsorbate, the energy of clean slab and the energy of adsorbate in the gas phase, respectively. $E(\text{H})$ is taken as one-half the total energy of the H_2 molecule during the calculation of hydrogen binding energy.

6.3 Results

6.3.1 Initial Characterization and Experimental Procedures

Commercial Ag, Sn, and Cu nanoparticles, representing a broad range of CO_2 reduction catalysts, were loaded on a GDL with a catalyst loading of 0.3 mg cm^{-2} using a dropcasting method as previously described.[18] SEM images (Figure E.1) show the well-dispersed nature of the nanoparticles on the GDL and the porosity of the catalyst layer, which is critical for maintaining the electrode-electrolyte interface

by allowing facile transport of gaseous reactants and products to and away from the catalytic surface. XRD (Figure E.2) of the as-purchased nanoparticles reveals the phase purity of the nanoparticles. In the case of Sn and Cu nanoparticles, the presence of oxidized Sn and Cu in the form of SnO and Cu₂O, respectively, is visible. The surface composition of the as-prepared electrodes was analyzed using *ex-situ* XPS (Figure E.3). In the case of Sn and Cu, the surfaces were partially-oxidized, most likely from air exposure during sample handling. CO₂ electrolysis with the presence of SO₂ impurity was performed in a flow-cell electrolyzer as described in Chapter 2.2. Although previous studies have shown that conducting CO₂ electrolysis in alkaline electrolytes (e.g. KOH) has improvement in CO₂ reduction performances,[18–20] CO₂ strongly reacts with OH⁻ to form a KHCO₃⁻/CO₃²⁻ mixture, which degrades the electrolyte and reduces the efficiency of CO₂ utilization.[21, 22] Therefore, CO₂ electrolysis experiments were conducted in near-neutral conditions in 1.0 M KHCO₃ solution. A syringe pump was used to accurately control the feed rate of SO₂ gas into the CO₂ feed before entering the flow-cell electrolyzer, and electrolysis was conducted in the constant current mode. In short, pure CO₂ was initially fed for 30 min, then SO₂ was introduced into the CO₂ feed for a duration of 30 min, and then SO₂ feed was stopped for the remainder of the electrolysis. The gaseous products were quantified by an in-line GC during operation while liquid products were collected and analyzed using NMR.

6.3.2 Influence of SO₂ on Ag and Sn–catalyzed CO₂ reduction

The influence of SO₂ on CO₂ (CO₂ + SO₂) reduction was first studied on Ag and Sn catalysts, as these materials are widely studied and commercial devices are currently being developed for the selective electrochemical conversion of CO₂ to CO and formic acid.[23, 24] As shown in Figure 6.2, when pure CO₂ was initially fed, indeed high selectivities (>85%) toward CO and formate, respectively, were achieved on Ag and Sn catalysts in near-neutral electrolyte. The fluctuation in voltage is due to the accumulation of gas products as bubbles and eventual flush out of the catholyte chamber. However, when both catalysts were subjected to a stream of 1% SO₂ (Figure 6.2,

red region), the total Faradaic efficiencies toward CO₂ reduction products decreased. The remaining charge balance is likely attributed to the reduction of SO₂ since it is thermodynamically more favorable to reduce SO₂ than CO₂ (e.g. SO₂ + 4H⁺ + 4e⁻ → S + 2H₂O $E^o = 0.50$ V, CO₂ + 2H⁺ + e⁻ → CO + H₂O $E^o = -0.11$ V). The standard reduction potential of SO₂ is more positive than CO₂, and XPS measurements confirmed the formation of metal sulfide species (Figures E.4 and E.5, Table E.1). Based on the peak positions at 161.7 and 161.6 eV, the metal sulfides were identified as Ag₂S and SnS₂ with surface concentrations of ~35.6 at.% and ~3.3 at.% on Ag and Sn catalysts, respectively.[25–28] Sulfite (SO₃²⁻) and sulfate (SO₄²⁻) were also detected. The former is likely formed during sample handling from residual surface metal oxides reacting with SO₂ in the presence of water when no potential is applied, and the latter is likely formed from the natural oxidation of metal sulfides.[29] It must be noted, that the exact surface characteristic under reaction condition remains unclear due to the lack of *in-situ* surface sensitive methods and the limitation of *ex-situ* measurements. SEM images (Figures E.6 and E.7), after 1 h of electrolysis with both catalysts subjected to a feed of 1% SO₂ for 30 min, show the formation of bulky particles with smooth surfaces, a common characteristic of metal sulfides.

Interestingly, when the feed of SO₂ was stopped, the CO₂ reduction performances recovered on both catalysts, and in the case of Sn, a slight improvement in formate Faradaic efficiency was observed. A recent study has suggested that doping Sn surfaces with sulfur (S) atoms, and then selectively removing S atoms can create highly active undercoordinated Sn sites for improved CO₂ reduction to formate.[28] Thermodynamically, Ag₂S and SnS₂ are not stable under CO₂ electrolysis conditions, and this was confirmed with post-reaction XPS that shows a decrease in metal sulfides (Table E.1). Post-reaction SEM images show particle aggregation, likely due to surface rearrangement from the reduction of metal sulfides (Figures E.6 and E.7). The SO₂ + CO₂ experiments suggest that the presence of small amounts of metal sulfides (Ag₂S and SnS₂) on Ag and Sn catalysts do not shift the CO₂ reduction product selectivities, as the dominant CO₂ reduction products remained as CO and formate, respectively.

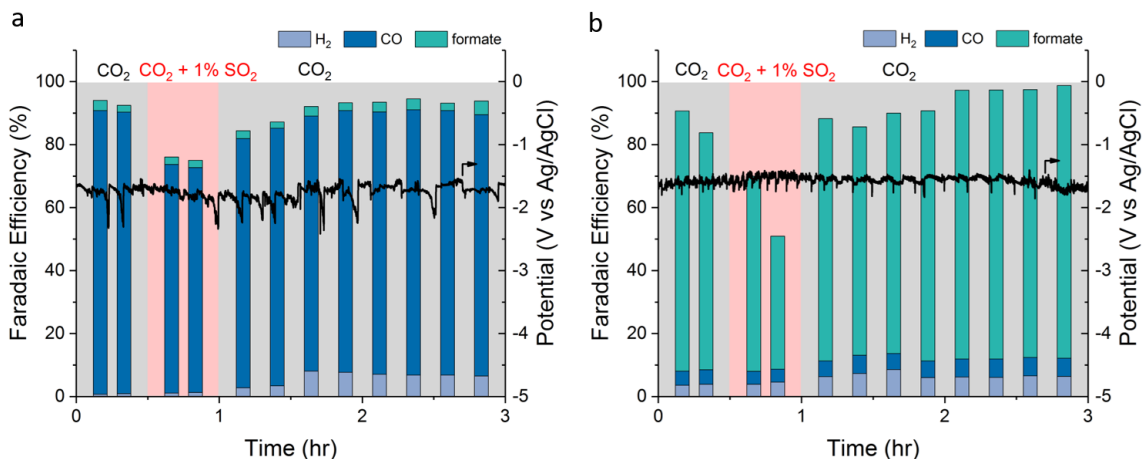


Figure 6.2: Performance of $\text{CO}_2 + \text{SO}_2$ electrolysis over a) Ag and b) Sn catalysts at constant current density of 100 mA cm^{-2} in 1 M KHCO_3 over the span of 3 h.

However, the reduction of the total CO_2 Faradaic efficiency indicates that SO_2 impurity can reduce the efficiency of converting CO_2 , since the reduction of SO_2 is more favorable than CO_2 .

6.3.3 Influence of SO_2 on Cu-catalyzed CO_2 reduction

Next, $\text{CO}_2 + \text{SO}_2$ reduction experiments were performed on Cu catalyst to study the influence of SO_2 on Cu-catalyzed CO_2 reduction, as Cu is the only monometallic material that can reduce CO_2 to high-value C_{2+} products with appreciable selectivities. As shown in Figure 6.3a, indeed Cu can convert CO_2 to an array of products including CO, formate, ethylene (C_2H_4), ethanol (EtOH), n-propanol (n-PrOH), and a small amount of acetate and CH_4 . Long-term CO_2 electrolysis over Cu catalyst demonstrates a stable performance of converting CO_2 to C_{2+} products (Figure E.8). When the Cu catalyst was subjected to 1% SO_2 (Figure 6.3a, red region), as similar to both Ag and Sn catalysts, the total CO_2 reduction Faradaic efficiency decreased, likely due to preferential reduction of SO_2 . Interestingly, the CO_2 reduction product selectivity shifted, and formate became the dominant CO_2 reduction product, while

the other CO₂ reduction products were suppressed. XPS analysis (Figures 6.3b&c) confirmed the formation of metal sulfide (Table E.1) after one hour of electrolysis and the peak position at ~162.0 eV was assigned to Cu₂S with a surface concentration of ~12 at.%.^[30] This peak assignment was also confirmed with commercial Cu₂S and CuS particles (Figure E.9). Again, sulfite and sulfate were also detected likely due to sample handling. Similarly, the formation of aggregated bulky-like particles after 1 h of electrolysis, subjected to a feed of 1% SO₂ for 30 min, can be seen (Figure E.10), and this observation was further confirmed with BF-TEM imaging (Figure 6.3d). The corresponding SAED pattern shows the presence of residual Cu₂S, metallic Cu, and CuO that was likely formed from air exposure during sample handling. HAADF-STEM and the corresponding EELS imaging (Figures 6.3e-j) show highly disperse S species positioned near the edge of the particles, suggesting that formation of Cu₂S likely resides near the surface. This observation was also confirmed with HR-TEM imaging and the corresponding FTT pattern (Figure E.11) also showing the formation of Cu₂S near the particle surface. Additional HAADF-STEM and EELS mapping can be found in the Appendix E (Figure E.12). It must be noted that for TEM work, FAA ionomer binder was used instead of Nafion, as Nafion has sulfonic functional groups that would convolute the detection of S species associated to metal sulfides. On the as-prepared Cu catalyst, there was no S species detected (Figure E.13). The utilization of FAA ionomer showed a similar trend in CO₂ + SO₂ reduction as Nafion, and thus, the ionomer is likely not the cause of the observed shift in selectivity (Figure E.14).

Interestingly, when the SO₂ feed was stopped, formate remained as the dominant CO₂ reduction product, and an incremental recovery was observed as the selectivity toward CO production slowly increased, followed by ethylene production. Mechanistically, this observation is consistent with literature as it is well known that the pathway toward C₂₊ products goes through a CO intermediate on Cu-catalyzed CO₂ reduction, while the pathway toward formate is a dead-end.^[31] Therefore, the observed trend in recovery is CO followed by C₂₊ products. In addition, an enhancement in hydrogen evolution was also observed during and after SO₂ injection. Similar to Ag₂S and SnS₂,

Cu₂S is also thermodynamically unstable under CO₂ electrolysis conditions. However, even after 5 h of electrolysis, Cu₂S was still detected on the Cu surface (Figures 6.3c and E.15), indicating that the reduction of Cu₂S is kinetically slow. The presence of Cu₂S may be the reason for the inability of the Cu catalyst to recover its initial performance, and the observation in the current study is consistent with previous works that have shown that S-modified nanostructured Cu catalysts can selectively convert CO₂ to formate.[32, 33] In addition, commercial Cu₂S particles were also examined and the dominant CO₂ reduction product was formate (Figure E.16), further supporting that surface Cu₂S is likely responsible for the change in selectivity.

To further probe the sensitivity of the Cu catalyst toward SO₂ impurity, similar experiments were conducted with lower SO₂ concentrations (0.1% and 0.01%). In both cases, a shift in selectivity toward formate was observed (Figures E.17 and E.18), and XPS measurements confirmed the presence of Cu₂S (Table E.2). With lower SO₂ concentrations, there was a relatively faster rate of recovery; however full recovery was not achieved even after 5 hours of electrolysis. Again, an incremental recovery of CO followed by C₂₊ products can be seen. A recovery up to ~10% and ~5% for CO and ethylene Faradaic efficiencies was achieved in 0.1% SO₂ after 5 h, respectively. At lower concentration of 0.01% SO₂, the recovery of CO and ethylene quickly plateaued to those same Faradaic efficiencies, and no further improvement was observed. Post-reaction XPS analysis after 5 h electrolysis shows similar Cu₂S composition on both catalytic surfaces after 0.1% and 0.01% SO₂ treatments (Table E.2), suggesting that there may be residual surface Cu₂S that are stable under CO₂ electrolysis conditions. In an attempt to recover the initial performance after 1% SO₂, the flow-cell electrolyzer was operated at 1 A cm² for 30 min under Ar to locally generate a high-flux of H₂ to potentially reduce the metal sulfides (Figure E.19). Although slight improvements were observed, a full recovery was not achieved, and post-reaction XPS analysis also indicated the presence of Cu₂S (Table E.2). These observations suggest that Cu catalysts are sensitive to SO₂ and that residual Cu₂S on the catalytic surface may dramatically impact the CO₂ reduction performance. Therefore, it is concluded that the CO₂ gas feed must be

relatively pure (SO_2 -free) for Cu-catalyzed CO_2 electrolysis.

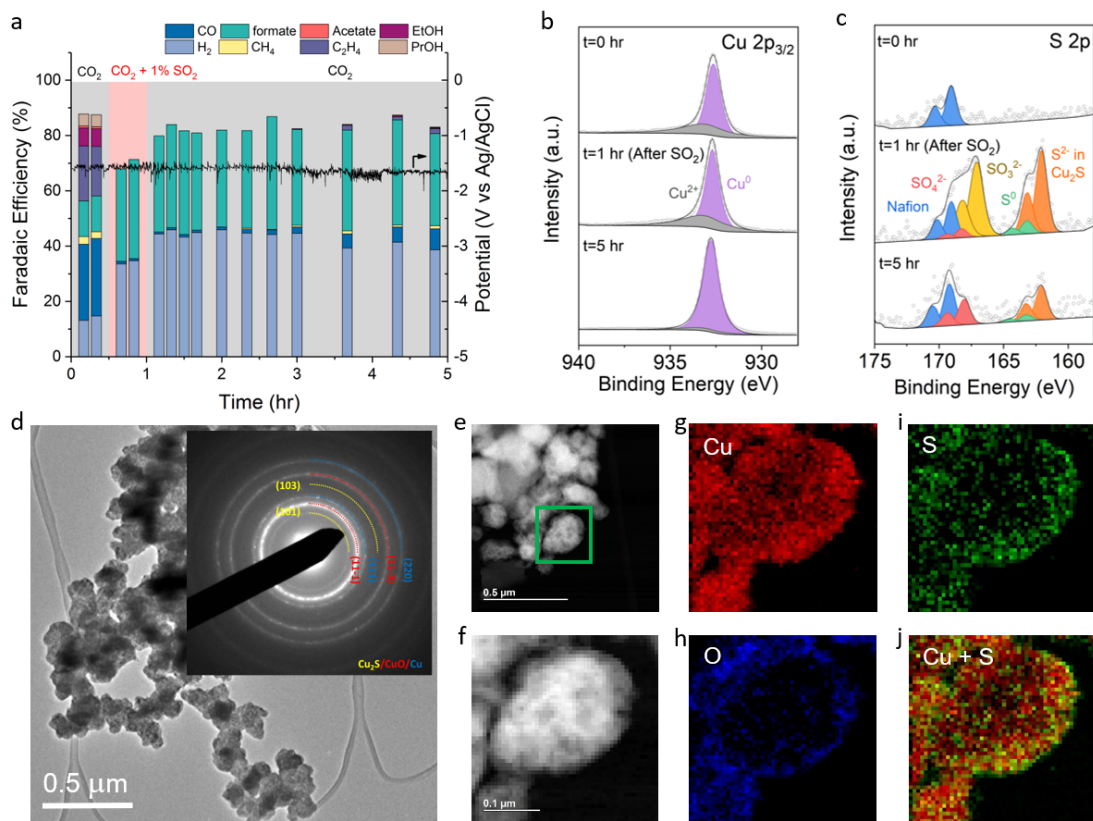


Figure 6.3: Performance of Cu catalyst at constant current density of 100 mA cm^{-2} in 1 M KHCO_3 with a $1\% \text{ SO}_2$ feed over the span of 5 h. XPS spectrum of the b) Cu and c) S region at various time points. d) BF-TEM image. Inset: SAED pattern, e-f) HAADF-STEM images, and g-j) EELS mapping of Cu catalyst after 1 hour of electrolysis in $\text{CO}_2 + 1\% \text{ SO}_2$ experiment.

6.3.4 Density Functional Theory Calculations

To further gain insight on the shift in selectivity, DFT calculations were performed on S modified Ag, Sn, and Cu catalysts, and the surfaces were modeled as S-doped Ag(111), Sn(111), and Cu(111), respectively. The binding energies of the hydrogen evolution reaction intermediate (e.g. *H) and CO₂ reduction intermediates for CO production (e.g. *COOH) and formate production (e.g. *OCHO) were calculated on clean and S-doped surfaces (Table E.3). The DFT optimized geometries on Cu(111) and S-doped Cu(111) (Figure 6.4) show that *H prefers to bind at a hollow site; *COOH binds at a top site via C atom and *OCHO binds at top sites via two O atoms. The binding geometries of these intermediates on undoped and S-doped (111) surfaces of Ag and Sn were also found to be similar to those on Cu(111). It is noted that *OCHO is relatively more stable than the *COOH intermediate on all surfaces and the stability of *OCHO increases in the order: Sn(111) > Ag(111) > Cu(111).

The binding energies (Table E.3) show that *OCHO is more stable than *COOH by 1.25 eV, 1.35 eV, and 1.13 eV on Ag(111), Sn(111) and Cu(111), respectively. In contrast, the *OCHO stability over *COOH (0.62 eV) decreases on S-doped Ag(111) compared to Ag(111). However, the *OCHO stability over *COOH increases on S-doped Sn(111) (1.54 eV) and S-doped Cu(111) (1.23 eV) compared to Sn(111) and Cu(111), respectively. To account for the formation of Cu₂S as experimentally observed, further DFT calculations were performed to calculate binding energies of *H, *COOH and *OCHO (Figure 6.4) on the Cu₂S(100) surface that has mixed Cu and S surface termination. Consistent with the prediction on S-doped Cu(111), the results show that the *OCHO stability over *COOH (1.24 eV; Table E.3) is enhanced on Cu₂S(100) compared to Cu(111). In summary, the DFT calculations predict that surface S atoms on Cu surfaces selectively stabilize *OCHO, and thus the formation of formate is promoted as in agreement with the experimental observations. A similar promotional effect on the formate selectivity is predicted on S-doped Sn(111). However, such promotion is not predicted on S-doped Ag(111) since the *OCHO stability over *COOH is less

on S-doped Ag(111) compared to Ag(111). It must be noted that there is a discrepancy between experimental and computational prediction on the Ag catalyst as DFT predicts that formate is more favorable than CO formation; while experimentally, CO was observed as the major CO₂ reduction product. A similar discrepancy is also highlighted in a recent work by Bohra et al.[34] However, by incorporating solvation effects on transition states and surface coverage of *H, *COOH and *OCHO, they successfully demonstrated the promotion of CO over formate formation on the Ag surface. Future work should also focus on exploring these effects on Sn- and Cu-catalyzed CO₂ reduction.

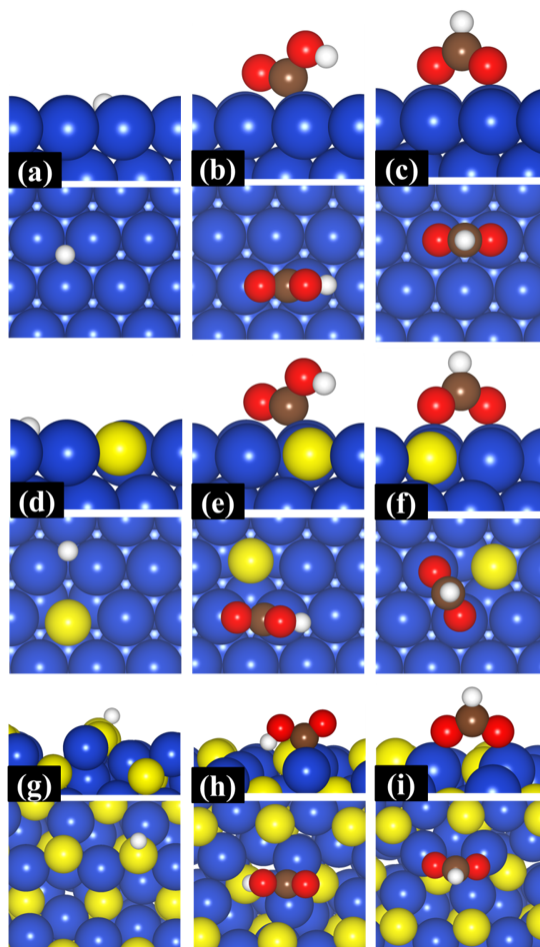


Figure 6.4: DFT optimized binding configurations of (a) *H, (b) *COOH, and (c) *OCHO on Cu(111), (d) *H, (e) *COOH and (f) *OCHO on S-doped Cu(111), and (g) *H, (h) *COOH, and (i) *OCHO on Cu₂S (100). Blue: Cu, yellow: S, red: O, brown: C and white: H.

6.4 Conclusions

In summary, the influence of SO_2 impurity in Ag, Sn, and Cu-catalyzed CO_2 electrolysis was studied in a flow-cell electrolyzer. The presence of SO_2 impurity reduces the efficiency of converting CO_2 as the reduction of SO_2 is thermodynamically more favorable. In the case of Ag and Sn, full recovery was observed after both catalysts were subjected to SO_2 and the selectivities of converting CO_2 to CO and formate were preserved, respectively. However, Cu is highly sensitive to SO_2 impurity and a shift in selectivity toward formate, accompanied by a suppression of C_{2+} products, was observed. The formation of surface Cu_2S , as confirmed with XPS characterization, is likely responsible for the shift in selectivity, as consistent with computational prediction.

Our experimental observations further motivate the use of a two-step process (Figure 1.3) for the production of value-added C_{2+} products. As Cu is highly susceptible to SO_2 as demonstrated, the first electrolyzer operating in neutral conditions can selectively convert CO_2 to CO, using a Ag catalyst that is less prone to SO_2 , and can simultaneously scrub the feed stream of trace SO_2 impurity. This will help prevent potential SO_2 impurity from contaminating the second electrolyzer where CO is then further converted to C_{2+} products over a Cu catalyst in alkaline electrolyte. Furthermore, as mentioned in Chapter 1, the direct one-step CO_2 electrolysis in alkaline electrolyte to produce C_{2+} products is inherently unsustainable due to the irreversible formation of HCO_3^- and CO_3^{2-} when CO_2 reacts with OH^- , further pushing for the development of a two-step process for CO_2 conversion. Another solution is the development of direct air capture technologies, as CO_2 feedstock obtained from such technologies would be relatively cleaner than that obtained from fossil-derived point sources such as power plants and chemical facilities. Another advantage of direct air capture is that it is not geographically limited, and thus, direct air capture can be coupled with distributed renewable energy sources that is expected to be inexpensive in the near future.[35]

6.5 Acknowledgments

This material is based upon work supported by the Department of Energy under Award Number DE-FE0029868. The authors at the University of Delaware also thank the National Science Foundation for financial support (Award No. CBET-1803200). DFT calculations were supported by the US Department of Energy, Catalysis Program (Grant No. DE-FG02-13ER16381). This research used resources of the Center for Functional Nanomaterials, which is a U.S. DOE Office of Science Facility, at Brookhaven National Laboratory under contract No. DE-SC0012704. I would like to personally thank Byung Hee Ko for assisting with this study and helping me to conclude this work.

REFERENCES

- (1) Hori, Y.; Wakebe, H.; Tsukamoto, T.; Koga, O. *Electrochimica Acta* **1994**, *39*, 1833–1839.
- (2) Hori, Y.; Konishi, H.; Futamura, T.; Murata, A.; Koga, O.; Sakurai, H.; Oguma, K. *Electrochimica Acta* **2005**, *50*, 5354–5369.
- (3) Wuttig, A.; Surendranath, Y. *ACS Catalysis* **2015**, *5*, 4479–4484.
- (4) Weng, Z.; Zhang, X.; Wu, Y. S.; Huo, S. J.; Jiang, J. B.; Liu, W.; He, G. J.; Liang, Y. Y.; Wang, H. L. *Angewandte Chemie-International Edition* **2017**, *56*, 13135–13139.
- (5) Zhai, Y. M.; Chiachiarelli, L.; Sridhar, N. *ECS Transactions* **2009**, *19*, 1–13.
- (6) Sanz-Perez, E. S.; Murdock, C. R.; Didas, S. A.; Jones, C. W. *Chemical Reviews* **2016**, *116*, 11840–11876.
- (7) Keith, D. W.; Holmes, G.; Angelo, D. S.; Heidel, K. *Joule* **2018**, *2*, 1573–1594.
- (8) Koytsoumpa, E. I.; Bergins, C.; Kakaras, E. *Journal of Supercritical Fluids* **2018**, *132*, 3–16.
- (9) Wu, X. M.; Yu, Y. S.; Qin, Z.; Zhang, Z. X. *Energy Procedia* **2014**, *63*, 1339–1346.
- (10) Last, G. V.; Schmick, M. T. *Identification and Selection of Major Carbon Dioxide Stream Compositions*; Report; 2011.
- (11) Hohenberg, P.; Kohn, W. *Physical Review B* **1964**, *136*, B864–B871.
- (12) Kohn, W.; Sham, L. J. *Physical Review* **1965**, *140*, A1133–A1138.
- (13) Blochl, P. E. *Physical Review B* **1994**, *50*, 17953–17979.
- (14) Perdew, J. P.; Burke, K.; Ernzerhof, M. *Physical Review Letters* **1996**, *77*, 3865–3868.
- (15) Kresse, G.; Furthmüller, J. *Physical Review B* **1996**, *54*, 11169–11186.
- (16) Kresse, G.; Hafner, J. *Physical Review B* **1993**, *47*, 558–561.
- (17) Monkhorst, H. J.; Pack, J. D. *Physical Review B* **1976**, *13*, 5188–5192.
- (18) Lv, J.-J.; Jouny, M.; Luc, W.; Zhu, W.; Zhu, J.-J.; Jiao, F. *Advanced Materials* **2018**, *0*, 1803111.
- (19) Verma, S.; Lu, X.; Ma, S. C.; Masel, R. I.; Kenis, P. J. A. *Physical Chemistry Chemical Physics* **2016**, *18*, 7075–7084.

- (20) Dinh, C.-T.; Burdyny, T.; Kibria, M. G.; Seifitokaldani, A.; Gabardo, C. M.; García de Arquer, F. P.; Kiani, A.; Edwards, J. P.; De Luna, P.; Bushuyev, O. S.; Zou, C.; Quintero-Bermudez, R.; Pang, Y.; Sinton, D.; Sargent, E. H. *Science* **2018**, *360*, 783.
- (21) Verma, S.; Hamasaki, Y.; Kim, C.; Huang, W.; Lu, S.; Jhong, H.-R. M.; Gewirth, A. A.; Fujigaya, T.; Nakashima, N.; Kenis, P. J. A. *ACS Energy Letters* **2018**, *3*, 193–198.
- (22) Dinh, C. T.; Garcia de Arquer, F. P.; Sinton, D.; Sargent, E. H. *ACS Energy Letters* **2018**, *3*, 2835–2840.
- (23) Liu, Z. C.; Yang, H. Z.; Kutz, R.; Masel, R. I. *Journal of the Electrochemical Society* **2018**, *165*, J3371–J3377.
- (24) Yang, H. Z.; Kaczur, J. J.; Sajjad, S. D.; Masel, R. I. *ECS Transactions* **2017**, *77*, 1425–1431.
- (25) Ghafoor, S.; Ata, S.; Mahmood, N.; Arshad, S. N. *Scientific Reports* **2017**, *7*.
- (26) Hota, G.; Idage, S. B.; Khilar, K. C. *Colloids and Surfaces a-Physicochemical and Engineering Aspects* **2007**, *293*, 5–12.
- (27) Liu, J.; Jing, L. Q.; Gao, G. F.; Xu, Y. G.; Xie, M.; Huang, L. Y.; Ji, H. Y.; Xie, J. M.; Li, H. M. *RSC Advances* **2017**, *7*, 46823–46831.
- (28) Zheng, X. L. et al. *Joule* **2017**, *1*, 794–805.
- (29) Aastrup, T.; Wadsak, M.; Leygraf, C.; Schreiner, M. *Journal of the Electrochemical Society* **2000**, *147*, 2543–2551.
- (30) Xie, Y.; Riedinger, A.; Prato, M.; Casu, A.; Genovese, A.; Guardia, P.; Sottini, S.; Sangregorio, C.; Miszta, K.; Ghosh, S.; Pellegrino, T.; Manna, L. *Journal of the American Chemical Society* **2013**, *135*, 17630–17637.
- (31) Ren, D.; Fong, J. H.; Yeo, B. S. *Nature Communications* **2018**, *9*.
- (32) Shinagawa, T.; Larrazabal, G. O.; Martin, A. J.; Krumeich, F.; Perez-Ramirez, J. *ACS Catalysis* **2018**, *8*, 837–844.
- (33) Deng, Y. L.; Huang, Y.; Ren, D.; Handoko, A. D.; Seh, Z. W.; Hirunsit, P.; Yeo, B. S. *ACS Applied Materials & Interfaces* **2018**, *10*, 28572–28581.
- (34) Bohra, D.; Ledezma-Yanez, I.; Li, G. N.; de Jong, W.; Pidko, E. A.; Smith, W. A. *Angewandte Chemie-International Edition* **2019**, *58*, 1345–1349.
- (35) Haegel, N. M. et al. *Science* **2017**, *356*, 141–143.

Chapter 7

CONCLUSIONS AND RECOMMENDATIONS

7.1 Conclusions

In this thesis, the fundamental study using bulk catalytic surfaces, scale-up of catalytic systems, reactor/process engineering, and synthesis of well-defined nanostructured catalysts were presented in efforts to address several key issues toward developing pathways for the electrified production fuels and chemicals. Although the challenges toward establishing a sustainable infrastructure span beyond what is covered in this thesis, lessons learned from these works can guide future efforts toward developing more efficient and selective electrochemical processes. A complete list of original works completed at University Delaware is summarized in Appendix F.

In Chapter 3, a combined computational and experimental study of Cu-based bimetallic electrocatalysts for H₂ evolution in alkaline conditions was performed in efforts toward identifying non-precious catalysts as replacement for Pt. Two systems of Cu-based catalysts were investigated: one system through alloying of Cu with first-row transition metals, and the other system through the deposition of first-row transition metal hydroxide/oxide clusters on Cu surfaces. Through a systematic study, we concluded that the synergistic effect between the oxophilic dopant and Cu enhances H₂ evolution where the oxophilic site can help adsorb water to the surface while a nearby Cu site can facilitate the formation of H_{ads}. These observations suggest that not only the HBE is important factor to consider, but also the OBE as well when designing non-precious catalysts for the HER in alkaline conditions.

In Chapter 4, the scale-up of a np-Ag catalyst, design of a custom CO₂ electrolyzer, and development of a process for continuous CO₂ to CO conversion with

high selectivity and single-pass conversion were presented in efforts to demonstrate a proof-of-concept for a new O₂ recovery process for deep space applications. This process combines an electrochemical CO₂ reduction step with a thermochemical CO decomposition step that theoretically can recovery 100% of O₂ from CO₂ at relatively mild temperatures compared to other technologies currently being explored. CO₂ electrolysis was conducted in a 25 cm² electrolyzer and achieved a current over 1 A with a maximum CO Faradaic efficiency of ~96% at 2.8 V. Furthermore, by optimizing the operating parameters, an average single-pass CO₂ conversion of ~86% was demonstrated, among the highest reported to date.

Utilizing lessons learned from the CO₂ electrolyzer development, a novel flow-cell electrolyzer was designed for CO electrolysis in order to circumvent mass transport limitations and was presented in Chapter 2.2. In Chapter 5, well-defined nanostructured Cu catalysts were synthesized and evaluated for CO reduction in efforts to understand C₂₊ product formation at high rates of electrolysis that has not been previously explored. In particular, freestanding two-dimensional Cu nanosheets that selectively exposed Cu{111} facets demonstrated high selectivity and activity for converting CO to acetate with a Faradaic efficiency as high as 48% and an acetate partial current density up to 131 mA cm⁻² in 2 M KOH. This performance is among the highest reported to date, and further analysis suggested that the enhanced acetate selectivity is due to the suppression of ethylene and ethanol formation, like from of the reduction of exposed (100) and (110) surfaces.

Finally in Chapter 6, the influence of impurities on CO₂ electrolysis, mainly SO₂, was studied as commercial CO₂ feedstock most likely will be obtained from fossil-derived resources in the near future. The study indicated that the small presence SO₂ has a reversible effect on Ag and Sn catalysts as full recovery was achieved on both catalysts after SO₂ exposure. However, SO₂ impurity has a detrimental effect on Cu catalyst as experimental results showed that SO₂ impurity leads to the suppression of C₂₊ products due to the formation of surface Cu₂S. This observation further motivates the development of direct air capture technologies as the CO₂ feedstock obtain from

such technologies would be cleaner than that obtained from fossil-derived resources.

7.2 Recommendations

Based on the studies completed in this thesis, there are several research thrusts that may be immediately explored. In the following sections, an overall summary of each research direction will be presented.

7.2.1 Nanostructured Catalysts for the HER

One direction stemming from the work completed in Chapter 3 is the development of practical nanostructured Cu-based bimetallic catalysts in efforts toward commercialization. Among the Cu-based bimetallics that were investigated, Cu-Ti showed the highest HER activity in alkaline conditions. From this study, a self-supporting nanoporous-CuTi, synthesized through a similar dealloying technique as presented in Chapter 4, has recently been developed that exhibits more than a 2-fold enhancement in HER activity compared to the state-of-the-art Pt/C. The combination of the synergistic effect between Cu and Ti and the unique hierarchical porous structure that allows for enhanced surface area and mass transport properties, is likely responsible for the improved activity. However, a major challenge regarding nanoporous materials is scale-up since these materials are not mechanically strong due to large void volumes (>70%). Thus, the implementation of nanoporous catalysts for large commercial electrolyzers may not be practical.[1] One possible direction is the development of CuTi nanoparticles or even nanoporous CuTi nanoparticles as an alternative. Erlebacher and co-workers have recently developed a nanoporous Au nanoparticle in which as-synthesized AgAu nanoparticles were electrochemically etched.[2] A similar technique can be adopted to develop nanoporous CuTi nanoparticles which can then be directly sprayed onto a PEM. With this architecture, the unique CuTi catalytic sites can be maintained while the membrane can provide an overall better structural support. Furthermore, the as-sprayed nanoparticles can be directly utilized in a MEA-based reactor for the commercialization of alkaline-based water-splitting electrolyzers.

7.2.2 System Integration of the Two-Step Process for CO₂ conversion to C₂₊ products

In Chapter 4, a CO₂ electrolyzer process was developed that can selectively convert CO₂ to CO with high single-pass conversion. In Chapter 5 a flow-cell electrolyzer was developed that can convert CO to C₂₊ products at high rates of electrolysis. Future work should focus on integrating the two electrolyzers to develop a continuous process that can selectively convert CO₂ to C₂₊ products. As shown in Figure 7.1, a CO₂/CO separator is needed to minimize unreacted CO₂ from entering the CO electrolyzer which could impede performance. If a separator is utilized, either a vacuum pump is needed or the CO₂ electrolyzer will have to operate at an elevated pressure such that there is a gradient that can drive the separation process. Also, the rate of chemical processing in each step needs to be closely matched to minimize recycle streams that could drive up additional operating costs. Overall, high single-pass conversion is needed in both electrolyzers to minimize separation costs and to improve CO₂/CO utilization.

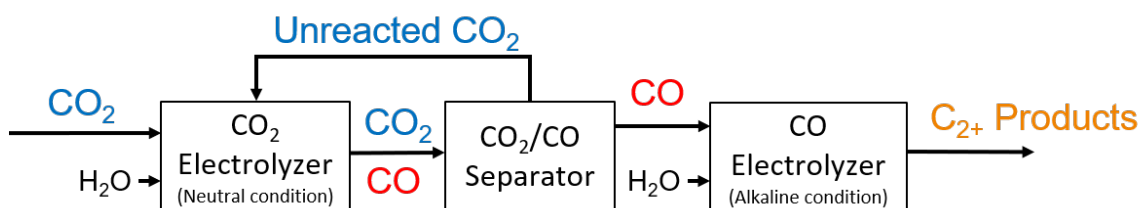


Figure 7.1: Schematic of a two-step process for CO₂ conversion with separation

The electrochemical process that was presented Chapter 4 benefits from high selectivity and single-pass conversion as the electrochemical reduction of CO₂ is performed in an aqueous system where gaseous CO₂ is dissolved in the electrolyte. As mentioned, theoretically, complete conversion can be obtained if the dissolving rate of CO₂ gas into the electrolyte matches the CO₂ consumption rate such that the electrolyte is always CO₂-saturated at steady-state. Further optimization of the CO₂ contactor is needed to enhancing the dissolving rate of gaseous CO₂ by tuning the pore

size of the contactor. However, due to the low solubility of CO_2 in aqueous electrolyte the current densities remain far below $>100 \text{ mA cm}^{-2}$ which is the regime needed to make CO_2 electrolysis commercially viable.[3]

On the contrary, in gas-phase electrolysis where gaseous CO_2 or CO reactant is directly fed to the electrode-electrolyte interface, much higher current densities $>100 \text{ mA cm}^{-2}$ can be achieved as demonstrated in Chapters 5 and 6. However, the single-pass conversion of these flow-cell electrolyzers is poor ($<30\%$) which poses a separation challenge. Recently, Kanan and co-workers, through reactor engineering, demonstrated high single-pass conversion of 68% at a current density of 101 mA cm^{-2} with a total CO reduction Faradiac efficiency of 65%–76% using a gas diffusion system that couples a robust Nafion membrane with an interdigitated flow-field.[4] Instead of a flow-cell electrolyzer configuration, a MEA-based electrolyzer design was utilized where a Cu-GDE was directly in contact with the Nafion membrane. They showed that it is possible to eliminate the use of a catholyte, and therefore, a highly concentrated product stream can be obtained. A similar MEA-based configuration can also be examined, and the development of novel flow-fields dedicated for CO_2/CO electrolysis can be explored to further improve single-pass conversion as majority of current flow-fields are specifically designed for water-splitting electrolyzers.[5]

7.2.3 Electrolyzer Development for Acetic Acid Production

In Chapter 5, freestanding Cu nanosheets were shown to exhibit high selectivity toward acetate formation due to the suppression of ethylene and ethanol formation. However, the production of acetate is not practical as acetate is a salt that will consume potassium ions and pose a separation challenge. On the contrary, acetic acid, the protonated form of acetate, can be easily separated and is a large commodity chemical for the production of paints and adhesives with a market size of \$15 billion. Recently, Masel and co-workers have developed a three-compartment cell configuration that utilized an anion and cation exchange membrane for the electrochemical conversion of CO_2 to formic acid, achieving current densities between $\sim 100\text{-}200 \text{ mA cm}^{-2}$ while operating

between 3.1-3.8 V.[6] Similarly, formic acid, the protonated form of formate, is more desirable. In short, the utilization of an AEM on the cathode allows for formate ions to diffuse through the membrane where formate is then protonated to formic acid in the middle chamber by protons diffusing through a CEM that are generated at the anode. A similar concept can be developed for the production of acetic acid; however, as a two membrane system will have high cell resistance, reactor engineering and membrane development are needed to improve ionic conductivity and minimize cell resistance such that the applied potential is reasonable (~ 2 V) for practical applications.[7]

7.2.4 Development of SO₂-Resistant Catalysts and Study of Other Gaseous Impurities

In Chapter 6, the influence of SO₂ impurity on CO₂ electrolysis was studied and the results showed that Cu is highly sensitive to SO₂ impurity. One potential area of research is the development of SO₂-resistant or improved SO₂ tolerant catalysts. For the industrial production of methanol, Cu/ZnO is typically used to facilitate the water-gas shift reaction.[8] As the feedstock is obtained from fossil-derived resources, this process is highly susceptible to S-poisoning. Besides its structural/catalytic role, ZnO is also employed as a sulfur trap through the formation of zinc sulfide, and it has been shown that with higher ZnO content, the catalyst is more tolerant to S-poisoning.[9] A similar strategy can also be employed for CO₂ electrolysis, where Cu can be supported on a secondary metal. The incorporation of the secondary metal can serve as sites for the preferential reduction of SO₂, potentially protecting the Cu sites. However, further work is necessary since the introduction of a secondary metal could promote the unwanted HER reaction.

Lastly, future work should also focus on studying the influence of NO_x as well as O₂ impurities in CO₂/CO electrolysis. Although SO₂ impurity was the focus in Chapter 6, NO_x and O₂ impurities are also present in CO₂ feedstocks obtained from fossil-derived resources.[10] These impurities may also have detrimental effects on CO₂/CO electrolysis as demonstrated by the SO₂ impurity study. Similarly, both NO_x and O₂

could co-adsorb on the catalytic sites under reducing potentials or interact with the electrolyte, potentially altering the local environment or surface structure and consequently influencing catalytic performance. In particular, the oxygen reduction reaction (ORR) could also compete with CO_2/CO reduction as there will be a large overpotential for ORR in the CO_2/CO reduction potential range. Furthermore, it has also been hypothesized that subsurface oxygen atoms in Cu-catalyzed CO_2/CO electroreduction may potentially enhance the formation of C_{2+} products and it would be interesting to determine if adsorbed oxygen species can influence the catalytic performance.[11]

REFERENCES

- (1) Luc, W.; Jiao, F. *ACS Catalysis* **2017**, *7*, 5856–5861.
- (2) Li, X.; Chen, Q.; McCue, I.; Synder, J.; Crozier, P.; Erlebacher, J.; Sieradzki, K. *Nano Letter* **2014**, *14*, 2569–2577.
- (3) Dinh, C. T.; Li, Y. G. C.; Sargent, E. H. *Joule* **2019**, *3*, 13–15.
- (4) Ripatti, D. S.; Veltman, T. R.; Kanan, M. W. *Joule* **2018**, *3*, 240–256.
- (5) Li, W.; Sabir, I. *International Journal of Hydrogen Energy* **2005**, *30*, 359–371.
- (6) Yang, H. Z.; Kaczur, J. J.; Sajjad, S. D.; Masel, R. I. *ECS Transactions* **2017**, *77*, 1425–1431.
- (7) Jouny, M.; Luc, W.; Jiao, F. *Industrial & Engineering Chemistry Research* **2018**, *57*, 2165–2177.
- (8) Behren, M.; Studt, F.; Kasatkin, I.; Kuhl, S.; Havecker, M.; Abild-Pedersen, F.; Zander, S.; Girgsdies, F.; Kurr, P.; Knief, B. L.; Tovar, M.; Fischer, R. W.; Norskov, J. K.; Schlögl, R. *Science* **2012**, *336*.
- (9) Beale, A.; Gibson, E.; O'Brien, M.; Jacques, S.; Cernik, R.; Di Michiel, M.; Cobden, P.; Pirgon-Galin, O.; van de Water, L.; Watson, M.; Weckhuysen, B. *Journal of Catalysis* **2014**, *314*, 94–100.
- (10) Last, G. V.; Schmick, M. T. *Identification and Selection of Major Carbon Dioxide Stream Compositions*; Report; 2011.
- (11) Eilert, A.; Cavalca, F.; Roberts, F. S.; Osterwalder, J.; Liu, C.; Favaro, M.; Crumlin, E. J.; Ogasawara, H.; Friebel, D.; Pettersson, L. G. M.; Nilsson, A. *Journal of Physical Chemistry Letters* **2017**, *8*, 285–290.

Appendix A

ASSEMBLY OF THE FLOW-CELL ELECTROLYZER

In this section, the assembly of the flow-cell electrolyzer will be reviewed. A photograph of the individual components is shown in Figure A.1. The main components that make the flow-cell electrolyzer are the end plates, flow chambers, electrodes, membrane, and the Teflon gaskets.

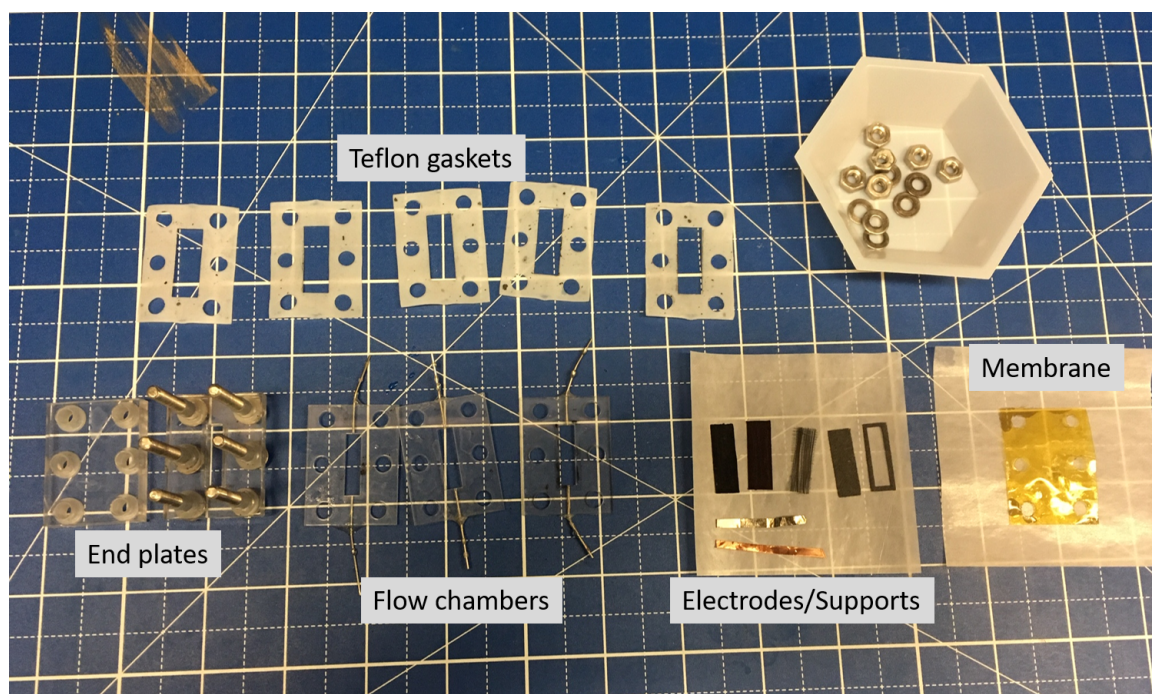


Figure A.1: Photograph of flow-cell electrolyzer components.

Figure A.2 shows the individual electrodes and supports. The cathode is Cu nanoparticles deposited on a GDL while the anode is IrO₂ deposited on GDL. It must be noted the anode will eventually degrade due to C oxidation. However, in a three-electrode setup used for CO₂/CO electrolysis, we only measure the cathode half-reaction, and therefore we can utilize the IrO₂ GDE as the anode. For practical applications, a more suitable anode is needed since the stability and performance of every component in an electrolyzer contributes to the overall performance of the device. The assembly of the flow-electrolyzer will be described in the following photographs (Figures A.3-A.16).

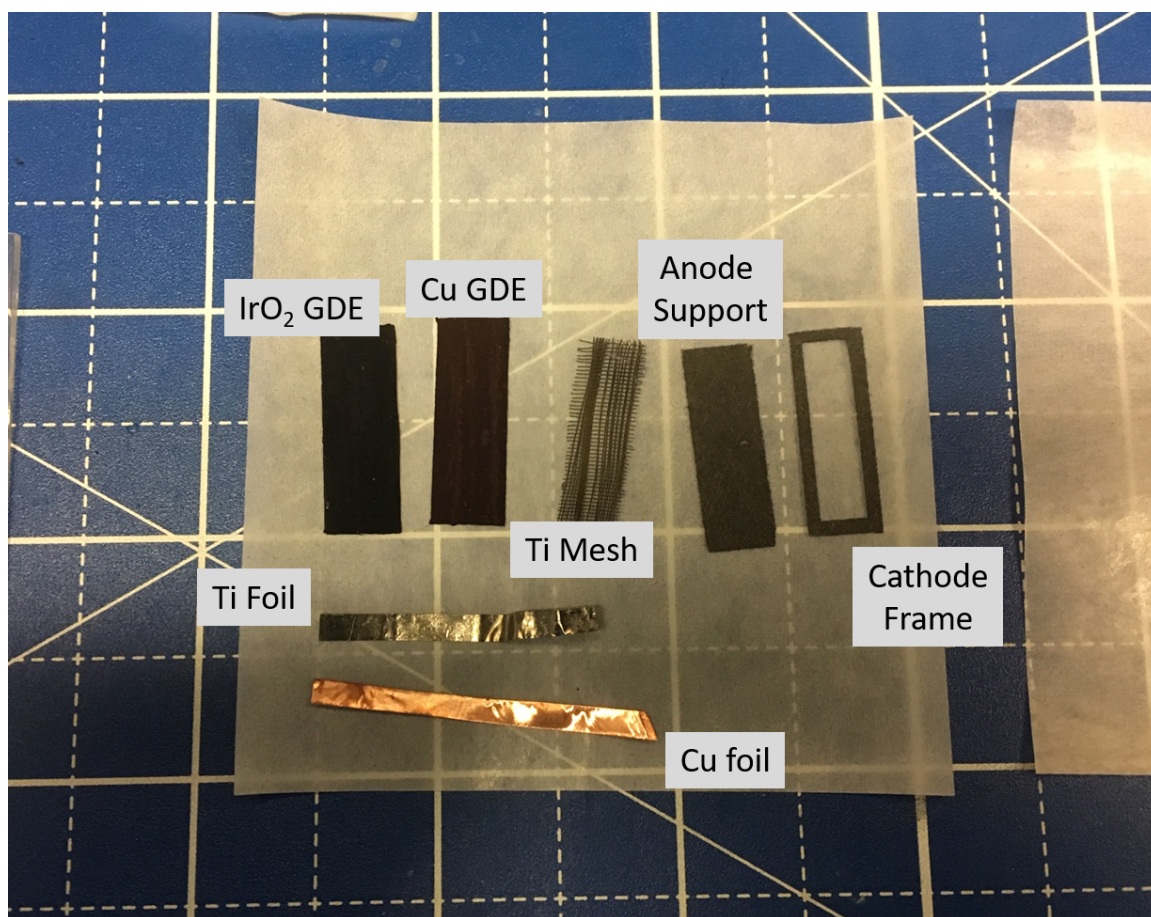


Figure A.2: Photograph of the electrodes and supports



Figure A.3: Step 1. Assemble the end plate by putting the screws through the back. The opening allows for O_2 to escape during electrolysis.

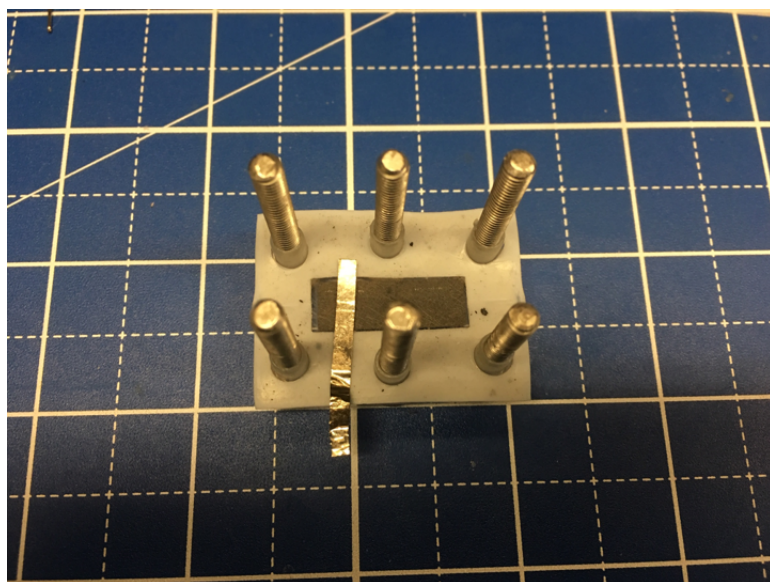


Figure A.4: Step 2. Place a Teflon gasket, anode support which is just a GDL without particles, and a Ti foil as shown. When pressed, the anode support helps with the electrical contact between the Ti foil and the anode GDE.

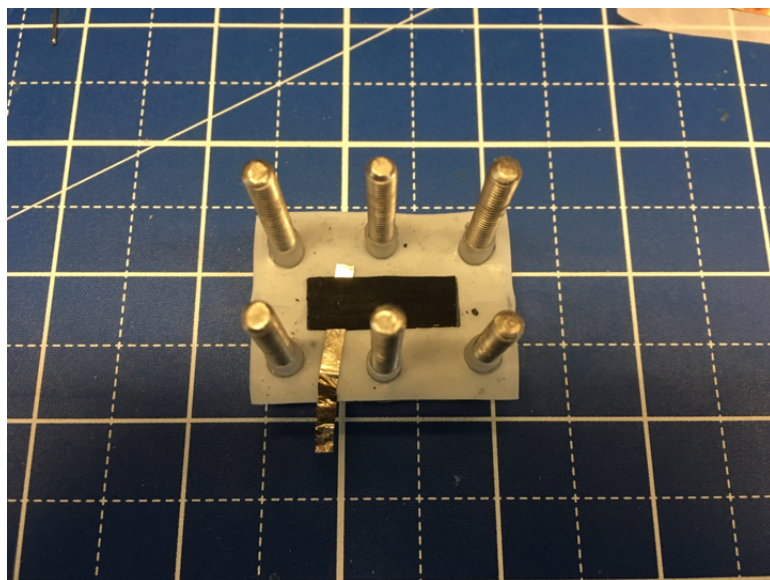


Figure A.5: Step 3. Place the IrO₂ GDE as shown and position the GDE well inside the window of the Teflon gasket or leakage will occur during electrolysis. In this photograph, the GDE is positioned with the catalyst layer facing up.

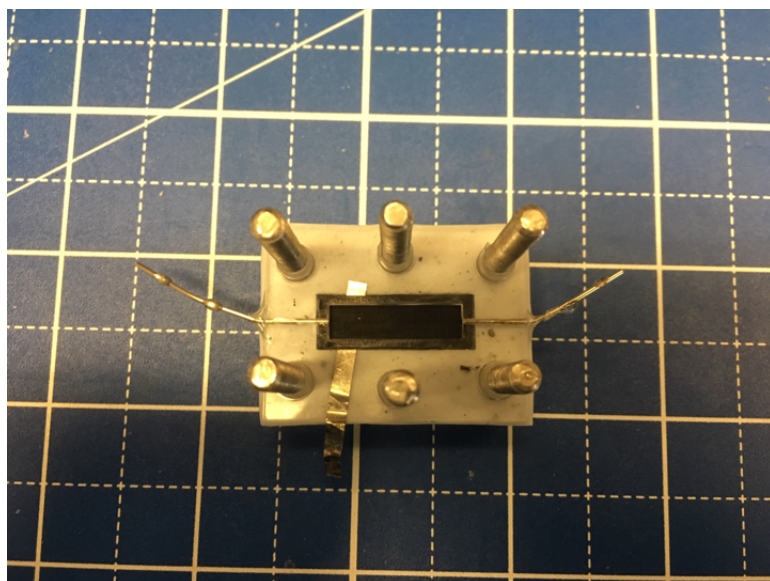


Figure A.6: Step 4. Firmly position the anode flow chamber as shown.

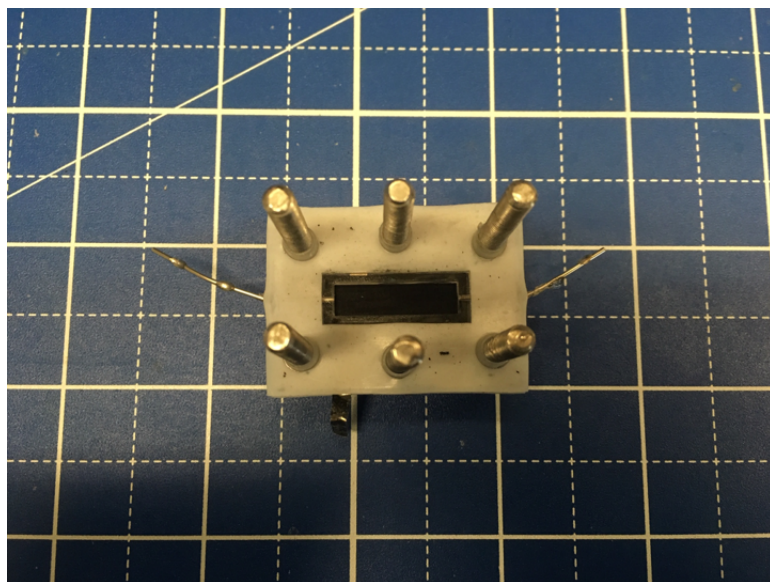


Figure A.7: Step 5. Position a Teflon gasket as shown.

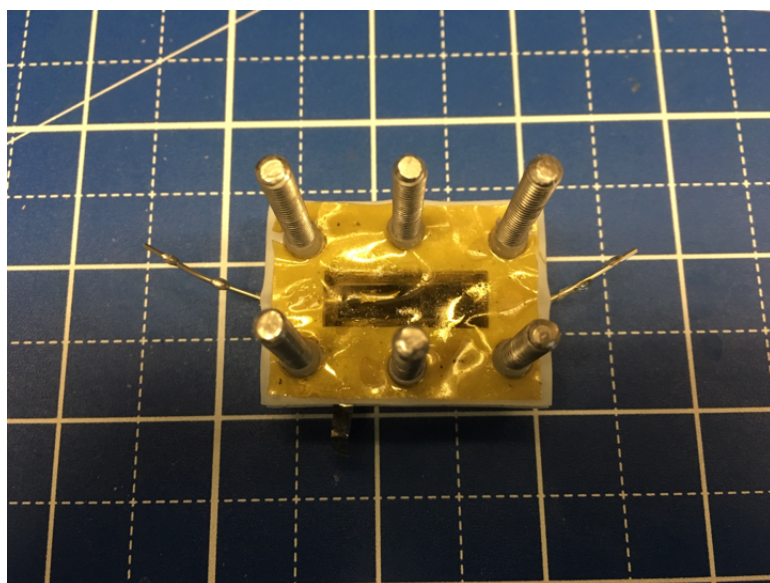


Figure A.8: Step 6. Position the membrane. In this picture, a Fumatech FAA-3 membrane is used and was soaked in 1 M KOH for at least 6 h.



Figure A.9: Step 7. Position another Teflon gasket to seal the membrane.

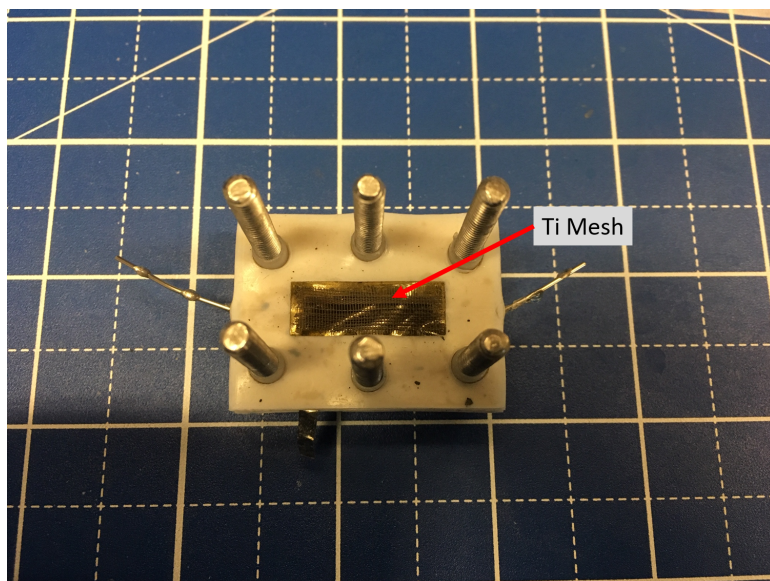


Figure A.10: Step 8. Place a Ti mesh. The mesh prevents the swelling of the membrane during electrolysis from interfering with the cathode flow chamber. It is important to be careful, as the Ti mesh could puncture the membrane.

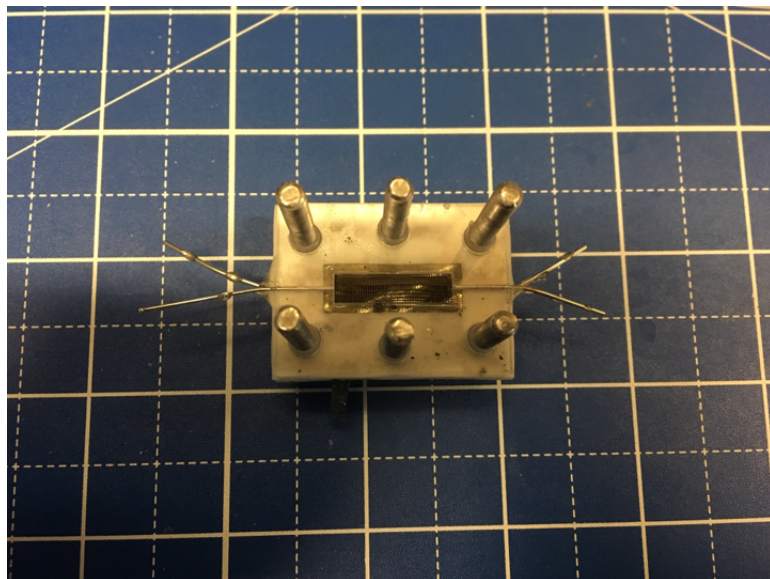


Figure A.11: Step 9. Firmly position the cathode flow chamber as shown.

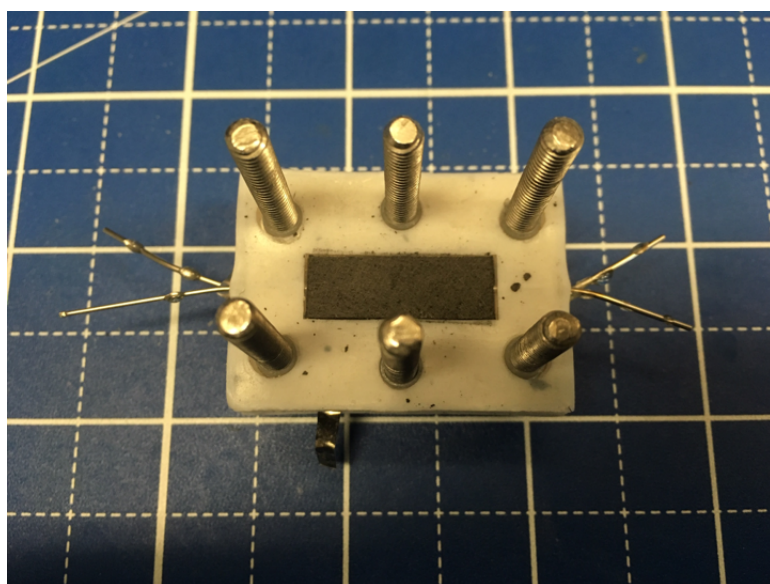


Figure A.12: Step 10. Position another Teflon gasket and the Cu GDE. In the photograph, the catalyst layer is positioned facing down toward the membrane.

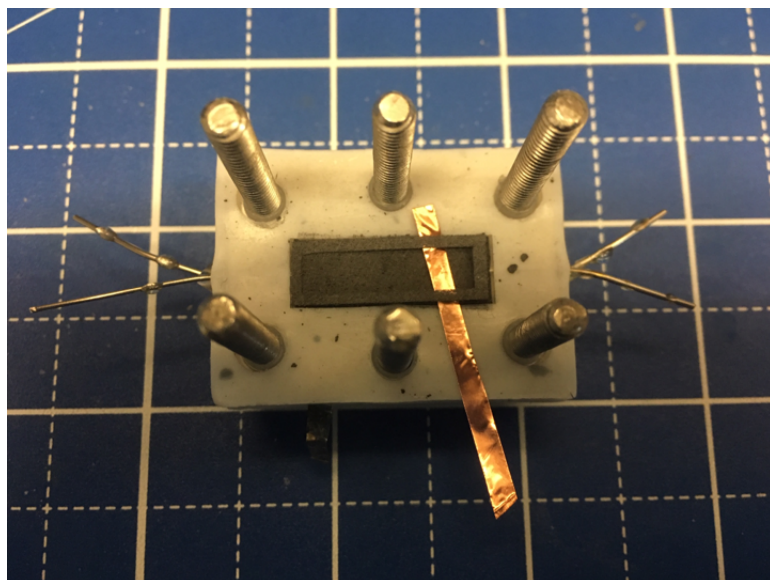


Figure A.13: Step 11. Place a Cu wire and the cathode frame. The frame helps with electrical contact between the GDE and the wire.

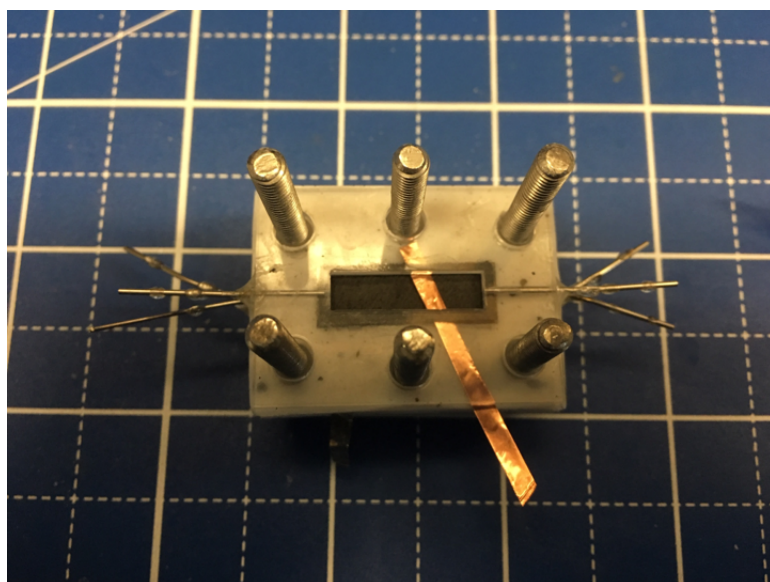


Figure A.14: Step 12. Firmly position the gas flow chamber as shown.

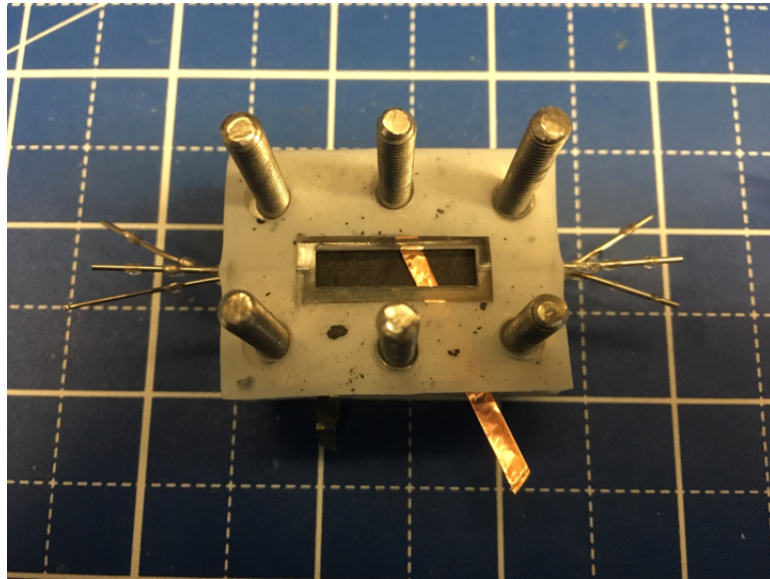


Figure A.15: Step 13. Firmly position another Teflon gasket to prevent gas leakage.

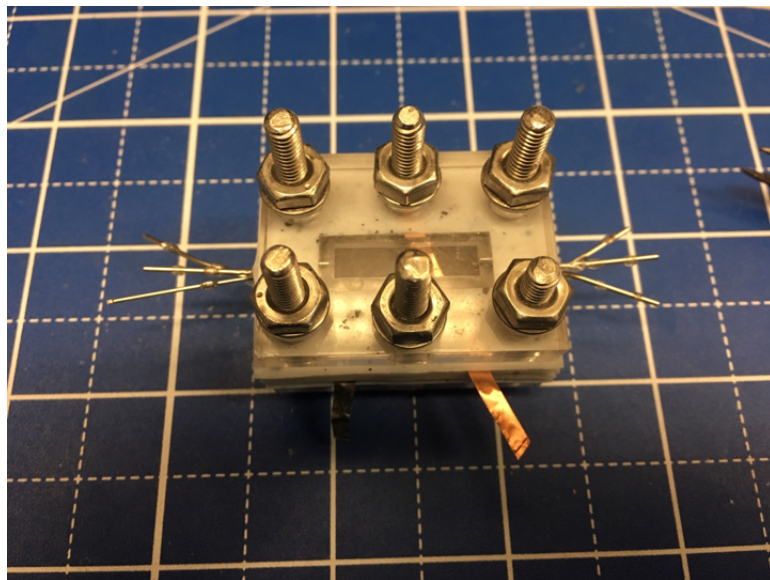


Figure A.16: Step 14. Position the other end plate and firmly tighten the screws.

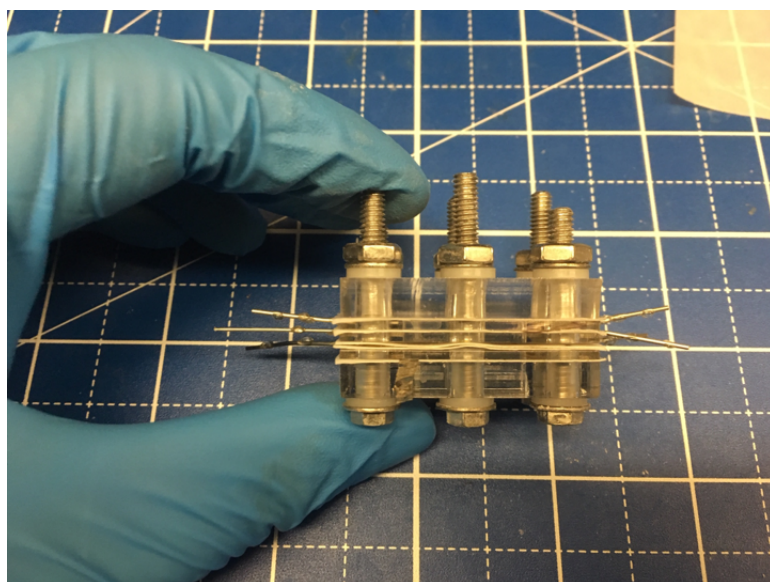


Figure A.17: Side view of the assembled flow-cell electrolyzer

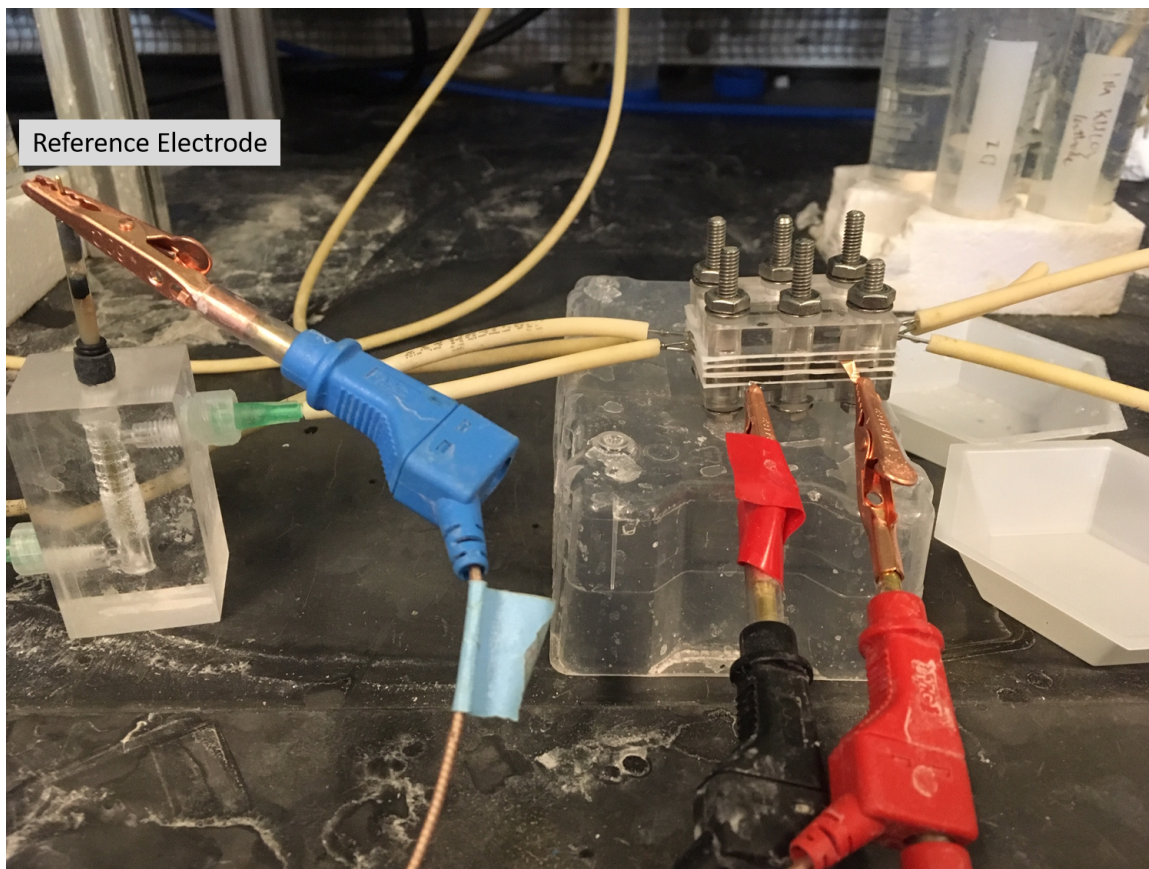


Figure A.18: Photograph of the three-electrode setup for flow-cell electrolyzer testing. The reference electrode is in-line with the cathode chamber.

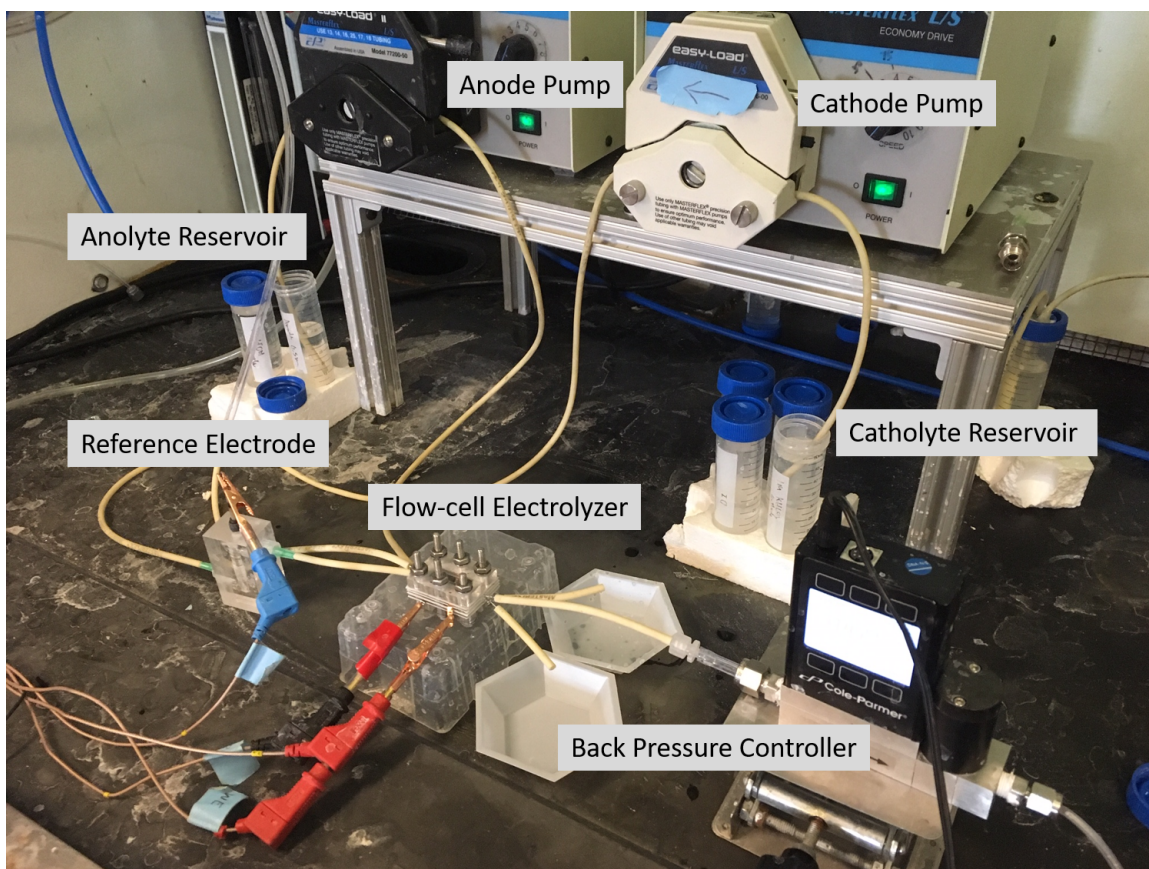


Figure A.19: Photograph of the overall setup for electrochemical evaluation. The cathode pump draws electrolyte from the catholyte reservoir and pushes the electrolyte through the reference electrode holder, and then finally through the cathode chamber. The anode pump draws electrolyte from the anolyte reservoir and pushes the electrolyte through the anode chamber. The back pressure controller is critical because it prevents flooding of the electrolyzer during prolonged electrolysis and consecutive GC injections. During injections, the GC pulls a slight vacuum which could accelerate flooding if the back pressure controller is not used.

Appendix B

SUPPLEMENTARY INFORMATION FOR CHAPTER 3: THE ROLE OF SURFACE OXOPHILICITY IN COPPER-CATALYZED WATER DISSOCIATION

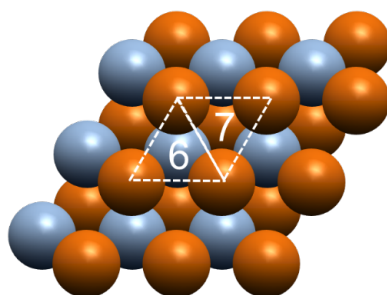


Figure B.1: Sub-layer substitution surface model with Cu and M = Ti, Co, or Ni atoms represented in orange and blue, respectively.

Table B.1: Calculated HBEs and OBEs for Cu–M(111) and Cu(111) surfaces

Model	Cu-Cu-M [3] HBE (eV)	Cu-Cu-M [3] OBE (eV)	Cu-M-M [5] HBE (eV)	Cu-M-M [5] OBE (eV)
Cu-Ti (111)	-0.41	-4.95	-0.80	-4.97
Cu-Co (111)	-0.50	-2.40	-0.69	-3.16
Cu-Ni (111)	-0.44	-2.08	-0.62	-2.50

[#]: Corresponding adsorption site on Figure 3.2.

Table B.2: Calculated HBEs and OBEs for Pt(111) surface

Model	Site [1] HBE (eV)	Site [1] OBE (eV)	Site [2] HBE (eV)	Site [2] OBE (eV)
Pt (111)	-0.46	-1.38	-0.41	-1.04

Note: Site [1] and [2] are FCC and HCP sites, respectively.

Table B.3: Calculated HBEs and OBEs for sub-layer substitution surface model

Model	Site [6] HBE (eV)	Site [6] OBE (eV)	Site [7] HBE (eV)	Site [7] OBE (eV)
Cu-Ti (111)	-0.28	-1.97	-0.29	-2.03
Cu-Co (111)	-0.30	-1.70	-0.32	-1.84
Cu-Ni (111)	-0.25	-1.53	-0.26	-1.65

[#]: Corresponding adsorption site on Figure B.1.

Table B.4: Calculated HBEs and OBEs for metal oxide cluster on Cu(111) surface model

Model	Site 1 HBE (eV)	Site 1 OBE (eV)	Site 2 HBE (eV)	Site 2 OBE (eV)
Ti ₃ O ₆ /Cu (111)	-0.30	-3.52	-0.29	-3.51
Ni ₃ O ₃ /Cu (111)	-0.27	-2.29	N/A	N/A

[#]: Corresponding adsorption site on Figure B.2.

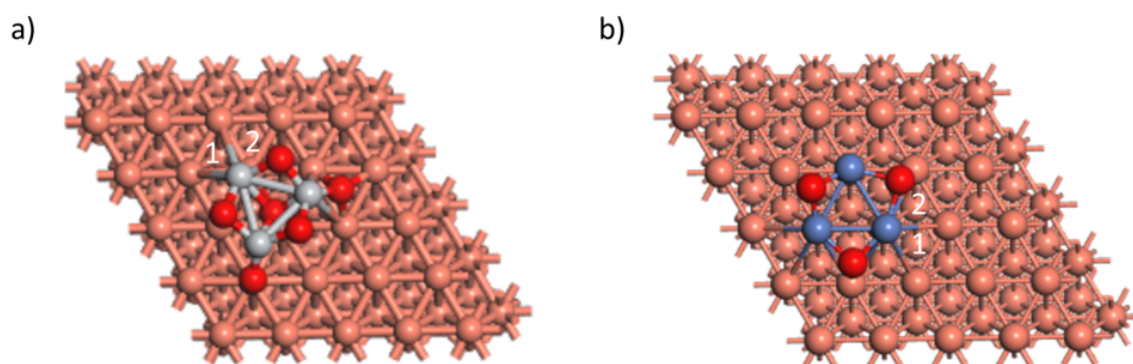


Figure B.2: Metal oxide cluster on Cu(111) surface model: a) $\text{Ti}_3\text{O}_6/\text{Cu}(111)$ surface where Cu, Ti, and O atoms are represented in orange, grey, and red, respectively. b) $\text{Ni}_3\text{O}_3/\text{Cu}(111)$ surface with Cu, Ni, and O atoms represented in orange, blue, and red, respectively. It must be noted that a $\text{CoO}_x/\text{Cu}(111)$ was not examined due to the intensive computational power that was needed.

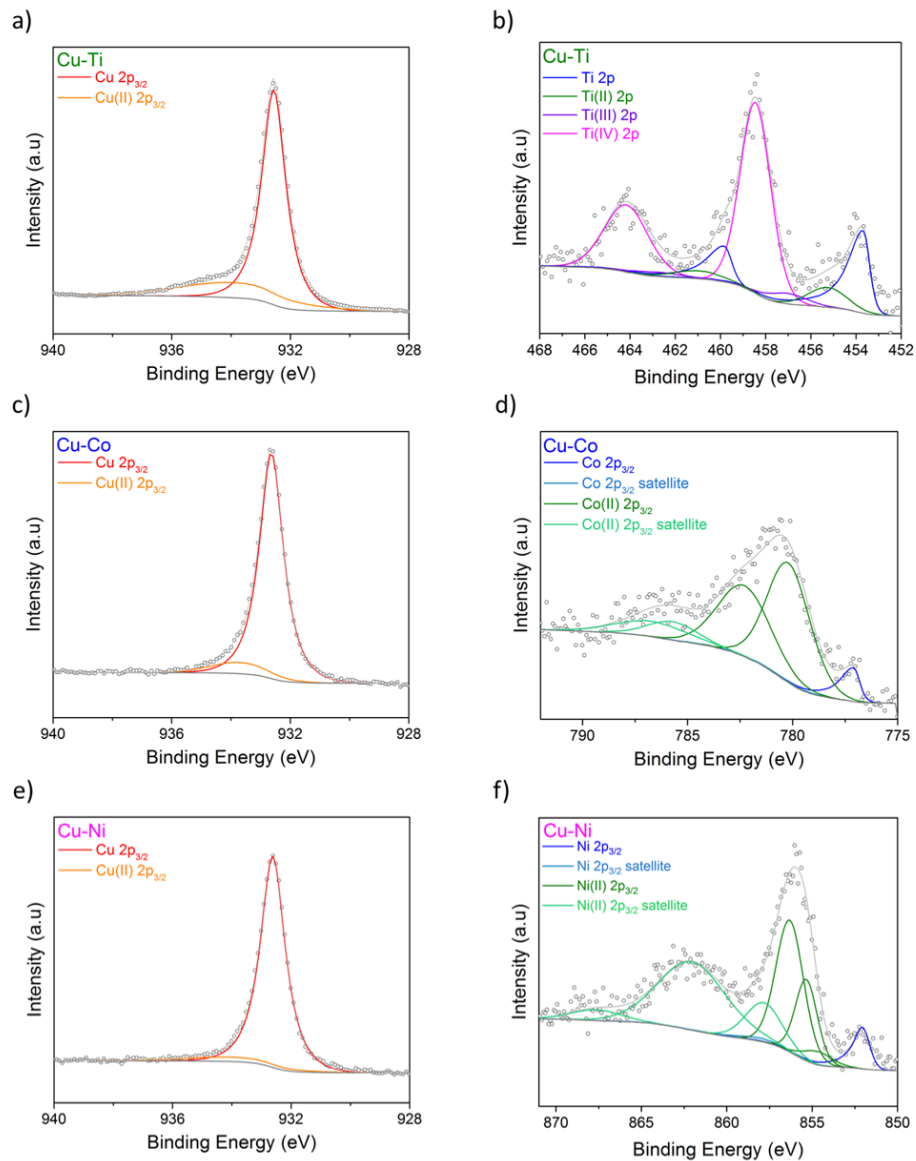


Figure B.3: XPS characterization of as-prepared Cu–M bimetallics. a&b) Cu 2p_{3/2} and Ti 2p spectra of Cu–Ti. c&d) Cu and Co 2p_{3/2} spectra of Cu–Co. e&f) Cu and Ni 2p_{3/2} spectra of Cu–Ni. Partial surface oxidation was observed.

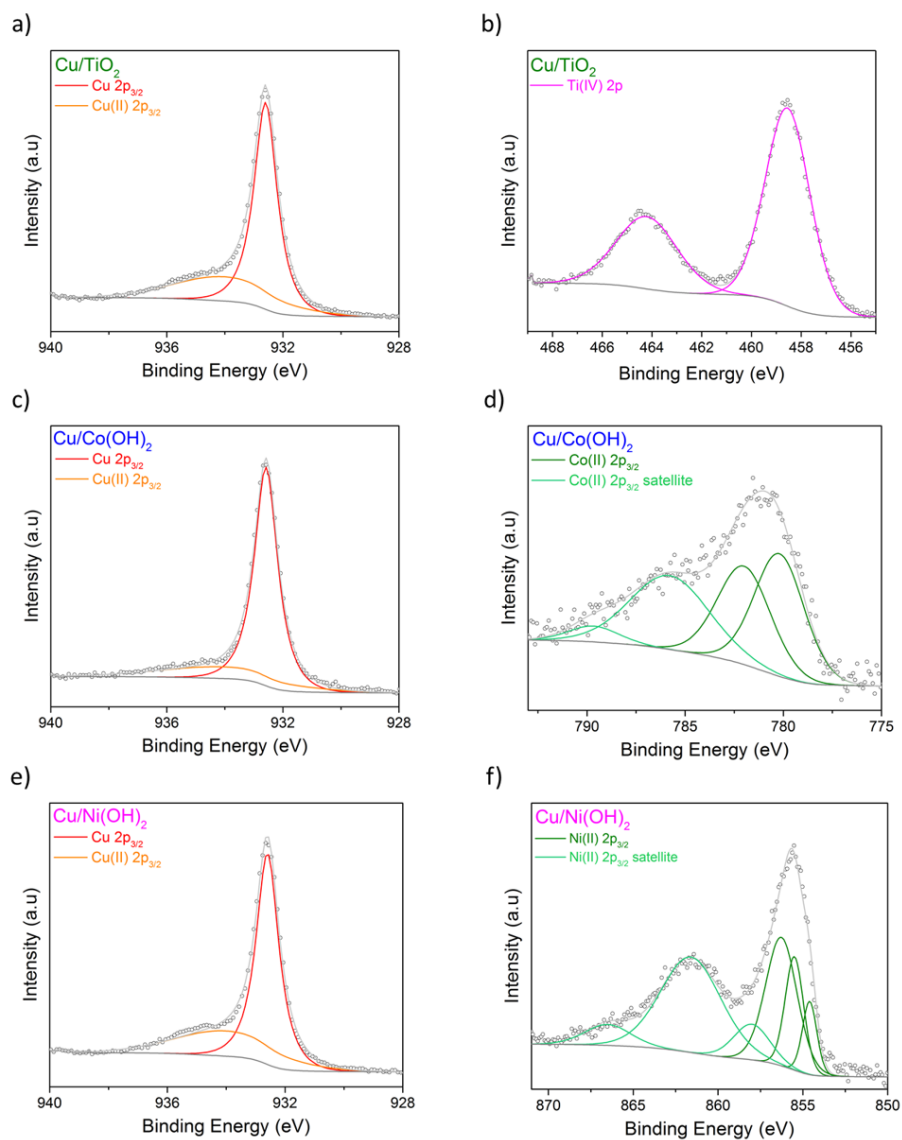


Figure B.4: XPS characterization of as-prepared Cu/MO/OH catalysts. a&b) Cu 2p_{3/2} and Ti 2p spectra of Cu–Ti. c&d) Cu and Co 2p_{3/2} spectra of Cu–Co. e&f) Cu and Ni 2p_{3/2} spectra of Cu–Ni. Partial surface oxidation was observed.

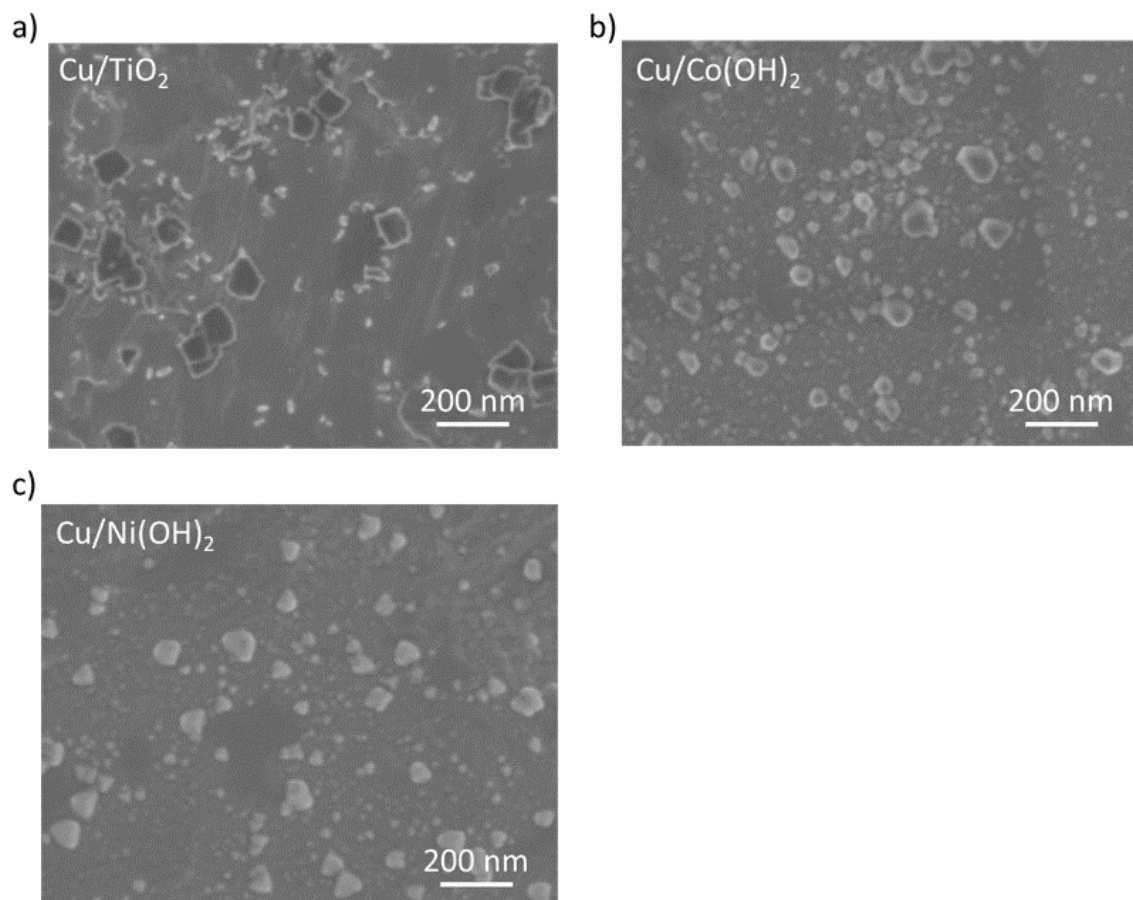


Figure B.5: SEM images of a) Cu/TiO₂, b) Cu/Co(OH)₂, and c) Cu/Ni(OH)₂.

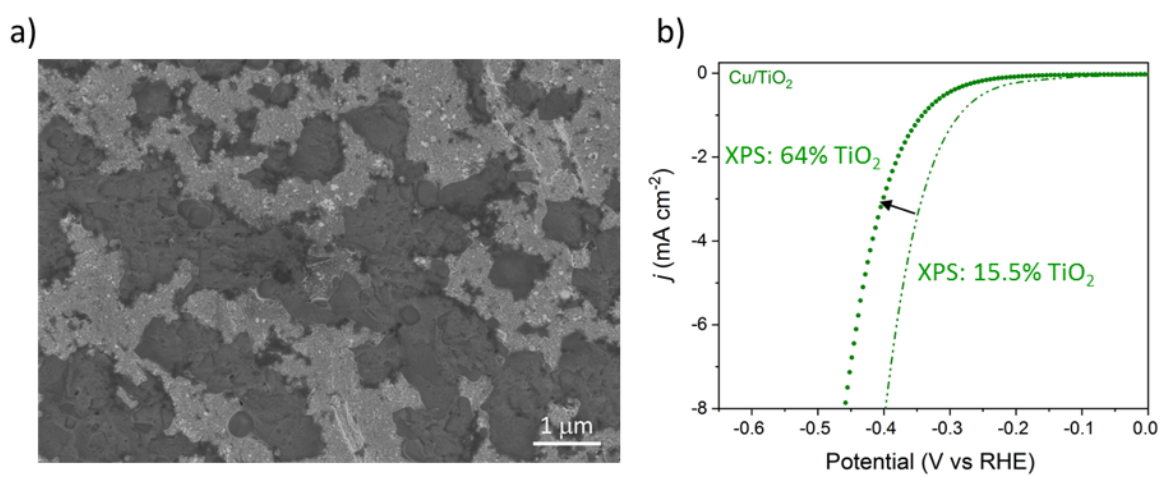


Figure B.6: a) SEM imaging of Cu with higher loading of TiO₂. b) Electrocatalytic performance of Cu with higher loadings of TiO₂.

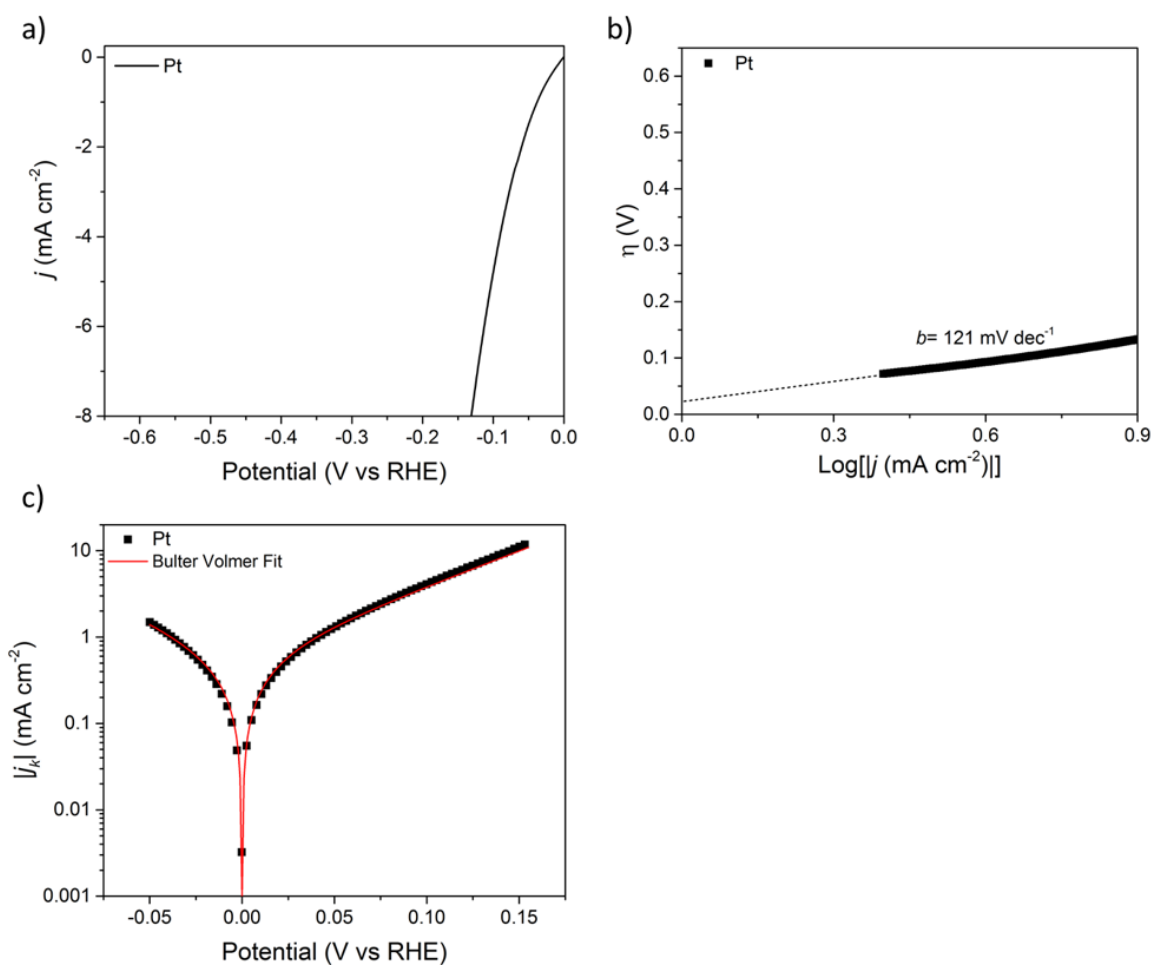


Figure B.7: Electrochemical characterization of Pt. HER activity of bulk Pt in H₂-saturated 0.1 M KOH after iR-correction, determined with a sweep rate of 10 mV s⁻¹ and a rotation rate of 1800 rpm at room temperature. b) Corresponding Tafel plot with a Tafel slope of 121 mV dec⁻¹. c) HER/HOR kinetic currents on bulk Pt surface and corresponding Butler-Volmer fit ($\alpha_a = 0.48$). The kinetic currents were corrected for iR loss, and the HOR branch was corrected for H₂ mass transport limitation. The exchange current was determined to be 610 $\mu\text{A cm}^{-2}$ as consistent with similar reported values.

Appendix C

SUPPLEMENTARY INFORMATION FOR CHAPTER 4: CARBON DIOXIDE SPLITTING USING AN ELECTRO-THERMOCHEMICAL HYBRID LOOPING STRATEGY

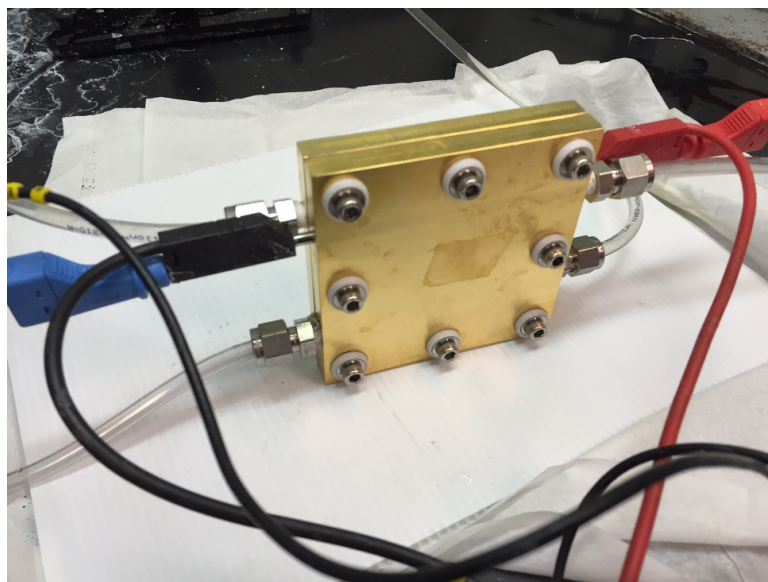


Figure C.1: Photograph of the CO₂ electrolyzer.

Table C.1: Long-duration test results of CO catalytic bed reactor (tests of two hours or longer)

Trial	Duration (min)	Catalyst mass (g)	Unloaded mass (g)	Inlet gas composition	Carbon mass (g)	Carbon to Catalyst (g/g)
1	121	5.0114	17.9931	95% CO ₂ , 5% H ₂ , 0% CO ₂	12.9817	2.59
2	180	5.6282	22.1732	95% CO ₂ , 5% H ₂ , 0% CO ₂	16.545	2.94
3	240	5.6575	31.2667	95% CO ₂ , 5% H ₂ , 0% CO ₂	25.6092	4.53
4	180	3.9954	22.794	95% CO ₂ , 5% H ₂ , 0% CO ₂	18.7986	4.71
5	155	4.8308	21.0664	95% CO ₂ , 5% H ₂ , 0% CO ₂	16.2356	3.36
6	128	5.0968	15.7039	80% CO ₂ , 20% H ₂ , 0% CO ₂	10.6071	2.08
7	157	4.922	18.2912	60% CO ₂ , 20% H ₂ , 20% CO ₂	13.3692	2.72

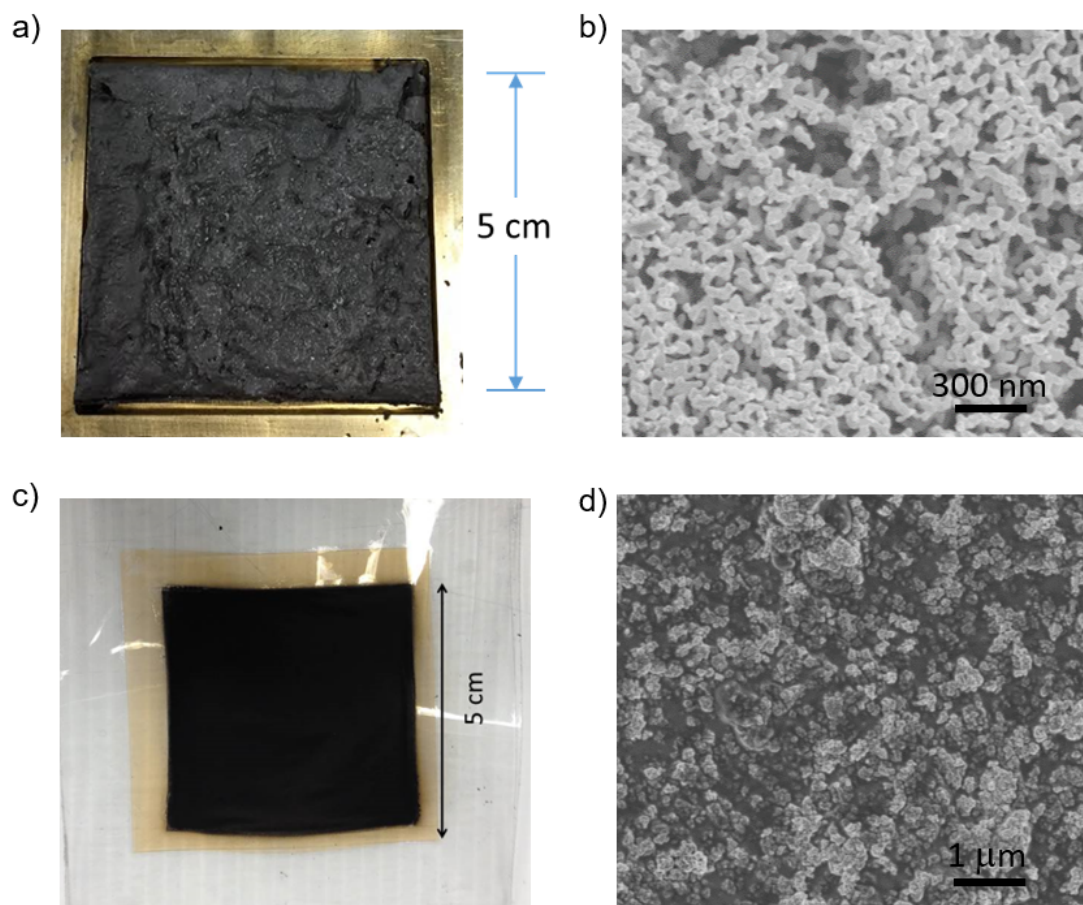


Figure C.2: CO₂ electrolyzer electrodes. a) Photograph and b) SEM images of the as-synthesized np-Ag catalyst. c) Photograph and d) SEM images of the Ir-CCM.

a)



b)

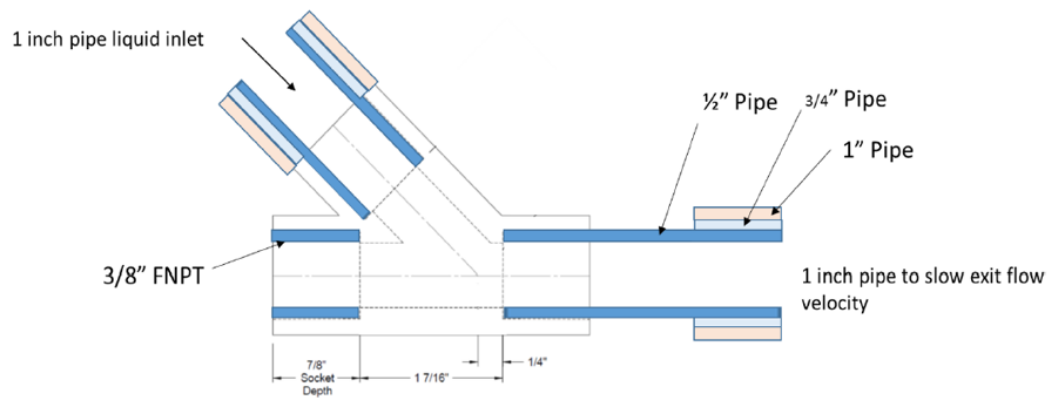


Figure C.3: a) Photograph and b) schematic of the in-line CO₂ contactor.

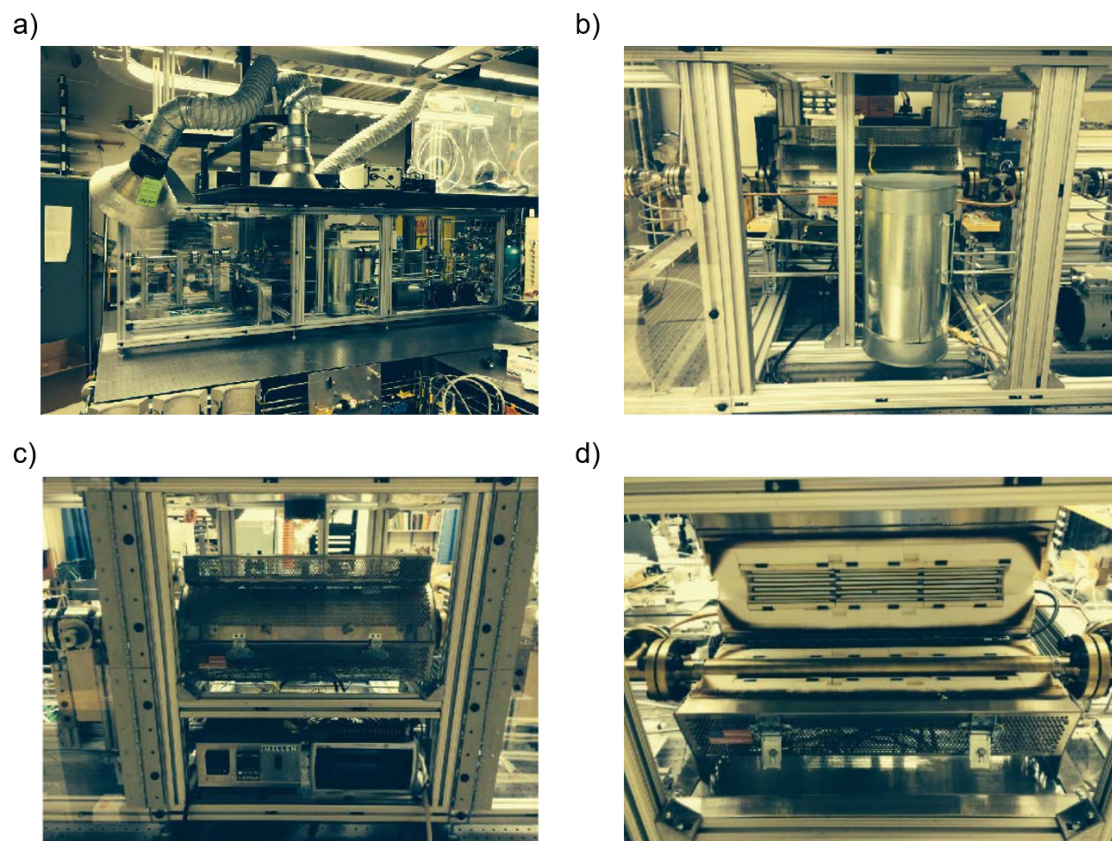


Figure C.4: CO catalytic bed reactor: Photographs of the a) rear view of the reactor assembly, b) recuperative heat exchanger, c) furnace and data acquisition system, and d) furnace opened with the view of the reactor chamber.

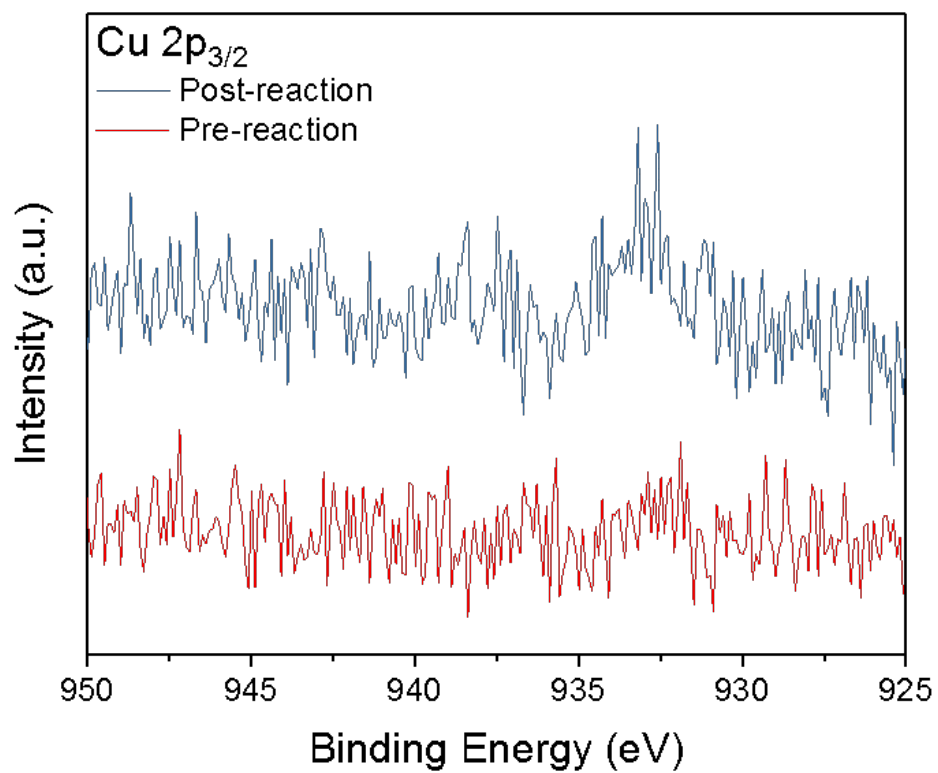


Figure C.5: Pre and post reaction XPS analysis of np–Ag catalyst.

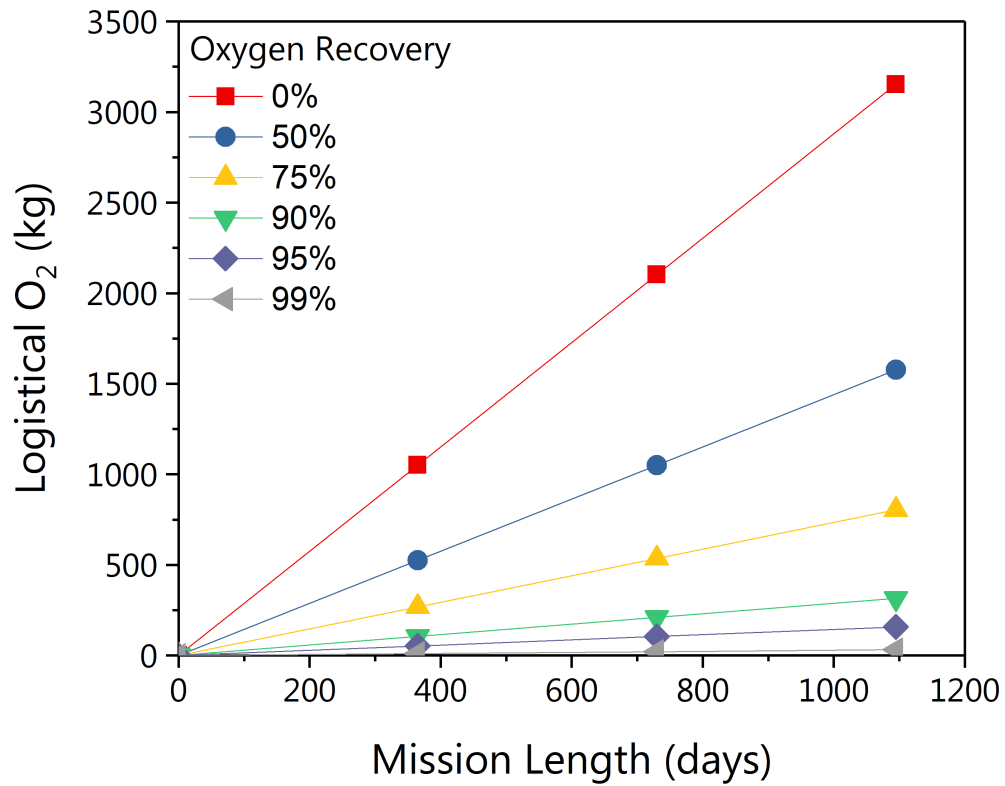


Figure C.6: Calculation of required O_2 needed to support a space crew of 4 individuals for 3 years based on 720 g of consumed O_2 per individual per day.

Oxygen Recovery Calculations:

If 90% O₂ recovery can be achieved, ~315 kg of logistical O₂ is needed to be brought on the spacecraft which is a significant reduction compared to the scenario if no oxygen recovery was implemented, ~3154 kg of O₂. If 99% O₂ recovery can be achieved, further reduction of logistical O₂ can be achieved as shown in Figure C.6.

Active area needed for CO₂ electrolyzer for one individual:

CO₂ metabolic production rate, ~990 g of CO₂ per day (1 individual)

CO₂ recycle rate from CO reactor, ~990 g of CO₂ per day

Total CO₂ processing rate for CO₂ electrolyzer, ~1980 g of CO₂ per day

CO₂ electrolyzer performance at 3.0V, 44 mA cm⁻², 92% CO Faradaic efficiency

Active area needed, ~2483 cm²

If 25 cm² cell is used, ~100 cells are needed

Total weight of catalyst needed for CO catalytic bed reactor to process ~3154 kg of O₂:

The stoichiometric molar ratio of C to O₂, 1

Deposited carbon to catalyst weight ratio, 4

Catalyst needed, ~300 kg of catalyst

The total weight of catalyst needed is less than 10% of the total weight of O₂ needed to support the space crew if no oxygen recovery system was implemented.

Appendix D

SUPPLEMENTARY INFORMATION FOR CHAPTER 5: TWO-DIMENSIONAL COPPER NANOSHEETS FOR ELECTROCHEMICAL REDUCTION OF CARBON MONOXIDE TO ACETATE

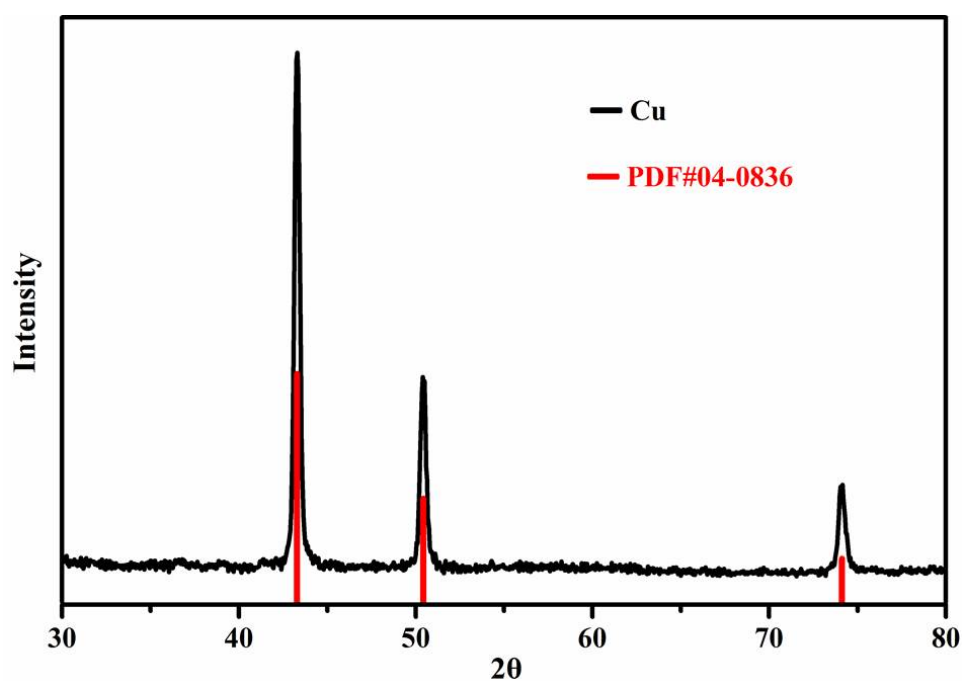


Figure D.1: XRD pattern of randomly deposited Cu nanosheets, revealing the *fcc* structure of Cu nanosheets. The three major peaks represent (111), (200), and (220), respectively.

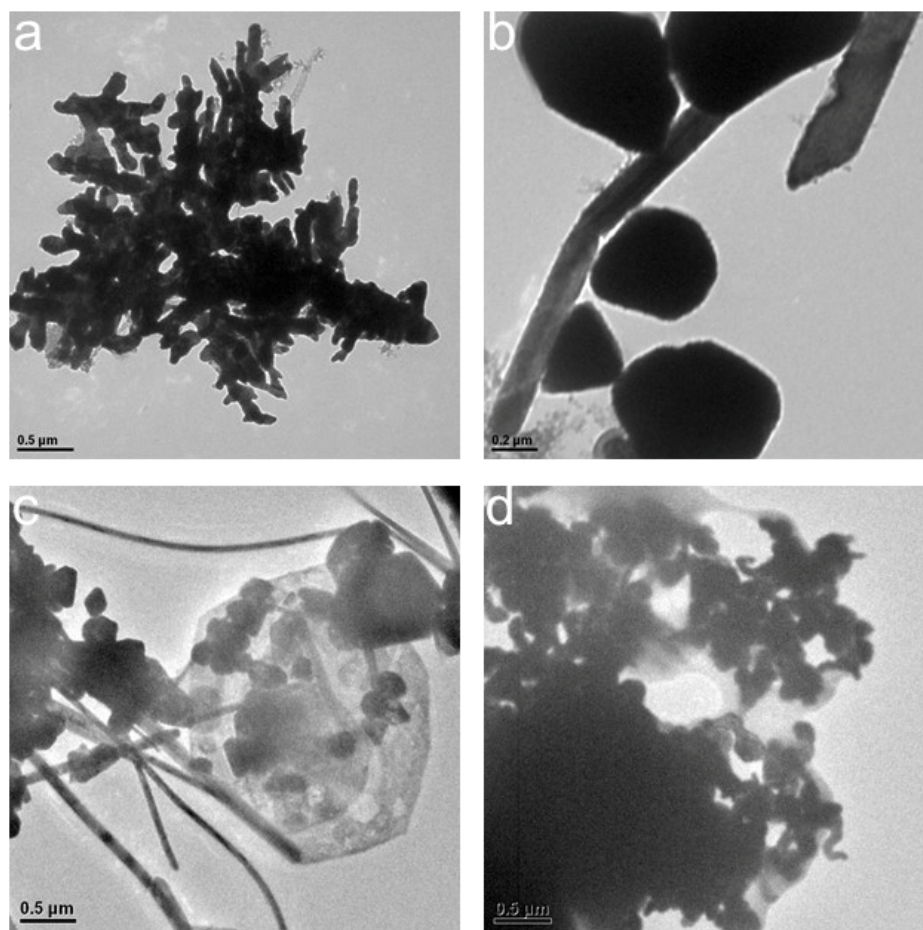


Figure D.2: Control experiments for Cu nanosheets synthesis: a) CTAB is replaced by mg sodium perfluorooctanoate, b) $\text{Cu}(\text{NO}_3)_2$ is replaced by CuCl_2 , c) CTAB is replaced by 2-Methylimidazole, d) hexamethylenetetramine is replaced by butylamine.

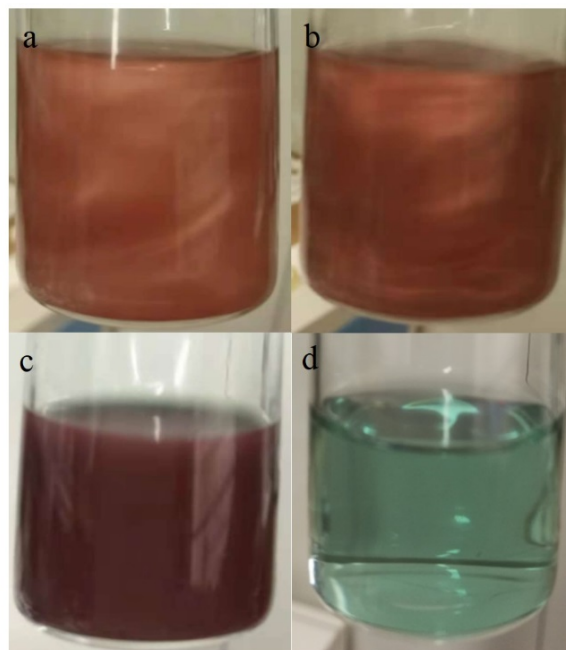


Figure D.3: Stability of as-synthesized Cu nanosheets. Photograph of a) as-synthesized Cu nanosheets and b) Cu nanosheets that are exposed to air for 60 days; c) as-synthesized Cu nanoparticles and d) Cu nanoparticles shown in c) were oxidized in air within one hour.

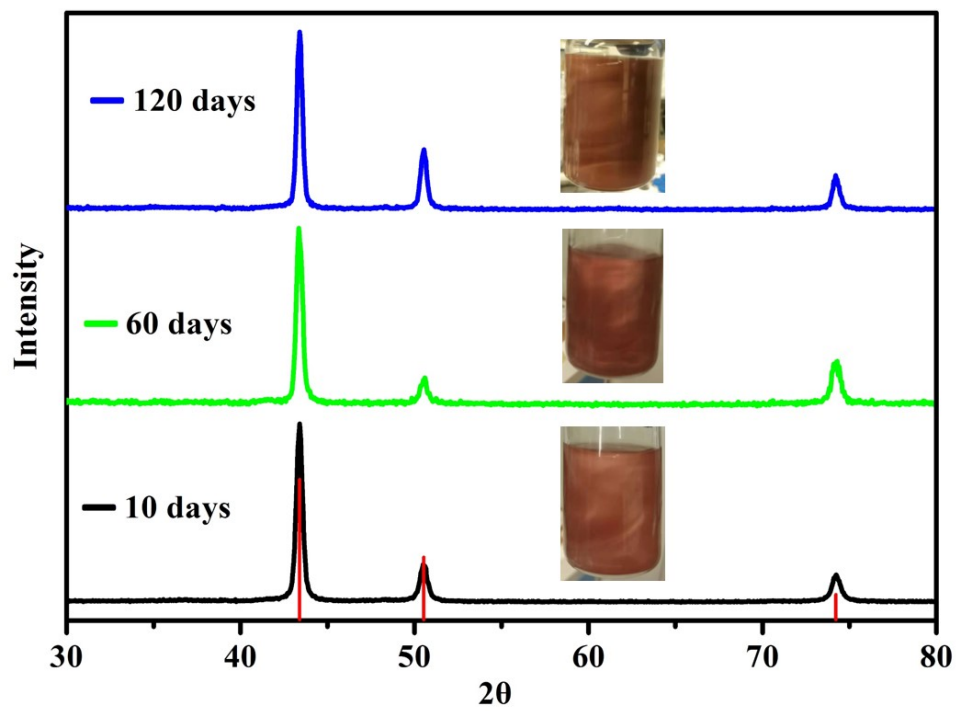


Figure D.4: XRD patterns of the Cu nanosheets after exposed in air at room temperature for 10 to 120 days, indicating that no substantial oxidation was observed.

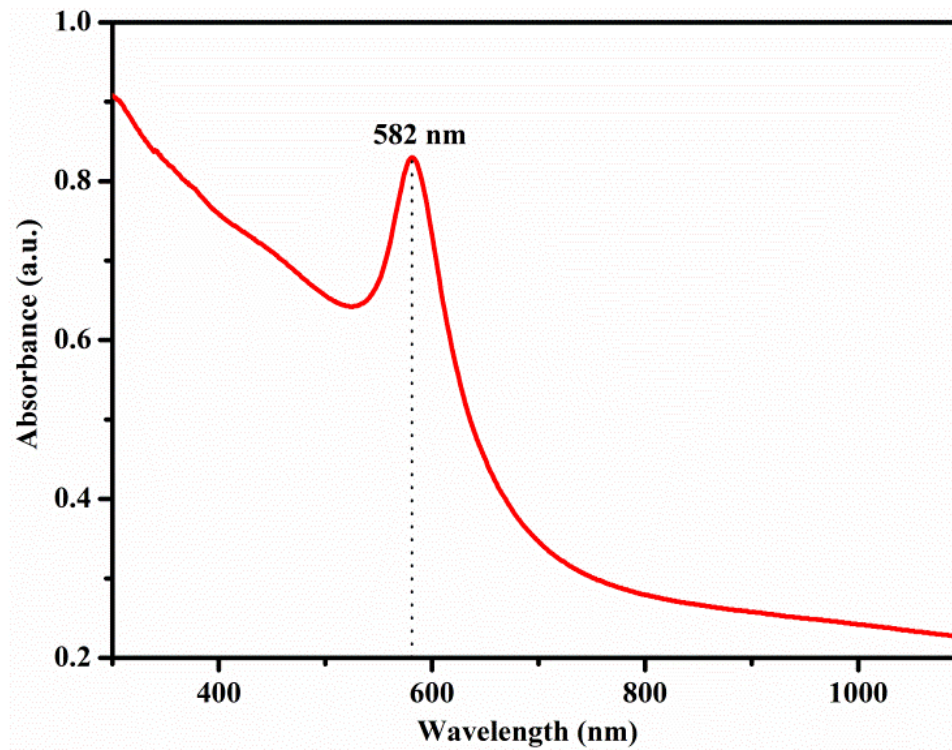


Figure D.5: UV-vis absorption spectrum of the dispersion of Cu nanosheets in ethanol.

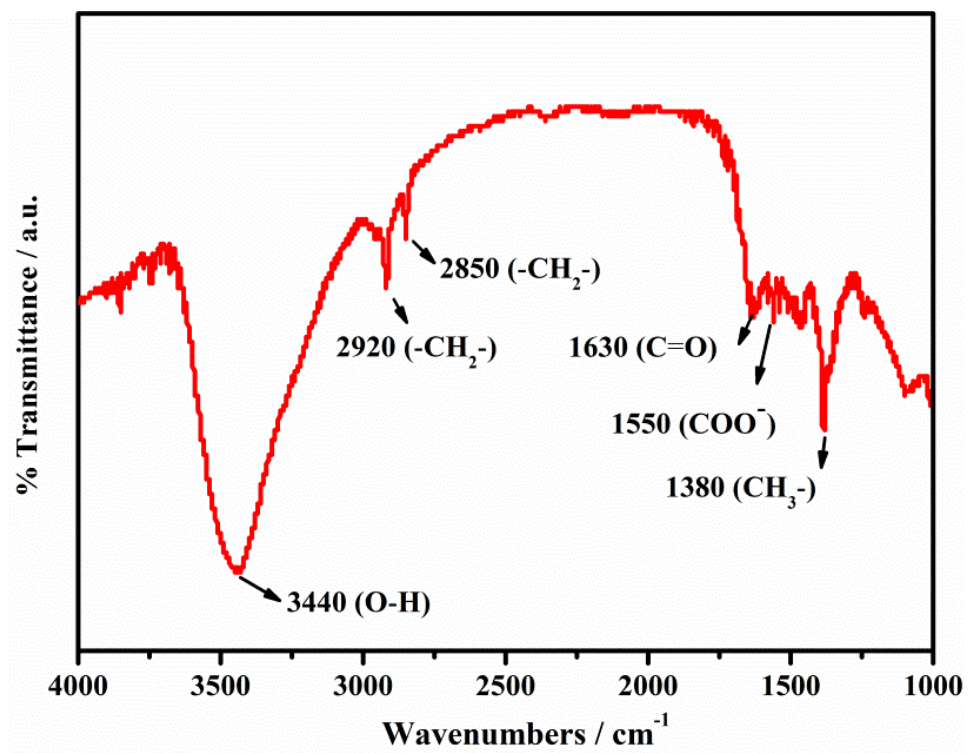


Figure D.6: DRIFT spectra of the Cu nanosheets.

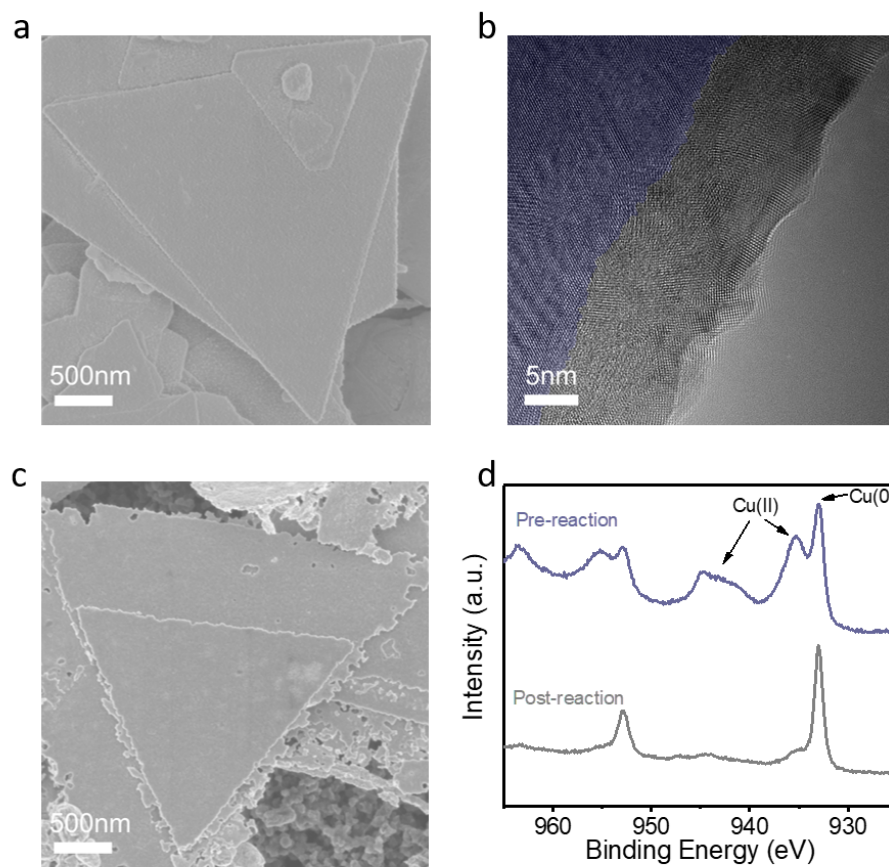


Figure D.7: Oxidation-tolerance of Cu nanosheets {111} facets. a) SEM image and b) TEM image of Cu nanosheets before CO reduction reaction, the blue shadow in (b) represents the Cu(111) single crystal domain; c) SEM image of Cu nanosheets after CO reduction showing corroded edges; d) XPS spectra of Cu nanosheets pre- and post- CO reduction experiment.

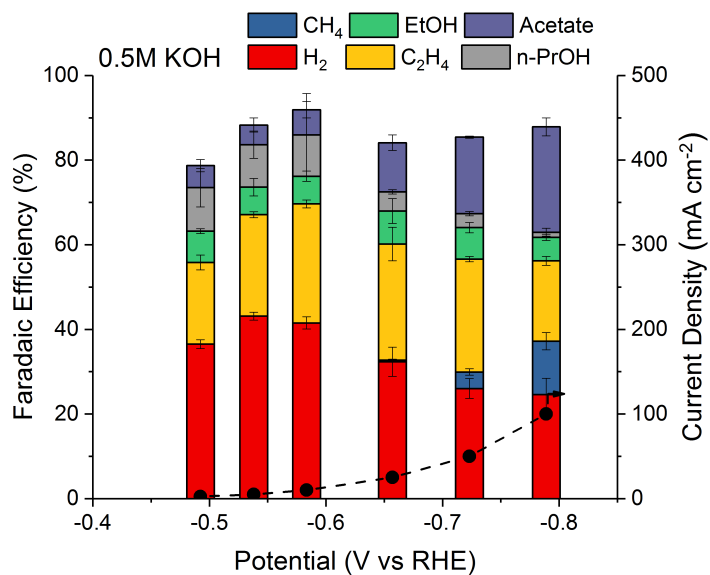


Figure D.8: CO reduction performance for Cu nanosheets in 0.5 M KOH. Error bars represent the standard deviation from at least three independent measurements.

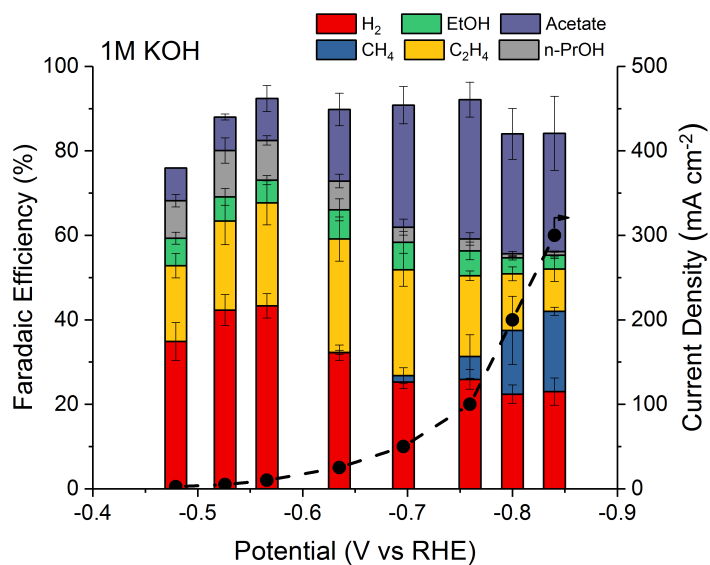


Figure D.9: CO reduction performance for Cu nanosheets in 1.0 M KOH. Error bars represent the standard deviation from at least three independent measurements.



Figure D.10: Photograph of *operando* XAS flow-cell electrolyzer.

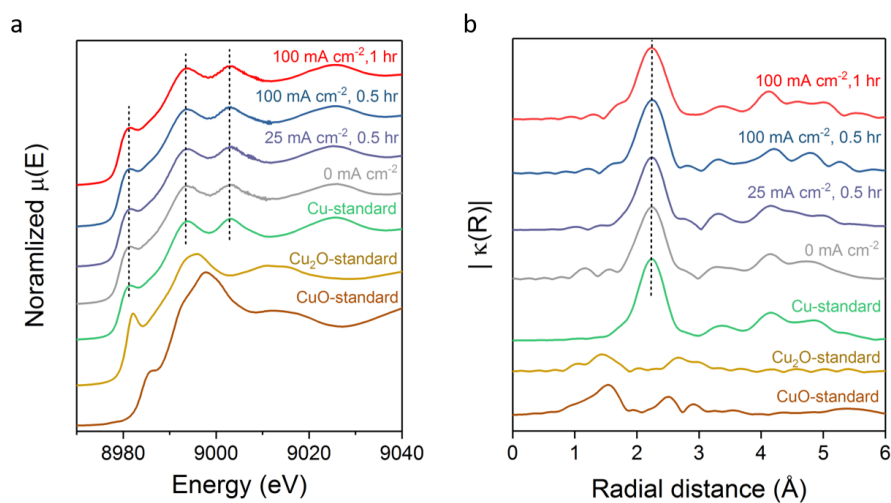


Figure D.11: *Operando* XAS measurements. a) XANES and b) EXAFS spectrums of Cu nanosheets during CO electrolysis and Cu standards.

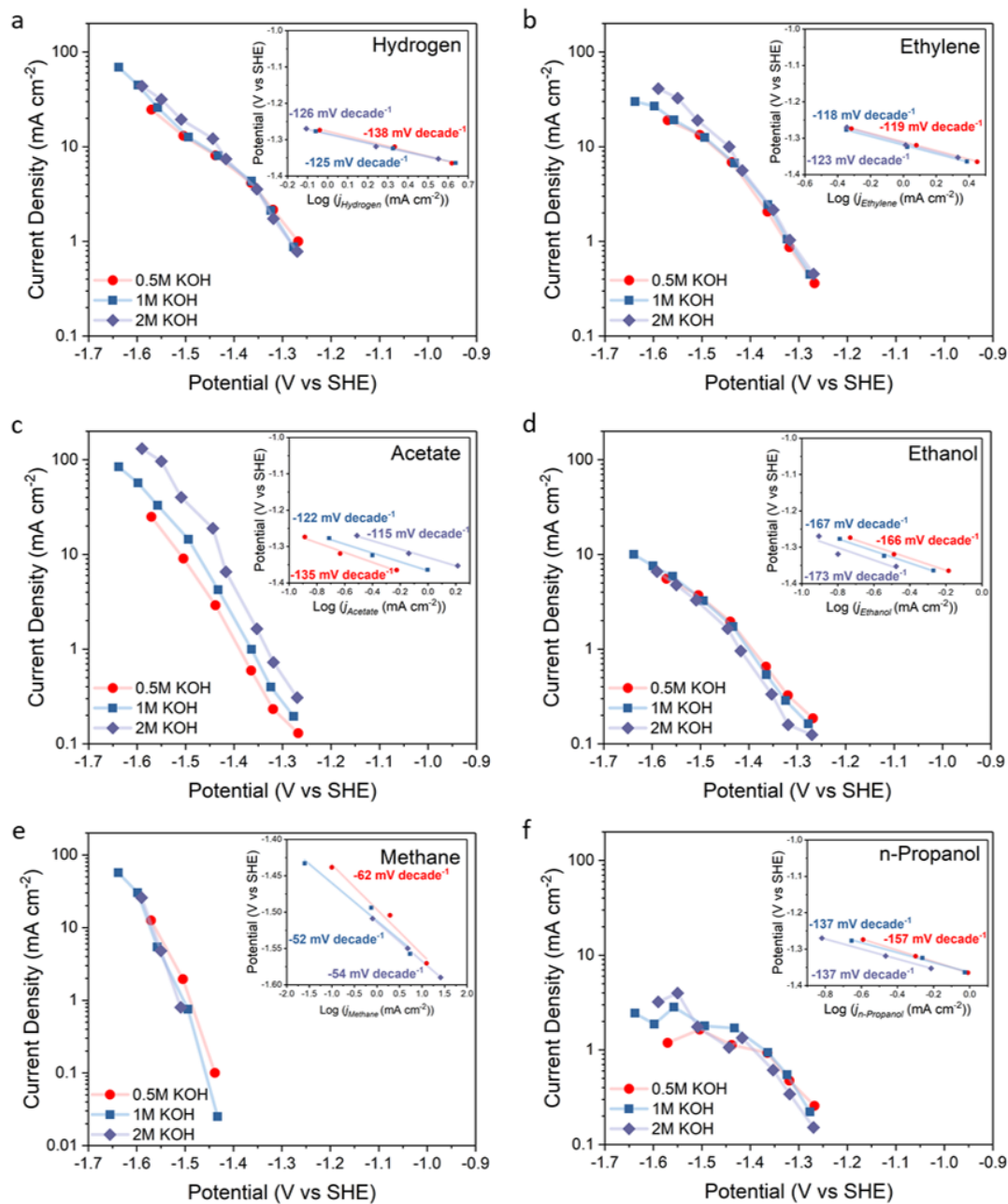


Figure D.12: Partial current densities plotted versus the absolute potential and inset) Tafel analysis of the three lowest partial current densities.

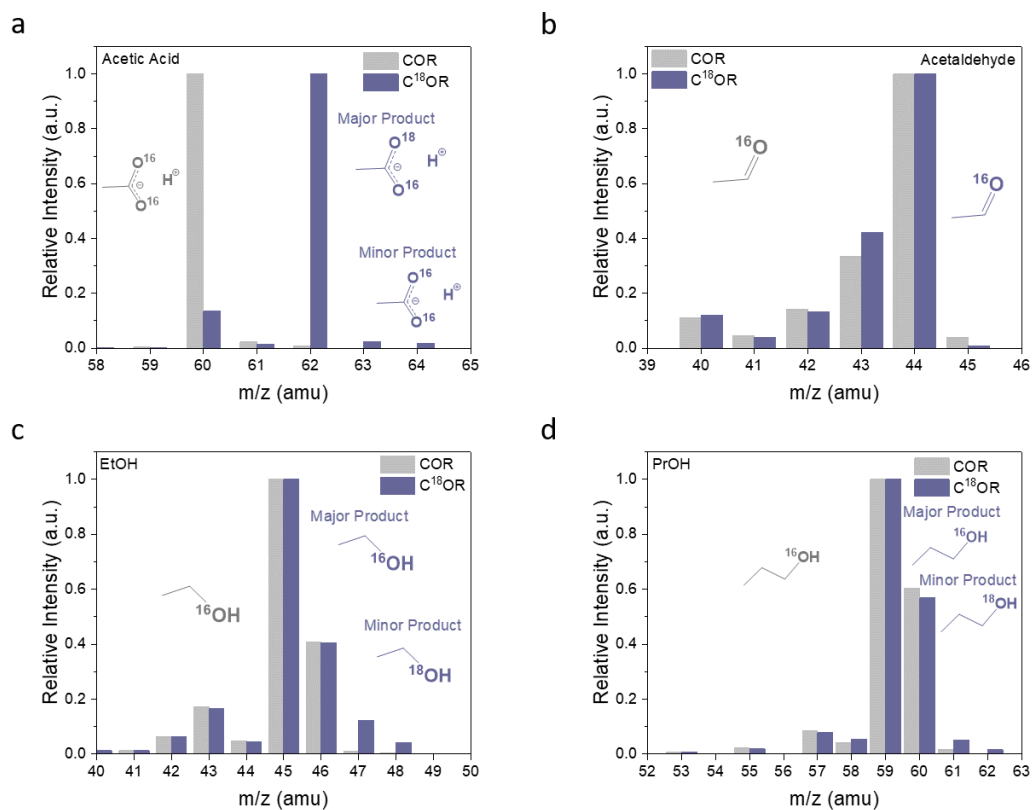


Figure D.13: GC-MS analysis. Mass spectrum of a) acetic acid, b) acetaldehyde, c) ethanol, and d) n-propanol products from unlabeled CO and labeled C¹⁸O reduction.

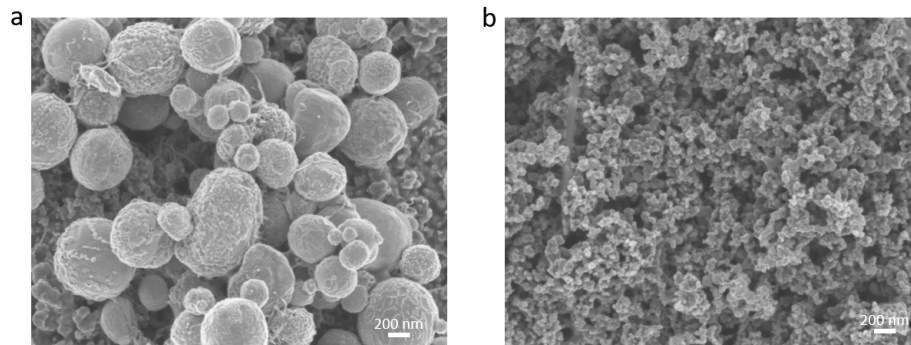


Figure D.14: Catalyst structural characterization. SEM image of a) 1 μm and b) 25 nm Cu particles deposited on GDL.

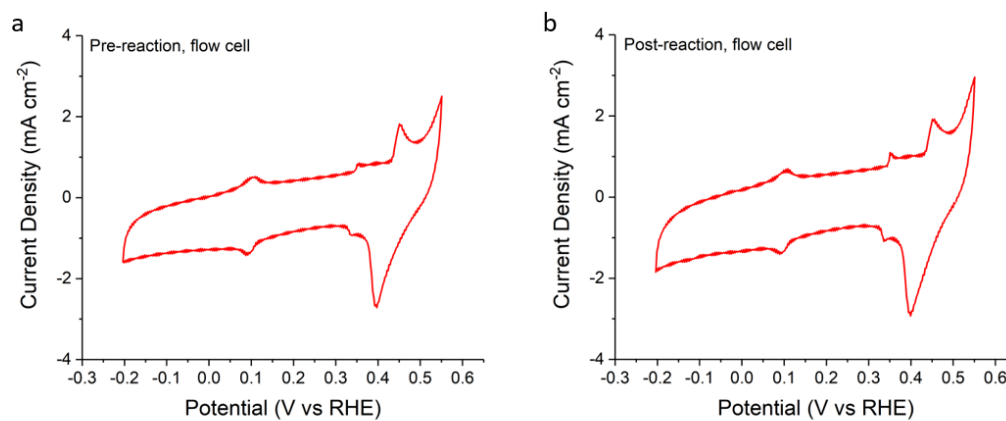


Figure D.15: *In-situ* OH_{ads} studies. a) Pre-reaction and b) post-reaction OH_{ads} cyclic voltammetry of Cu nanosheets in 1 M KOH in flow-cell electrolyzer.

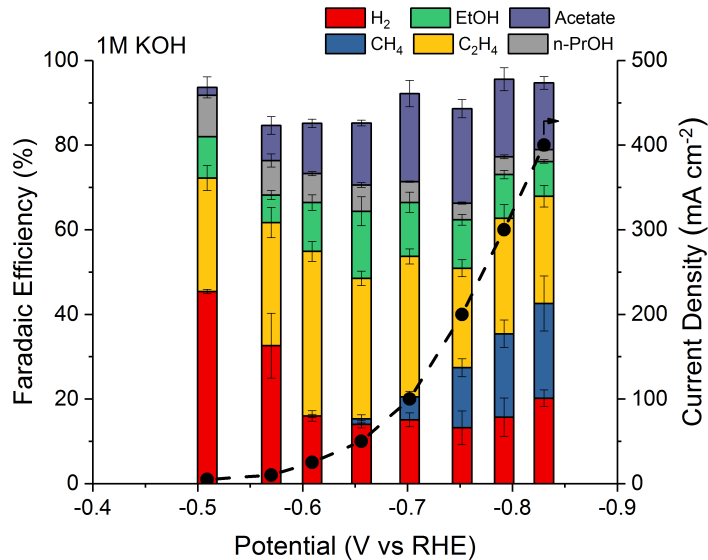


Figure D.16: CO reduction performance for 1 μm Cu particles in 1 M KOH. Error bars represent the standard deviation from at least three independent measurements.

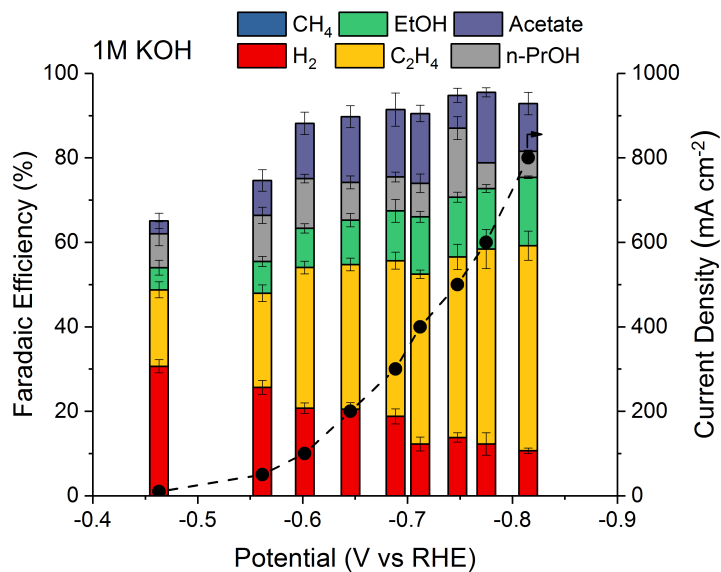
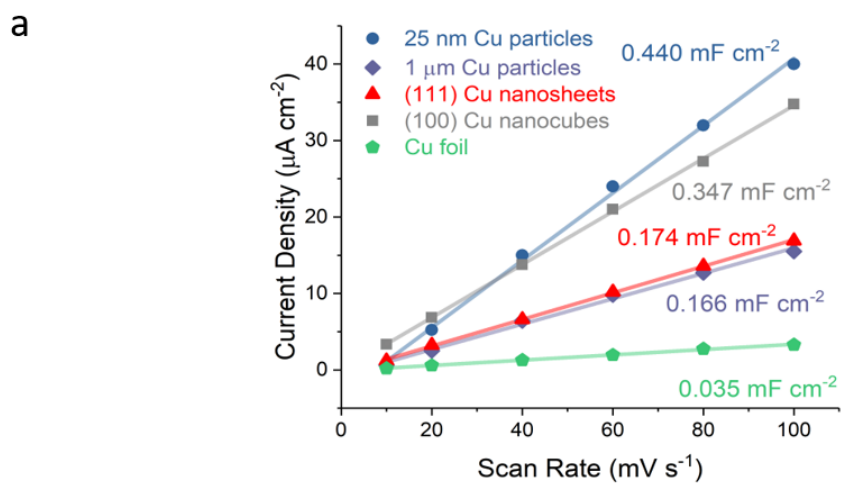


Figure D.17: CO reduction performance for 25 nm Cu particles in 1 M KOH. Error bars represent the standard deviation from at least three independent measurements.



b

Sample	C _{double layer} (µF cm ⁻²)	Roughness Factor Normalized
Cu foil	35	1
(100) Cu nanocubes	347	9.9
(111) Cu nanosheets	174	5
1 µm Cu particles	166	4.7
25 nm Cu particles	440	12.6

Figure D.18: ECSA characterization. a) ECSA measurements of Cu catalysts conducted in Ar-purged 0.1 M HClO₄ in H-cell and b) measured specific double layer capacitance for copper samples and corresponding roughness factors.

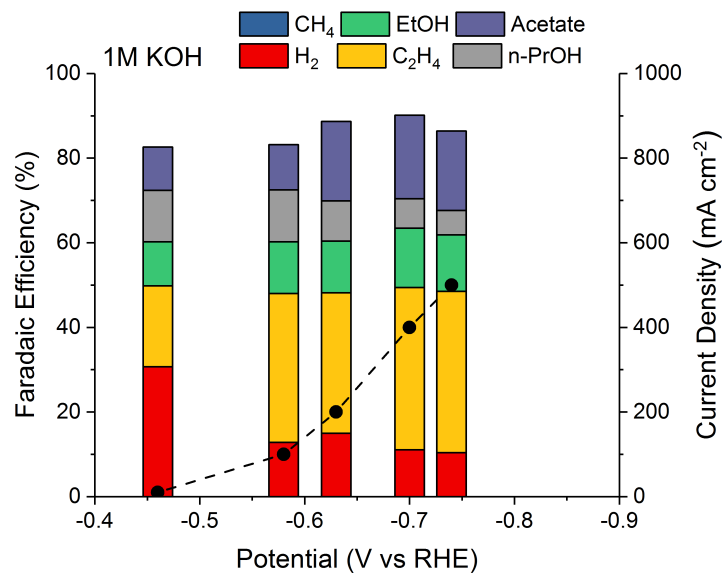


Figure D.19: CO reduction performance for ascorbic acid treated 25 nm Cu particles in 1 M KOH.

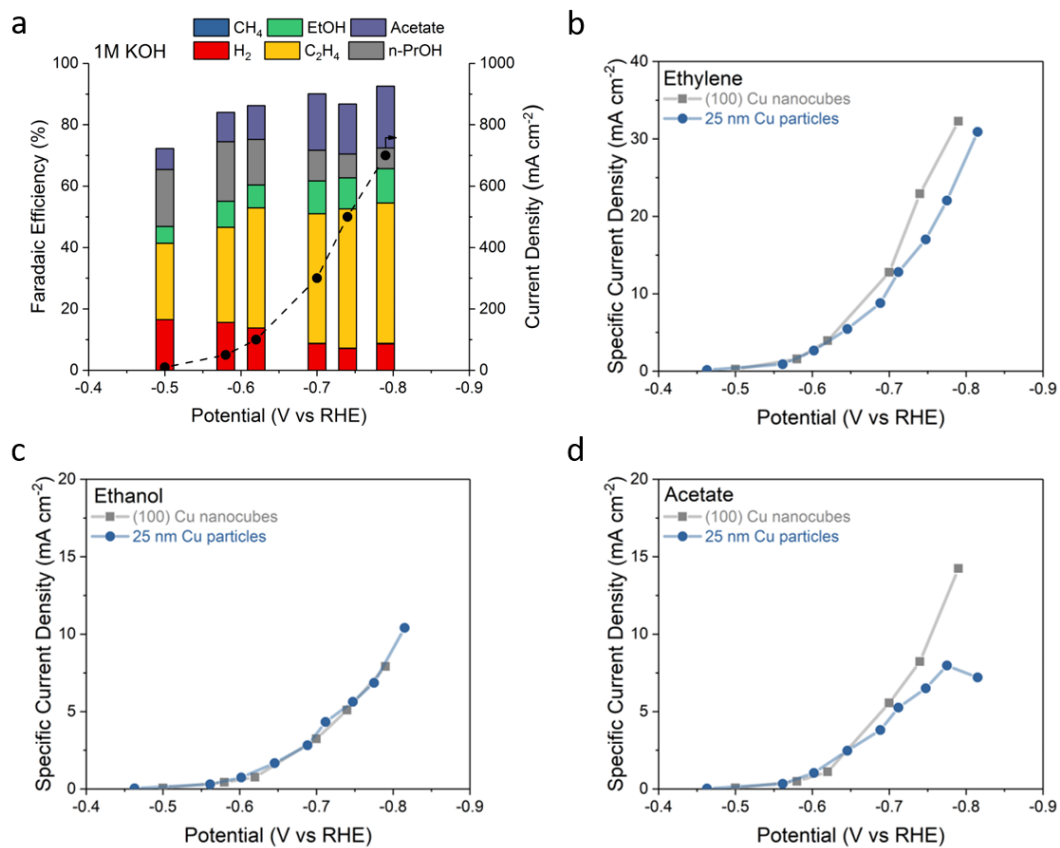


Figure D.20: CO reduction performance of Cu nanocubes. a) CO reduction performance for (100) Cu nanocubes in 1 M KOH. b-d) ECSA corrected ethylene, ethanol, and acetate partial current densities, respectively of (100) Cu nanocubes in comparison to 25 nm Cu particles.

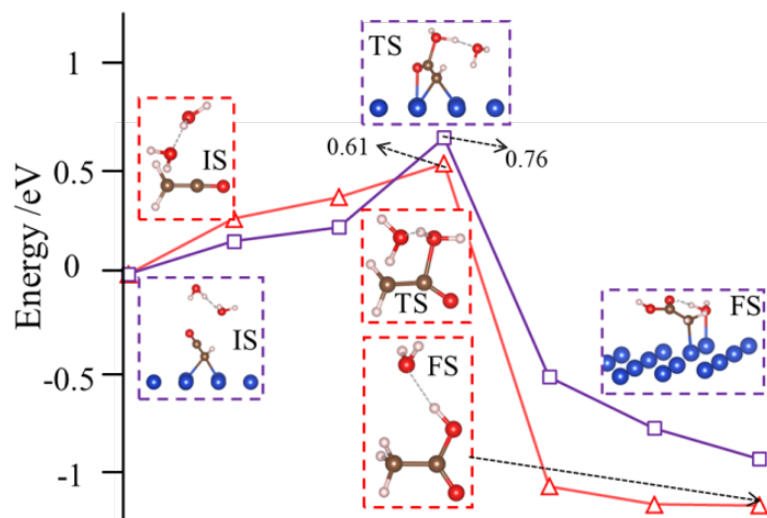


Figure D.21: Energy and structure evolution for water incorporation into ketene and $^*CH-CO$. IS: initial state; TS: transition state; FS: final state. Note that the ketene is adsorbed very weakly on Cu(111) (with a binding energy of 0.06 eV), therefore we do not consider Cu surface in its calculation. For $^*CH-CO$, only the top Cu layer is shown for clarity.

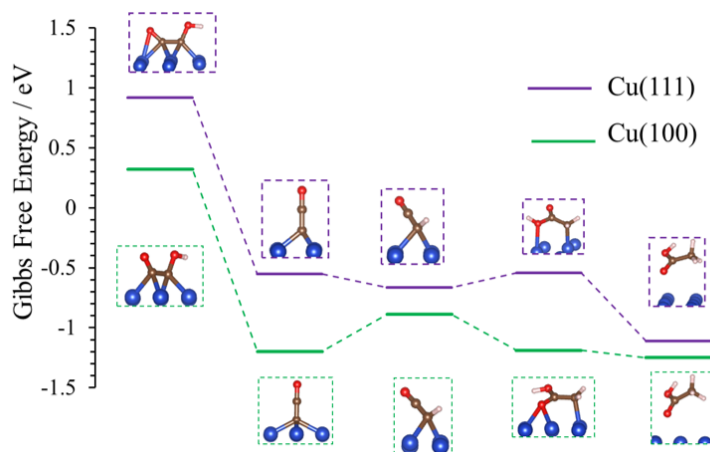


Figure D.22: CO reduction reaction free energy profiles (starting from $^*CO-COH$ intermediate) at different U: a) 0 V (vs RHE), calculated using computational hydrogen electrode model. The purple and green lines show the reaction paths for the formation of acetate on Cu(111) and (100) surface, respectively. Blue: Cu, Red: O, Brown: C, Pink: H.

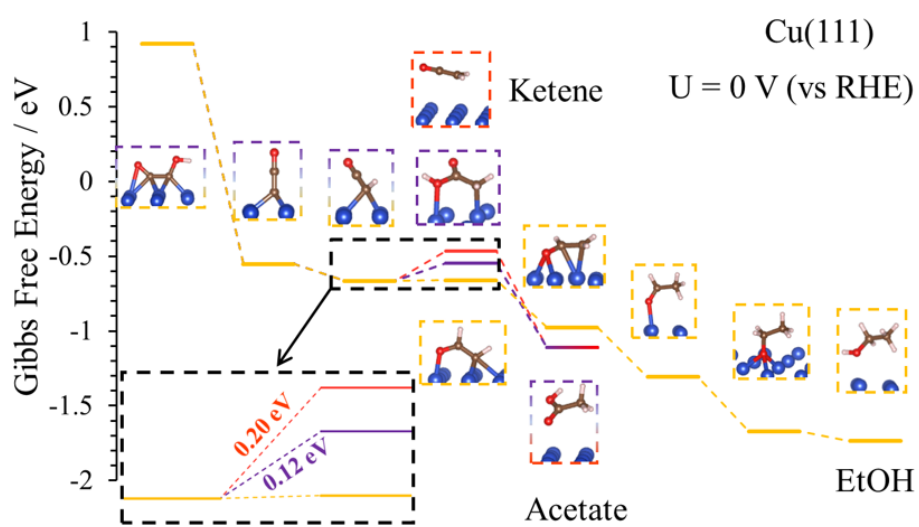


Figure D.23: CO reduction reaction free energy profiles for acetate formation from ketene intermediate and ethanol formation on Cu(111). Blue: Cu, Red: O, Brown: C, Pink: H.

Appendix E

SUPPLEMENTARY INFORMATION FOR CHAPTER 6: THE INFLUENCE OF SULFUR DIOXIDE IMPURITY ON CARBON DIOXIDE ELECTROLYSIS

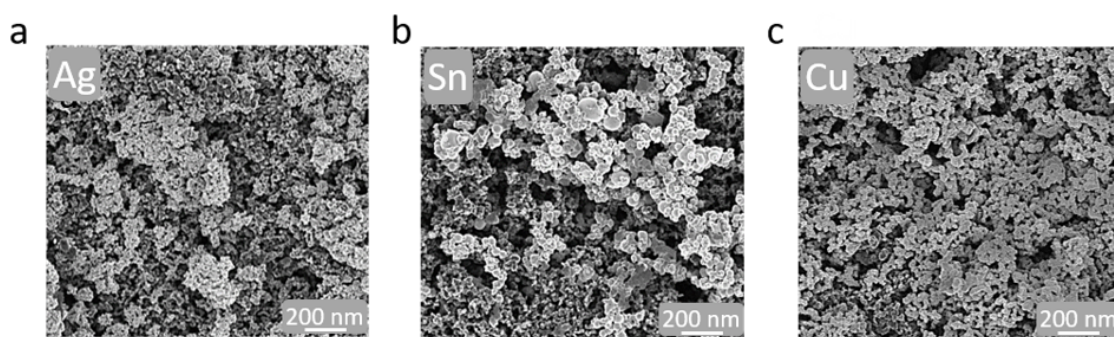


Figure E.1: SEM images of as-prepared a) Ag, b) Sn, and c) Cu electrodes.

Table E.1: Surface atomic concentrations of metal sulfides in Ag, Sn, and Cu samples obtained from XPS

Sample time (hr)	Ag ₂ S (%)	SnS ₂ (%)	Cu ₂ S (%)
0	0	0	0
1	35.6	3.3	12.0
3	8.4	0	-
5	-	-	3.6

Note that atomic concentrations have been calculated based on concentrations of metals and S in S²⁻ peaks

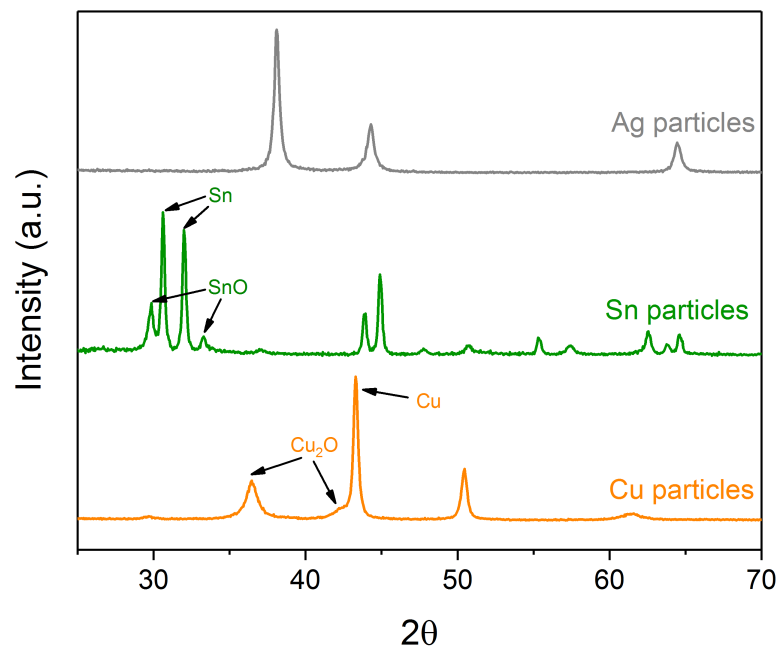


Figure E.2: PXR D pattern of commercial Ag, Sn, and Cu particles.

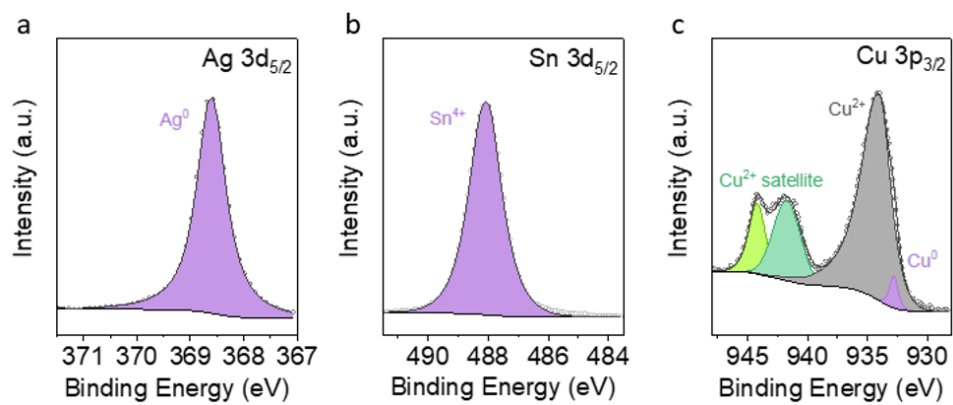


Figure E.3: XPS spectrum of as-prepared a) Ag, b) Sn, and c) Cu electrodes.

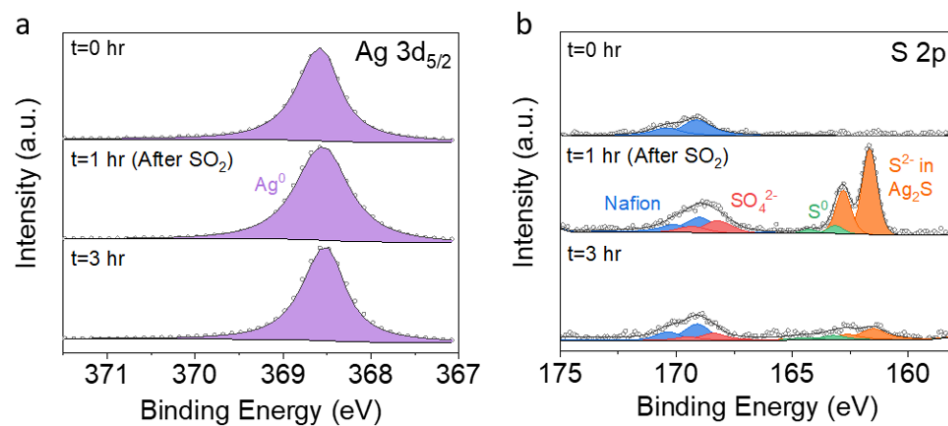


Figure E.4: XPS spectrum of a) Ag and b) S region at various time points of CO₂ + 1% SO₂ experiment.

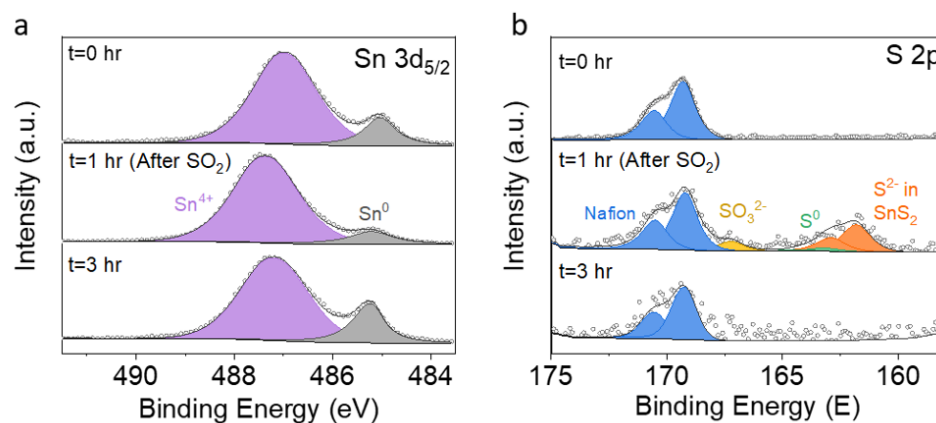


Figure E.5: XPS spectrum of a) Sn and b) S region at various time points of CO₂ + 1% SO₂ experiment.

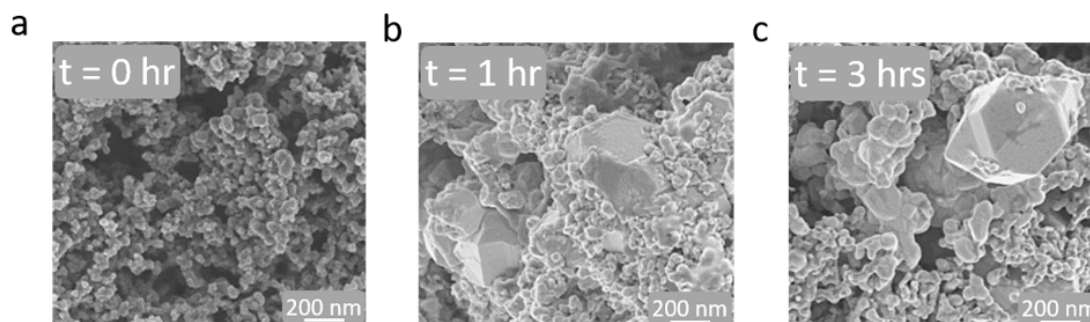


Figure E.6: SEM images of Ag catalysts at various time points of $\text{CO}_2 + 1\% \text{SO}_2$ experiment.

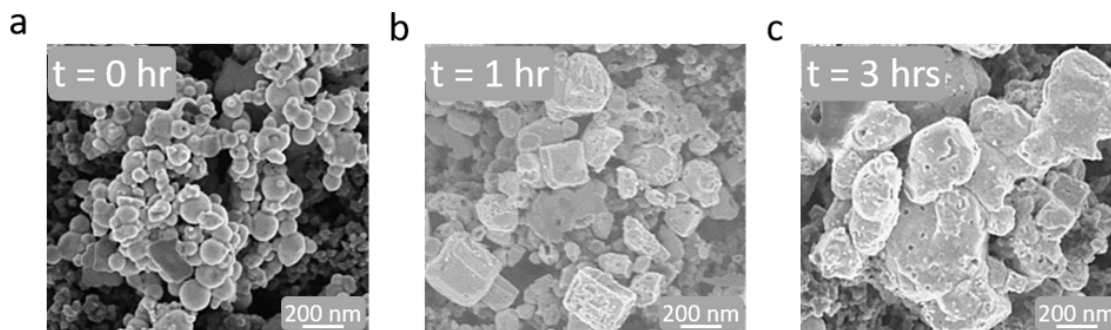


Figure E.7: SEM images of Sn catalysts at various time points of $\text{CO}_2 + 1\% \text{SO}_2$ experiment.

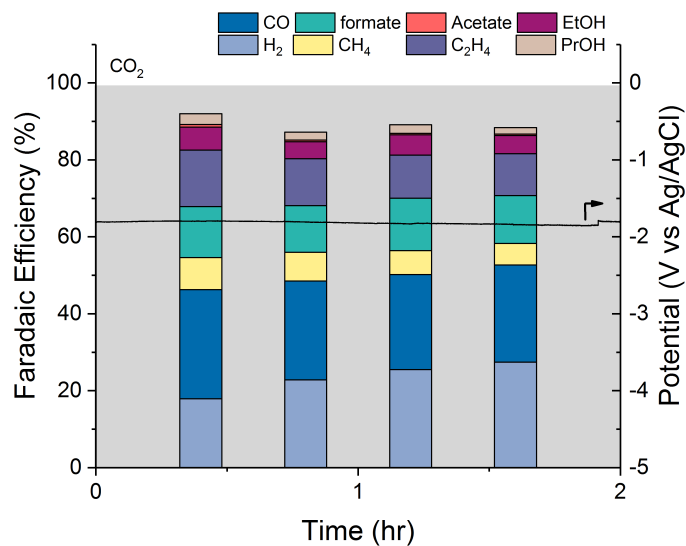


Figure E.8: CO₂ reduction over Cu catalyst in 1 M KHCO₃ at 100 mA cm⁻².

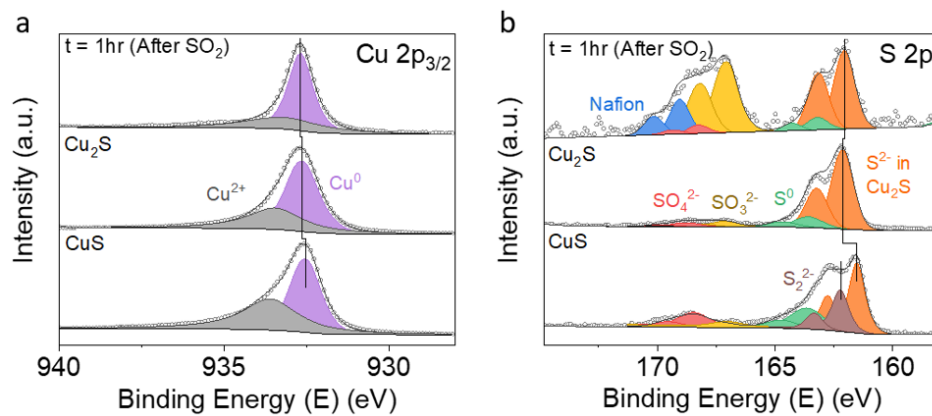


Figure E.9: XPS spectrum of a) Cu and b) S region of Cu after 1 hr electrolysis in CO₂ + 1% SO₂ experiment, Cu₂S standard, and CuS standard.

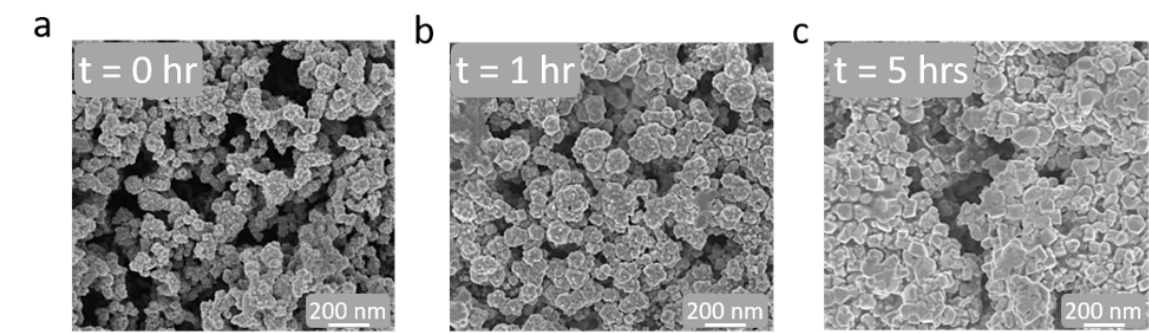


Figure E.10: SEM images of Cu catalysts at various time points of $\text{CO}_2 + 1\% \text{SO}_2$ experiment.

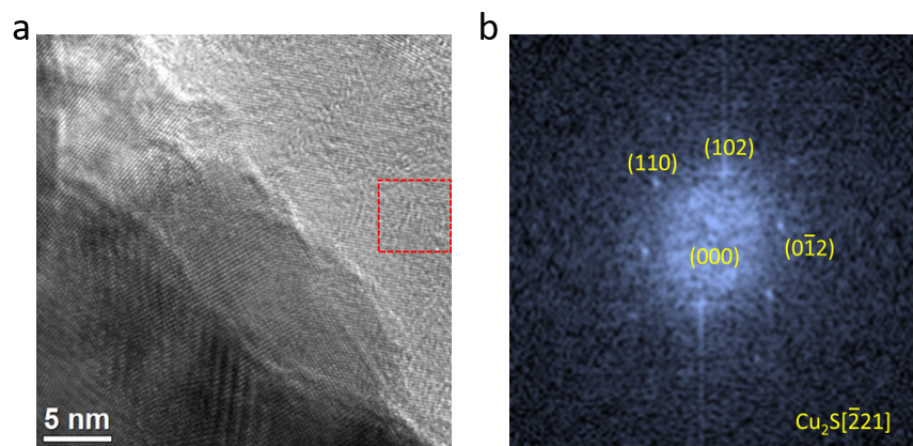


Figure E.11: a) HRTEM of Cu_2S on particle surface and b) corresponding FFT pattern of the selected area marked in the red box.

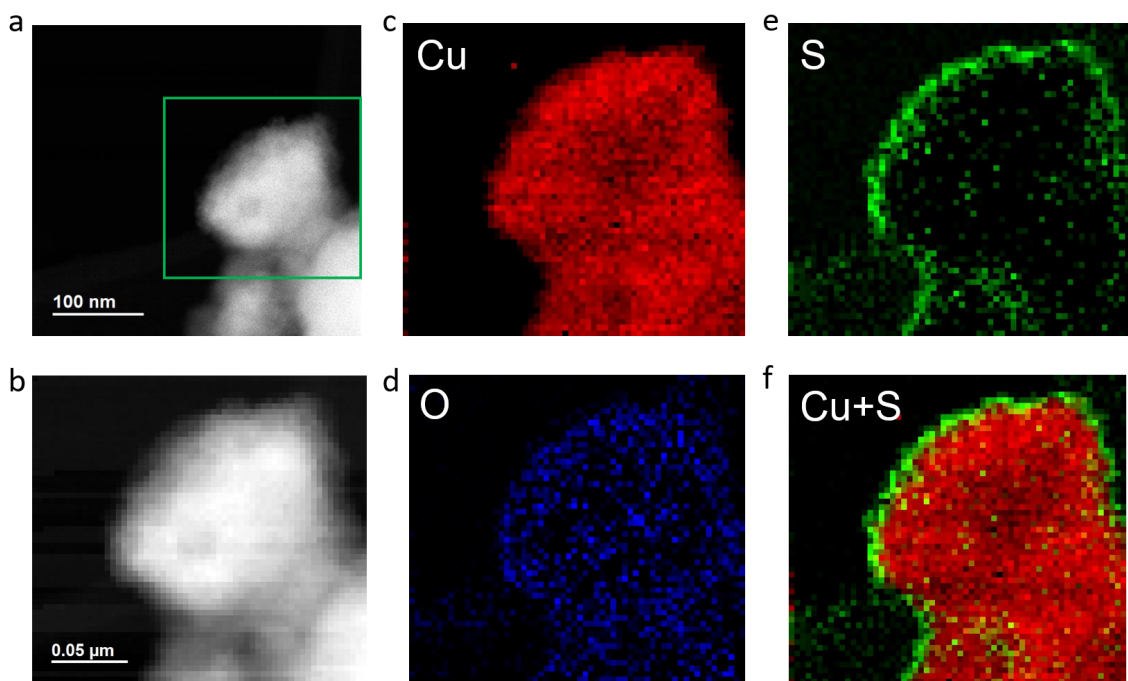


Figure E.12: Additional HAADF-STEM images and EELS mapping of Cu catalyst after 1 hour of electrolysis in $\text{CO}_2 + 1\% \text{SO}_2$ experiment.

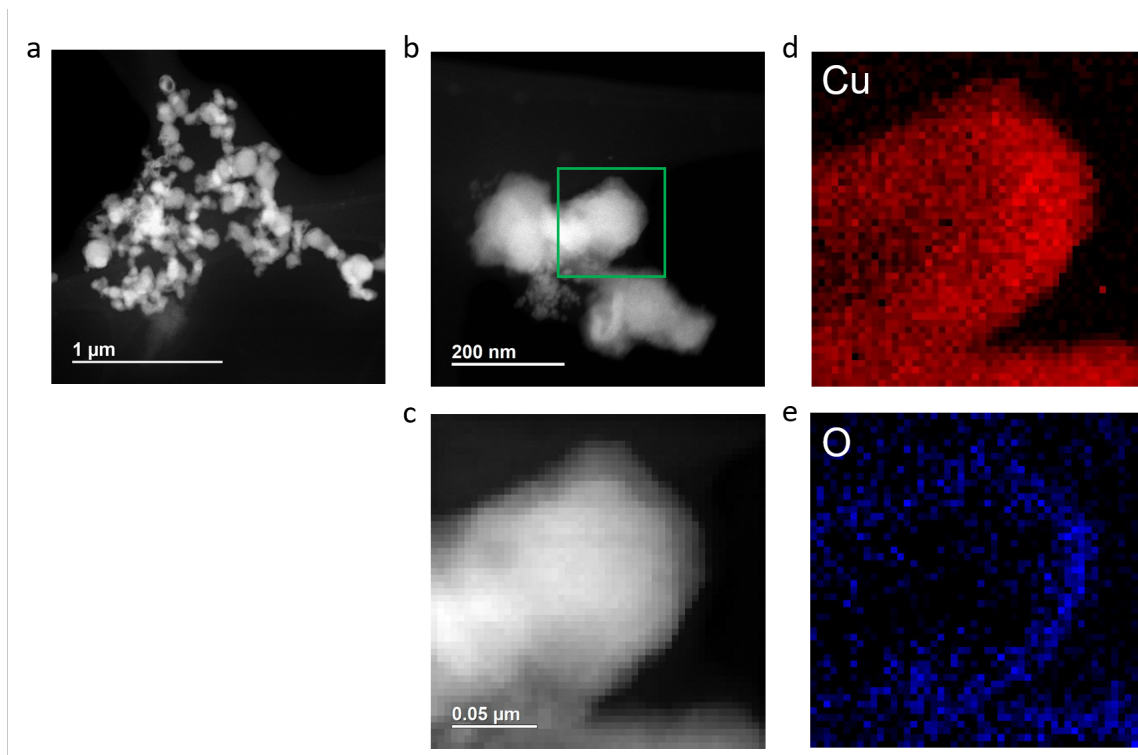


Figure E.13: HAADF-STEM images and EELS mapping of as-prepared Cu catalyst.

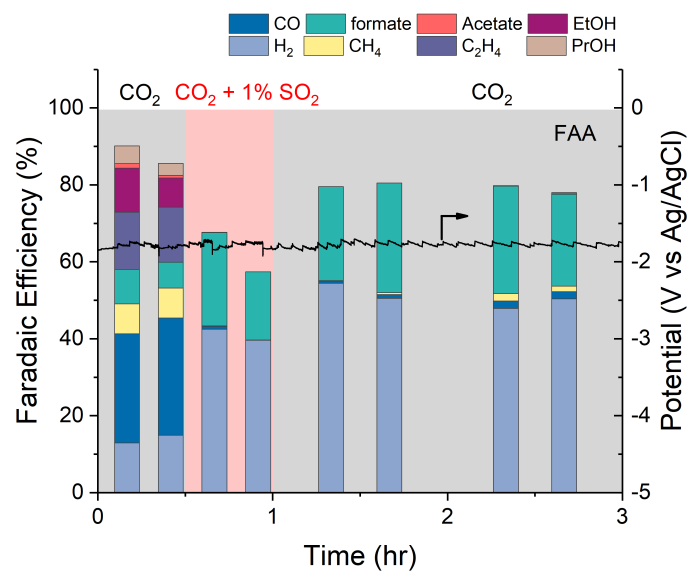


Figure E.14: CO₂ reduction over Cu catalyst with FAA ionomer in 1 M KHCO₃ at 100 mA cm⁻².

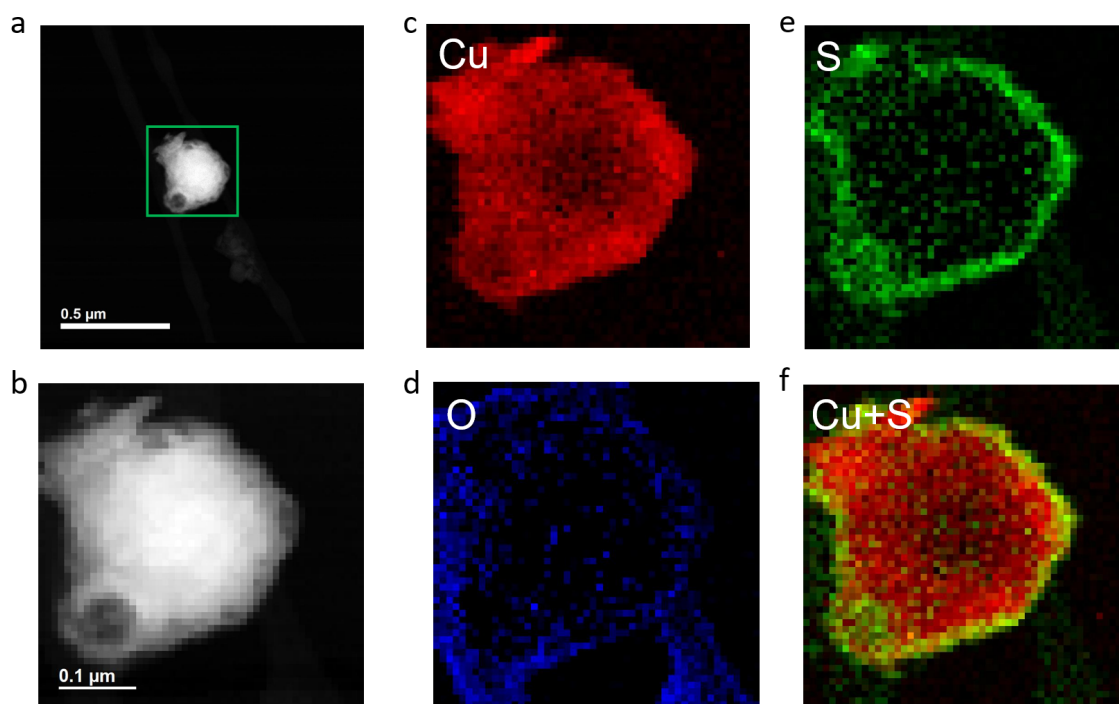


Figure E.15: HAADF-STEM images and EELS mapping of Cu catalyst after 5 hour of electrolysis in $\text{CO}_2 + 1\% \text{SO}_2$ experiment.

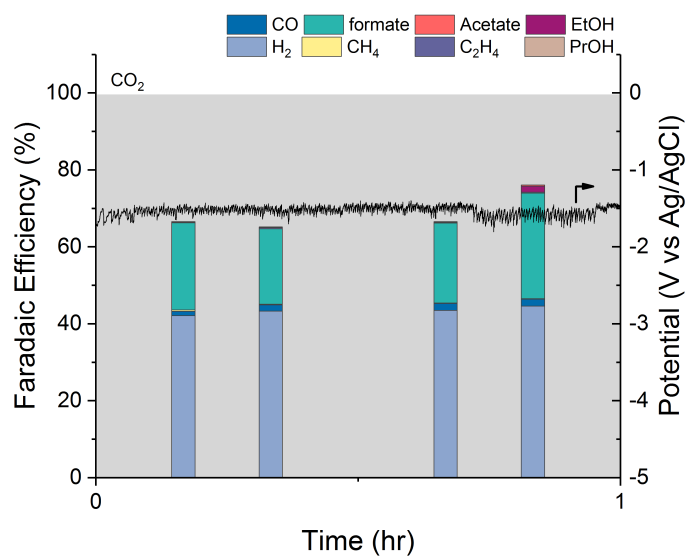


Figure E.16: CO₂ reduction over commercial Cu₂S particles in 1 M KHCO₃ at 100 mA cm⁻².

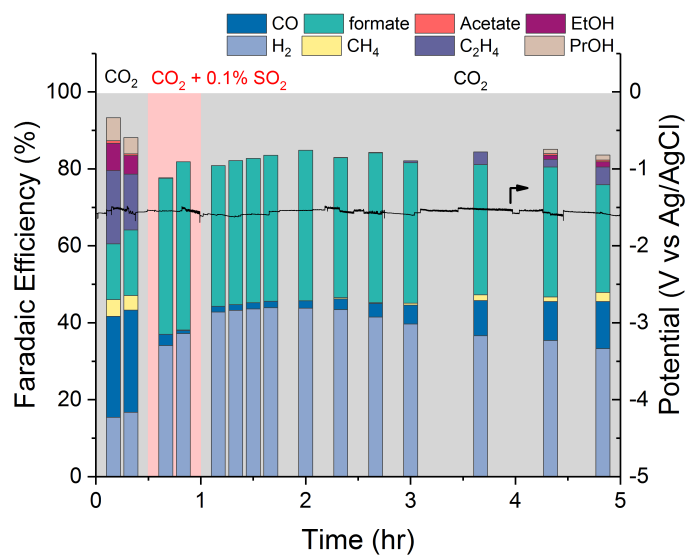


Figure E.17: The performance of Cu catalyst at constant current density of 100 mA cm⁻² in 1 M KHCO₃ with a feed of 0.1% SO₂ feed.

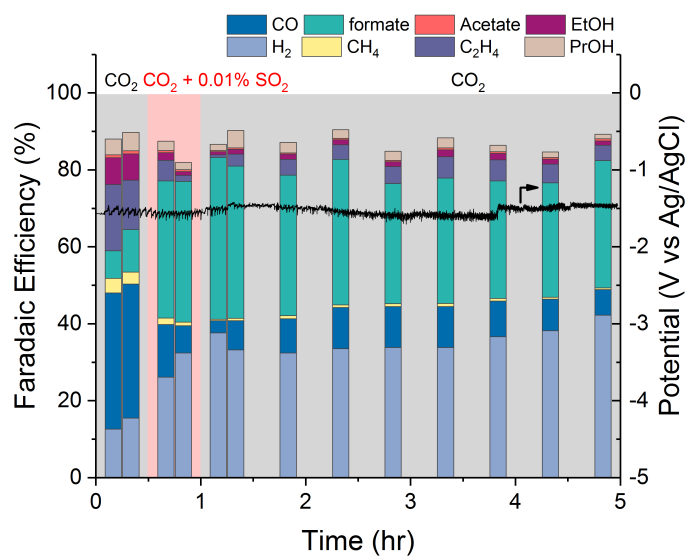


Figure E.18: The performance of Cu catalyst at constant current density of 100 mA cm^{-2} in 1 M KHCO_3 with a feed of $0.01\% \text{ SO}_2$ feed.

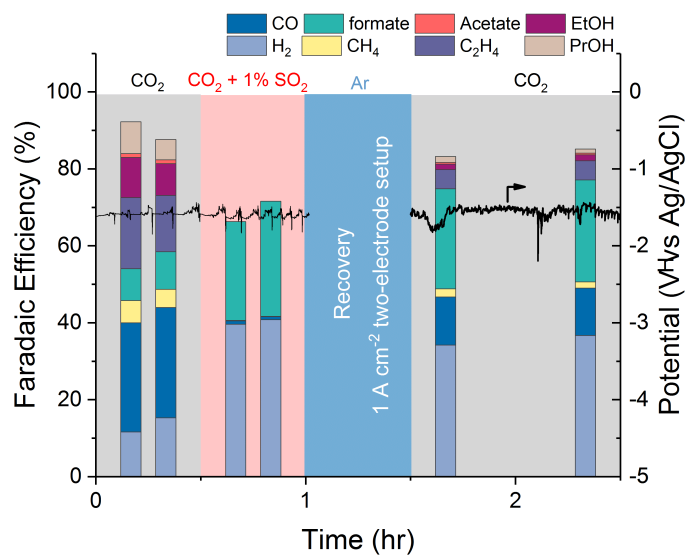


Figure E.19: Attempted recovery through local generation of H₂ on Cu catalyst.

Table E.2: Surface atomic concentrations of Cu₂S in Cu samples with different concentration of SO₂ and 1 A cm⁻² recovery obtained from XPS

Sample time (hr)	1% SO ₂ (%)	0.1% SO ₂ (%)	0.01% SO ₂ (%)	1A cm ⁻² recovery (%)
0	0	0	0	0
1	12.0	8.7	3.4	-
2.5	-	-	-	1.8
5	3.6	2.9	2.7	-

Note that atomic concentrations have been calculated based on concentrations of metals and S in S²⁻ peaks

Table E.3: DFT calculated binding energies (in eV) of HER and CO₂RR intermediates: *H, *COOH and *OCHO on various surfaces.

Adsorbates	Ag		Sn		Cu		
	Ag(111)	S-doped Ag(111)	Sn(111)	S-doped Sn(111)	Cu(111)	S-doped Cu(111)	Cu ₂ S(100)
*H	0.22	0.12	-0.77	-0.46	-0.19	-0.18	0.09
*COOH	-1.13	-1.95	-2.98	-2.00	-1.55	-1.68	-1.22
*OCHO	-2.38	-2.57	-4.33	-3.54	-2.68	-2.91	-2.46

Appendix F

ORIGINAL CONTRIBUTIONS

* denotes equal contribution

1. **Luc, W.***, Ko, B. H.*, Kattel, S., Li, S., Su, D., Chen, J. G., Jiao, F. SO₂-induced Selectivity Change in CO₂ Electroreduction. *Submitted*.
2. **Luc, W.***, Fu, X. B.*, Shi, J. J., Lv, J. J., Jouny, M., Ko, B. H., Xu, Y. B., Tu, Q., Hu, X. B., Wu, J. S., Yue, Q., Liu, Y. Y., Jiao, F., Kang, Y. J. Two-Dimensional Copper Nanosheets for Electrochemical Reduction of Carbon Monoxide to Acetate. *Nature Catalysis* (in press).
3. Sriramagiri, G. M., **Luc, W.**, Jiao, F., Ayers, K. E., Dobson, K. D., Hegedus, S. Computation and assessment of solar electrolyzer field performance: comparing coupling strategies. *Sustainable Energy & Fuels* 3, 422-430 (2019).
4. Lv, J. J.*, Jouny, M.*, **Luc, W.**, Zhu, W. L., Zhu, J. J., Jiao, F. A Highly Porous Copper Electrocatalyst for Carbon Dioxide Reduction. *Advanced Materials* 30, 1803111 (2018).
5. Jouny, M., **Luc, W.**, Jiao, F. High-rate electroreduction of carbon monoxide to multi-carbon products. *Nature Catalysis* 1, 748-755 (2018).
6. **Luc, W.**, Jiang, Z., Chen, J. G., Jiao, F. Role of Surface Oxophilicity in Copper-catalyzed Water Dissociation. *ACS Catalysis* 8, 9327-9333 (2018).
7. Dunwell, M.*, **Luc, W.***, Yan, Y., Jiao, F., Xu, B. Understanding Surface-Mediated Electrochemical Reactions: CO₂ Reduction and Beyond. *ACS Catalysis* 8, 8121-8129 (2018).
8. **Luc, W.**, Jouny, M., Rosen, J., Jiao, F. Carbon Dioxide Splitting using an Electro-Thermochemical Hybrid Looping Strategy. *Energy & Environmental Science* 11, 2928-2934 (2018).
9. Jouny, M., **Luc, W.**, Jiao, F. General Techno-Economic Analysis of CO₂ Electrolysis Systems. *Industrial & Engineering Chemistry Research* 57, 2165-2177 (2018).

10. Sriramagiri, G. M., Ahmed, N., **Luc, W.**, Dobson, K. D., Hegedus, S. S., Jiao, F. Toward a Practical Solar-Driven CO₂ Flow Cell Electrolyzer: Design and Optimization. *ACS Sustainable Chemistry & Engineering* 5, 10959-10966 (2017).
11. **Luc, W.** & Jiao, F. Nanoporous Metals as Electrocatalysts: State-of-the-Art, Opportunities, and Challenges. *ACS Catalysis* 7, 5856-5861 (2017).
12. **Luc, W.**, Collins, C., Wang, S. W., Xin, H. L., He, K., Kang, Y. J., Jiao, F. Ag-Sn bimetallic catalyst with a core-shell structure for CO₂ reduction. *Journal of the American Chemical Society* 139, 1885-1893 (2017).
13. **Luc, W.**, Rosen, J., Jiao, F. An Ir-based anode for a practical CO₂ electrolyzer. *Catalysis Today* 288, 79-84 (2017).
14. **Luc, W.** & Jiao, F. Synthesis of nanoporous metals, oxides, carbides, and sulfides: beyond nanocasting. *Accounts of Chemical Research* 49, 1351-1358 (2016).
15. Lu, Q.*, Chen, C.-J.*, **Luc, W.**, Chen, J. G., Bhan, A., Jiao, F. Ordered mesoporous metal carbides with enhanced anisole hydrodeoxygenation selectivity. *ACS Catalysis* 6, 3506-3514 (2016).

Appendix G
COPYRIGHT PERMISSIONS

This appendix contains the copyright permissions for all figures and text reproduced in this dissertation.

Permission to reprint figures and text as part of Chapter 1. Blanket permission is granted for all figures and text. Figure 1.2 was reproduced in part with permission from Jouny, M., Luc, W., Jiao, F. General Techno-Economic Analysis of CO₂ Electrolysis Systems. *Industrial & Engineering Chemistry Research* 57, 2165-2177 (2018). doi:10.1021/acs.iecr.7b03514 Copyright 2018 American Chemical Society.



RightsLink®

Home Account Info Help



Title: General Techno-Economic Analysis of CO₂ Electrolysis Systems
Author: Matthew Jouny, Wesley Luc, Feng Jiao
Publication: Industrial & Engineering Chemistry Research
Publisher: American Chemical Society
Date: Feb 1, 2018
Copyright © 2018, American Chemical Society

Logged in as:

Wesley Luc

LOGOUT

PERMISSION/LICENSE IS GRANTED FOR YOUR ORDER AT NO CHARGE

This type of permission/license, instead of the standard Terms & Conditions, is sent to you because no fee is being charged for your order. Please note the following:

- Permission is granted for your request in both print and electronic formats, and translations.
- If figures and/or tables were requested, they may be adapted or used in part.
- Please print this page for your records and send a copy of it to your publisher/graduate school.
- Appropriate credit for the requested material should be given as follows: "Reprinted (adapted) with permission from (COMPLETE REFERENCE CITATION). Copyright (YEAR) American Chemical Society." Insert appropriate information in place of the capitalized words.
- One-time permission is granted only for the use specified in your request. No additional uses are granted (such as derivative works or other editions). For any other uses, please submit a new request.

BACK

CLOSE WINDOW

Copyright © 2019 Copyright Clearance Center, Inc. All Rights Reserved. [Privacy statement](#). [Terms and Conditions](#). Comments? We would like to hear from you. E-mail us at customercare@copyright.com

Permission to reprint figures and text as part of Chapter 3. Blanket permission is granted for all figures and text. Chapter 3 was reproduced with permission from Luc, W., Jiang, Z., Chen, J. G., Feng, J. Role of Surface Oxophilicity in Copper-catalyzed Water Dissociation. *ACS Catalysis* 8, 9327-9333 (2018). doi:10.1021/acscatal.8b01710 Copyright 2018 American Chemical Society.



RightsLink®

Home

Account Info

Help



ACS Publications
Most Trusted. Most Cited. Most Read.

Title: Role of Surface Oxophilicity in Copper-Catalyzed Water Dissociation
Author: Wesley Luc, Zhao Jiang, Jingguang G. Chen, et al
Publication: ACS Catalysis
Publisher: American Chemical Society
Date: Oct 1, 2018
Copyright © 2018, American Chemical Society

Logged in as:

Wesley Luc

LOGOUT

PERMISSION/LICENSE IS GRANTED FOR YOUR ORDER AT NO CHARGE

This type of permission/license, instead of the standard Terms & Conditions, is sent to you because no fee is being charged for your order. Please note the following:

- Permission is granted for your request in both print and electronic formats, and translations.
- If figures and/or tables were requested, they may be adapted or used in part.
- Please print this page for your records and send a copy of it to your publisher/graduate school.
- Appropriate credit for the requested material should be given as follows: "Reprinted (adapted) with permission from (COMPLETE REFERENCE CITATION). Copyright (YEAR) American Chemical Society." Insert appropriate information in place of the capitalized words.
- One-time permission is granted only for the use specified in your request. No additional uses are granted (such as derivative works or other editions). For any other uses, please submit a new request.

BACK

CLOSE WINDOW

Copyright © 2019 Copyright Clearance Center, Inc. All Rights Reserved. [Privacy statement](#). [Terms and Conditions](#).
Comments? We would like to hear from you. E-mail us at customercare@copyright.com

Permission to reprint figures and text as part of Chapter 4.

Material published by the Royal Society of Chemistry and other publishers is subject to all applicable copyright, database protection, and other rights. Therefore, for any publication, whether printed or electronic, permission must be obtained to use material for which the author(s) does not already own the copyright. This material may be, for example, a figure, diagram, table, photo or some other image.

Author reusing their own work published by the Royal Society of Chemistry

You do not need to request permission to reuse your own figures, diagrams, etc, that were originally published in a Royal Society of Chemistry publication. However, permission should be requested for use of the whole article or chapter except if reusing it in a thesis. If you are including an article or book chapter published by us in your thesis please ensure that your co-authors are aware of this.

Reuse of material that was published originally by the Royal Society of Chemistry must be accompanied by the appropriate acknowledgement of the publication. The form of the acknowledgement is dependent on the journal in which it was published originally, as detailed in 'Acknowledgements'.

The following paper was reproduced in this dissertation by the permission of the Royal Society of Chemistry:

Luc, W., Jouny, M., Rosen, J., Jiao, F. Carbon Dioxide Splitting Using an Electro-thermochemical Hybrid Lopping Strategy, *Energy & Environmental Science* 11, 2928-2934 (2018). doi:10.1039/C8EE00532J

Permission to reprint figures and text as part of Chapter 5. Chapter 5 was reproduced with permission from Luc, W., Fu, X. B., Shi, J. J., Lv, J. J., Jouny, M., Ko, B. H., Xu, Y. B., Tu, Q., Hu, X. B., Wu, J. S., Yue, Q., Liu, Y. Y., Jiao, F., Kang, Y. J. Two-Dimensional Copper Nanosheets for Electrochemical Reduction of Carbon Monoxide to Acetate. *Nature Catalysis* (in press).



RightsLink®

Home

Account Info

Help



SPRINGER NATURE

Title: Two-dimensional copper nanosheets for electrochemical reduction of carbon monoxide to acetate

Author: Wesley Luc et al

Publication: Nature Catalysis

Publisher: Springer Nature

Date: Apr 8, 2019

Copyright © 2019, Springer Nature

Logged in as:

Wesley Luc

Account #:

3001429837

LOGOUT

Author Request

If you are the author of this content (or his/her designated agent) please read the following. If you are not the author of this content, please click the Back button and select no to the question "Are you the Author of this Springer Nature content?".

Ownership of copyright in original research articles remains with the Author, and provided that, when reproducing the contribution or extracts from it or from the Supplementary Information, the Author acknowledges first and reference publication in the Journal, the Author retains the following non-exclusive rights:

To reproduce the contribution in whole or in part in any printed volume (book or thesis) of which they are the author(s).

The author and any academic institution, where they work, at the time may reproduce the contribution for the purpose of course teaching.

To reuse figures or tables created by the Author and contained in the Contribution in oral presentations and other works created by them.

To post a copy of the contribution as accepted for publication after peer review (in locked Word processing file, of a PDF version thereof) on the Author's own web site, or the Author's institutional repository, or the Author's funding body's archive, six months after publication of the printed or online edition of the Journal, provided that they also link to the contribution on the publisher's website.

Authors wishing to use the published version of their article for promotional use or on a web site must request in the normal way.

If you require further assistance please read Springer Nature's online [author reuse guidelines](#).

For full paper portion: Authors of original research papers published by Springer Nature are encouraged to submit the author's version of the accepted, peer-reviewed manuscript to their relevant funding body's archive, for release six months after publication. In addition, authors are encouraged to archive their version of the manuscript in their institution's repositories (as well as their personal Web sites), also six months after original publication.

v1.0

BACK

CLOSE WINDOW

Copyright © 2019 [Copyright Clearance Center, Inc.](#) All Rights Reserved. [Privacy statement](#). [Terms and Conditions](#). Comments? We would like to hear from you. E-mail us at customercare@copyright.com

Permission to reprint figures and text as part of Chapter 6 from submitted work that has not yet been published. Chapter 6 is reproduced with permission from the Journal of American Chemical Society, submitted for publication. Unpublished work copyright 2019 American Chemical Society.